

Experimental deformation of forsterite,  
wadsleyite and ringwoodite: Implications for  
seismic anisotropy of the Earth's mantle

presented by H el ene Couvy

of the Fakult at f ur Biologie, Chemie und Geowissenschaften der  
Universit at Bayreuth and of the Universit e des Sciences et  
Technologies de Lille

A dissertation submitted in fulfilment of the requirement for the  
degrees of:

Doktor der Naturwissenschaften (Dr.rer.nat.)

and

Docteur de l'Universit e de Lille 1 (Sp ecialit e: Sciences de Mat eriaux)

1<sup>st</sup> March 2005, Bayreuth (Germany)



Experimental deformation of forsterite,  
wadsleyite and ringwoodite: Implications for  
seismic anisotropy of the Earth's mantle

Von der Fakultät für Biologie, Chemie und Geowissenschaften der  
Universität Bayreuth  
und der Université des Sciences et Technologies de Lille

zur Erlangung der Würde eines  
Doktors der Naturwissenschaften (Dr.rer.nat.)

und

Docteur de l'Université de Lille 1 (Spécialité: Sciences des Matériaux)  
genehmigte Dissertation

vorgelegt von

Hélène Couvy

Bayreuth, im März 2005

Prüfungsausschuss

Prof. J. Breu (Universität Bayreuth)	Vorsitzender
Prof. F. Langenhorst (Universität Bayreuth)	deutscher Gutachter
Prof. P. Cordier (Universität Lille)	französischer Gutachter
Prof. D. C. Rubie (Universität Bayreuth)	
Prof. H. Leroux (Universität Lille)	



N° d'ordre: 3603 bis

Thèse en co-tutelle

présentée

à l'Université des Sciences et Technologies de Lille et à la Fakultät für

Biologie, Chemie und Geowissenschaften der Universität Bayreuth

pour l'obtention des grades de:

Docteur de l'Université de Lille 1 (Spécialité: Sciences de Matériaux)

et

Doktor der Naturwissenschaften (Dr.rer.nat.)

par Hélène Couvy

Experimental deformation of forsterite, wadsleyite  
and ringwoodite: Implications for seismic  
anisotropy of the Earth's mantle

soutenue le 1 Mars 2005 à Bayreuth, Allemagne

Jury

Prof. J. Breu (Université de Bayreuth)	Président
Prof. F. Langenhorst (Université de Bayreuth)	Rapporteur
Prof. D. Mainprice (Université de Montpellier)	Rapporteur
Prof. D.C Rubie (Université de Bayreuth)	Examineur
Prof. H. Leroux (Université de Lille)	Examineur
Prof. P. Cordier et F. Langenhorst	Directeurs de Thèse



The thesis has been co-directed by Prof. Falko Langenhorst (Bayerisches Geoinstitut, University of Bayreuth, Germany) and by Prof. Patrick Cordier (Laboratoire des Structures et Propriétés de l'Etat Solide, University of Lille, France) from September 2001 and January 2005.

Manuscript given the **1<sup>st</sup> December 2004**

Defense passed the **1<sup>st</sup> March 2005 (Bayreuth, Germany)**

I was supported by the Visiting Scientist Program of the Bayerisches Geoinstitut (17.09.2001 – 16.11.2002 and 17.11.2003 – 16.01.2004), by the EU-program “Marie Curie Host Fellowship/ Training Sites” (Contract N° HPMT-CT-2001-00231) (17.11.2002 – 16.11.2003) and by the Deutsche Forschungsgemeinschaft (Project N°: FR 1555/2-1) (17.01.2004–16.01.2005). Moreover, travels have been also funding by the French-Bavarian cooperation program (CCUFB-BFHZ) and by the German Academic Exchange Service within the bilateral French-German Procope Program.

All these financial supports are gratefully acknowledged.



Je voudrais remercier tout d'abord Patrick Cordier, initiateur de ce passionnant sujet et Falko Langenhorst pour avoir encadrer cette thèse à Bayreuth. Votre confiance et votre soutien m'ont permis d'évoluer et de m'épanouir dans mon travail. Un grand merci à Stephen Mackwell pour m'avoir accueilli au BGI. Ce travail expérimental a été possible avec à l'aide de Dan Frost et Florian Heidelbach. Merci à vous. Danke schön ! à Hubert Schulze, le magicien des lames minces et autres coupes à 45°, Georg Herrmannsdörfer et Heinz Fischer pour la réparation des pannes en tout genre et l'usinage des précieux assemblages. Un grand merci à Stefan Keyssner, Petra Ständner et Lydia Kison-Herzing pour votre grande générosité et tous les services rendus.

Le plaisir de la co-tutelle ne se limitant pas aux joies administratives, elle m'a permis de travailler dans deux labos bien différents mais qui m'ont accueillis aussi chaleureusement l'un que l'autre. Je les en remercie.

Je tiens à remercier vivement David Mainprice et Andréa Tommasi de l'université de Montpellier pour les simulations VPSC et le calcul de propriétés sismiques ainsi que pour leur précieux soutien.

Mon travail m'a amené à découvrir le monde du synchrotron et ses nuits blanches. Je voudrais remercier William Durham et Yanbin Wang pour leur aide lors les expériences menées à APS ainsi que Don Weidner, Jihua Chen et Paul Raterron pour celle mené à NSLS.

Merci à Tamás Ungár et Krisztián Nyilas de l'université de Budapest pour leurs mesures effectuées sur mes échantillons.

Enfin, ces trois années n'auraient pu être ce qu'elles ont été sans Sylvie, Tiziana, Florian, Burkhard, Fabrice, Christian ein und zwei, Julian, Fabrizio, Julien (un merci spécial pour toi qui m'a fait une place dans ton bureau et qui a supporté la rédaction), Philippe ...

Merci à David Rubie, Joseph Breu, David Mainprice et Hugues Leroux pour avoir accepté de juger ce travail.

A vous tous qui avez rendu cette thèse non seulement possible mais aussi qui l'avez transformée en un agréable moment (de plus de trois ans !), je vous remercie.

Merci à toi, Makram, pour ton immense patience ...

# Table of contents

<u>Summary</u> .....	1
<u>Zusammenfassung</u> .....	2
<u>Résumé</u> .....	5
<u>Introduction</u> .....	9
<b><u>Chapter I. Forsterite, wadsleyite and ringwoodite: structural and rheological data</u></b>	
I – Forsterite: pure magnesium end-member of olivine.....	19
II – Wadsleyite.....	23
III – Ringwoodite.....	27
<b><u>Chapter II. Experimental techniques and developments.</u></b>	
I – High pressure techniques: presentation of apparatus and developments.	33
I.1 – Deformation-DIA (D-DIA).....	34
I.2 – Kawai-type multianvil apparatus.....	36
I.2.1 – Presentation of the press.....	36
I.2.2 – Using the multianvil press as a deformation apparatus.....	42
I.3 – Experimental developments and calibration performed during this study.....	44
I.3.1 – Developments performed for the D-DIA press.....	44
I.3.2 – Developments performed for deformation in the Kawai-type multianvil press.....	50
I.4 – Presentation of the starting materials ( $Mg_2SiO_4$ ).....	55
II – <i>In situ</i> measurements in the D-DIA.....	55
II.1 – Technical setup.....	56

II.2 – Strain measurement.....	58
II.3 – Lattice strains analysis.....	59
III – Technical analyses on recovered samples.....	61
III.1 – Scanning Electron Microscopy (SEM) and Electron BackScattering Diffraction (EBSD).....	62
III.1.1- Sample preparation for SEM and EBSD.....	62
III.1.2 – SEM and imaging.....	62
III.1.3 – Electron BackScattering Diffraction technique.....	63
III.2 – Transmission Electron Microscopy (TEM).....	64
III.2.1 – Sample preparation for TEM.....	64
III.2.2 – Presentation of the microscope.....	65
III.2.3 – Diffraction mode: Selected Area Electron Diffraction (SAED).....	66
III.2.4 – Imaging mode and observation of dislocations.....	67
III.3 – Other analytical methods.....	69
III.3.1 – Micro-Raman spectroscopy.....	69
III.3.2 – Fourier Transform InfraRed spectroscopy (FTIR).....	69

### **Chapter III. Results**

I – Deformation of forsterite at high pressure.....	73
I.1 – Deformation experiments using the Kawai-type multianvil apparatus..	73
I.1.1 – Strain marker rotation and piston displacement.....	75
I.1.2 – Microstructural characterisation: SEM and EBSD.....	77
I.1.3 – Microstructural characterisation: X-ray peak broadening.....	89
I.1.4 – Microstructural characterisation: TEM.....	91
I.1.5 – InfraRed spectrometry characterisation.....	94
I.2 – Deformation experiments using the D-DIA apparatus.....	96
I.2.1 – Starting material.....	96
I.2.2 – Annealing experiments under hydrostatic pressure in the D-DIA.....	98

I.2.3 – Deformation experiments performed at the Bayerisches Geoinstitut.	100
I.2.4 – Deformation experiments performed at APS.....	104
I.2.5 – Deformation experiments performed at NSLS.....	109
II – Deformation on wadsleyite.....	114
II.1 – Phase identification.....	115
II.2 – SEM and EBSD characterisation.....	117
II.3 – TEM investigation.....	129
II.4 – InfraRed spectrometry characterisation.....	130
III – Deformation of ringwoodite.....	131
III.1 – Phase identification.....	132
III.2 – SEM and EBSD characterisation.....	133
III.3 – TEM characterisation.....	137
IV – Influence of a phase transformation on plastic deformation: the case of the forsterite-wadsleyite transformation.....	139
IV.1 – SEM and EBSD characterisation.....	141
IV.2 – TEM characterisation.....	148

## **Chapter IV. Discussion**

I – Deformation experiments at high pressure and temperature: progresses and limits.....	153
I.1 – Deformation in the D-DIA.....	154
I.1.1 – Sample preparation.....	154
I.1.2 – Deformation history in D-DIA experiment.....	154
I.2 – Deformation in the Kawai-type multianvil apparatus.....	158
I.2.1 – Starting material.....	158
I.2.2 – Deformation history in a shear deformation experiment.....	159
I.3 – Conclusion on deformation techniques under high pressure and temperature.....	165

II – Deformation of Mg <sub>2</sub> SiO <sub>4</sub> polymorphs under upper mantle and transition zone.....	167
II.1 – Deformation mechanism of forsterite at 11 GPa and 1400°C.....	167
II.1.1 – Changing the deformation mechanisms with pressure.....	167
II.1.2 – Physical origin for a pressure sensitivity of the olivine slip system.....	174
II.1.3 – Linking microscopic to macroscopic: crystallographic preferred orientation.....	176
II.1.4 – Conclusion and open questions.....	183
II.2 – Deformation of wadsleyite and ringwoodite under pressure – temperature conditions of the transition zone.....	184
II.2.1 – Deformation of wadsleyite at 16 GPa–1400°C and effect of the phase transformation forsterite wadsleyite on deformation.....	184
II.2.1.1 – Deformation of wadsleyite at 16GPa and 1400°C.....	185
II.2.1.2 – Influence of the forsterite → wadsleyite phase transformation.....	194
II.2.2 – Deformation of ringwoodite at 22 GPa and 1300°C.....	197
II.3 – Main conclusions on the deformation of the Mg <sub>2</sub> Si <sub>4</sub> system.....	203
III – Implications for the seismic anisotropy of the Earth’s upper mantle and the transition zone.....	204
III.1 – Pressure sensitivity of olivine slip systems: implications of the seismic anisotropy of the lowermost upper mantle.....	204
III.2 – Predicting strain-induced seismic anisotropy in the upper part of the transition zone.....	212
III.3 – Conclusion.....	220
<b><u>Conclusions and open questions</u></b> .....	223

**Appendix**

Appendix I – Strain calculation from the strain marker rotation.....	229
--	-----

Appendix II – X-ray diffraction peak broadening analysis technique and evaluation of strain anisotropy..... 233

Appendix III – Crystal preferred orientation modelling: ViscoPlastic Self Consistent (VPSC) method..... 237

**References**..... 243

**Erklärung**..... 265

**Articles**..... 267



# Summary

The rheological properties of the major minerals of the Earth's mantle are still not well constrained. However, these properties are crucial for the understanding of a wide range of processes in the Earth's interior such as mantle convection. The purpose of this work is to address the issue of the rheology of the lowermost upper mantle and of the transition zone through the mechanical properties at high pressure of olivine (with forsterite composition  $\text{Mg}_2\text{SiO}_4$ ) and of its high-pressure polymorphs wadsleyite and ringwoodite. Indeed, the properties of the Earth's mantle can be inferred as a first approximation from the mechanical properties of those polymorphs which volumetrically dominate the mineralogy of the region of concern.

Deformation experiments have been performed on hot-pressed forsterite samples and on pre-synthesized wadsleyite and ringwoodite samples under pressure conditions of the Earth's mantle and at 1300–1400°C. The possible influence of the phase transformation from forsterite to wadsleyite on rheology has been also investigated. Deformation has been achieved by shear using the Kawai-type multianvil apparatus. Complementary experiments on forsterite have been performed in the newly developed Deformation-DIA. Some of them have been carried out on a synchrotron beam line to perform *in-situ* stress and strain measurements. In order to gain a maximum of information on the deformation mechanisms and on the Crystallographic Preferred Orientation (CPO), a special attention has been devoted to the microstructural characterisation of the samples. Electron BackScattering Diffraction (ESBD) and Transmission Electron Microscope (TEM) have been mainly used.

An important pressure-induced change in deformation mechanism is shown in forsterite. The deformation of forsterite at high pressure and temperature is dominated by the  $[001]\{hk0\}$  slip system rather than the  $[100](010)$  glide which is extensively observed at low pressure and high temperature..

Concerning the high-pressure polymorphs, their plastic behaviour has been studied with a strong emphasis on the formation of CPO. ViscoPlastic Self Consistent (VPSC) modelling is used to link the CPO with known elementary deformation mechanisms of these phases. The main features of the CPO of wadsleyite are characterized by the alignment of the  $[100]$  axes parallel to the shear direction and the alignment of the  $[001]$  axes toward the normal to the shear plane. Too many uncertainties remain on the ringwoodite CPO for them being used to interpret seismic anisotropy.

Finally, we suggest that strain-induced CPO might be responsible for the seismic anisotropy observed in the lowermost upper mantle and in the upper part of the transition zone. The low seismic anisotropy of the lowermost upper mantle can be explained from the slip system change in forsterite and the CPO of wadsleyite point toward a dominant tangential flow in the upper part of the transition zone.

# Zusammenfassung

Die rheologischen Eigenschaften der Hauptminerale des Erdmantels sind derzeit nahezu unbekannt. Die Kenntnis dieser Eigenschaften ist aber entscheidend für das Verständnis vieler Prozesse und Eigenschaften des Erdmantels wie Konvektion, Entwicklung seismischer Anisotropien oder Festigkeit subduzierter Lithosphäre. Ziel dieser Arbeit ist es, die Rheologie des unteren Bereichs des oberen Erdmantels und der Übergangszone über die mechanischen Eigenschaften von Olivin und seiner Hochdruckpolymorphe Wadsleyit und Ringwoodit ( $\text{Mg}_2\text{SiO}_4$ ) – die volumenmäßig wichtigsten Phasen dieses Regimes – abzuleiten. Die Eigenschaften des Erdmantels können nämlich in erster Näherung aus den mechanischen Eigenschaften dieser Polymorphe berechnet werden.

Deformationsexperimente wurden bei Drucken des Erdmantels und bei Temperaturen von 1300–1400°C an gesintertem Forsterit und zuvor synthetisierten Wadsleyit- und Ringwoodit-Proben durchgeführt. Der mögliche Einfluß der Phasenumwandlung von Olivin in Wadsleyit auf das rheologische Verhalten wurde ebenso untersucht. Die Deformation wurde durch Scherung der Proben in einer Vielstempelpresse vom Typ Kawai erreicht. Komplementäre *in-situ* Experimente wurden mit einer neu entwickelten Deformations-DIA-Apparatur an Forsterit durchgeführt. Der thermomechanische Verlauf der Deformation wurde erstmals in den Hochdruckpressen durch zeitaufgelöste Experimente dokumentiert. Um ein Maximum an Information über die Deformationsmechanismen und die kristallographische Vorzugsorientierung (CPO) zu erhalten, wurde auf die Charakterisierung der zurückgewonnenen Proben besonders Wert gelegt.

Beugung rückgestreuter Elektronen (EBSD) und Transmissionselektronenmikroskopie (TEM) kamen hierbei zum Einsatz.

Die Hochdruckexperimente an Forsterit belegen eine druckinduzierte Änderung des Deformationsmechanismus. Die Deformation von Forsterit ist bei hohen Drucken und Temperaturen durch das  $[001]\{hk0\}$  Gleitsystem geprägt, während bei niedrigen Drucken und Temperaturen üblicherweise  $[100]$ -Gleitung vorherrscht.

Bei den Hochdruckpolymorphen wurde die plastische Deformation im wesentlichen über die Ausbildung von kristallographischen Vorzugsorientierungen (CPO) erfasst. Viskoplastische eigen-konsistente Modellierung (VPSC) wurde genutzt, um die kristallographische Vorzugsorientierung (CPO) durch bekannte elementare Deformationsmechanismen zu erklären. Die Hauptmerkmale der kristallographischen Vorzugsrichtungen von Wadsleyit sind die Ausrichtung der  $[100]$ -Achsen parallel zur Scherrichtung und die Ausrichtung der  $[001]$ -Achsen senkrecht zur Scherebene. Im Gegensatz dazu entwickelte sich in Experimenten mit Ringwoodit keine deutliche kristallographische Vorzugsrichtung (CPO).

Die deformationsbedingten kristallographischen Vorzugsrichtungen (CPO) liefern schließlich eine Erklärung für die beobachteten seismischen Anisotropien im unteren Teil des oberen Erdmantels und in der Übergangszone. Die geringe seismische Anisotropie des unteren Teils des oberen Erdmantels kann durch eine Änderung des Gleitsystems in Forsterit erklärt werden, während die kristallographische Vorzugsrichtung von Wadsleyit auf tangenciales Fließen im oberen Teil der Übergangszone hindeutet.

# Résumé

L'étude de la plasticité des minéraux du manteau terrestre sous pression joue un rôle majeur dans la compréhension et la modélisation des grands processus actifs à l'intérieur de la Terre tels que la convection mantellique. Cependant, les propriétés des minéraux du manteau sont toujours, à ce jour, mal connues. L'objectif de ce travail est d'étudier la rhéologie de la partie inférieure du manteau supérieur et de la zone de transition, à travers l'étude des propriétés mécaniques de la forsterite ( $\text{Mg}_2\text{SiO}_4$ ) et de ses deux polymorphes de haute pression (wadsleyite et ringwoodite). En effet, ces phases sont les constituants principaux des zones étudiées et on peut considérer, en première approximation, qu'elles contrôlent les propriétés du manteau.

Des échantillons de forsterite frittés et de wadsleyite et de ringwoodite synthétisés sous pression ont été déformés dans les conditions de pression du manteau et à 1300–1400°C. L'influence de la transformation de phase forsterite–wadsleyite sur la rhéologie a également été étudiée. Les expériences de déformation en cisaillement ont été menées dans la presse multi-enclumes de type « Kawai ». Quelques expériences complémentaires sur la forsterite ont été menées dans la nouvelle presse Deformation–DIA. Certaines ont été réalisées sur synchrotron afin de mesurer contraintes et déformations *in situ*. Les microstructures des échantillons obtenus ont été caractérisées par Microscopie Electronique en Transmission et leurs textures ont été déterminées à l'aide de la technique de diffraction des électrons rétrodiffusés.

En ce qui concerne la forsterite, nous avons mis en évidence un important changement de système de glissement induit par la pression. A haute pression et température, la déformation de la forsterite est dominée par le glissement  $[001]\{hk0\}$  alors que le glissement  $[100]$  a largement été observé à basse pression et haute température dans les travaux antérieurs.

La plasticité de la wadsleyite et de la ringwoodite a été étudiée principalement aux travers des textures. La méthode de simulation ViscoPlastic Self Consistent a été utilisée pour faire le lien entre les textures et les mécanismes de déformation supposés pour ces deux phases. Les grandes caractéristiques des textures de la wadsleyite sont l'alignement des axes  $[100]$  avec la direction de cisaillement alors que les axes  $[001]$  sont normaux au plan de cisaillement. Pour la ringwoodite, aucune texture fiable ne peut être proposée.

Enfin, les textures produites par la déformation plastique des trois polymorphes peuvent être proposées comme étant à l'origine de l'anisotropie sismique du manteau supérieur et de la zone de transition. Le changement de système de glissement dominant de la forsterite permet d'expliquer la faible anisotropie sismique observée dans la partie inférieure du manteau supérieur et la texture de la wadsleyite indique un écoulement horizontal dominant dans la partie supérieure de la zone de transition.

# Introduction



## INTRODUCTION

---

It is now agreed that many geophysical and geological phenomena at the surface of the Earth are the consequences of thermal convection in the underlying mantle. Direct consequences include the plaque tectonics, volcanism in its various tectonic setting, seismic activity.... The thermal convection is itself driven by the internal heat of the Earth. Mantle convection is then a fundamental component of the dynamics of the Earth's mantle and it is one of the most puzzling problems of modern geophysics. The current understanding of the nature of mantle convection is based on a combination of observations made at the surface and depends on our knowledge of the physical properties of mantle materials.

The radial structure of the Earth is mainly determined from the seismic observations. As the seismic waves velocities (P waves and S waves) depend on mineral properties (namely density and elastic properties), a density profile of the Earth can be established from the inversion of the travel time data of seismic waves. Seismological models display the primary structures of the inner Earth. The profile determined from PREM (Preliminary Reference Earth Model, Dziewonski and Anderson, 1981) is presented Figure 1. We can see several velocity or density jumps that corresponds to the main discontinuities between upper mantle, transition zone and lower mantle (the discontinuities between lower mantle, outer and inner core are not represented).

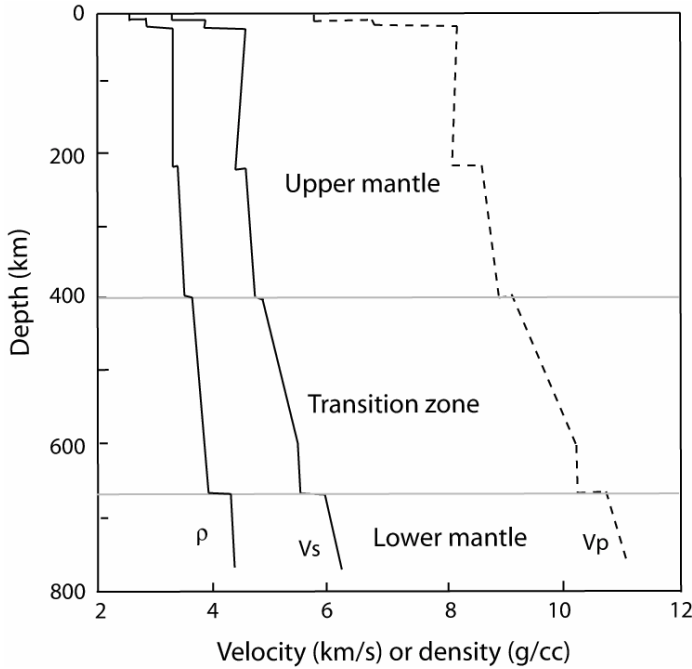


Figure 1 -Seismic velocities and density function of depth. PREM from Dziewonski and Anderson (1981).

Although, seismic observations provide information about the radial structure of the mantle, they do not constrain the chemical composition. As the dynamic of the mantle is largely controlled by the rheological properties of its main components, the mineralogy of the whole mantle has to be known.

A classical model of global composition for the mantle has been proposed by Green and Ringwood (1963): it is named pyrolite. This is a hypothetic composition derived from experimental and petrologic studies of the complementary relationship between basaltic magna and refractory peridotite. From the pyrolitic model, the mineralogical composition of the mantle (Figure 2) can be deduced. The upper mantle is composed of olivine

**INTRODUCTION**

---

(Mg,Fe)<sub>2</sub>SiO<sub>4</sub>, pyroxene (Ca,Mg,Fe)(Mg,Fe,Al)(SiAl)<sub>2</sub>O<sub>6</sub> and garnet (Ca,Mg,Fe)<sub>3</sub>(Mg,Fe,Al)<sub>2</sub>(SiAl)<sub>3</sub>O<sub>12</sub> (see Agee (1998)). At ca. 410 km, the phase transition olivine-wadsleyite occurs. In the transition zone, clinopyroxenes dissolve in the garnets. Deeper (at ca. 520 km), wadsleyite is transformed to ringwoodite. Then, garnet and ringwoodite are decomposed in two kinds of perovskite (Mg,Fe,Al)(Si,Al)O<sub>3</sub> and CaSiO<sub>3</sub> and in magnesiowüstite (Mg, Fe)O.

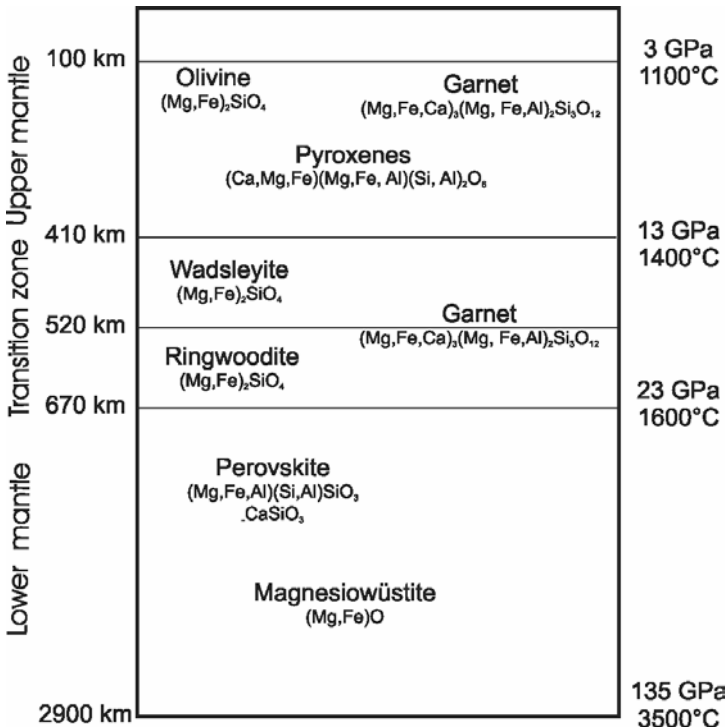


Figure 2 – Simplified mineralogical model of the Earth's mantle.

The phase transformations which are experienced by pyrolitic composition between 100 and 800 km can account for the seismic P and S velocity profile throughout this region (Figure 3). Therefore, the pyrolitic composition can be considered as a relevant first order model for the Earth's mantle composition.

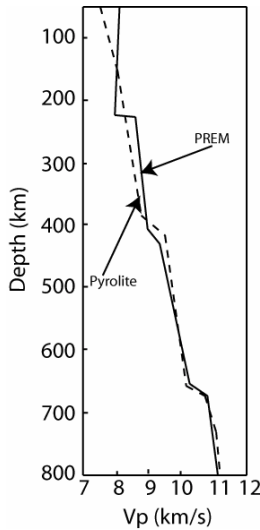


Figure 3 - Compressional velocity (P-waves) versus depth diagram comparing pyrolite velocity with seismic velocity model PREM (from Agee (1998))

Another important body of evidence is seismic anisotropy. It is illustrated by the variation of shear wave polarization anisotropy (Figure 4). The mantle presents a strong anisotropy from the crust to about 1000 km depth and then in the D'' layer, (a complex layer above the core-mantle boundary). Seismic anisotropy is a characteristic feature of the mantle that may derive from many processes. It can be related either to the anisotropic structural settings in rocks (Shape Preferred Orientation) or to the intrinsic anisotropy of the minerals (Crystallographic Preferred Orientation). It has

been established that the major cause of the seismic anisotropy observed in the upper mantle is the CPO induced by plastic deformation of minerals. It is then controlled by the deformation of the olivine. However, samples from depths greater than 220 km are inaccessible and fading of seismic anisotropy of the lowermost upper mantle is still poorly understood as well as seismic anisotropy in the transition zone.

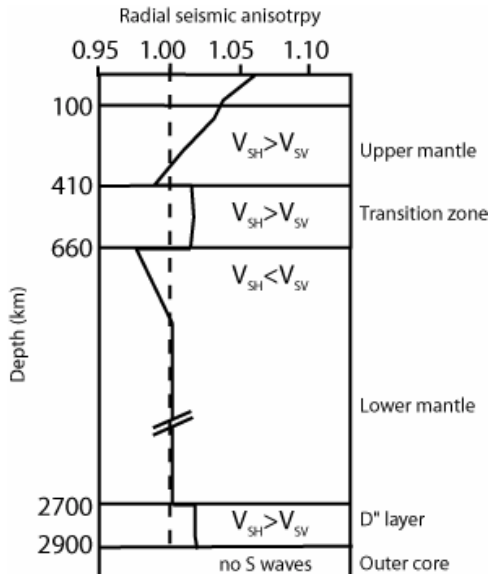


Figure 4 - Evolution with depth of radial variation of the shear wave polarization seismic anisotropy (model SP6-F from Montagner and Kennett (1996))

The aim of this study is to address the rheology of the lowermost upper mantle and the transition zone, regions of the mantle where seismic anisotropy is the more pronounced and accessible with the large volume apparatus. This is done through the study of the rheological properties of

forsterite, wadsleyite and ringwoodite, the most volumetrically important phases of the upper mantle and the transition zone. Up to now, these properties are still poorly constrained. Experimental studies in laboratory are then required. However, achieving plastic deformation experiments under pressure-temperature conditions of the Earth's mantle is one of the most challenging issues. In this study, pure magnesium composition of olivine ( $Mg_2SiO_4$ ) is used. Figure 5 shows the experimental conditions performed in this study in the pressure-temperature phase diagram of  $Mg_2SiO_4$ . Superimposed is the typical geotherm of the mantle.

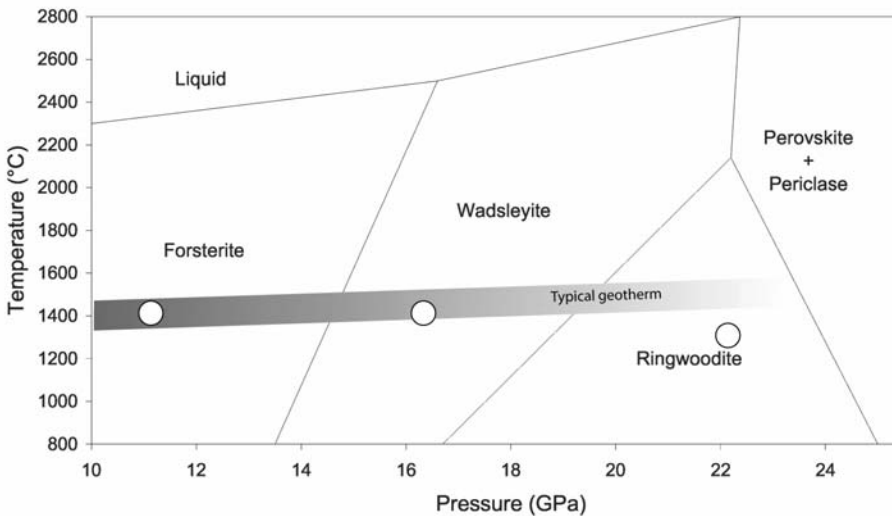


Figure 5 - Pressure temperature diagram of  $Mg_2SiO_4$  and the typical geotherm. The circles represent the experiments performed in this study.

The structure and rheological data of the  $Mg_2SiO_4$  polymorphs are first presented in Chapter I. Then, the experimental techniques used in this

## INTRODUCTION

---

study and the development realised to performed experiments at high pressure and temperature are described (Chapter II). The results of our deformation experiments as well as the samples characterisations are presented in Chapter III. The last chapter (IV) discusses the technical advances and limitations of experimental deformation at high-pressure as well as mechanical properties of  $\text{Mg}_2\text{SiO}_4$  polymorphs. Finally we present the implications of our study on interpretation of seismic anisotropy in the Earth's mantle.



# Chapter I

## Forsterite, wadsleyite and ringwoodite: structural and rheological data

The goal of the present study is to investigate the rheology of the lowermost upper mantle and of the transition zone through the mechanical properties of olivine at high pressure and of its high-pressure polymorphs wadsleyite and ringwoodite. As a first approximation, we have used pure forsterite compositions ( $\text{Mg}_2\text{SiO}_4$ ) either for the olivine phase or for the high-pressure polymorphs. While deformation of olivine has been extensively studied at high temperature, studies on olivine at high pressure as well as on wadsleyite and ringwoodite in their stability fields are still insufficient. This is a consequence of difficulties in deforming minerals at high pressure and high temperature. Significant progress have been achieved in this field since a decade, they are presented Chapter II. Some data on these three phases relevant for the present study are exposed here.



## I – Forsterite: pure magnesium end-member of olivine

Olivine forms a solid solution between two end-member phases: forsterite ( $\text{Mg}_2\text{SiO}_4$ ) and fayalite ( $\text{Fe}_2\text{SiO}_4$ ). The structure of olivine is based on a distorted hexagonal close-packed oxygen sublattice. The Bravais lattice is orthorhombic and the space group is  $Pbnm$ . Figure I.1 presents a view of one cell unit of forsterite. The cell parameters of forsterite are  $a = 4.75 \text{ \AA}$ ,  $b = 10.19 \text{ \AA}$  and  $c = 5.97 \text{ \AA}$ . One unit cell contains four formula units. This orthosilicate presents four isolated tetrahedra ( $\text{SiO}_4$ ) per cell unit with two types of octahedral sites: called  $M_1$  and  $M_2$ .  $M_1\text{O}_6$  shares four edges with adjacent octahedra and two edges with  $\text{SiO}_4$  tetrahedra whereas  $M_2\text{O}_6$  shares two edges with adjacent octahedra and one edge with a tetrahedron.  $\text{Fe}^{2+}$  and  $\text{Mg}^{2+}$  are randomly distributed in  $M_1$  and  $M_2$ . Olivine is also named  $\alpha$ -phase.

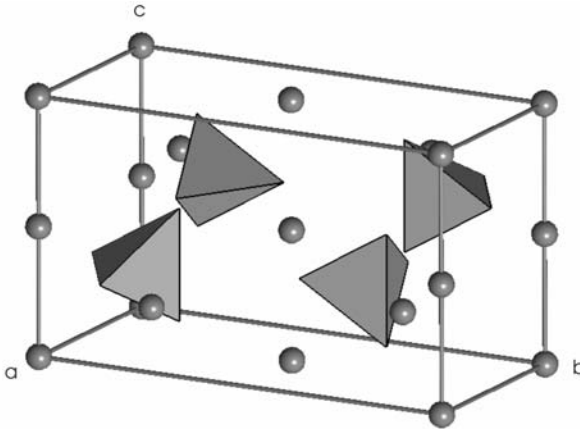


Figure I.1 – The forsterite unit cell.  $\text{SiO}_4$  tetrahedrons and Mg atoms are represented.

Olivine is by far the most abundant mineral of the upper mantle. It is also considered to be the weakest phase and hence to control the rheology of the upper mantle. For this reason, it has been clear for a long time that modelling the nature of convection in the outer 400 km of the Earth's mantle requires a good knowledge of the plastic properties of olivine. Many studies have been conducted to investigate the deformation mechanisms and flow laws of olivine.

Raleigh (1968) has deformed peridotite samples at low pressure (5 kbar), at temperature up to 1000°C and at strain rate of  $10^{-2}$  to  $10^{-6}$  s<sup>-1</sup>. Under 1000°C or at high strain rate, he observed [001] glide on {110}, (010) and (100). If the temperature is upper, the slip systems change and the deformation is dominated by [100]{0kl}. The same phenomenon is observed if the strain rate is decreased. Several study on polycrystalline samples, (e.g. Carter and Ave'lallemant, 1970; Chopra and Paterson, 1981, 1984; Karato *et al.*, 1986; Hirth and Kohlstedt, 1995a, b; Mei and Kohlstedt, 2000a, b) as well as on single crystals (e.g. Phakey *et al.*, 1972; Blacic and Christie, 1973; Kohlstedt and Goetze, 1974; Durham and Goetze, 1977; Darot, 1980; Darot and Gueguen, 1981; Kashima *et al.*, 1982; Mackwell *et al.*, 1985; Bai *et al.*, 1991; Bai and Kohlstedt, 1992a, b, 1993) have been confirmed this tendency to activate [100] at high temperature and low strain-rate whereas [001] glide is activated at low temperature and high strain-rate. Deformation tests on single crystals allow promoting preferentially one or several slip systems. Usually the single crystal is oriented along [110]c (i.e. promoting [100] glide on (010) plane), [011]c or [101]c. From deformation of single crystal, it is possible to collect mechanical data on one particular slip system and with different kinds of deformation test (creep, at constant strain rate ...).

From those various experiments, it appears that the common slip system at high temperature involve  $[100]$  slip on several planes:  $(010)$ ,  $\{031\}$ ,  $\{021\}$ ,  $\{011\}$  and  $(001)$  (Figure I.2). Cross slip between these different planes is frequent. Dislocation lines exhibit marked crystallographic orientation characteristic of high lattice friction, even at high temperature. In  $(010)$ , long edge segment are observed with short curved screw segments. This is observed in natural samples (Gueguen, 1979a) as well as in experiments (Durham, 1975; Jaoul *et al.*, 1979). Edge  $[100]$  dislocations gliding in  $(001)$  exhibit a peculiar microstructure with zig-zag line configuration corresponding to the stabilisation of  $\langle 110 \rangle$  segments. When several slip system  $[100](0kl)$  are activated one can find free screw dislocations located between  $[100]$  tilt boundaries (Durham, 1975; Gueguen, 1979b). At low temperature and high stresses, slip occurs along  $[001]$  in  $(100)$ ,  $\{110\}$  and  $(010)$  (Figure I.2).  $[001]$  screw dislocations are always found to exhibit very marked crystallographic characters and are more pervasive than edge segments. Twist boundaries are very common; they are usually constituted of  $[100]$  and  $[001]$  screw dislocations.

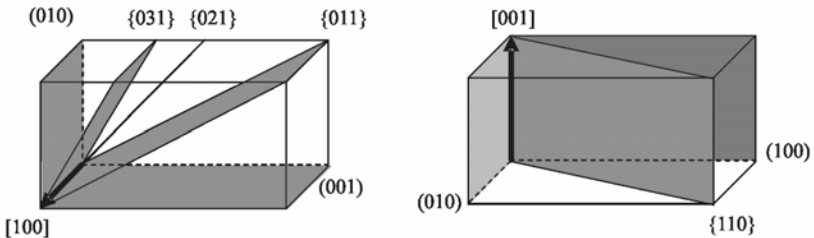


Figure I.2 – Olivine: possible glide planes of  $[100]$  dislocations (left) and of  $[001]$  dislocations (right).

High temperature creep experiments performed on single crystal strained along various orientations have in common to follow a power-law creep equation with a stress exponent  $n \approx 3.5$  compatible with dislocation controlled by climb of edge dislocations.

Crystallographic preferred orientation of naturally deformed olivine, in the different geophysical environments of the upper mantle, have been compiled in a data base (Ben Ismaïl and Mainprice, 1998 and reference herein). The authors show that whatever the geophysical context, ninety-five percent of the 110 samples analysed display a CPO characterized by the [100] axes aligned in the lineation direction. Those patterns can be interpreted as resulting from dislocations glide on [100]{0kl} (with predominance for the gliding on (010) rather than on (001)). Olivine experimentally deformed confirm the tendency (Zhang and Karato, 1995; Bystricky *et al.*, 2000; Zhang *et al.*, 2000) as well as numerical modelling of CPO development on olivine aggregates from the easier slip systems observed at high temperature (Tommasi, 1998; Tommasi *et al.*, 1999; Wenk and Tomé, 1999). CPO characterized by the [001] axes aligned parallel to the shear direction have been observed in experiments made by Jung and Karato (2001) and in natural occurrences (Frese *et al.*, 2003; Mizukami *et al.*, 2004) and have been attribute to the presence of water. A bimodal CPO characterized by the [100] axes and the [001] axes both parallel to the shear direction has been recently observed (Vauchez *et al.*, 2003).

Although a wide range of thermo-chemical environments have been considered in the past, the physical conditions investigated remained quite narrow (mostly 1 atm of pressure and high-temperature). Only recently has the influence of large strains (Bystricky *et al.*, 2000; Zhang *et al.*, 2000) and high-pressure (Karato and Rubie, 1997; Jung and Karato, 2001; Karato and

Jung, 2003; Li *et al.*, 2003; Li *et al.*, 2004; Raterron *et al.*, 2004) been considered. Pressure has been shown to have a strong influence on the point defect chemistry (and hence on rheology) under "wet" conditions (Mackwell *et al.*, 1985; Mei and Kohlstedt, 2000a, b; Jung and Karato, 2001). Experiments performed on olivine powders at 8 GPa and temperature to 1475 K in a multianvil apparatus have emphasised the importance of dynamic recrystallization under these conditions (Li *et al.*, 2003). However, elementary deformation mechanisms (slip system, ...) and rheology of olivine at high pressure are still insufficiently documented.

## II – Wadsleyite

Wadsleyite (or  $\beta$ -phase) is volumetrically the main component of the upper transition zone, between 410 and 520 km of depth. This mineral is a sorosilicate with a spinelloid structure. The Bravais lattice is orthorhombic and the space group is *Imma*. This structure is made of  $\text{SiO}_4$  isolated tetrahedra (Figure I.3) and of three types of octahedral sites named  $M_1$ ,  $M_2$  and  $M_3$ .  $M_1\text{O}_6$  and  $M_2\text{O}_6$  share six edges with adjacent octahedra.  $M_3\text{O}_6$  share seven edges with adjacent octahedra. Some tetrahedra share an apex but none of them shares an edge with an octahedron. The cell parameters of  $\text{Mg}_2\text{SiO}_4$  wadsleyite are  $a = 5.698 \text{ \AA}$ ,  $b = 11.438 \text{ \AA}$  and  $c = 8.256 \text{ \AA}$  (Horiuchi and Sawamoto, 1981).

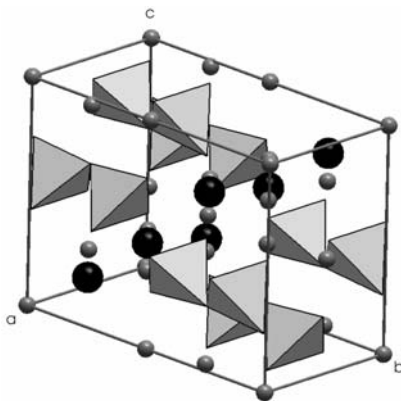


Figure I.3 – The wadsleyite unit cell.  $\text{SiO}_4$  tetrahedrons, Mg atoms (gray) and O atoms (black) are represented.

This phase is not stable at ambient conditions. It has been synthesised for the first time by Ringwood and Major (1966) and discovered in natural occurrence in a Peace River meteorite (Price, 1983). First microstructural observations of wadsleyite have been done on natural occurrence (Peace River or Catherwood) and they show staking fault  $\frac{1}{4}[010](010)$  and  $\frac{1}{2}\langle 101 \rangle(010)$  (Madon and Poirier, 1983; Price, 1983). Madon and Poirier (1983) show that the fault  $\frac{1}{4}[010]$  create a layer with ringwoodite structure. The first deformation experiments have been performed recently using multianvil apparatus (see Chapter II). Sharp *et al.* (1994) and Dupas *et al.* (1998) have transformed natural San Carlos olivine in the wadsleyite stability field at 1450°C and at 900°C respectively. After a long annealing time under pressure and at 1450°C to allow for significant creep to take place, dislocations commonly occur in walls although tangles are also observed.  $[100]$  dislocations have been characterised and orientations of dislocation segments in subgrain boundaries suggest (010) as

slip plane (Sharp *et al.*, 1994).  $\frac{1}{4}[010](010)$  and  $\frac{1}{2}\langle 101 \rangle(010)$  stacking faults have also been observed. Dupas *et al.* (1998) found dislocations mostly in remnant olivine grains. In wadsleyite, dislocations with  $[100]$  and  $\frac{1}{2}\langle 111 \rangle$  Burgers vectors are observed.  $[100]$  dislocations are arranged in subgrain boundaries. This led suggested by the authors that recovery by dislocation climb is active in wadsleyite from 900°C.

Relatively few defects have been observed in a synthesized harzburgite transformed in wadsleyite stability field (14 GPa at 1100–1200°C) by Dupas *et al.* (1994). Almost only stacking faults in (010), in contrast with remnant olivine grains which display high densities of  $[001]$  screw dislocations. The only dislocations observed are emitted at grain boundaries to relax local stress concentrations. The following slip systems have been characterized:  $[100]\{021\}$  (predominance of screw) and  $\frac{1}{2}\langle 111 \rangle\{101\}$ .

Most recent study have been performed by Thurel (2001), Thurel *et al.* (2003a; 2003b). Plastic deformation on pre-synthesized wadsleyite samples (forsterite composition) have been performed in a compression assembly in a multianvil apparatus (Cordier and Rubie, 2001 and see Chapter II) at 15–19 GPa at temperatures up to 1800°C. Complex microstructures are produced with dislocations in glide configurations and many slip systems activated. Five slip system are activated:  $\frac{1}{2}\langle 111 \rangle\{101\}$ ,  $[100](010)$ ,  $[100](001)$ ,  $[100]\{011\}$ ,  $[100]\{021\}$  and three other are activated at low temperature and high stress only:  $[010](001)$ ,  $[010]\{101\}$  and  $\langle 101 \rangle(010)$ . Except for  $\{021\}$ , the slip planes are selected among those which do not shear the strong  $\text{SiO}_4$  bonds. It is also interesting to note that  $[001]$  dislocations are almost absent. Detailed observation shows that  $[010]$  and  $\langle 101 \rangle$  dislocations are dissociated.  $\langle 101 \rangle$  dislocations are dissociated in the

(010) plane into two  $\frac{1}{2}\langle 101 \rangle$ . [010] dislocations decompose spontaneously into two  $\frac{1}{2}\langle 111 \rangle$  dislocations (screw segments) in a {010} plane or dissociate into four  $\frac{1}{4}[010]$  partial dislocations. Such relaxation events suggest a complex thermo-mechanical history. Indeed, experiment in which the specimens were loaded at high pressure in the deformation assembly, but not heated, could show any significant plastic deformation of wadsleyite during pressurization at room temperature. To overcome this problem, further deformation experiments have been performed on pre-synthesized wadsleyite samples with the shear deformation assembly designed by Karato and Rubie (1997) (see Chapter II). This experiment allows to obtain large strains at high temperature and thus high-temperature microstructures to overprint low-temperature ones. Experiments performed at 14 GPa, 1300°C on wadsleyite with Fo<sub>90</sub> composition confirmed that  $\frac{1}{2}\langle 111 \rangle\{010\}$ , [100](010) and [100]{011} (Figure I.4) are the easy slip systems of wadsleyite under these conditions (Thurel, 2001; Thurel *et al.*, 2003b). The CPOs were not characterized in those studies.

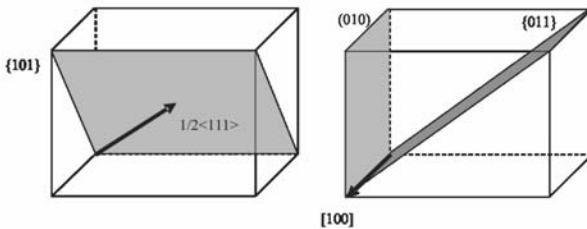


Figure I.4 – Easy slip systems in wadsleyite at high temperature and high pressure.

### III – Ringwoodite

From about 510 km of depth, wadsleyite transforms into a slightly denser phase: ringwoodite (or  $\gamma$ -phase). Ringwoodite has a spinel structure with the nominal face-centered-cubic packing of the oxygen sublattice. Ringwoodite belongs to the cubic system (space group  $Fd\bar{3}m$ ). The  $\text{SiO}_4$  tetrahedra are isolated and do not share edges. The octahedral sites are occupied by  $\text{Mg}^{2+}$  and  $\text{Fe}^{2+}$  and they share six edges with adjacent octahedra. The lattice parameter of  $\text{Mg}_2\text{SiO}_4$  ringwoodite determined by Ringwood and Major (1970) is  $a = 8.071 \text{ \AA}$ . The unit cell contains eight formula units (Figure I.5).

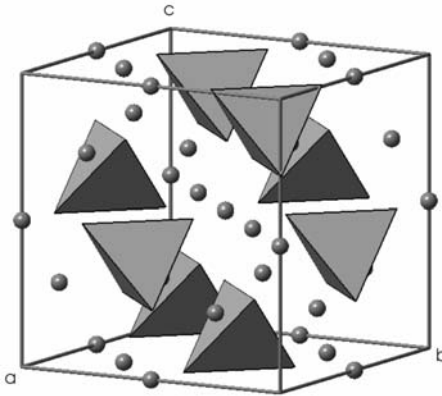


Figure I.5 – The ringwoodite unit cell.  $\text{SiO}_4$  tetrahedra and Mg atoms are represented.

The first natural occurrences of ringwoodite have been observed in meteorites (e.g. Binns *et al.*, 1969; Smith and Mason, 1970; Coleman, 1977).

In the spinel structure, the slip direction is always observed to be parallel to the  $\langle 110 \rangle$  close packed direction of the fcc lattice (Mitchell, 1999).  $\frac{1}{2}\langle 110 \rangle$  is then the shortest perfect Burgers vector. On the other hand, the observed slip plane is variable among the dense planes of the oxygen sublattice. The most common glide planes are  $\{111\}$  and  $\{110\}$ , although  $\{100\}$  has been reported in magnetite, nickel ferrite, and chromite (Mitchell, 1999 and references herein).

The first defect characterizations of crystal defects in ringwoodite have been performed on shocked chondrites. Madon and Poirier (1980; 1983) have observed ringwoodite grains formed in shock veins from Tenham. They contain pervasive planar defects on the three families of  $\{110\}$  planes as well as  $\frac{1}{2}\langle 110 \rangle$  dislocations with a  $60^\circ$  character lying in  $\{111\}$  planes. The usual splitting of spinel dislocations:  $\frac{1}{2} [110]$  into two  $\frac{1}{4} [110]$  has not been observed.

Plastic shear deformation experiments of  $(\text{Mg, Fe})_2\text{SiO}_4$  ringwoodite have been performed at high-pressure, high-temperature by Karato *et al.* (1998). Synthetic olivine aggregates have been transformed to ringwoodite and deformed at 16 GPa and temperatures in the range 1400–1600 K. Although small-grained samples ( $\approx 0.5 \mu\text{m}$ ) show evidence for grain-boundary sliding mostly, large-grained samples (above  $3 \mu\text{m}$ ) deform by dislocation creep. TEM investigation showed that deformation occurs mostly through slip of  $\frac{1}{2}\langle 110 \rangle$  dislocations over  $\{111\}$  planes although  $\{100\}$  was also noted. In a recent study, Thurel (2001) has studied  $\text{Mg}_2\text{SiO}_4$  ringwoodite deformation in compression configuration (Cordier and Rubie, 2001) at 22 GPa and 1000–1400°C. This study confirms that  $\frac{1}{2}\langle 110 \rangle\{111\}$  and  $\frac{1}{2}\langle 110 \rangle\{110\}$  are important slip systems. In both cases, dislocations appear to be in glide configurations with marked crystallographic orientations

(screw, 45°, 60° or edge) and show no dissociation in weak-beam dark-field TEM micrographs.

Xu *et al.* (2003) have been established the flow law of ringwoodite at 20 GPa and up to 1350°C. They show that above 1000°C, the flow may be controlled by power-law creep relation with a stress exponent  $n \approx 3.5$  compatible with dislocations glide.

Recently a CPO characterisation of ringwoodite has been provide by Wenk *et al.*(2004) from *in-situ* measurements in diamond anvil cell. They show that ringwoodite deformed at room temperature and at 20–40 GPa presents a CPO characterized by  $\langle 110 \rangle$  direction normal to the compression axis. This presupposes that the  $\langle 110 \rangle$  glide is dominant. The slip plane are  $\{111\}$  and  $\{011\}$  at 50 GPa and  $\{011\}$  at 43 GPa.



# Chapter II

## Experimental techniques and developments

Achieving plastic deformation experiments under pressure-temperature conditions of the Earth's mantle is one of the most challenging issues in mineral physics. This field is then evolving very rapidly. It is now possible to perform deformation experiments to ca. 10 GPa using the newly developed Deformation-DIA where differential stress is controlled independently from pressure and where relatively large strains (several tens of %) can be reached. A D-DIA has been installed in the Bayerisches Geoinstitut in 2000. The geometry of this apparatus allows coupling with a synchrotron light source in order to measure stress and strain *in situ* during this experiment. For pressures above 10 GPa, it is necessary to use conventional high-pressure experiments such as the Kawai-type multianvil press or the diamond anvil cell. In the course of the present study, only large-volume multianvil apparatus have been used. Plastic deformation can be achieved with this apparatus provided modified assemblies are developed.

In this chapter, the principles of the techniques used in this study are presented as well as the technical developments achieved. Most experiments were performed in Bayreuth without *in situ* measurements of mechanical data. Our strategy was to perform detailed microstructural characterisations on recovered samples. The various analytical techniques used are also presented in this chapter.



## I – High pressure techniques: presentation of apparatus and developments

One of the important parameter of any high-pressure technique is the pressure-temperature domain accessible. Figure II.1 shows the possibilities of most experiments available that can be used for deformation experiments. The D-DIA, installed in Bayreuth, is obviously adapted to the study of upper mantle materials. Concerning the transition zone, it is necessary to take advantage of high pressure experiments that are not originally designed for deformation experiments. We have extensively used the large volume Kawai-type multianvil apparatus for which the BGI is very well equipped. The main characteristics of these techniques are briefly presented below following by the developments and the modifications achieved.

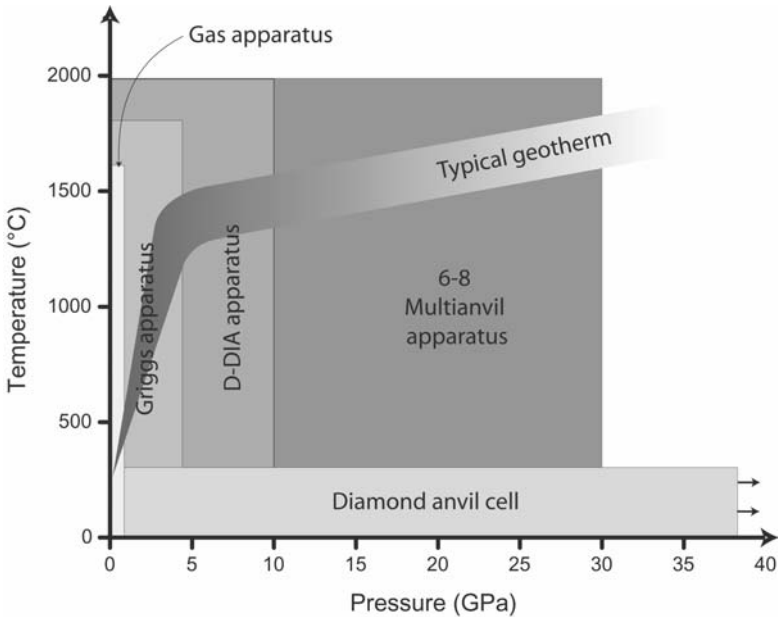


Figure II.1 – Pressure–temperature domains covered by high pressure apparatus. The typical geotherm is also shown.

### I.1 – Deformation-DIA (D-DIA)

The development of a high-pressure deformation apparatus must face several constraints: control of the differential stress independently from pressure and measurement of stress and strain. Until recently, two devices were available: the Griggs and the Paterson apparatus.

The Griggs apparatus derives from the piston cylinder apparatus (Griggs *et al.*, 1960). The sample is embedded in a soft solid pressure-medium and an extra piston is introduced to strain the sample. Recent developments made on this apparatus (e.g. Green II and Borch, 1989;

Gleason and Tullis, 1993; Rybacki *et al.*, 1998) have aimed at reducing friction forces and at extending the pressure range to ca. 4 GPa.

Another deformation press has been developed by Paterson (1970). Frictions are minimised by using a gas as confining medium. Deformation experiments can be performed in three configurations (compression, extension and torsion) up to large strains. For security reasons, pressure and temperature are limited to 300 MPa and 1300°C. The major drawback of these experiments is their limited pressure range which does not allow reaching conditions corresponding to depths below 100 km.

This pressure range has been expanded recently to about 10 GPa and 2000°C with the newly developed high-pressure deformation apparatus: the deformation-DIA (Wang *et al.*, 2003) (Figure II.2). This apparatus is a modification of the DIA cubic-anvil apparatus (Osugi *et al.*, 1964), which is used in isotropic solid-media compression experiments. The device compresses a cubic pressure assembly quasi-hydrostatically by the advancement of six cBN or WC anvils. The cell contains the sample electrically heated using a graphite or LaCrO<sub>3</sub> furnace and a W3%Re-W25%Re thermocouple for temperature measurement. This cell plays also the role of gasket in flowing between the six anvils. In the D-DIA, once pressure and temperature are reached, the top and bottom anvils can be advanced independently thus applying a compressive stress in the vertical direction while the four side anvils are retracted to allow the volume and pressure to remain constant. Very low strain rates can be achieved, similar to those attainable with a Paterson type deformation apparatus. Both sample stress and strain can be determined using *in situ* synchrotron techniques.

As the D-DIA press was not operational at the Bayerisches Geoinstitut, the design of the cell and the pressure calibrations had to be

performed in the course of this study. This part of my work is presented below (§ I.3.1).

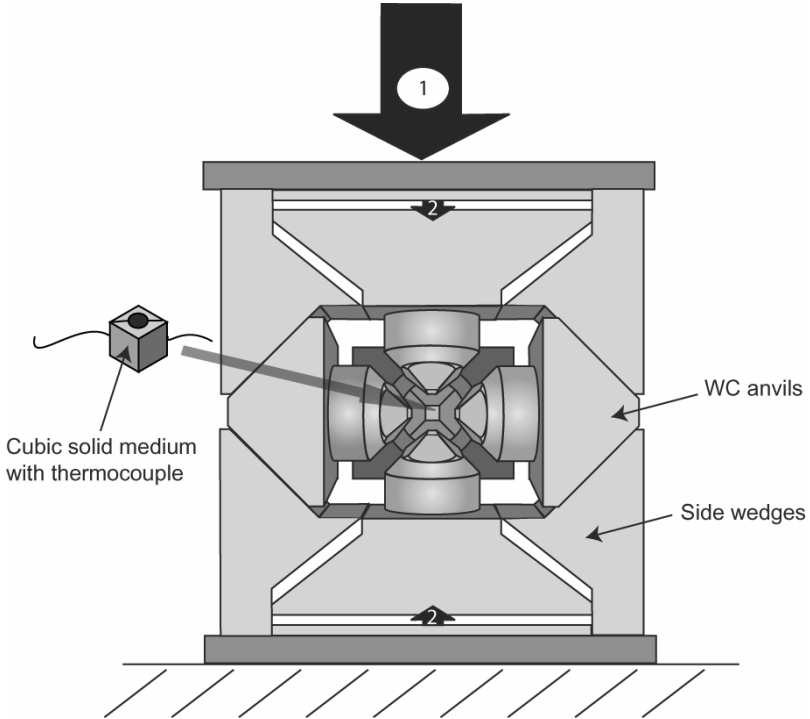


Figure II.2 – Schematic diagram of the D-DIA. Arrow 1 shows the main ram and arrows 2 show the differential ram.

## I.2 – Kawai-type multianvil apparatus

### I.2.1 – Presentation of the press

The Kawai-type multianvil apparatus, developed in Japan in the early 1980s (e.g. Kawai and Endo, 1970; Ito *et al.*, 1984), is well adapted to study the behaviour of minerals under mantle P–T conditions. The multianvil press is a two-stage type of apparatus able to reach pressure up to 25 GPa

and temperatures around 2000°C. The first stage is a pair of permanently glued steel guide blocks which encloses the second stage in a cubic cavity. The force is applied to the guide blocks by a single ram (Figure II.3).

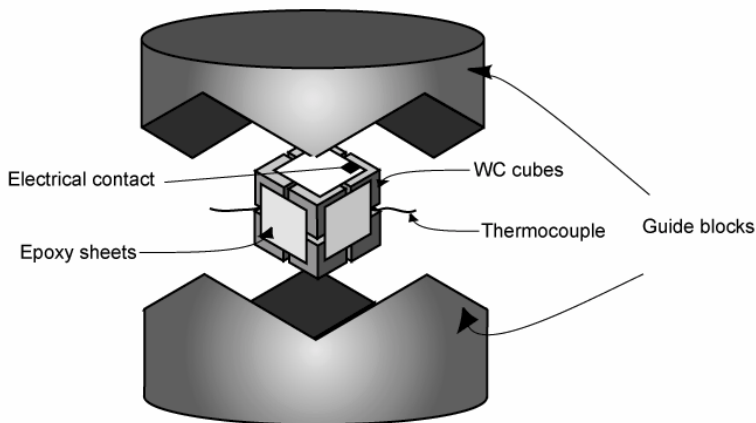


*Figure II.3 – Kawai type multianvil: schematic diagram of the second of anvils in between the first one.*

The second stage of anvils consists in eight tungsten carbide cubes with truncated corners. These cubes are maintained all together using epoxy-impregnated fibreglass laminate sheets which also insure electrical insulation with the guide blocks. The pressure cell is a sintered MgO octahedron doped with 5% of  $\text{Cr}_2\text{O}_3$ . It is compressed in the octahedral cavity formed by the truncated cubes (Figure II.4).

The sample loaded in this octahedron (Figure II.5) is heated by a stepped cylindrical furnace ( $\text{LaCrO}_3$  in our case, it can also be graphite). In a stepped cylindrical furnace, the wall thickness of the central part of the heater is thicker than the two end sections. The consequence is that the central part has a relatively low resistance and does not generate as much

heat as the two end parts. The effect of this type of geometry is to reduce the temperature gradients. A  $ZrO_2$  sleeve is inserted around the heater for thermal insulation and a  $MgO$  sleeve avoids chemical reaction between  $LaCrO_3$  and sample materials at high temperature. The temperature is measured close to the sample using a thermocouple (W3%Re-W25%Re in most cases) in an  $Al_2O_3$  sleeve.

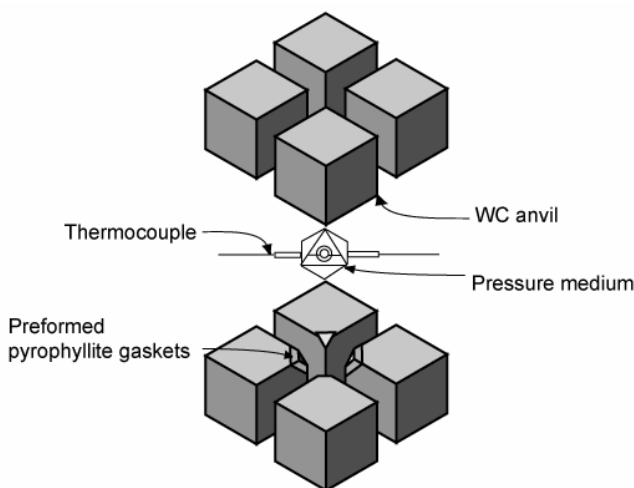


*Figure II.4 - Kawai-type multi-anvil apparatus: schematic diagram of the second stage of anvils containing the octahedron.*

High pressures are generated with tungsten carbide anvils. Pyrophyllite gasket and extruding pressure medium support the large stress gradients generated in the anvils. Cardboard and Teflon tape are also placed on the surface of the cubes behind the gaskets to electrically insulate the thermocouple wires and to provide extra support to the gaskets.

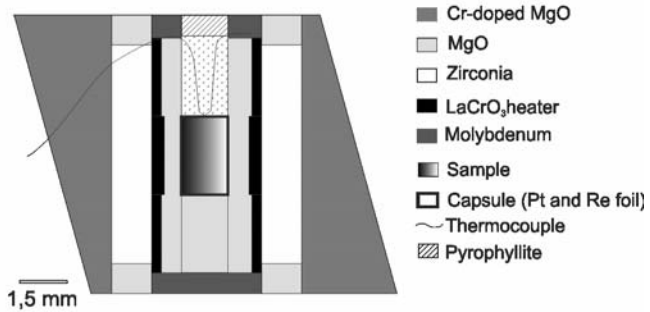


Figure II.5 – Kawai type multianvil: cross-section through a standard 18/11 assembly.

The press is driven by an hydraulic system. The pressure generated in the cell depends on the truncation edge-length (TEL) of the WC cube and on the octahedral edge-length (OEL) of the octahedron as well as on materials used and on the cross-sectional dimensions of the gaskets (Liebermann and Wang, 1992). Different assemblies are named after the ratio of these two lengths: OEL/TEL in mm. Table II.1 displays the sample volume and the pressure range for different assemblies for a 1000–2000t capacity hydraulic press. Increasing the OEL/TEL ratio results in a decrease of the sample size and in an increase of the pressure range.

OEL/TEL	Sample volume (mm <sup>3</sup> )	Pressure range (GPa)
18/11	12	4–12
14/8	5–8	11–17
10/4	1	22–26

Table II.1 – Sample volume and pressure range for the different assemblies used in the Kawai-type multianvil

The aim of the two-stage configuration of the Kawai-type multianvil is to amplify the loading force with a succession of amplifier elements between the single ram and the sample. One of the difficulties is then to infer the pressure applied to the sample from the loading force and the OEL/TEL ratio. This is done through calibrations. At room temperature, calibrations are made by monitoring *in situ* variation of electrical resistance of materials during phase transformations. For instance, the transformation Bi-I to Bi-II and Bi-III to Bi-IV occur at 2.52 GPa and 7.7 GPa respectively (Lloyd, 1971; Getting, 1998). At high temperature, the pressure efficiency is different and specific calibrations must be done. Various factors are involved which cause either increase or decrease of the cell pressure from the value determined at room temperature. For instance, increasing temperature first produces a thermal expansion of the cell which increases the pressure. Then, the gaskets begin to flow which results in decreasing the pressure. The calibration has to be performed for different temperatures using known equilibria such as coesite-stishovite (Zhang *et al.*, 1996),  $\alpha$ -Mg<sub>2</sub>SiO<sub>4</sub> to  $\beta$ -Mg<sub>2</sub>SiO<sub>4</sub> (Morishima *et al.*, 1994) and  $\beta$ -Mg<sub>2</sub>SiO<sub>4</sub> to  $\gamma$ -Mg<sub>2</sub>SiO<sub>4</sub> (Suzuki *et al.*, 2000) transformations, etc. Figure II.6 presents the calibration curves used in the Bayerisches Geoinstitut (including for this study). The uncertainties in pressure calibrations at high temperature are estimated about  $\pm 0.5$  GPa; such estimates are based on reproducibility and on how precisely an equilibrium boundary can be bracketed. In fact the uncertainties may depend on the starting material used for the pressure calibration and on the sample volume. Hence, they may be significantly larger in some cases (Rubie, 1999).

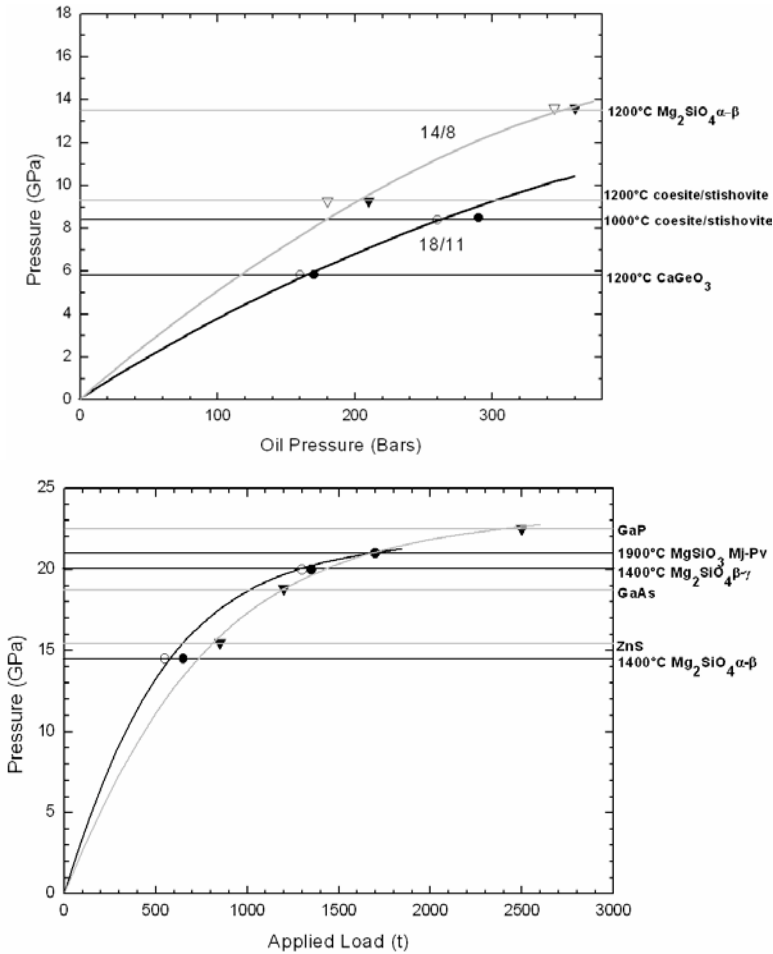


Figure II.6 – Top: calibration curves for the Sumitomo press (1200t). Calibration for 18/11 (black) and calibration for 14/8 (gray). At same nominal pressure, a ratio of 0.6 has to be applied on oil pressure for the Hymag press (1000t). Bottom: calibration curves for the Zwick press (5000t). Room (gray) and high-temperature (black) (from Frost et al.(2004)). For high-temperature calibration, high or low-pressure phase at each transformation is indicated by either filled or opened signs respectively.

### I.2.2 – Using the multianvil press as a deformation apparatus

The assembly presented above has been developed to perform quasi-hydrostatic experiments. Some modifications are necessary to plastically deform a sample in a non-hydrostatic environment. As the Kawai-type multianvil apparatus does not allow independent control of differential stresses and pressure, the idea is to produce differential stresses during compression from a non-hydrostatic pressure cell. Early proposed by Fujimura *et al.*, (1981), this approach has triggered a number of studies in the past few years (Green II and Borch, 1989; Liebermann and Wang, 1992; Bussod *et al.*, 1993; Sharp *et al.*, 1994; Weidner, 1998; Cordier and Rubie, 2001; Cordier *et al.*, 2002; Thurel and Cordier, 2003a; Thurel *et al.*, 2003b). The usual cell involves stiff alumina pistons on both ends of the specimen (Figure II.7). During cold compression, large differential stresses are built up. When temperature is increased, the stresses are relaxed in the assembly as well as in the sample which is then plastically deformed at high pressure and high temperature. It is important to note that pressure and differential stresses are not monitored independently, nor can one have an internal force gauge in the cell. As relaxation proceeds, the strain rate decreases and, finally, deformation stops. This technique usually induces limited plastic strain. In order to achieve larger strains, Karato and Rubie (1997) have proposed a shear design (Figure II.7). The setup is basically the same as above except for the alumina pistons that are cut at 45°. The sample is now a thin slice (usually 200µm) placed between the pistons. High temperature stress relaxation results in the shearing of the specimen and large strains can be reached (over 100%; according to Karato and Rubie (1997)). A strain

marker in the sample provides a measurement of the total deformation after the experiment.

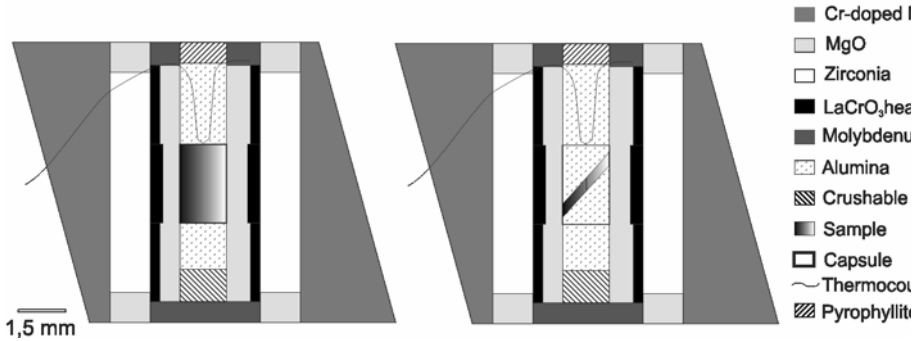
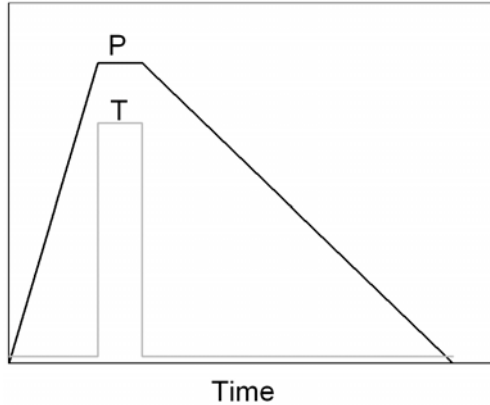


Figure II.7 - Cross-section through the compression (left) and shear (right) deformation assemblies.

In this study, the deformation experiments using the multi-anvil apparatus are performed in the shear design assembly in order to create large strain (Karato and Rubie, 1997).

Once the second-stage of anvils is inserted into the press, the run procedure applied for every experiment of this study (Figure II.8) consists of increasing the loading oil pressure at room temperature and holding it constant during heating. At pressure, the sample is heated up slowly (50°–100°C/ min). Then 10 to 15 minutes are necessary to attain 1400°C, temperature used in this study. The temperature is maintained constant automatically. At the end of the experiment, the power supply of the heater is shut off and (due to its small size) the sample is quenched to room temperature within a few seconds. Then the pressure is decreased slowly

within 10-20 hours to avoid damaging the WC cubes. The sample is then extracted from the compressed cell for microstructural investigation.



*Figure II.8 – Typical experimental procedure for Kawai-type multianvil experiments. Black: oil pressure versus time. Gray: temperature versus time.*

### **I.3 – Experimental developments and calibrations performed during this study**

#### **I.3.1 – Developments performed for the D-DIA press**

As the D-DIA press was only recently installed in the Bayerisches Geoinstitut, a new design for the cubic pressure cell had to be developed for this study. Several tests (Table II.2) were necessary to design a deformation cell which could be used at high temperature. Most of these tests were performed at 5 GPa and 1100-1300°C. The starting design came from the compression assembly developed for the multianvil Kawai-type press (see Figure II.5).

**EXPERIMENTAL TECHNIQUES AND DEVELOPMENTS**

Run #	Kind of test - Modifications	Problems observed
DD07	One of the first test	Zirconia damages the furnace
DD16	Pyrex replaced zirconia - Pressure calibration	Pistons are too long/ Crush the capsule
DD17	New piston lengths - Pressure calibration	Pistons are too long/ Crush the capsule
DD19	New piston lengths - Pressure calibration	Pistons length seems ok / Pressure calibration done
DD20	Test for piston lengths with hot pressed sample	Pistons are too long
DD21	New piston lengths with hot pressed capsule - Top and bottom crushable $Al_2O_3$ plugs with Pt ring around	Pistons have right length/ Problem with heating - disconnection between Pt and heater
DD22	Thicker Pt rings	Pyrex intruded the heater
DD23	Crushable $Al_2O_3$ sleeve replaces Pyrex	Hot spot created - Melt inside cube
DD24	Graphite rings replace Pt rings	Instability of the temperature
DD26	New test at lower temperature	Good but reaction between the pyrophyllite and the crushable $Al_2O_3$ sleeve
DD27	Crushable $Al_2O_3$ sleeve between heater and Pyrex	High temperature stable
DD28-29	Deformation test	Good

*Table II.2 – Experiments performed to provide a pressure cell able to support high pressure and temperature. Pt=platinum*

Figure II.9 and Figure II.10a show respectively a schematic and a cross section of the cell finally proposed in this study. The different elements composing this cell and their functions are described below.

The first modification was to replace the  $\text{LaCrO}_3$  heater by a graphite heater which is more transparent to X-rays. A stepped heater is used to minimize the thermal gradient. The top and bottom molybdenum rings present in the octahedral cell (see Figure II.5) were replaced by two types of rings: thick platinum foils or graphite rings. Because of a larger thickness, the graphite rings were preferred; they ensure a better contact between the heater and the anvil.

Thermal insulation is provided by a borosilicate glass (Pyrex) sleeve. Previous tests showed that zirconia was too hard and damaged the heater. Crushable  $\text{Al}_2\text{O}_3$  was also tested; however, this material reacted with pyrophyllite cube and the reaction product melted at high temperature (DD23-24). Another advantage of Pyrex is that it is soft and flows at high temperature during deformation providing a homogenous pressure medium.

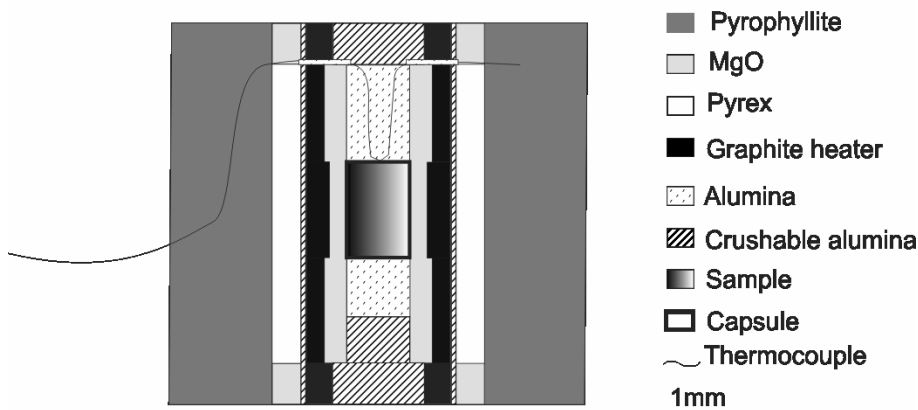


Figure II.9 – Cross-section through the D-Dia assembly designed in the Bayerisches Geoinstitut

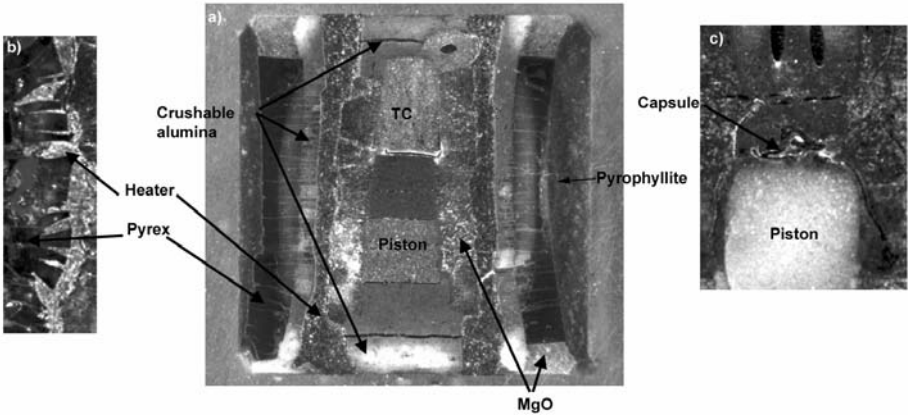


Figure II.10 – a) Cross section of the final cell

b) Detail of DD19: the Pyrex damages the heater during cold compression

c) Detail of DD16: the capsule is squeezed between piston and thermocouple (TC)

A sleeve of crushable  $\text{Al}_2\text{O}_3$  surrounds the heater in order to protect it from intrusion of Pyrex during cold compression (DD27) (Figure II.10b).

The sample is loaded by two hard  $\text{Al}_2\text{O}_3$  pistons placed at both ends of the sample; the top one also contains the thermocouple. Different lengths of pistons have been tested (DD16–17–19–20–21) to avoid damaging the top and bottom anvils and to minimize deformation during cold compression (Figure II.10c).

Crushable  $\text{Al}_2\text{O}_3$  has been used to accommodate the deformation introduced during the cold compression accompanying pressurization. Due to the lengths of the pistons and to keep the sample in central position in the heater after compression, two plugs of crushable  $\text{Al}_2\text{O}_3$  were placed at both ends.

The cell can also be used for quasi-hydrostatic experiments by replacing the bottom piston by a piece of crushable  $\text{Al}_2\text{O}_3$ .

Two sizes of cubes are used in this study: 6/8 and 4/6 (edge-length of the anvil/edge-length of the cube in mm). Table II.3 summarises the sample volume and the pressure range that can be reached with these assemblies.

	Sample volume ( $\text{mm}^3$ )	Pressure range (GPa)
6/8	2-3	1-4
4/6	0.5-1	2- 6

*Table II.3 - Sample volume and pressure range for the different D-DIA assemblies.*

Pressure calibration of these two assemblies has been carried out using the  $\alpha$ - $\beta$  phase transition in  $\text{Mn}_2\text{GeO}_4$  which occurs at 4.7 GPa at 1100°C (Morimoto *et al.*, 1969). The calibration curves are presented in Figure III.11.

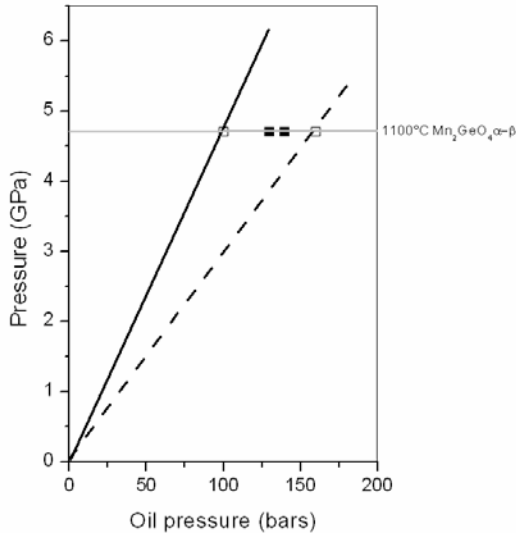


Figure II.11 – Pressure calibration curves of the D-DIA press in Bayreuth. Filled symbols: low pressure phase, opened symbols: mixture of low and high pressure phase. Solid line: 4/6 deformation assembly, dashed line: 6/8 deformation assembly.

Once the cube is loaded into the press, the oil pressure is increased at room temperature and held constant during the rest of the run (Figure II.12, thick solid line). Then the sample is heated up slowly (50°–100°C/ min) to a given temperature (gray solid line). The sample is annealed during one or two hours to erase possible deformation microstructures introduced during cold compression. To start the deformation experiment, the pressure in the differential ram (fine dash line) has to be larger than the pressure in the main ram. When the friction forces of the main ram are passed over, the top and bottom anvils start to move (thin solid line: displacement recorded using transducers on the top and bottom anvil) and a constant strain rate is imposed using a stepping motor. During deformation, the four side anvils are

retracted to maintain pressure and sample volume constant. When the desired strain is achieved, the displacement of the differential ram is stopped and the sample is immediately quenched to room temperature in a few seconds by shutting off the current in the heater. Then the pressure of the main ram and in the differential ram are decreased slowly to avoid damaging the WC anvils and so as not to further deform the sample at room temperature.

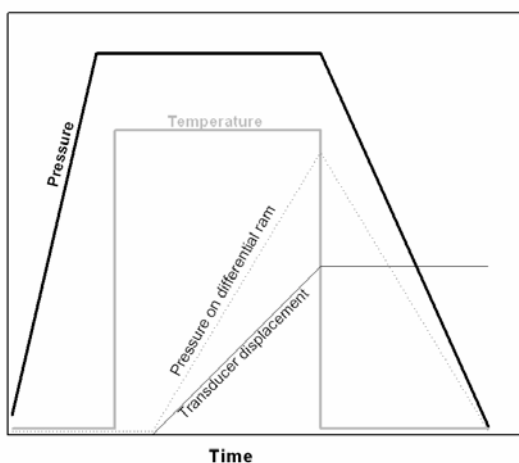


Figure II.12 - Experimental procedure for D-DIA experiments. See text for details.

### I.3.2 - Developments performed for deformation in the Kawai-type multianvil press

In this study, the mechanical properties of the three polymorphs of  $\text{Mg}_2\text{SiO}_4$  (forsterite, wadsleyite and ringwoodite) have been explored at  $1400^\circ\text{C}$  (see Figure 5). Since the pressure range covered by the experiments

is large (from 11 GPa for forsterite to 22 GPa for ringwoodite), two sizes of octahedron and two types of hydraulic presses have been necessary.

For experiments at 11 GPa on forsterite, the 18/11 assembly has been used to maximise the sample volume (see Table II.1). As Karato and Rubie (1997) developed the shear assembly in the 14/8 assembly only, their design had to be adapted to the 18/11 assembly (Figure II.13). The critical parameter is the length of the alumina pistons. Indeed, if the pistons are too small the deformation might not be sufficient and if they are too long they can apply large stresses on the second stage of anvils and damage the cubes.

For experiments on wadsleyite, a 14/8 assembly had to be used to reach the pressure stability field of this phase (Figure II.13). The 1000t (Hymag) or 1200t (Sumitono) presses were used to perform experiments on these two phases.

To reach the ringwoodite pressure range, one option is to use 10/4 assembly which exhibits a much smaller sample volume. The other solution is to take advantage of the 5000t press at the Bayerisches Geoinstitut (Frost *et al.*, 2004). This press is the scale-up version of 1000–2000t multianvil apparatus. It has been developed at the Bayerisches Geoinstitut for experiments performed over ranges of pressure and temperature attainable in conventional systems but with much larger sample volumes. In this press, experiments could be performed in the ringwoodite stability field (19 to 24 GPa at 1400°C) using a 18/8 assembly. Once again the shear deformation design had to be adapted to this pressure cell (Figure II.13).

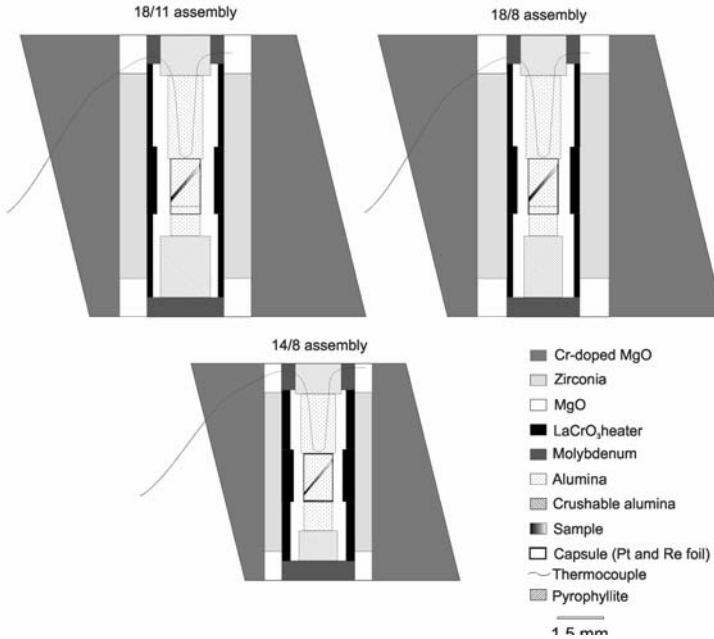


Figure II.13 - Cross-sections of the 18/11, the 18/8 and the 14/8 shear deformation assemblies (same scale for each).

In every experiment of this study, a strain marker is placed in the sample to record the total strain and measure it on recovered samples. It consists in a platinum coating deposited on a cut parallel to the axial compression so as not to record a possible compression of the specimens. Tungsten pistons used by Karato and Rubie (1997) in the capsule have been replaced by  $\text{Al}_2\text{O}_3$ .

The thermal gradient in the cell at pressure is an important parameter and must be evaluated. It depends on the assembly design and on the materials used. It can be estimated from different methods (Rubie, 1999). Temperature distribution has been measured in our 18/11 and 14/8 assemblies (standard and shear deformation design), using a 1:1 enstatite-

diopside mixture and by measuring the partitioning of Mg and Ca between these two phases (Nickel *et al.*, 1985). These measurements were made using a JEOL JXA-8200 electron microprobe at the Bayerisches Geoinstitut. The chemical composition of several couples of enstatite grain and diopside grain were measured on both side of the grain boundary. Using the BSE imaging of the microprobe, the two types of grains are easily recognized. Then using the two-pyroxenes thermometry equation given by Nickel *et al.* (1985), these two data points give a temperature value. Figure II.14 shows the temperature distribution maps measured in our experiments. The temperature read at the thermocouple of these assemblies is 1300°C (except for the 14/8 cell for which T= 1500°C). The gradient for standard assemblies is around  $75\pm 10^\circ\text{C}/\text{mm}$  with a hot-spot in the middle of the furnace (a bit toward the top of the capsule due to some vertical displacement). For the deformation assemblies the temperature is more homogenous probably due to the small thickness of the specimen; the maximal thermal gradient is  $50\pm 20^\circ\text{C}$ .

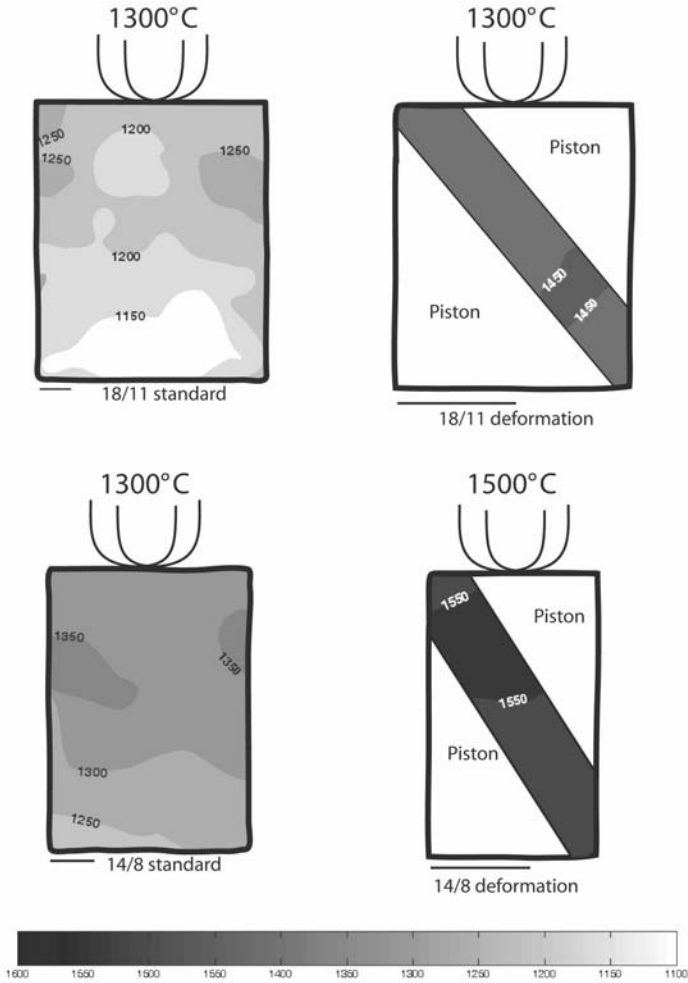


Figure II.14 – Temperature distribution map of 18/11 and 14/8 assemblies for standard and deformation (cross-section) designs. The thermocouple is on the top of each sample. Gray scale from 1100°C (white) to 1600°C (black). Isotherm: 50°C. Scale bars: 25  $\mu$ m.

Finally, a pressure calibration has been made at room temperature in the 14/8 shear assembly using the semi-conductor to metal transition in ZnS (15.5) GPa. The calibration shows that the nominal pressure at room temperature is about 20 GPa for 264 bars for the Hymag (1000t) press.

#### I.4- Preparation of the starting materials ( $\text{Mg}_2\text{SiO}_4$ )

Forsterite has been prepared from a mixing of MgO and SiO<sub>2</sub> in stoichiometric proportion. After firing the preparation at 1000°C and grounding it with acetone three times, a last fire was made at 1400°C and the powder was ground very fine (<5µm). Two portions of powder have been prepared using this procedure: Fo1 and Fo2. X-ray analyses show that Fo1 is pure forsterite and Fo2 contains some excess MgO and SiO<sub>2</sub> components.

## II – *In situ* measurements in the D-DIA

One of the major breakthrough in high-pressure rheology is the possibility of performing *in situ* stress and strain measurements by coupling with a synchrotron light source (e.g. Weidner *et al.*, 1998; Durham *et al.*, 2002; Chen *et al.*, 2004; Li *et al.*, 2004). The geometry of the D-DIA is well adapted for those measurements. Sample dimensions, and hence strains can be directly measured from radiograph images while stresses are derived through the multiple measurements of the sample along different orientations relative to the principal stress directions. This type of measurements needs a high energy X-ray source, not available at the Bayerisches Geoinstitut. Two sets of *in situ* measurements on deformation experiments have been

done at Argonne National Laboratory (Chicago, USA) and Brookhaven National Laboratory (New York, USA) where a D-DIA press is installed on a beam line. The general principles of these *in situ* measurements are presented below.

## II.1 – Technical setup

The geometry of the D-DIA is well adapted to bring an X-rays beam onto the sample. Of course an intense beam such as the one emitted from a synchrotron, is necessary and transparent materials are chosen for the sample environment (including the anvils: e.g. cBN). In recent years, specific techniques have been developed in Stony Brook to perform *in situ* stress and strain measurements under these experimental conditions (Weidner, 1998; Weidner *et al.*, 1998; Chen *et al.*, 2004; Li *et al.*, 2004).

In the course of this study, two sets of *in situ* measurements on deformation experiments using D-DIA have been performed at the GSEcars beamline of the Advanced Photon Source (APS, Argonne National Laboratory, Chicago) and at the X17B2 beamline at the National Synchrotron Light Source (NSLS, Brookhaven National Laboratory, New York).

Experiments are conducted using high energy white X-rays beams. A set of slits defines the size of the X-rays beam illuminating the sample. This set is mounted on a motor driven stage and the slits can be move in or out of the position changing the beam size according to the type of measurements. The typical beam size for sample imaging is 2mm x 2mm and the slits define a 100 $\mu$ m x 100 $\mu$ m beam size for X-ray diffraction. To gain the accessibility to the sample, the 6 WC edge anvils are replaced by 6 sintered cubic boron nitride anvils. The cBN has low X-ray absorption then

the diffracted X-rays can be in the diffraction plane with any angle to the vertical axis.

At NSLS, the diffraction spectra are collimated by a conical slit (Figure II.15) and collected simultaneously with four detectors. All technical detail are described in Chen et al.(2004). Inside the conical slit, two horizontal detectors collect the diffraction in the vertical plane and two vertical detectors collect the diffraction in the horizontal plane (Figure II.16). The virtual apex of the conical slit is placed at the sample centre then the four detectors sample the same area. A CCD camera records the image in visible light from a YAG crystal fluorescent screen (Figure II.16).

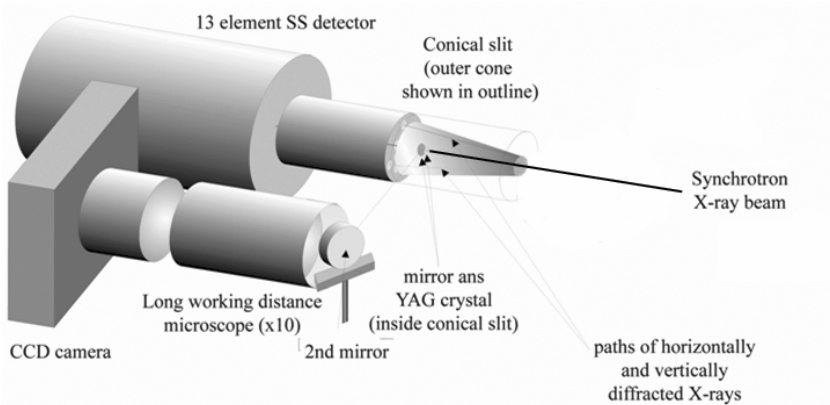


Figure II.15 – X-ray diffraction detector and imaging system at NSLS (from Chen et al. (2004))

At APS, only one vertical detector is present to collect the diffraction in the horizontal plane and the image of the sample is also recorded using YAG crystal fluorescent screen combined with a CCD camera.

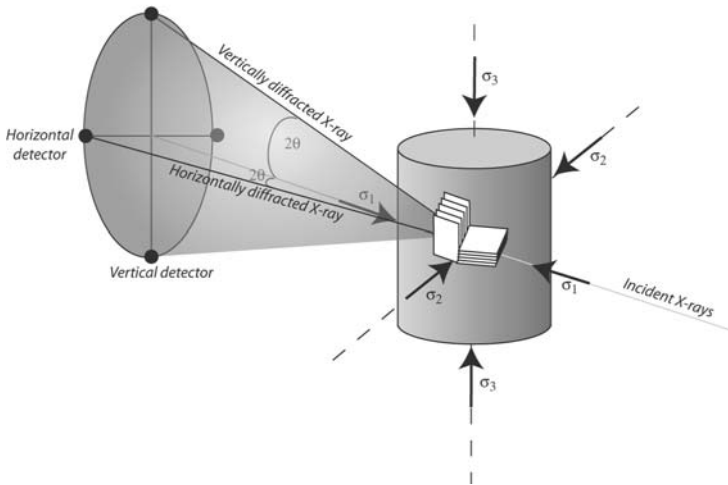


Figure II.16 – Geometry of X-ray diffraction and stress field in D-DIA apparatus.  $\theta$  is the Bragg angle of the X-ray diffraction (from Chen et al. (2004)).

## II.2- Strain measurement

A rhenium foil is placed at both ends of the sample in order to measure the strain and the strain rate *in situ*. Indeed, Re has very high X-ray absorption and is imaged in black on the radiographic picture (Figure II.17). The length of the sample is then well defined. The absolute variation of the sample length can be monitored throughout the experiment and measured with an accuracy of a micrometer. From this measurement, the strain rate can be calculated with an accuracy of  $10^{-6}\text{s}^{-1}$ .

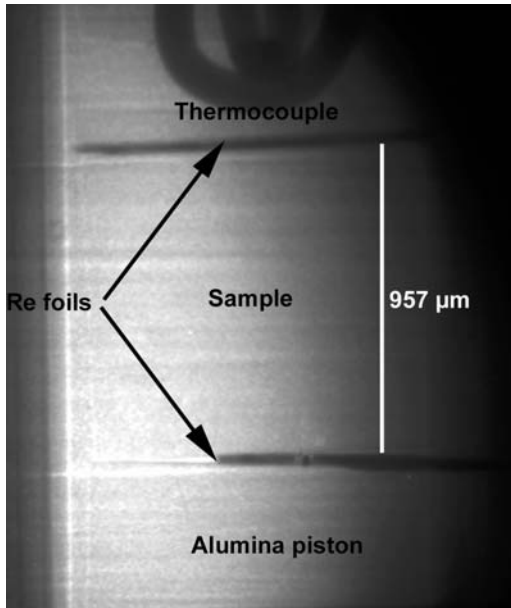


Figure II.17 – Radiograph image of a forsterite sample FOR21 before pressurisation. The shallow on the left and on the right of the picture comes from the BN anvil. The Re foils are used as strain marker.

### II.3 – Lattice strains analysis

Applying stress on a sample induces microscopic lattice strains, which result in a shift of the X-ray peaks. In the D-DIA configuration,  $\sigma_3$  is taken parallel to the compression axis, i.e. in vertical position,  $\sigma_1$  and  $\sigma_2$  are normal to the compression axis, in the horizontal plane (Figure II.16). Moreover, cylindrical symmetry is assumed implying that  $\sigma_1$  is equal to  $\sigma_2$ . Analysis of the lattice strain measurements under non hydrostatic pressure is described below. The stress field in the sample is:

$$\sigma_{ij} = \begin{pmatrix} \sigma_1 & 0 & 0 \\ 0 & \sigma_2 & 0 \\ 0 & 0 & \sigma_3 \end{pmatrix} = \begin{pmatrix} \sigma_p & 0 & 0 \\ 0 & \sigma_p & 0 \\ 0 & 0 & \sigma_p \end{pmatrix} + \begin{pmatrix} -t/3 & 0 & 0 \\ 0 & -t/3 & 0 \\ 0 & 0 & 2t/3 \end{pmatrix}$$

where  $\sigma_p$  is the hydrostatic pressure (mean normal stress) and  $t$  is the differential stress:

$$\sigma_p = 1/3(\sigma_1 + 2\sigma_3) \quad \text{and} \quad t = \sigma_3 - \sigma_1$$

In term of the measured  $d$  spacing,  $d_m(hkl)$ , the strain produced by the deviatoric stress component is given by:

$$\varepsilon(hkl) = \frac{d(hkl)_m - d(hkl)_p}{d(hkl)_p} \quad (1)$$

where  $d(hkl)_p$  is the spacing under the pressure  $\sigma_p$ . From Singh *et al.* (1998), the equation for the lattice strain is:

$$d_m(hkl) = d_p(hkl) \left( 1 + (1 - 3 \cos^2 \psi) Q(hkl) \right) \quad (2)$$

where  $\psi$  is the angle between  $\sigma_3$  and the diffracting vector, and  $Q(hkl)$  is :

$$Q(hkl) = (t/3)(2 * G(hkl)^{-1}) \quad (3)$$

$G(hkl)$  is an effective elastic modulus calculated in anisotropic elasticity for one plane ( $hkl$ ) at pressure and temperature conditions (Singh *et al.*, 1998). From (1), (2) and (3),  $t$  is equal to:

$$t = 2 * G(hkl) * \frac{d(hkl)_V - d(hkl)_H}{d(hkl)_P}$$

where  $d(hkl)_V$  and  $d(hkl)_H$  are the  $d$  spacings measured from the X-ray spectra collected on the vertical and horizontal detectors, respectively.

### III – Analytical techniques on recovered samples

Most samples deformed in this study were characterized *post-mortem*. A lot of efforts have been placed in sample characterization with a view to get information on the behavior of the sample during the experiment as well as on the experiment itself. The main techniques used are presented here. Some complementary characterizations performed through collaborations with other groups are described in appendices.

### III.1 - Scanning Electron Microscopy (SEM) and Electron BackScattering Diffraction (EBSD)

#### III.1.1 - Sample preparation for SEM and EBSD

Cross-section and planar section (parallel to the shear plane) of samples are put in epoxy cylinder and polished down to  $3\mu\text{m}$ . These preparations were made in the Bayerisches Geoinstitut by Hubert Schultze. As the EBSD measurements are very sensitive to the quality of the sample surface, a colloidal silica suspension is used to provide a final chemical polishing, in order to remove the shallow layers damaged by mechanical grinding.

#### III.1.2 - SEM and imaging

All the SEM measurements were performed at the Bayerisches Geoinstitut with a Leo Gemini 1530 SEM equipped with a field emission gun (FEG) and an EBSD detector. The parameters of the beam for imaging and for measurements are an accelerating voltage of 20 kV, a working distance of ca. 20 mm and a probe current of 3.5 nA.

Cross-sections and planar section of the whole samples were imaged using the SEM in order to examine the grain size and shape as well as to measure the strain marker rotation. These images have been taken using Back Scattered Electrons (BSE) with Orientation Contrast (OC). The orientation contrast is a control of the variation of BSE signal intensity by the lattice orientation. This type of contrast is preferred to the Z-contrast because it allows seeing the individual grain due to their different orientations.

### III.1.3 – Electron BackScattering Diffraction technique

Crystallographic preferred orientation (CPO) analysis was performed using the EBSD technique (Dingley, 1984). In the SEM chamber, the sample is tilted at  $70^\circ$  to the beam (Figure II.18). When the electron beam is focused onto a single grain from the polished sample surface, the backscattered electrons that re-exit the sample surface form a diffraction pattern that is equivalent to the well-known Kikuchi pattern in transmission electron microscopy. This Electron BackScattering Pattern (EBSP) is recorded with a phosphorus screen and can be indexed, yielding the complete crystallographic orientation of the grain underneath the beam. Through automation of this procedure (Adams *et al.*, 1992), the microstructure and texture at the sample surface can be mapped. However, this automatic procedure cannot be used in the case of wadsleyite because of the possibility of pseudosymmetric mis-indexing. Pseudosymmetric mis-indexing occurs where two orientations cannot easily be distinguished due to an apparent n-fold rotation axis especially in lower symmetry crystal structures. For example an orthorhombic structure with similar lengths of the a- and b- axis appears to be pseudo- tetragonal when viewed down its c-axis. Manual indexing of Kikuchi pattern is then required to get unambiguous results (see Chapter III, §II.2). In order to obtain representative fabrics, 100 grains have been analysed on each samples (Ben Ismail and Mainprice, 1998). From these measurements, pole figures are derived showing the orientation of each crystal axis relative to the sample coordinates. The discrete point distributions are converted into densities by grouping them within a  $5^\circ$  area and then smoothing with a Gaussian function

with a  $15^\circ$  FWHM. The resulting density distributions are normalised and contoured.

Automated indexing was performed with the software CHANNEL 5 (HKL Technology) and the pole figures were plotted using PFch5, freeware developed by David Mainprice (Laboratoire de Tectonophysique, University of Montpellier II, France).

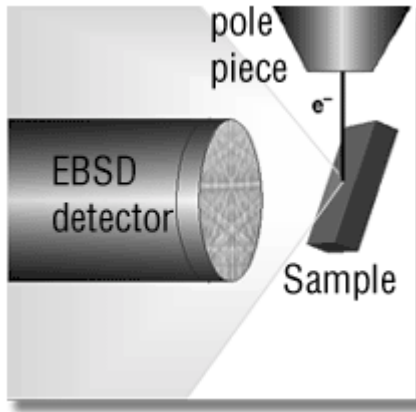


*Figure II.18 – EBSD: position of the sample relative to the beam and the detector in the SEM chamber.*

## III.2 – Transmission Electron Microscopy (TEM)

### III.2.1 – Sample preparation for TEM

Doubly polished thin ( $25\ \mu\text{m}$ ) sections have been prepared from recovered specimens for TEM observation. This preparation has been made in the Bayerisches Geoinstitut by Hubert Schultze. The samples have been

glued on a Cu grid and ion milled at 4.5 kV under a low beam angle of 15° until electron transparency is reached.

### III.2.2 – Presentation of the microscope

TEM observations were carried out in Lille with both a Philips CM30 microscope operating at 300 kV and a 200 kV Jeol 200CX and in Bayreuth with a Philips CM20 FEG microscope.

A TEM is composed by an electron gun and several electromagnetic lenses, which have a fixed position and variable focal lengths (Figure II.19). The electron beam is produced by the gun. The objective lens gives an image of the object which is scaled up several times by the intermediate lens and projected on the fluorescent screen.

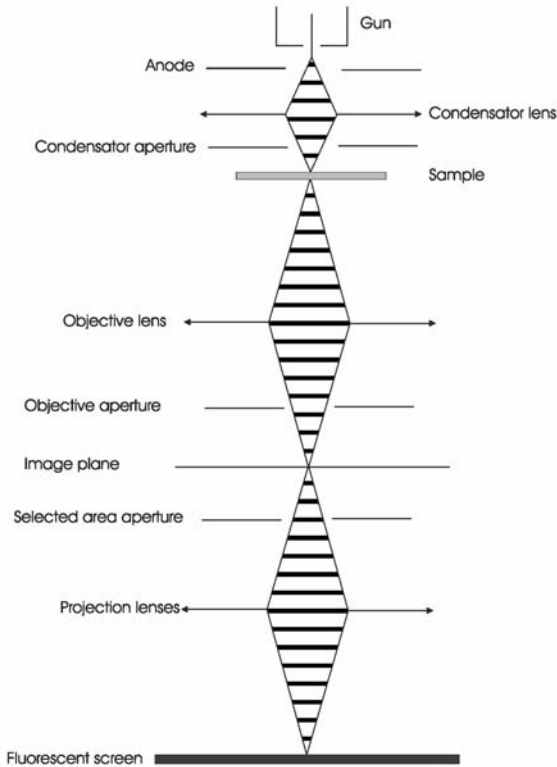


Figure II.19 – Simplified schematics of a TEM.

### III.2.3 – Diffraction mode: Selected Area Electron Diffraction (SAED)

The electron diffraction patterns are obtained with a parallel electron beam. The studied area of the sample is selected using a selected area aperture. Part of the incident beam is diffracted by the planes which are in Bragg orientation. The plane family  $\{hkl\}$  is in Bragg orientation if

$\theta_i = \theta_B$ , ( $\theta_i$  is the angle between the (hkl) plane and the incident beam) and  $\theta_B$  satisfying the Bragg's law:

$$2 \cdot d_{hkl} \cdot \sin \theta_B = n \cdot \lambda$$

where  $\lambda$  is the wavelength of the electrons. This other part of the incident beam is transmitted with an angle of  $2\theta_B$  with the diffracted beam. These beams converge into spots in the back focal plane of the objective lens giving the diffraction pattern of the selected area.

### III.2.4 – Imaging mode and observation of dislocations

The diffraction contrast can be obtained when an image is formed in the image plane from either the transmitted beam or a diffracted beam. For this purpose, the chosen beam is selected using the objective aperture which is located in the back focal plane. Usually, the studied crystal is tilted in suitable orientation to have only one set of (hkl) plane in Bragg condition. This condition is named “two-beam”.

If the transmitted beam is selected, a so-called “bright field” image is obtained. In this mode, the areas which do not diffract are bright and those which diffract are darker. The alternative mode is named « dark field » where the objective aperture selects the diffracted beam. In this mode, the diffracted areas are bright and the non-diffracting areas are dark.

Crystal defects like dislocations induce local bending of crystal planes close to the defects. They give rise to a characteristic contrast in the TEM which can be used to characterize them. When the diffracting plane is in exact Bragg orientation for the perfect crystal, the contrast arise for a relatively large region around the dislocation core where the lattice planes are distorted. The dislocation image is the relatively broad. An image of the

dislocation with a higher resolution can be obtained in the so-called weak-beam mode. In this mode, derived from the dark-field, one set of planes has to be orientated in two-beam conditions and slightly moved away from the exact Bragg conditions tilting along  $[hkl]^*$ . Only lattice planes very close to the dislocation core (the most distorted lattice planes) are left in exact Bragg orientation and give rise to a visible contrast (Figure II.20). The dislocation image is then much narrower and its position is closer from the actual position of the dislocation core. This mode is very useful to check for small dislocation dissociations which are of primary importance for dislocation mobility.

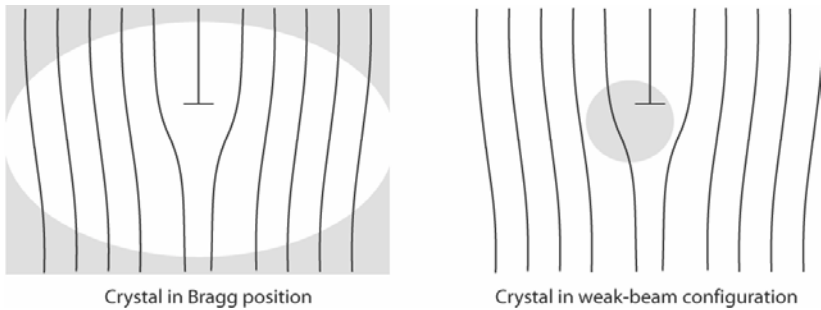


Figure II.20 – Origin of the contrast of a dislocation

On the left, the perfect crystal is in Bragg orientation – Bright field.

On the right, Weak-beam dark-field configuration, the diffracting zone (in gray) giving rise to the observed contrast is smaller and closer to the dislocation core.

A crystal defect is characterized by its displacement field  $\vec{R}$ , which creates a phase shift  $\alpha$  of the diffracted beam:

$$\alpha = 2\pi \times \vec{g} \cdot \vec{R}$$

where  $\vec{g}$  is the diffraction vector.

For a screw dislocation, the displacement field is parallel to the Burgers vector  $\vec{b}$ . The dislocation is then out of contrast for some specific diffracted beams verifying:

$$\vec{g} \cdot \vec{b} = 0;$$

This condition can be used to characterize a dislocation. It is then necessary to find two diffraction vectors  $\vec{g}$  for which the dislocation is out of contrast. In case of an edge dislocation, the displacement field is slightly more complicated. The extinction condition is then:

$$\vec{g} \cdot \vec{b} = 0; \quad \vec{g} \cdot (\vec{b} \wedge \vec{u}) = 0$$

where  $\vec{u}$  is the unit vector along the dislocation line.

### III.3 – Other analytical methods

#### III.3.1 – Micro-Raman spectroscopy

In several cases, phase identification of synthesised samples has been made using Raman spectroscopy. Raman spectra were collected in the 100–1100  $\text{cm}^{-1}$  range using a LabRam spectrometer with an He-Ne laser (632 nm). Spectral resolution is 2  $\text{cm}^{-1}$ . High-magnification objective (x100) and co-focal optical system provide spatial resolution within 5  $\mu\text{m}$ .

#### III.3.2 – Fourier Transform InfraRed spectroscopy

##### (FTIR)

The hydroxyl content of forsterite and wadsleyite samples were measured using a Bruker™ IFS 120 HR high-resolution FTIR spectrometer coupled with a Bruker™ IR microscope. Measurements were carried out

using a tungsten light source, a CaF<sub>2</sub> beam-splitter and a high-sensitivity, narrow-band MCT detector. Two hundred scans were accumulated for each spectrum. During the measurement, the optics of the spectrometer were evacuated and the microscope was purged with a stream of H<sub>2</sub>O- and CO<sub>2</sub>-free purified air. We used a spot size of 100 μm allowing several grains to be measured together. More technical details of the design of FTIR spectrometer based on the Michelson interferometer are given in Siesler *et al.*, (2002). Unpolarized FTIR spectra were obtained at room temperature on polished fine sections. To determine the concentration of hydroxyl groups in the deformed samples, the infrared spectra were integrated from 3625 to 3300 cm<sup>-1</sup>, the region dominated by the stretching vibrations due to the OH bonds. The integration was carried out using the calibration proposed by Paterson (1982).

# Chapter III

## Results

Through the present experimental study on the mechanical properties of olivine at high pressure and of its high-pressure polymorphs, we address the rheology of the Earth's mantle down to 670 km depth. For sake of simplicity and to allow comparison, most experiments have been carried out at 1400°C. Besides the intrinsic mechanical behaviour of each phase, the possible role on rheology of a phase transformation at the olivine-wadsleyite transition has been investigated.

Given the pressure range in the mantle transition zone and in the lowermost upper mantle, the Kawai-type multianvil apparatus appears to be the most well adapted technique. As a complex thermo-mechanical history is associated with this kind of experiments, a special attention has been devoted to the evolution of deformation with time duration. For this purpose, detailed characterisations of the samples recovered after the experiments have been performed at different scales.

Although its pressure range does not give a direct access to the transition zone conditions, the Deformation-DIA, which possesses very attractive possibilities on the control of deformation parameters, has been used here to extend the range of the experiments performed on forsterite.

These experiments as well as the results of these microstructural characterisations are presented in this chapter and will be discussed in the next chapter.



## I – Deformation of forsterite at high pressure

### I.1 – Deformation experiments using the Kawai-type multianvil apparatus

The aim of this first series of experiments is for, the first time, to investigate the mechanical properties of forsterite at high pressure and high temperature. Given the complexity of deformation experiments in the multianvil apparatus, a special attention has been devoted to the evolution of strain and deformation microstructures with time duration.

Deformation experiments in the Kawai-type multianvil apparatus have been performed on samples prepared from Fo1. The powder is first hot-pressed in a standard 18/11 assembly at 5 GPa and 1100°C for 4 hours. Thin (200µm) samples slices are cut at 45° from this hot-pressed cylinder. A second vertical cut is made to divide the specimen into two parts and the two exposed surfaces are vacuum coated with platinum to provide the strain marker. The slices are then placed into the shear deformation 18/11 assembly. The deformation experiments are summarised in Table III.1.

**RESULTS**

Run #	Sample # (Hot- pressing stage)	Oil pressure (bar)	Nominal pressure (GPa)	Temp- erature (°C)	Duration (min)	Strain marker rotation (deg.)	Piston displacement (µm)
S2964 <sup>(1)</sup>	S2911	360	11	-	-	6 (4)	80 (10)
S2970 <sup>(1)</sup>	S2947	360	11	-	-	9 (3)	89 (10)
S3024 <sup>(1)</sup>	S3017	360	11	-	-	10 (11)	200 (40)
S2996	S2961	360	11	1400	1	9 (3)	93 (30)
S2997	S2961	360	11	1400	1	10 (4)	93 (50)
S2917	S2897	360	11	1500	60	5 (3)	119 (20)
S2954 <sup>(2)</sup>	S2910	360	11	1400	60	8 (2)	142 (40)
S2955 <sup>(2)</sup>	S2911	360	11	1400	60	13 (5)	145 (20)
S2993	S2947	360	11	1400	60	11 (6)	123 (30)
S2994	S2961	360	11	1400- 1500	60	6 (2)	137 (40)
S2984	S2947	360	11	1400	480	15 (8)	133 (20)
S2998	S2897	360	11	1400	480	8 (4)	100 (20)
S3079	S3017	360	11	1400	480	13 (14)	77 (20)

*Table III.1 - Experimental conditions for forsterite deformation in the multianvil apparatus (S: Sumitomo press). <sup>1)</sup> Samples cold-compressed and not heated - <sup>2)</sup> Samples cooled down over in few minutes (the others are quenched).*

Experiments have been deformed at 11 GPa and 1400°C during one minute, one hour and eight hours to follow the evolution of deformation with time at high-temperature. Some experiments have been cold compressed and immediately decompressed without heating to investigate the

microstructures induced in the samples after cold compression. Several experiments were performed for each duration time to test the reproducibility of the experiment.

### **I.1.1 – Strain marker rotation and piston displacement**

After the experiments, the recovered assemblies are observed at the optical microscope in cross section. As an illustration, Figure III.1 presents a few pictures from high-pressure shear deformation assemblies which have been compressed to 11 GPa. Figure III.1a shows that the deformation column is perfectly aligned after compression and that the sample is still located at the centre of the furnace. An enlargement of a sample capsule is displayed in Figure III.1b which shows that straining of the sample has been accompanied by a displacement of the upper piston with respect to the lower piston. The strain marker is visible in Figure III.1c. Note that it was vertical prior to the experiment. The function of the strain marker is to record the total strain undergone by the sample (Karato and Rubie, 1997) as this information is not directly accessible during the experiment.

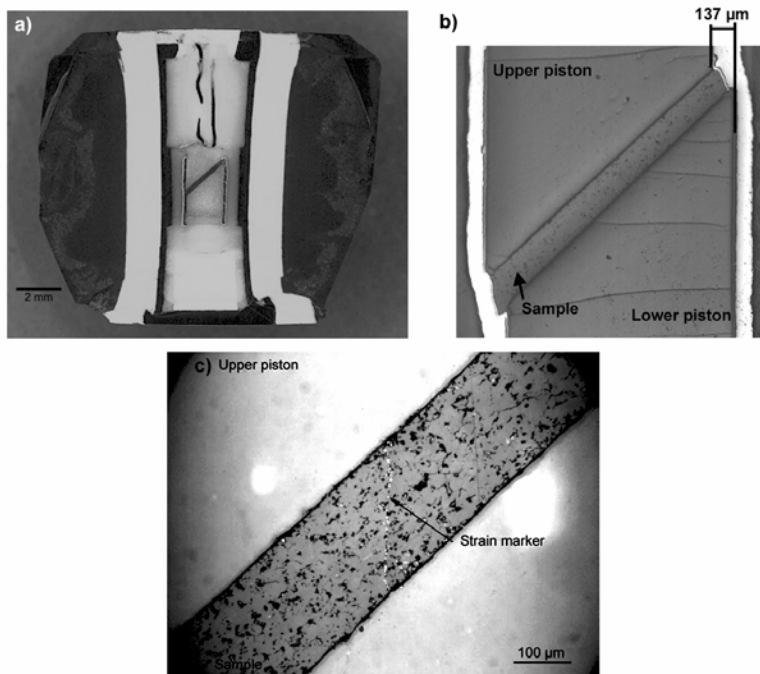


Figure III.1 – Optical micrographs of high-pressure cells after deformation of forsterite.

a) Cross section of the octahedron. Cold compressed sample (S2970).

b) Enlargement of a sample capsule. Note the piston displacement on both sides. After one hour at 1400°C-11GPa (S2994)

c) Central part of the specimen showing the strain marker. After one minute of heating at 1400°C 11GPa (S2997).

Strain marker rotations have been imaged and measured on SEM pictures from cross section. The value reported in Table III.1 show that in all cases the strain marker rotation is small, probably lower than 10°. Indeed, specimens that were compressed but not heated exhibit a non-zero strain marker rotation between 6° and 10°. No marked evolution is found between "one minute" and "eight hour" experiments. As a complementary approach,

we tried to use the piston displacement as an estimate of shear. The measured values are recorded Table III.1. As for the strain marker, the piston displacement is not found to evolve significantly with time passed at high-temperature. Altogether, these measurements do not support the idea, suggested by previous studies (Karato and Rubie, 1997; Karato *et al.*, 1998), that large strain have been achieved. From these measurements, it is estimated that the total shear strain undergone by our forsterite specimens deformed at 11 GPa, 1400°C is below  $\gamma = 0.3$  (see Appendix I for the shear strain calculation from the strain marker rotation). No measurable change has been found in the sample thickness, which suggests that the compression is negligible during the experiment.

### **I.1.2 – Microstructural characterisation: SEM and EBSD**

Every sample has been characterised using the SEM. Figure III.2 presents typical microstructures at various stages.

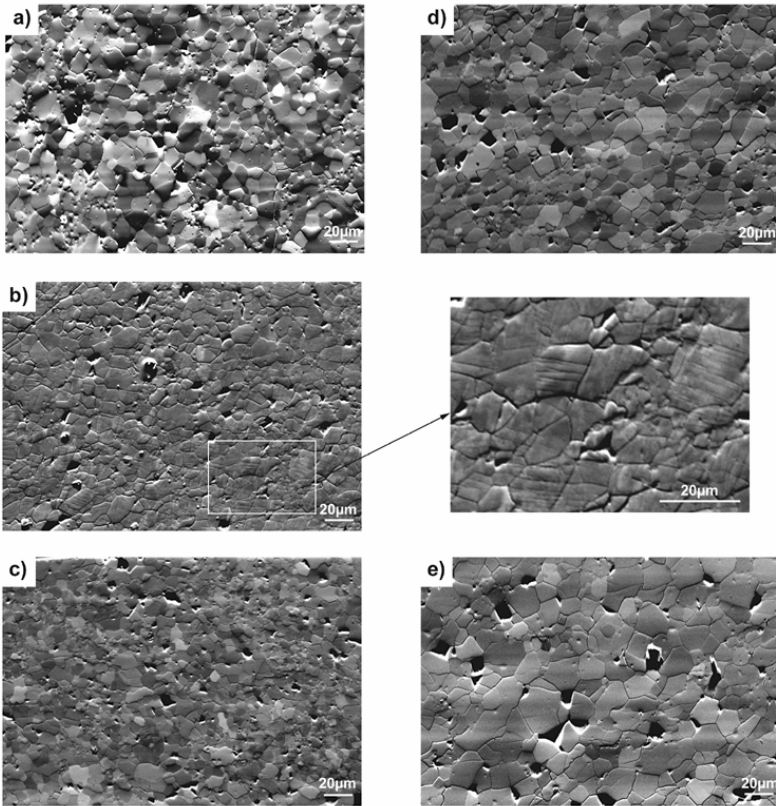


*Figure III.2 - SEM pictures in orientation contrast of forsterite samples. Cross section, shear direction horizontal and shear sense dextral.*

*a) After hot-pressing*

*b) After cold compression at 11GPa (S2964)*

*c) After one minute at 11GPa and 1400°C (S2996)*

*d) After one hour at 11GPa and 1400°C (S2955)*

*e) After eight hours at 11GPa and 1400°C (S3079)*

The starting material (after hot pressing) is shown in Figure III.2a. It consists of equilibrated grains with a mean size of 10 μm. After cold compression (Figure III.2b), the overall microstructure is unchanged although

most grains exhibit significant damage (cracks) (see enlargement of Figure III.2b). This damage is no longer visible after heating and only one minute spent at 1400°C (Figure III.2c). For longer time durations (one and eight hours: Figure III.2d-e), the only visible modification is a slight increase in the grain size.

The grain size has been measured from the SEM images using ImageTool software (University of Texas Health Science Center, San Antonio), which calculates the area of each grain from a redrawn SEM picture. The diameter corresponding to a circle having the same area of the grain is determined. This diameter is multiplied by 1.56 to obtain an equivalent 3D-grain size (Chiang and Kingery, 1989). Figure III.3 shows four examples of grains size distributions and Figure III.4 displays the evolution of the grains sizes with time. The mean grain size after hot-pressing and cold compression is in the range 11-16  $\mu\text{m}$ . After one hour of heating, the increase of grain size is small, as the mean value is about 14 to 17  $\mu\text{m}$ . After eight hours of heating, grain growth is measurable (mean grain size: 21  $\mu\text{m}$ ) although it is still modest.

## RESULTS

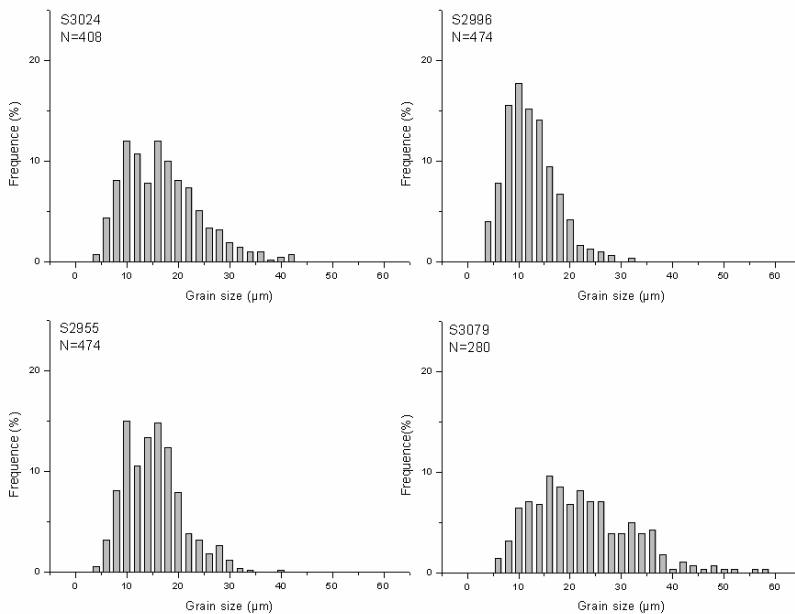


Figure III.3 – Forsterite grain size distributions for samples S3024 (cold compression), S2996 (one minute), S2955 (one hour) and S3079 (eight hours).

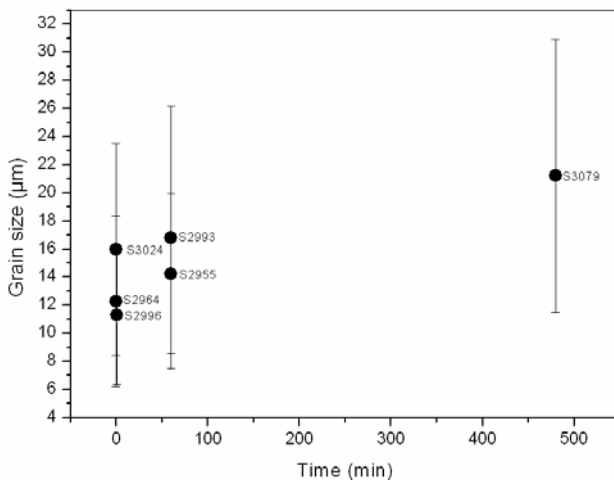


Figure III.4 – Forsterite evolution of the mean grain size with time for six samples. Bars represent data scattering ( $2\sigma$  standard deviation).

The results of EBSD characterisation are presented in Figures III.5 to Figure III.8. For the starting material (hot-pressing) S2897, Y corresponds to the axis of the furnace of the high-pressure cell. For the other samples deformed in shear, X is parallel to the shear direction and Y is normal to the shear plane. The shear sense is dextral.

The starting material (from hot-pressing: S2897) and the cold compressed sample (S3024) display no significant CPO; the concentrations observed for [100] directions are not related to the [010] maxima or to the [001] maxima (Figure III.5).

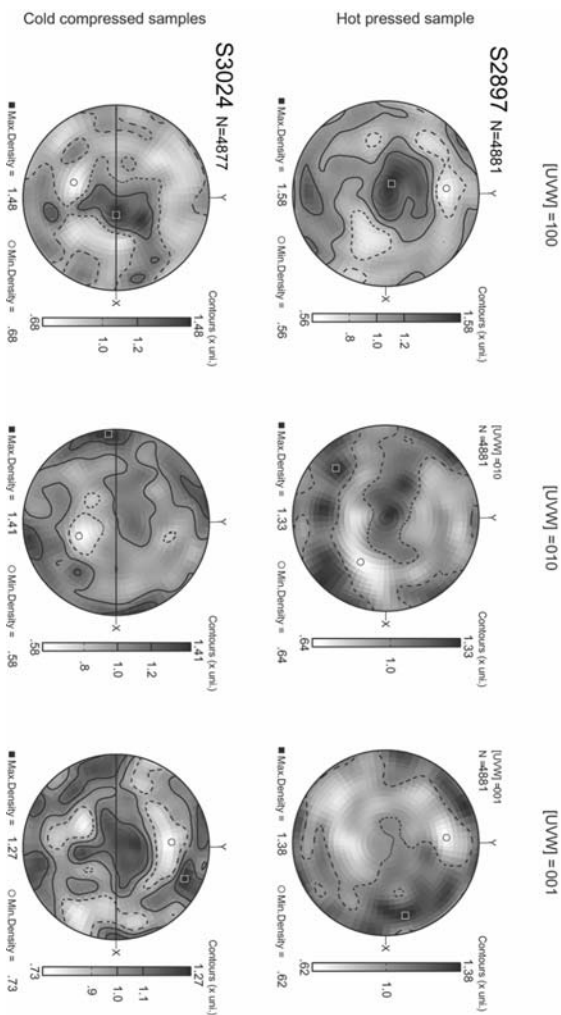


Figure III.5 - EBSD pole figures of crystal axis for the hot-pressed forsterite sample used as a starting material (S2897) and after cold compression (S3024). For S2897, Y is along the furnace axis of the high pressure cell. For S3024, the shear direction is aligned with X and Y is perpendicular to the shear plane; the shear sense is dextral. Lower hemisphere equal-area projections, contours at intervals of 0.2 multiple of a uniform distribution.

## RESULTS

---

After one minute of heating (Figure III.6), the [100] and the [001] axes both align with the normal of the shear plane as well as with the shear direction. But each concentration of [100] does not coincide with a concentration of [001]. [010] tend to cluster in the shear plane perpendicular to the shear direction.

RESULTS

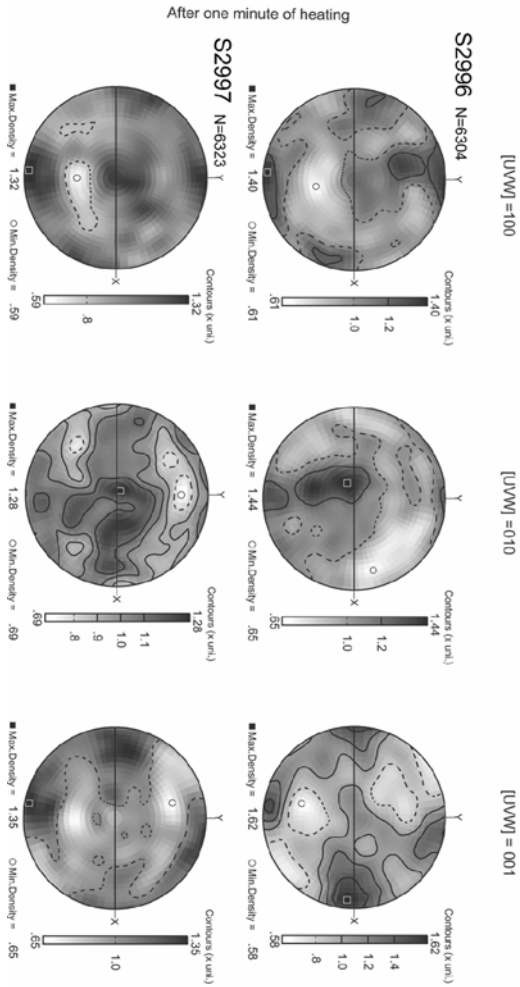


Figure III.6 - EBSD pole figures of crystal axis for forsterite samples after one minute of heating (S2996 and S2997). The shear direction is aligned with X and Y is perpendicular to the shear plane; the shear sense is dextral. Lower hemisphere equal-area projections, contours at intervals of 0.2 multiple of a uniform distribution.

Only after one hour, appears a more significant CPO (Figure III.7). For samples S2954, S2955 and S2994, the [001] axes are aligned toward the shear direction. Clustering is higher for S2994 which presents also a weak secondary [001] maximum perpendicular to the shear direction within the shear plane. The concentration of [001] axes in S2954 and S2955 is at low angle from the shear direction, in conformity with the imposed dextral shear sense. On the opposite, in S2993, the [001] axes tend to align with the normal to the shear plane. In S2954, S2955 and S2993, the [100] axes are concentrated at low angle from the normal to the shear plane, in agreement with the imposed dextral shear sense. S2954, S2955 and S2993 present also a weak secondary [100] maximum in the shear plane normal to the shear direction. S2994 displays the [100] axes clustered in the shear plane normal to the shear direction. For all these “one hour” samples, [010] display a girdle normal to [001], with a stronger concentration close to the shear plane normal, to the shear direction (S2954 and S2993) or close to the normal to the shear plane (S2955 and S2994).

For all these samples but S2993 (for which the CPO cannot be interpreted) the CPO suggest a major contribution of [001]{hk0}.

RESULTS

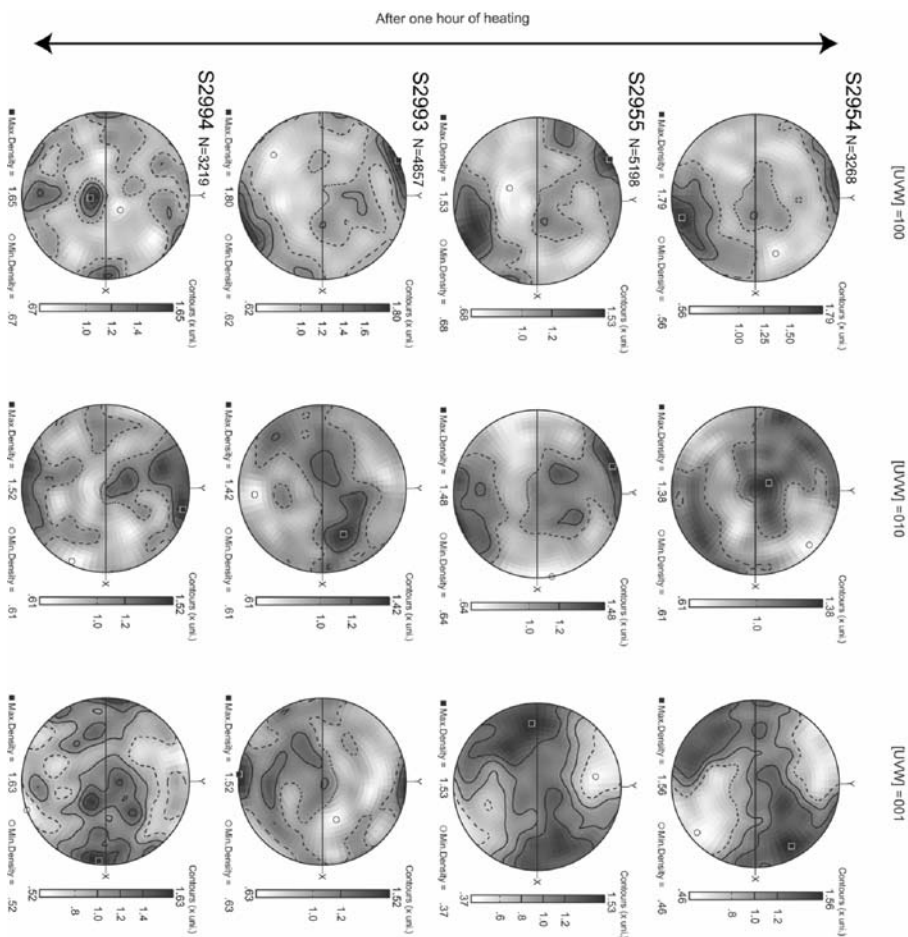


Figure III.7 – EBSD pole figures of crystal axis for forsterite sample after one hour of heating (S2954, S2955, S2993 and S2994). The shear direction is aligned with X and Y is perpendicular to the shear plane; the shear sense is dextral. Lower hemisphere equal-area projections, contours at intervals of 0.2 multiple of a uniform distribution.

After eight hours of heating (Figure III.8), S2998 and S3079 show the [001] axes aligned at low angle from the shear direction (ca.30°) and

## RESULTS

---

[010] are mainly concentrated toward the normal to the shear plane. The [100] axes orientation is more complex: they present a maximum normal to the shear direction within the shear plane and secondary maxima at low angle from the shear direction as well as from the normal of the shear plane. The CPO of “eight hour” samples suggests that, for heating time over one hour, the CPO weaken.

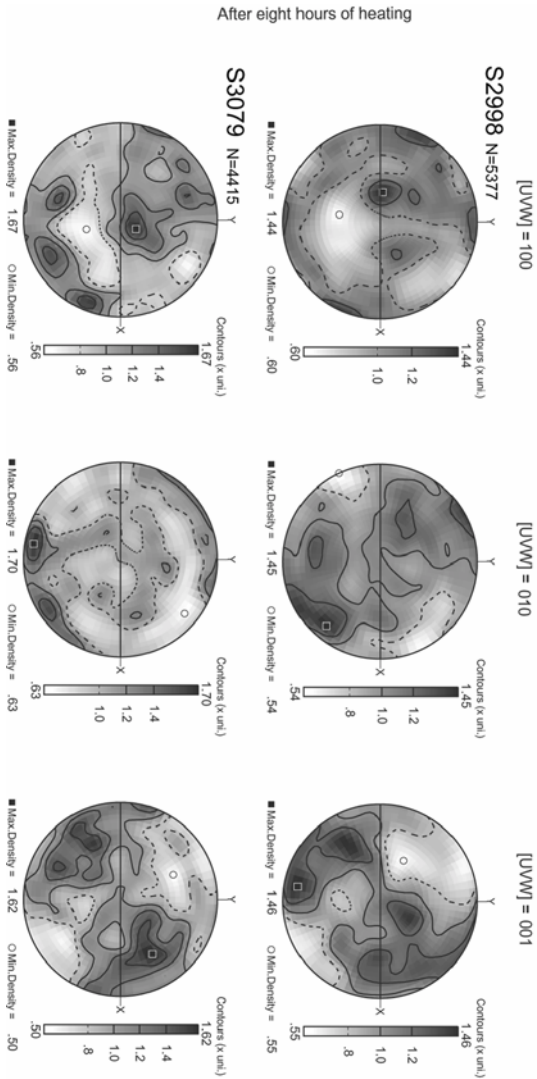


Figure III.8 - EBSD pole figures of crystal axis for forsterite samples after eight hours of heating (S2998 and S3079). The shear direction is aligned with X and Y is perpendicular to the shear plane; the shear sense is dextral. Lower hemisphere equal-area projections, contours at intervals of 0.2 multiple of a uniform distribution.

Note that for all these samples, the maximal densities are relatively weak, between 1.27 and 1.80 multiple of a uniform distribution.

### I.1.3 – Microstructural characterisation: X-ray peak broadening

The average dislocation density can be determined at the sample scale from X-ray diffraction peak broadening (e.g. Castelnau *et al.*, 2001; Schafner *et al.*, 2001; Ungár *et al.*, 2001a). This investigation has been done on our samples by T. Ungár and K. Nyilas (Department of General Physics, University Budapest, Hungary). The original method, developed on cubic and hexagonal crystals, is described in Wilkens (1970); Ungár *et al.* (1999) and Ungár *et al.* (2001b) for instance. For this study, the method has been adapted to orthorhombic symmetry (see Appendix II for details).

Samples recovered after cold compression (S2964), after one minute of heating (S2996), after one hour of heating (S954, S2955 and S9993) and after eight hours of heating (S2998) have been investigated by X-ray diffraction. Five forsterite reflections planes have been analysed: {021}, {101}, {002}, {130} and {220}. Typical peak profiles for {101} reflections as a function of the duration of the experiment are shown in Figure III.9a. It can be seen that the cold compressed specimen displays the largest broadening and that peak broadening decreases with holding time at high temperature. The detailed analysis of these peak profiles provide the average dislocation densities (Ungár *et al.*, 2001b) as well as the average mean crystallite diameter  $\langle x \rangle_{\text{area}}$  (Hinds, 1982) and the median,  $m$ , and the variance,  $\sigma$ , of a log-normal size distribution function (Wilkens, 1970). The size corresponds to the size of the smallest undisturbed volume in the

crystal. This needs not to be the grain size which is accessible e.g. from a TEM micrograph.

These values (including the dislocation densities) obtained from our specimens are listed in Table III.2. The dislocation densities found with this method are in good agreement with the few densities measured on TEM micrographs.

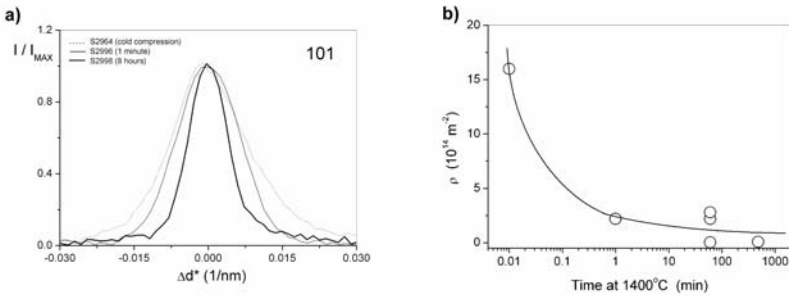


Figure III.9 – a) Typical profiles of 101 Bragg peaks in three different specimens of forsterite. The decrease of peak width with annealing time can be observed.

b) Dislocation densities as a function of duration at 1400°C. The open circle at 0.01 min corresponds to the cold compressed specimen. The line is a guide for the eye only.

The evolution (in log scale) of dislocation densities as a function of time is presented Figure III.9b. The dislocation density decreases drastically (from the high value induced by cold compression:  $16 \times 10^{14} \text{ m}^{-2}$ ) as soon as the specimen is heated a value of  $2 \times 10^{14} \text{ m}^{-2}$  is obtained after only one minute at nominal temperature. Then, the dislocation density reaches a quasi-constant level around  $10^{14} \text{ m}^{-2}$ , for longer experiment duration.

## RESULTS

Specimen #	$m$ [nm]	$\sigma$	$\langle x \rangle_{\text{area}}$ [nm]	$\rho$ [ $10^{14} \text{ m}^{-2}$ ]
S2964 (cold compression)	55 (5)	0.38 (0.05)	80 (5)	16 (4)
S2996 ( 1 min of heating)	161 (10)	0.01 (0.01)	160 (10)	2.2 (0.5)
S2954 ( 1 hour of heating)	94 (10)	0.19 (0.05)	105 (10)	2.2 (0.5)
S2955 ( 1 hour of heating)	63 (5)	0.36 (0.05)	90 (5)	2.8 (0.5)
S2993 ( 1 hour of heating)	118 (10)	0.06 (0.02)	120 (10)	0.04 (0.02)
S2998 ( 8 hours of heating)	122 (10)	0.12 (0.05)	130 (10)	0.09 (0.02)

*Table III.2 – Forsterite deformation: results of X-ray peak broadening analysis. Median,  $m$  and variance,  $\sigma$  of the crystallite size distribution functions, area-averaged mean crystallite diameters,  $\langle x \rangle_{\text{area}}$ , and average dislocation densities,  $\rho$  for samples listed in the first column. Margin of error are also indicated.*

### I.1.4 – Microstructural characterisation: TEM

The salient observation in every specimen observed at the TEM is the pervasive occurrence of [001] dislocations. However, the microstructures are found to evolve significantly with time duration at high-temperature. After cold compression, all grains contain high densities of dislocations, as already shown by X-ray peak broadening. These dislocations, with [001] Burgers vectors, exhibit marked line orientations along edge and screw directions (Figure III.10a) characteristic of a high lattice friction on both characters. Very comparable microstructures are observed in specimens heated for one minute although the density of edge

segments begins to decrease. After one hour, the microstructure of every grain is dominated by straight screw  $[001]$  dislocations (Figure III.10b). One can also find in some grains of these specimens a few widely dissociated dislocations (Figure III.10c). Stereographic analysis shows that these defects involve stacking faults in  $\{021\}$  (Figure III.10c). In specimens annealed for eight hours, most grains are pristine. Some grains, however, still contain  $[001]$  screw dislocations in addition to some subgrain boundaries (Figure III.10d).

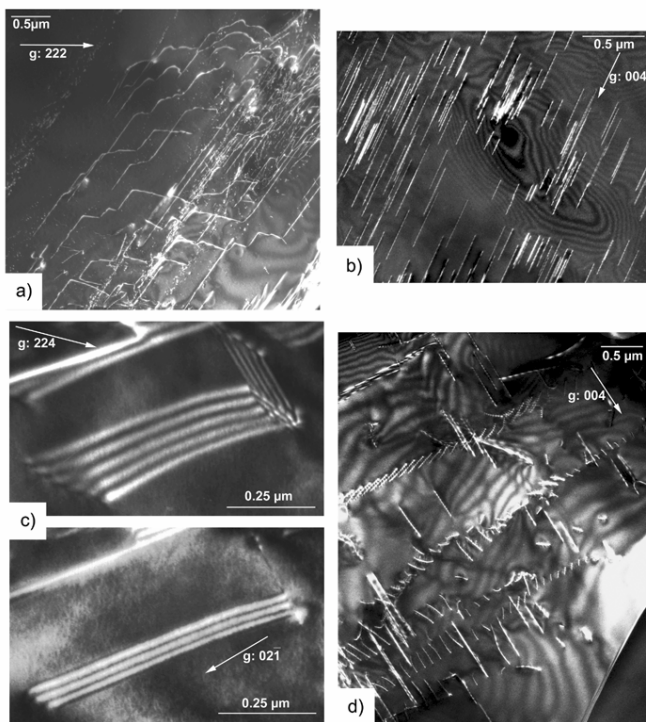


Figure III.10 - TEM micrographs of forsterite grains. Weak-beam dark-field

a) Sample S3024, cold compressed at 11 GPa and not heated.  $[001]$  dislocations in glide configuration. Note the abundant edge segments exhibiting lattice friction.  $g:222$ .

b) Sample S2954, deformed for one hour at 11 GPa, 1400°C.  $[001]$  screw dislocations.  $g:004$ .

c) Sample S2994, deformed for one hour at 11 GPa, 1400°C. Extended stacking faults.

Top: viewed inclined.  $g:224$

Bottom: viewed edge-on. The stacking fault is parallel to  $(021)$ .  $g:021$

d) Sample S2984, deformed for eight hours at 11 GPa, 1400°C. Subgrain boundaries containing  $[001]$  dislocations.  $g:004$ .

### I.1.5 – InfraRed spectrometry characterisation

Although the role of « water » on forsterite deformation is not specifically addressed in this study, the hydroxyl contents of our samples and their evolution with time has been performed by infrared spectrometry (water refers to any water-related species detected as O-H stretching bands with an infrared spectrometer). Samples cold compressed (S3024) and heated for one minute (S2996), one hour (S29955 and S2993) and eight hours (S3078) have been investigated. The results of these infrared measurements are presented in Table III.3.

Three points of measurement have been done in a cross-section of every sample. The values in Table III.3 correspond to the mean hydroxyl content. It appears from these measurements that every samples originally contains some hydroxyls at the thousands  $H/10^6Si$  level. It also appears that this hydroxyl content is heterogeneous within the samples. Despite this heterogeneity, Table III.3 shows a weak trend suggesting that the hydroxyl content decreases with times spent at high temperature to reach a level of a few hundreds of  $H/10^6Si$  after eight hours. Figure III.11 illustrates this decrease of the hydroxyl content: the intensity of the absorption peaks decreases between the cold compressed sample (S3024) and the “eight hour” sample (S3079). For both samples, the thickness has been normalised to one centimetre.

**RESULTS**

Specimen	Hydroxyl content (H/10 <sup>6</sup> Si)
S3024 (cold compression)	1902 (884)
S2996 ( 1 minute)	1888 (276)
S2955 ( 1 hour)	2248 (468)
S2993 ( 1 hour)	853 (446)
S3078 ( 8 hours)	289 (34)

*Table III.3 – Hydroxyl content of specimens recovered after deformation, as measured using infrared spectrometry.*

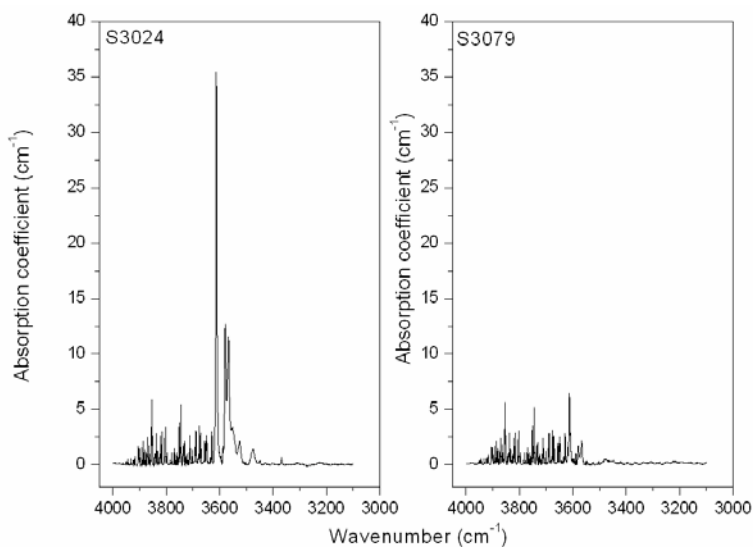


*Figure III.11 – Infrared spectra of a cold compressed forsterite sample (S3024) and after eight hours of heating (S3079).*

## I.2 – Deformation experiments using the D-DIA apparatus

Deformation of forsterite in the Kawai-type multianvil press at 11GPa and 1400°C has shown unexpected dislocation microstructures dominated by [001] dislocations. Usually (i.e. at ambient pressure), the occurrence of [001] dislocations is associated with low temperature or high strain-rate conditions (see Chapter I). This observation raises the question of the possible influence of pressure on plastic deformation mechanisms in forsterite which is discussed in Chapter III. To provide a further contribution to this important issue, additional deformation experiments have been carried out at intermediate pressures (i.e. between 11 GPa and ambient pressure). The newly developed deformation-DIA appears to be very well adapted to this study for several reasons. First of all, the D-DIA is a genuine deformation apparatus as differential stress loading is independent from pressurisation (see Chapter I). Its pressure range fits with the one needed for this study. Finally, it is expected that experiments coupled with synchrotron radiation will allow constraining the stress conditions borne by the samples. Experiments have been performed on several machines. Beyond the one in Bayreuth with which the original deformation assembly has been developed, two sets of experiments have been performed at APS and NSLS X-ray synchrotron sources.

### I.2.1 – Starting material

One of the most important parameter for experiments involving in situ X-ray diffraction is the grain size and the homogeneity of the grain size. The grain size has to be small for enough grains contributing to the

formation of the spectra in a volume of  $100 \times 100 \mu\text{m}^2$  (size of the diffracting volume). The grain size also has to be homogeneous for a better quality of X-ray diffraction spectra.

In order to perform several deformation experiments from a homogeneous starting material, a large amount of Fo2 powder was sintered using the Paterson press.

A first hot-pressing experiment (P0332) has been performed at 300MPa and 1100°C (during a few hours) at the Bayerisches Geoinstitut by Julian Mecklenburg. SEM characterisation of the sample shows that the grains size is large (10  $\mu\text{m}$ ) and heterogeneous (Figure III.12a). This material cannot be used for experiments involving in situ X-ray diffraction. However, it was used for off-line experiments (performed in Bayreuth) since the grain size is a less critical parameter in that case.

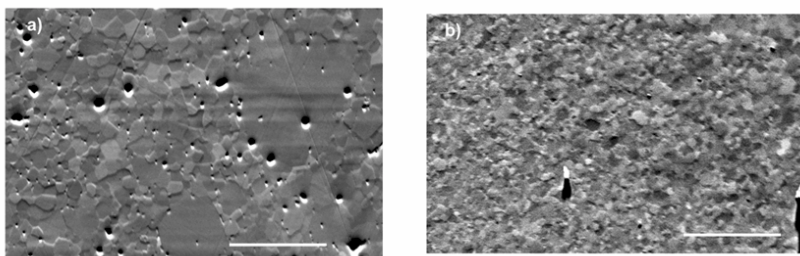


*Figure III.12 – Hot-pressed forsterite. SEM images in orientation contrast. Scale bars: 20  $\mu\text{m}$*

*a) P0332 first hot-pressing, from Fo2*

*b) P0333 second hot-pressing, from Fo2 power grounded thinner*

Fo2 powder was then grounded thinner and a second hot-pressing (P0333) has been performed at the University of Manchester (Department of Earth Sciences) by Julian Mecklenburg. The experimental conditions were

identical to P0332. The new hot-pressed sample (P0333) exhibits very small (around 4-5  $\mu\text{m}$ ) and homogeneous grains that are compatible with in situ X-ray diffraction measurements (Figure III.12b).

P0332 and P0333 samples have been cored and cut in cylinders 1.4 mm long and 1.4 mm in diameter for the 6/8 assembly and in cylinders 1 mm long and 1 mm in diameter of the 4/6 assembly, respectively.

Taking advantage on the experience gained on previous experiments, these cylinders have been dehydrated at 1000°C during several hours to perform experiments on hydroxyl-free samples. The hydroxyl content has been measured using Infrared spectrometry. Cylinders from P0332 exhibit, after dehydration, hydroxyl content of  $369 \pm 44 \text{ H}/10^6 \text{ Si}$  while the hydroxyl content of the cylinders from P0333 is under the detection limit of the spectrometer and could not be determined.

### I.2.2 - Annealing experiments under hydrostatic pressure in the D-DIA

These experiments have been performed in a 6/8 D-DIA assembly at the Bayerisches Geoinstitut from the hot-pressed samples P0332. The aim of these experiments is to check for possible grain growth in D-DIA experiments and for possible deformation microstructures that might have been introduced during cold compression. Two experiments performed at 2 GPa, 1300°C during two and four hours are presented in Table III.4.

## RESULTS

Run #	Sample #	Oil pressure	Nominal pressure (GPa)	Temperature (°C)	Heating time (min)
DD10	P0332	70 bar	2	1300	240
DD14	P0332	70 bar	2	1300	120

*Table III.4 - Experimental conditions for hydrostatic experiments on forsterite performed in the D-DIA at the Bayerisches Geoinstitut.*

The temperature for every D-DIA experiments is lower (1300°C) compared to the experiments performed in Kawai-type multianvil to prevent grain growth.

Microstructures of DD10 and DD14 samples have been characterized by optical microscopy and SEM respectively. The grain size of both samples has been determined from these images using ImageTool. After two hours of annealing, DD14 presents a mean grain size of about 64  $\mu\text{m}$  (38 $\mu\text{m}$  of standard deviation) and after four hours of heating, the mean grain size of DD10 reaches ca. 110  $\mu\text{m}$  (71 $\mu\text{m}$  of standard deviation).

TEM observations on DD10 sample show that more than 80% of observed grains are free of dislocations.

A compromise has been done between a strong annealing of the microstructures introduced during cold compression and a limited grain growth. The annealing time of two hours will be used for the following deformation experiments.

The hydroxyl content ( $347 \pm 15 \text{ H}/10^6 \text{ Si}$ ) measured after two hours of heating (DD14) shows no significant evolution from the one of the starting material.

### I.2.3 – Deformation experiments performed at the Bayerisches Geoinstitut

Three experiments have been performed in Bayreuth: two from P0332 at 2 GPa and 1300°C and one from P0333 at 6 GPa and 1300°C. The experimental conditions are summarized in Table III.5.

Run #	Sample #	Oil pressure (bar)	Nominal pressure (GPa)	Temperature (°C)	Total strain (%)	Mean strain rate ( $10^{-5}\text{s}^{-1}$ )
DD12	P0332	70	2	1300	24(0.5)	8(1)
DD13	P0332	70	2	1300	25(0.5)	4(1)
DD31	P0333	120	6	1300	25 (0.5)	5 (1)

*Table III.5- Experimental conditions for forsterite deformation in the D-DIA at the Bayerisches Geoinstitut.*

These experiments have been deformed after two hours of annealing under hydrostatic conditions.

The total strain and the strain rate of these experiments (Table III.5) were deduced from the transducer measurements. The two transducers measure the displacement between the guide block and the upper and lower independent anvils. Measuring the sample and the pistons before and after the experiment, we checked that the displacement recorded by the transducers is mostly due to sample shortening. The contribution of the pistons shortening is null and the extrusion of the gaskets is negligible. The three samples have been deformed at a strain rate of  $10^{-5}\text{s}^{-1}$  and to a total strain of ca. 25%.

The CPO of DD12 and DD31 has been measured by EBSD. They are presented in Figure III.13.

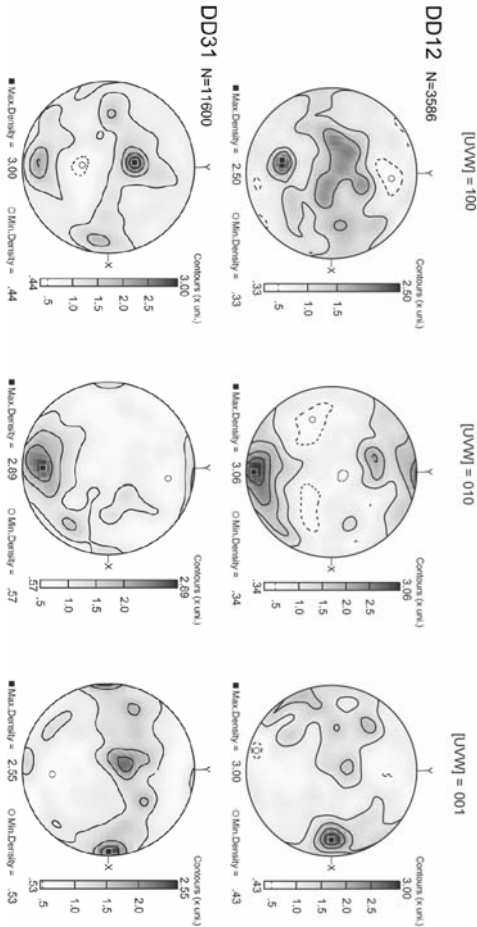


Figure III.13 – EBSD pole figure of forsterite samples: DD12, deformed to 24% at 2 GPa, 1300°C and  $8 \times 10^{-5} \text{s}^{-1}$  and of DD31 deformed 25% at 6 GPa, 1300°C and  $5 \times 10^{-5} \text{s}^{-1}$ . The compression axis is aligned with Y. Lower hemisphere equal-area projections, contours at intervals of 0.5 multiple of a uniform distribution.

The compression axis is aligned with Y. Both CPO are characterized by a concentration of the [010] axes close to the compression axis and a distribution of [100] axes and [001] axes forming a rough girdle normal to [010] axes. The [100] axes present also a maximum at low angle from the compression axis (at ca. 30°) within the YZ plane. The [100] and [001] girdles are not homogeneously distributed. These axes are more concentrated close to Z and close to X respectively.

Figure III.14 presents typical microstructures observed at the TEM in DD13. The sample presents dislocation density of  $10^{13}\text{m}^{-2}$ . [100] and [001] dislocations have been systematically observed in this sample as shown in Figure III.14, where the same grain is observed with two diffraction vectors 400 and 004. They are in glide configuration. The relative frequencies of these two slip systems could not be determined due to limited sampling. Few grain boundaries are also observed.

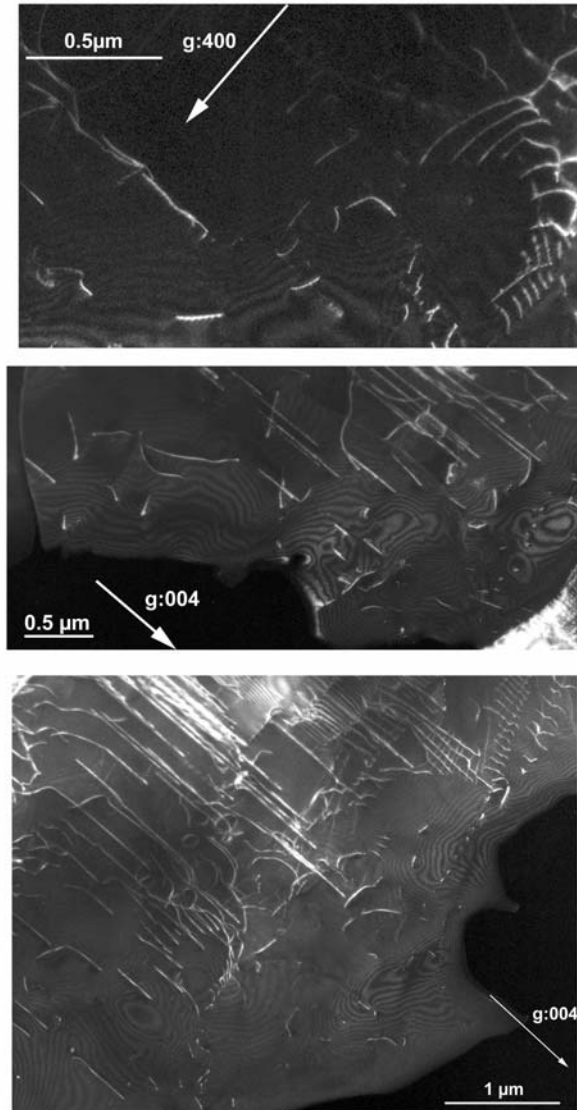


Figure III.14 - TEM micrographs of forsterite grains. DD13 deformed to 24% at 2GPa 1300°C and  $4 \times 10^{-5} \text{ s}^{-1}$ . Weak-beam dark-field micrographs.

### I.2.4 – Deformation experiments performed at APS

The deformation experiments performed at APS have been made using a D-DIA press coupled with a synchrotron beam line. These experiments were performed from P0333 starting material. The experimental conditions are summarised in Table III.6. Experiments have been performed with WC anvils.

Run #	Sample # (Hot- pressing)	Load (t)	Nominal pressure (GPa)	Temp- erature (°C)	Total strain (% )	Mean strain rate ( $10^{-5}\text{s}^{-1}$ )
D0504	P0333 + MgO+ BN	70	~3	1300	Fo:1.5( 0.5) MgO:13 (0.5)	Fo:2(1) MgO:9(1)
D0501	P0333	60	~2.7	1300	6(0.5)	1(1)

*Table III.6 – Experimental conditions for forsterite deformation in the D-DIA press at APS*

D0504 is used as a pressure calibration experiment for the D-DIA at APS. The capsule of D0504 is made of two layers: one (250  $\mu\text{m}$  thick) of hot-pressed forsterite (P0333) and the second one (750  $\mu\text{m}$  thick) of a mixture 3:2 of MgO and boron nitride powders (Figure III.15). These layers are separated by Pt foils that are used as strain markers. Boron nitride avoids MgO grain growth for a better quality of X-ray spectra. The cell is loaded at 70t and heated at 1300°C. It has been annealed one hour at 1300°C and slightly deformed.

D0501 has been loaded at 60t, heated at 1200°C and annealed two hours in a hydrostatic environment. Then the sample was heated at 1300°C and deformed.

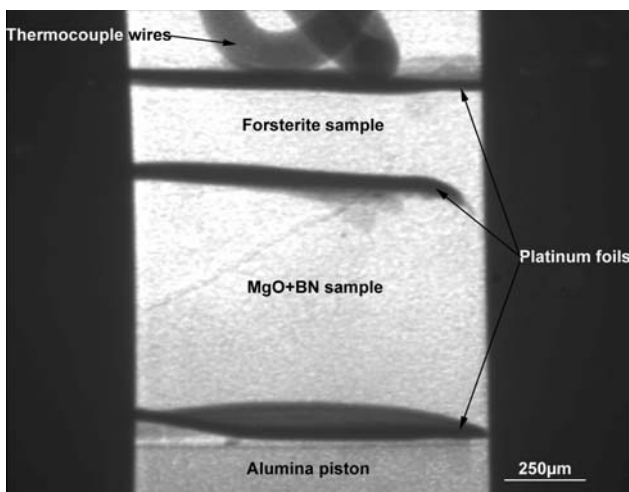


Figure III.15 – Open-press radiograph image of D0504 (pressure calibration experiment at APS). The two vertical black bands are the shallow of edges WC anvils.

The strain-rate and the strain of both experiments were directly measured from the radiograph images.

D0501 has been deformed to 6% at a strain-rate of  $10^{-5}\text{s}^{-1}$ . Figure III.16 shows two radiograph images of D0501 at 60t and 1300°C, one before deformation and one after 84 minutes of deformation at  $10^{-5}\text{s}^{-1}$ . We can observe between these two pictures a sample shortening of 46 μm. The window through which the sample is imaging is small. Indeed we are looking at the sample through the gaskets; the WC anvils absorb X-ray too strongly.

## RESULTS

This window is smaller than in open-press configuration (Figure III.15) because gaskets thickness decreases with the pressure.

In D0504, the forsterite sample has been deformed to 1.5% at  $2 \times 10^{-5} \text{ s}^{-1}$  while MgO has been deformed to 13% at  $9 \times 10^{-5} \text{ s}^{-1}$ .

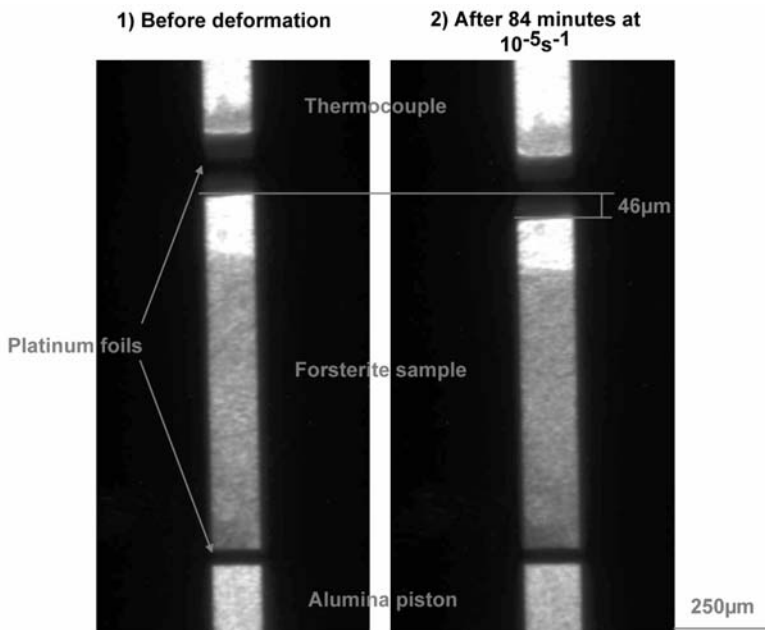


Figure III.16 -Radiograph images of D0501 at 60t and 1300°C 1) before deformation and 2) after deformation.

The pressure in D0504 has been deduced from lattice strain measurements in MgO. In APS, only one vertical detector was used to record X-ray diffraction on horizontal crystallographic planes for which lattice strains are deduced. The horizontal crystallographic planes d-spacing not only depend on pressure, they are also sensitive to vertical differential stresses (see Figure II.16 Chapter II). Since the differential stress is

generally large during cold compression, the pressure measurement is then over-estimated. However the calculated pressure might be closer to the actual hydrostatic pressure value after heating, due to the stress relaxation (Chen *et al.*, 2004). The pressure deduced from the horizontal lattice strains must then be used with care.

Lattice strains measurements for pressure calculation have been done by using the most narrow diffraction peaks. {021}, {101}, {120}, {002}, {130}, {131}, and {112} were chosen for forsterite and {111}, {200} and {220} were selected for MgO.

The evolution of pressure during D0504 is presented Figure III.17. The apparent pressure has been calculated from MgO (black dots) as well as from forsterite (gray dots). The heating path is also represented. The calculated pressure at 70t and room temperature measured in the MgO powder and in the forsterite solid sample is about 5.5 GPa and 4.5 GPa respectively. The pressure measured from the MgO powder starts to decrease dramatically after 500°C to attain 3 GPa at 1300°C. This level is maintained during the rest of the experiment even during the deformation stage.

The pressure measured from forsterite increases during heating to reach, at 500°C, a level 5.7 GPa which decreases slightly at 4.5 GPa and 900°C, and which is maintained until the end of the experiment. The error bars on these pressure values are more important due to the bad quality of the X-ray diffraction spectra observed from the forsterite sample.

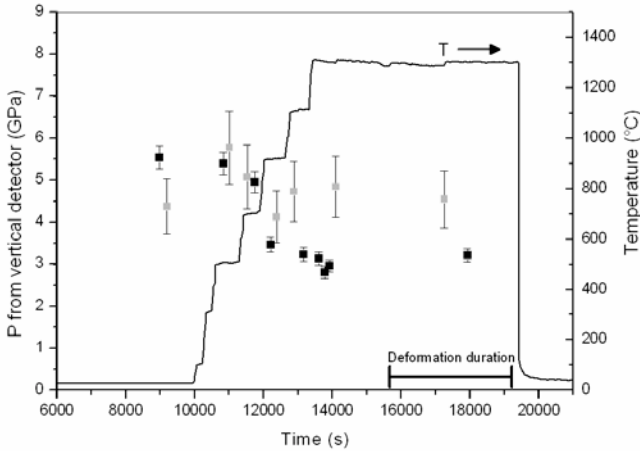


Figure III.17 – Apparent pressure calculated on D0504 from X-ray diffraction in forsterite sample (gray dots) and in MgO + BN mixture (black dots).

We can assume that the best estimate of the hydrostatic pressure is given from the lattice strain of the MgO+BN mixture at 1300°C. At 70t and 1300°C, the pressure of the D-DIA press at APS is ca. 3 GPa. From this pressure calibration, D0501 is estimated to be deformed at about 2.7 GPa. The differential stress cannot be measured at APS due to the lack of a second horizontal detector.

The observation of the dislocation microstructure in D0501 has been performed by TEM. Most grains are free of dislocations. However, some grains contain a low dislocation density ( $10^{12} \text{ m}^{-2}$ ) with [100] and [001] dislocations in glide configuration (Figure III.18).

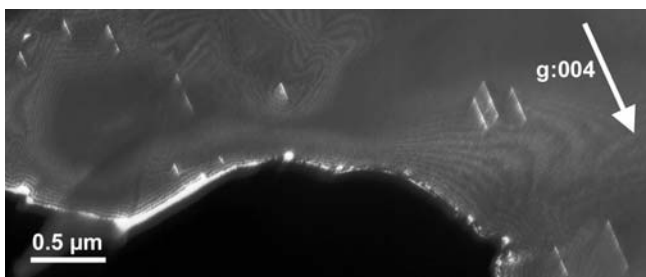


Figure III.18 - TEM micrographs of forsterite. D0501 deformed to 6 % at 2.7 GPa 1300°C and  $1 \times 10^{-5} \text{ s}^{-1}$ . Weak-beam dark-field micrographs showing [001] dislocations.

### I.2.5 – Deformation experiments performed at NSLS

One deformation experiment has been performed at NSLS in a D-DIA press coupled with a synchrotron source. The experiment was performed from starting material P0333. The experimental conditions are summarised in Table III.7. This experiment has been performed with cBN anvils.

Run #	Sample # (Hot- pressing)	Load (t)	Nominal pressure (GPa)	Temp- erature (°C)	Total strain (%)	Mean strain rate ( $10^{-5} \text{ s}^{-1}$ )
FOR21	P0333	50	~4	1300	10 (0.5)	2.5 (1)

Table III.7- Experimental conditions for forsterite deformation in the D-DIA press coupled with a synchrotron at NSLS.

FOR21 has been loaded at 50t, heated at 1000°C and annealed at least two hours before deformation at 1300°C. The temperature path of this experiment has been strongly dependent on the availability of the beam. The

## RESULTS

temperature has been decreased twice, at 600°C and at 1000°C to avoid grain growth during beam cuts (Figure III.20).

The strain-rate and the strain of this experiment were directly measured from the radiograph images. FOR21 has been deformed to 10% at a strain-rate of  $2.5 \times 10^{-5} \text{ s}^{-1}$ . Figure III.19 presents two radiograph images of FOR21 at 50t and 1300°C. The left one has been taken before deformation and the right one has been taken after 71 minutes of deformation at  $2.5 \times 10^{-5} \text{ s}^{-1}$ . The shortening sample is 73  $\mu\text{m}$ . The shadows that cover left and right part of the sample are due to the cBN anvils. They have low X-ray absorption and they allow larger view of the sample compared to WC anvils (see Figure III.16)

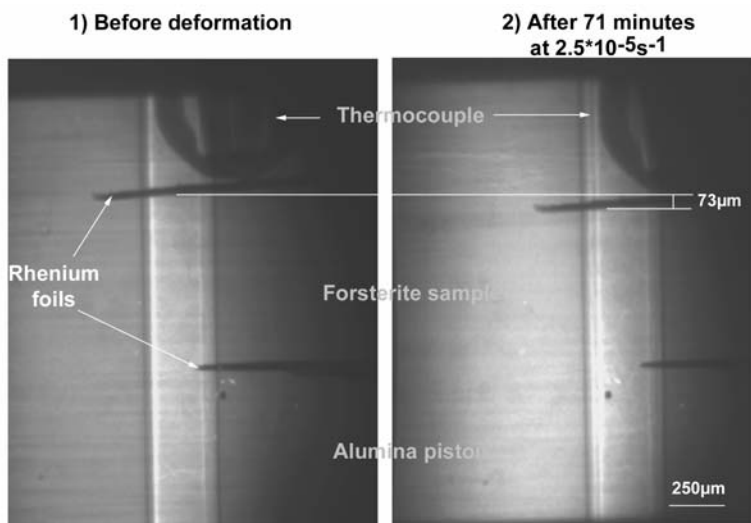


Figure III.19 – Radiograph images of FOR21 at 50t and 1300°C 1) before deformation and 2) after deformation. The gap between top and bottom Re foils is made during the assembly of the cell.

Pressure as well as differential stresses was deduced from lattice strains measurements (Singh *et al.*, 1998; Chen *et al.*, 2004, see chapter II § II.3) from the forsterite sample (Figure III.20). The narrow diffraction peaks {021}, {101}, {120}, {002}, {130}, {131}, and {112} from forsterite were used for these calculations.

The vertical detector and the horizontal detector record the X-ray beams diffracting on the horizontal crystallographic planes and the vertical crystallographic planes, respectively.

On Figure III.20, the hydrostatic pressure from both detectors is represented with black squares. The differential stress is represented with open diamond and the temperature path with the gray dotted line.

At 50t and room temperature, the differential stress is about 1.5-2 GPa. The hydrostatic pressure is then close to 4.5 GPa. As soon as the sample is heated at 1000°C, the differential stress decreases drastically below 0.5 GPa. The differential stress stays below 0.5 GPa during deformation at 1300°C and a strain rate of  $2.5 \times 10^{-5} \text{s}^{-1}$ . The hydrostatic pressure decreases to 4 GPa and stays constant during deformation.

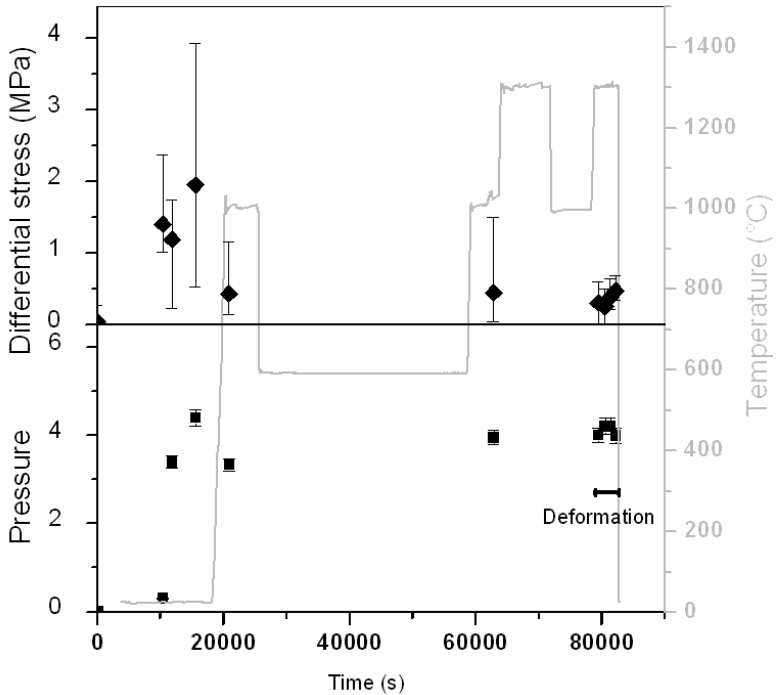


Figure III.20 – Pressures and differential stress calculated from lattice strains on the forsterite sample. Hydrostatic pressure : black squares. Differential stress: open diamond. In dot gray line, the temperature path. The plotted values of stress are an average of the calculated values from the different diffraction peaks. Error bars represent the range of the values from these peaks.

The results of EBSD characterisation of FOR21 are presented in Figure III.21. The compression axis is aligned with Y. The [010] axes are concentrated close to the compression axis and [100] and [001] are distributed in a girdle normal to [010]. [010] are less clustered than the previous CPO (DD12 and DD31).

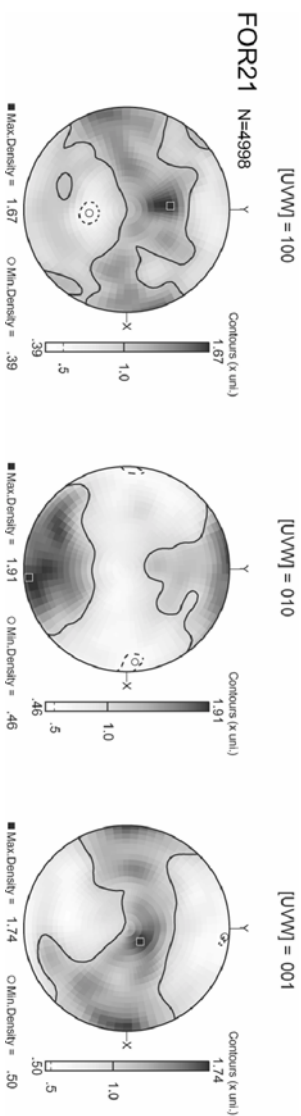


Figure III.21 – EBSD pole figure of crystal axis for forsterite sample (FOR21) deformed 10% at 4 GPa, 1300°C and  $2.5 \times 10^{-5} s^{-1}$ . The compression axis is aligned with Y. Lower hemisphere equal-area projections, contours at intervals of 0.5 multiple of a uniform distribution.

## II – Deformation of wadsleyite

Wadsleyite with  $Mg_2SiO_4$  forsterite composition has been deformed at high pressure and temperature in shear and characterised in order to follow the behaviour of the sample during the experiment as well as to obtain CPO of this phase produced at high pressure and high temperature.

Wadsleyite was synthesised from Fo1 in a 14/8 assembly at 16 GPa and 1500°C for 3 hours. Thin (200 $\mu$ m) samples slices are cut at 45° from this hot-pressed cylinder. A second vertical cut is made to divide the specimen into two parts and the two exposed surfaces are vacuum coated with platinum to provide the strain marker. The slices are then placed into the shear deformation 14/8 assembly. The deformation experiments are summarised in Table III.8.

## RESULTS

Run #	Sample # (from Fo1)	Oil pres- sure (bar)	Nominal pres- sure (GPa)	Temp- erature (°C)	Duration (min)	Strain marker rotation (deg.)	Piston display- cement (µm)
H1951 <sup>(1)</sup>	H1949	264	16	-	-	-	326(15)
H1978 <sup>(1)</sup>	H1967	264	16	-	-	-	222(50)
H1953	H1949	264	16	1400	1	15(2)	353(32)
H1954	H1949	264	16	1400	1	0	289(32)
H1979	H1967	264	16	1400	1	-	381(86)
H1981	H1967	264	16	1400	1	15(4)	221(14)
H1882	S3137	264	16	1400	60	23 (3)	-
H1945	H1941	264	16	1400	60	7 (2)	397(33)
H1864 <sup>(2)</sup>	S3116	264	16	1400	480	13(2)	515(45)
S3213	H1939	300	16	1400	480	25	354(32)

*Table III.8 - Experimental conditions for wadsleyite deformation in the multianvil apparatus (S:sumitomo press, H: Hymag press). <sup>1)</sup>cold compressed samples, <sup>2)</sup>temperature uncertain.*

Deformation experiments have been performed at 16 GPa and 1400°C during one minute, one hour and eight hours. Some experiments have been cold compressed only. Several experiments were performed for each duration time to test the reproducibility of the experiment.

### II.1 - Phase identification

The nature of the phases was checked after the experiment on recovered samples using micro-Raman spectroscopy.

Cold compressed samples and samples annealed one hour and eight hours confirm the occurrence of wadsleyite (Figure III.22). The Raman spectra of wadsleyite (H1945) is characterised by two main peaks at 722 and 918  $\text{cm}^{-1}$  (Liu *et al.*, 1994). However, it has been found that heating and holding at 1400°C for one minute, induces back transformation of pre-synthesized wadsleyite to forsterite (Figure III.22). The Raman spectra of forsterite (H1981) is characterised by two main peaks at 826 and 856  $\text{cm}^{-1}$  (Gillet *et al.*, 1997). This transformation is systematically observed in “one minute” samples. No evidence for retained wadsleyite has been detected in those samples by Raman spectroscopy.

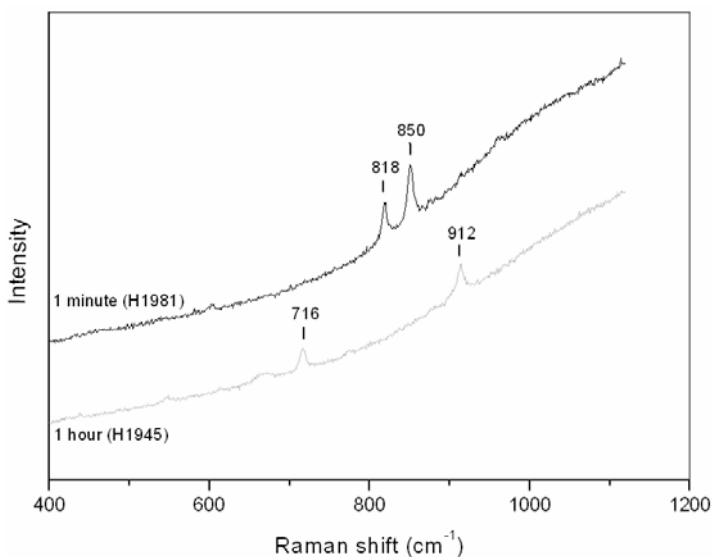
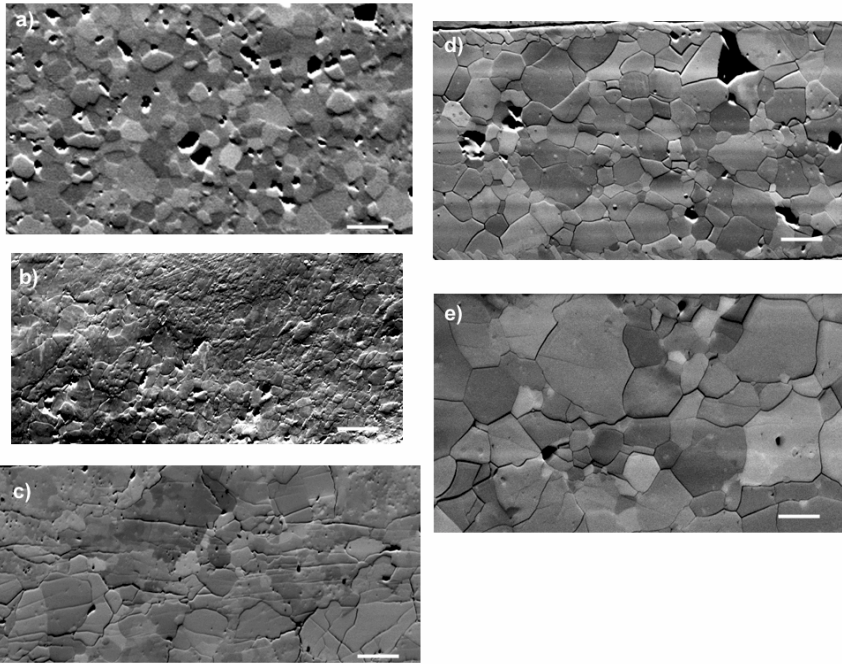


Figure III.22 – Raman spectra of wadsleyite (H1945, in grey) and forsterite (H1981, in black).

## II.2 – SEM and EBSD characterisation

The microstructures of deformed samples have been imaged using SEM. Figure III.23 presents typical microstructures of the recovered samples. The starting material (as synthesised: Figure III.23a) exhibits an isotropic fabric with a heterogeneous grain size. Cold compression introduces so much damage in the overall microstructure that several orientation contrast are observed in some grains and that grain boundaries are not always easily visible (Figure III.23b). Figure III.23c shows a typical microstructure of a “one minute” sample, after back-transformation in forsterite. The transformation erases the damages observed after cold compression in wadsleyite. The grain size is heterogeneous and some grains are quite large. The horizontal cracks probably result from decompression. After one and eight hours of heating (Figure III.23d-e), wadsleyite microstructures exhibit very heterogeneous grain sizes with evidence of grain boundary migration (boundaries exhibiting convex shapes).



*Figure III.23 -SEM pictures of wadsleyite (orientation contrast). Cross section, shear direction horizontal and shear sense dextral. The scale bar is equal to  $20\mu\text{m}$*

- a) After synthesis (S3137, wadsleyite)*
- b) After cold compression at 16 GPa (H1978, wadsleyite)*
- c) After one minute at 16 GPa and  $1400^{\circ}\text{C}$  (H1953, forsterite)*
- d) After one hour at 16 GPa and  $1400^{\circ}\text{C}$  (H1945, wadsleyite)*
- e) After eight hours at 16 GPa and  $1400^{\circ}\text{C}$  (S3213, wadsleyite)*

The grain size has been measured from these pictures using ImageTool software. Figure III.24 and Figure III.25 present respectively the grain size distributions and the grain size evolution. Due to the series of transformation wadsleyite  $\rightarrow$  forsterite  $\rightarrow$  wadsleyite, the grain size

## RESULTS

evolution is complex. The starting material and the cold compressed samples display the same grain size distribution. After back-transformation into forsterite, the grain size increases. Further transformation to wadsleyite decreases the grain size. From one to eight hours of heating, the mean grain size grows from 15  $\mu\text{m}$  to 25  $\mu\text{m}$ .

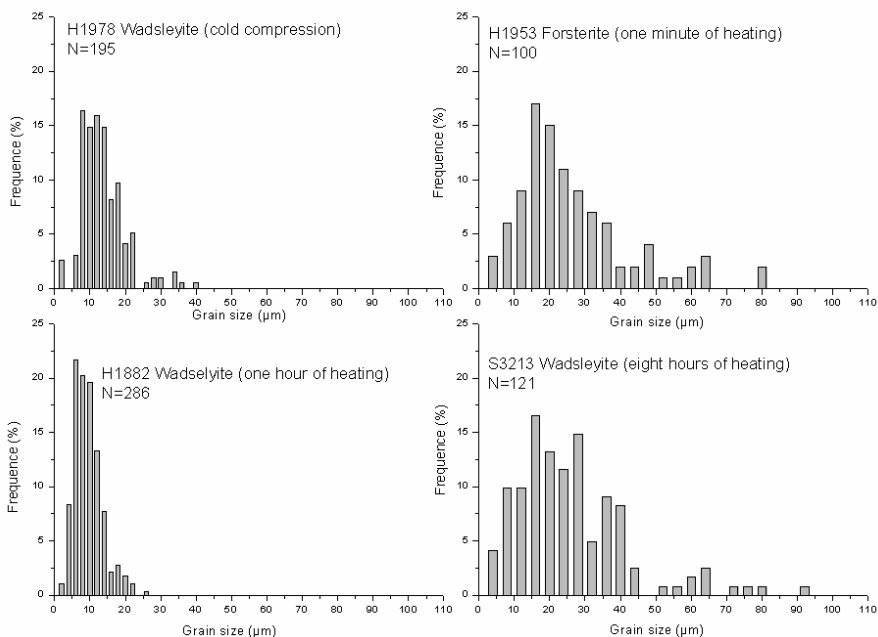


Figure III.24 – Wadsleyite: grain size distribution for the sample H1978 (cold compression), H1953 (one minute), H1882 (one hour) and S3213 (eight hours)

## RESULTS

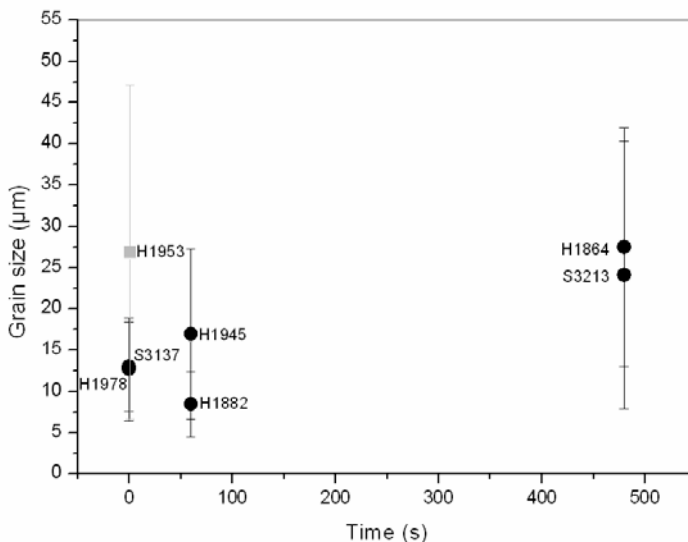


Figure III.25 – Evolution of the grain size with time. Bars represent data scattering ( $2\sigma$  standard deviation). Black dots: wadsleyite. Gray square: forsterite.

Strain marker rotations and the relative displacement of the pistons have been measured from SEM pictures (Table III.8). The measurements of strain marker rotation are not possible on H1951 and H1978 because the strain marker is not visible (maybe not enough platinum has been coated). As the strain marker of H1979 presents a curved shape, no rotation can be measured. The strain marker rotation of the other experiments vary between 0 and 15° after one minute of heating (back-transformed samples) and between 7 and 25° after one and eight hours of heating. It seems that the mean strain marker rotation is slightly larger for longer heating time. Moreover, the mean piston displacement seems also to be slightly larger for samples heated one or eight hours (between 354 µm and 515 µm) than for

samples only pressurised or heated one minute (between 221  $\mu\text{m}$  and 381  $\mu\text{m}$ ). However, we do not know the influence of successive transformations wadsleyite  $\rightarrow$  forsterite  $\rightarrow$  wadsleyite on strain marker rotation and piston displacement.

Wadsleyite CPO have been measured using EBSD. As explained in Chapter II (§III.1.3), the manual mode had to be used to avoid mis-indexing due to the pseudosymmetry. Figure III.26 shows an example of this pseudosymmetry on a wadsleyite grain (from H1945). Figure III.26 presents an experimental EBSP and two simulated EBSP proposed by Channel 5. The zone axis on top of the picture is indexed as  $\langle 011 \rangle$  in both simulations. The difference between those two solutions is the  $120^\circ$  rotation of the simulated EBSP around this zone axis. Only solution 1 is valid. In solution 2, one band is missing (dashed line) and some bands predicted by the simulation are not found experimentally. This mis-indexing effect can be minimized by different ways (bringing the detector closer, increasing the minimum number of band used for indexing...). It depends also very much on the sample quality.

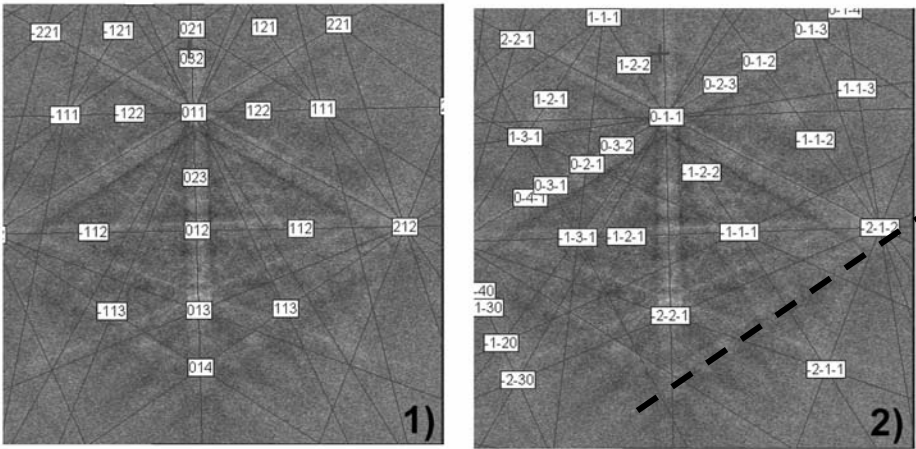


Figure III.26 – Wadsleyite: example of an experimental EBSD pattern (background) and two indexing possibilities proposed by Channel 5.

Figure III.27 and Figure III.28 present the results of EBSD characterisations on wadsleyite samples. For the synthesised sample, Y corresponds to the axis of the furnace in the high-pressure cell. For the other samples (deformed in shear) X represents the shear direction and Y the normal to the shear plane. The shear sense is dextral. Due to the important lattice distortions in the grains of cold compressed samples, the Kikuchi patterns can not be properly indexed. Then, no analyse has been performed on those samples.

The CPO appears to be random in the synthesized samples (Figure III.27).

After one hour (Figure III.27), the textures of H1882 and H1945 are characterized by a  $[100]$  girdle along the shear direction while the  $[010]$  axes cluster normal to the shear direction within the shear plane.  $[001]$  is roughly aligned toward the normal of the shear plane with a maximum at ca.

## RESULTS

---

30° of the shear direction within the YZ plane for H1945 and with in a plane at 45° to the YZ plane for H1882.

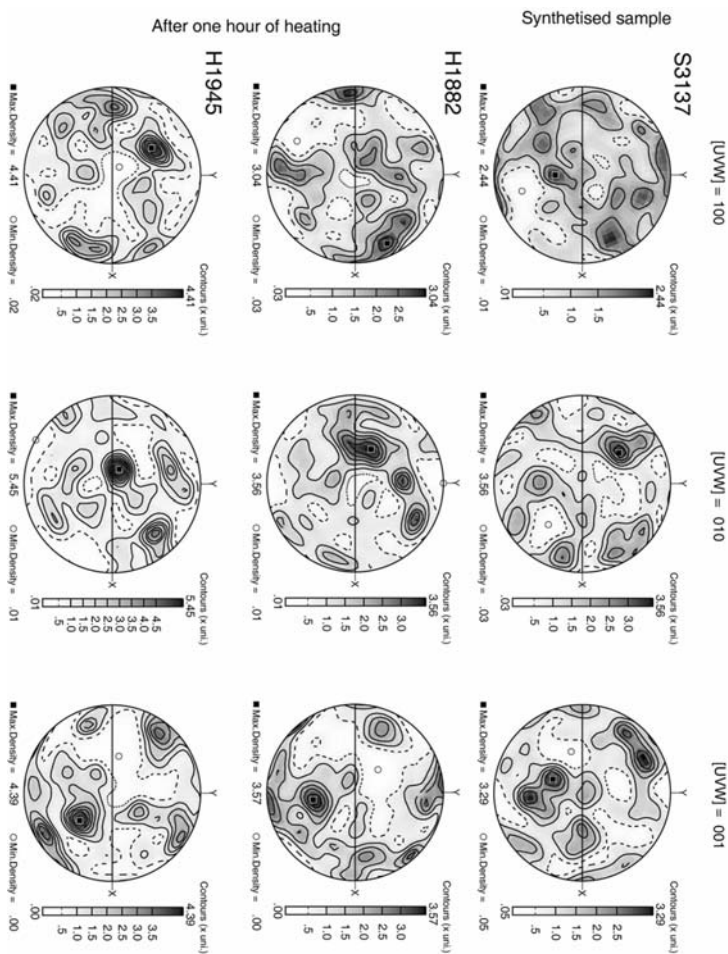


Figure III.27 - EBSD pole figures of crystal axis for wadsleyite samples: synthesised sample (S3137) and after one hour (H1882 and H1945). For S3137, Y is in furnace axis. For the other samples (deformed in shear), the shear direction of the samples is aligned with X and Y is perpendicular to the shear plane; the shear sense is dextral. Lower hemisphere equal-area projections, contours at intervals of 0.5 multiple of a uniform distribution.

After eight hours of heating (Figure III.28), H1864 and S3213 present a [100] girdle at low angle (ca.  $10^\circ$ ) from the shear direction. [010] is still clustered in the shear plane normal to the shear direction. The [001] axes are concentrated toward the normal of the shear direction and also at low angle ( $10^\circ$ ) from the shear direction for H1864. Clustering of [001] is more marked for S3213.

The CPO do not seem to weaken after eight hours of heating as observed with forsterite.

The maximal densities are still weak however, between 3.04 and 5.45 multiple of a uniform distribution.

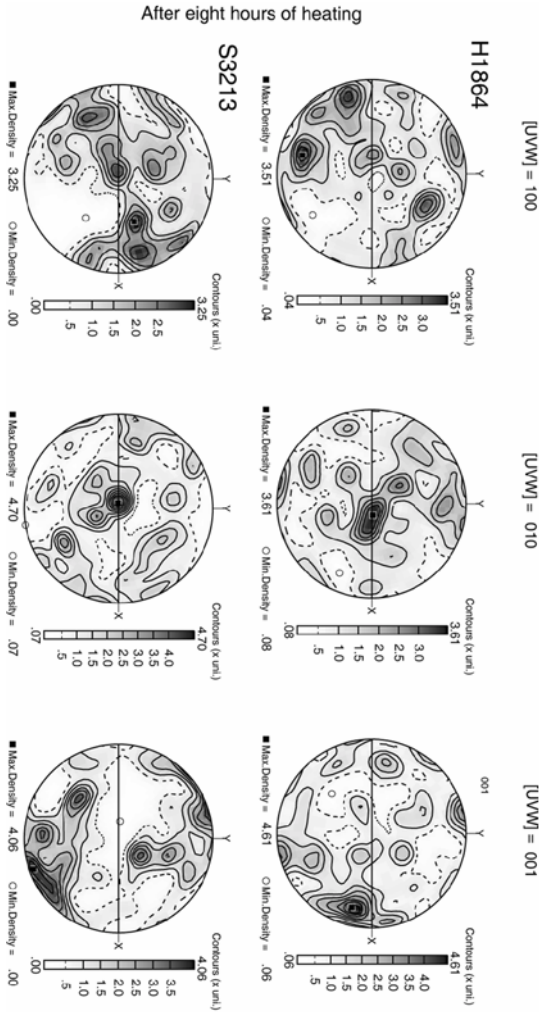


Figure III.28 - EBSD pole figures of crystal axis for wadsleyite samples: eight hours (H1864 and S3213) of heating. The shear direction of the samples is aligned with X and Y is perpendicular to the shear plane; the shear sense is dextral. Lower hemisphere equal-area projections, contours at intervals of 0.5 multiple of a uniform distribution.

Figure III.29 shows the CPO obtained on the two back-transformed samples (“one minute”). These measurements have been done in automatic mode as the samples are made of olivine grains. Y is parallel to the normal of the shear plane and X is aligned with the shear plane. H1953 exhibits alignment of [100] normal to the shear direction within the shear plane, while [010] is aligned toward the normal to the shear plane and [001] is parallel to the shear direction. These three axes are significantly clustered. For H1954, [100] is normal to the shear direction, [010] is aligned with the shear direction and [001] presents a girdle normal to [100].

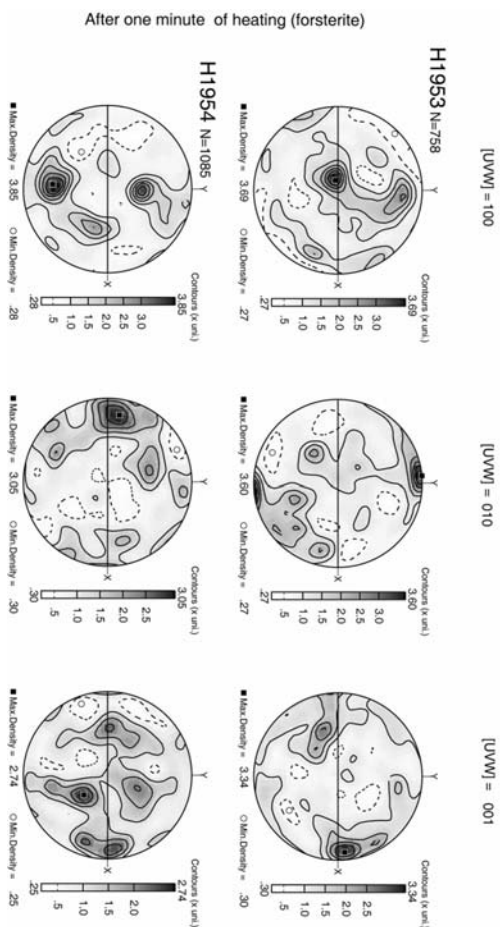


Figure III.29 - EBSD pole figures of crystal axis for the samples back-transformed in forsterite (H1953 and H1954). The shear direction of the samples is aligned with X and Y is perpendicular to the shear plane; the shear sense is dextral. Lower hemisphere equal-area projections, contours at intervals of 0.5 multiple of a uniform distribution.

### II.3 – TEM investigation

Figure III.30 presents the microstructures observed at the TEM. After cold compression, the microstructures display very high dislocation densities (Figure II.30a). No dislocation characterisation is possible with such high densities. After one minute of heating, Raman spectroscopy and EBSD have shown that the sample is back-transformed in forsterite. However, TEM reveals the presence of inclusions of wadsleyite within the grains as well as in the grain boundaries that represent newly nucleated grains. These inclusions do not exhibit dislocations as well as no particular relationships with the forsterite dislocations.

After one hour of heating, wadsleyite grains display many dislocations in glide configuration (Figure III.30c). Most of the dislocations characterized are of the [100] type (these dislocations are out of contrast with  $g:010$ ). However limited sampling precludes any quantitative evaluation of the activity of the various slip systems activated in those samples. Very comparable microstructures are observed in the samples heated for eight hours. The dislocation density is about to  $10^{13} \text{ m}^{-2}$  after one hour of heating. After eight hours of heating, numerous grains are pristine and the dislocation density of the grains that contain dislocations is also about  $10^{13} \text{ m}^{-2}$ . Only rare stacking faults and no subgrain boundaries have been observed in those samples.

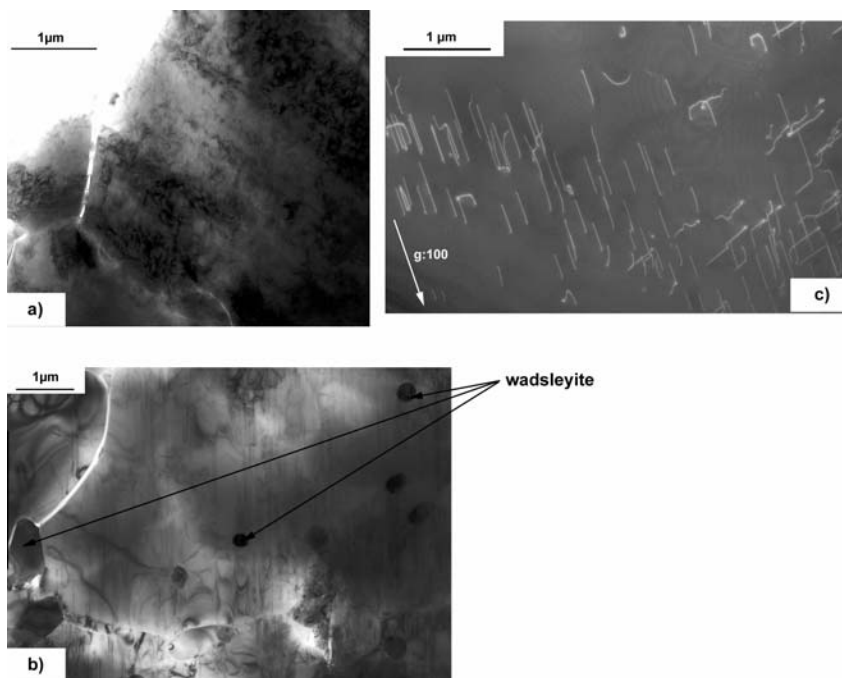


Figure III.30 – TEM micrographs of deformed wadsleyite  
a) Sample H1951, cold compressed at 16 GPa and not heated  
b) Sample H1954, deformed for one minute at 16 GPa, 1400°C. Matrix of forsterite with inclusions of wadsleyite  
c) Sample H1882, deformed for one hour at 16 GPa, 1400°C. [100] screw dislocations. Weak-beam dark-field

#### II.4 – InfraRed spectrometry characterisation

The hydroxyl content of the samples has been measured using Infrared spectrometry. This characterisation has been performed on samples after cold compression (H1978), one hour of heating (H1882) and eight hours of heating (H1864). The results of the infrared measurements are presented in Table III.9. These measurements shows that the hydroxyl content in

wadsleyite decreases when the sample is hold for several hours at high – temperature and pressure.

Specimen	Hydroxyl content (H/10 <sup>6</sup> Si)
H1978 (cold compression)	3192 (303)
H1882 ( 1 hour)	3380 (339)
H1864 ( 8 hours)	746 (135)

*Table III.9 - Hydroxyl content on wadsleyite samples recovered after deformation, as measured using infrared spectrometry.*

### III – Deformation of ringwoodite

The deformation experiments of Mg<sub>2</sub>SiO<sub>4</sub> ringwoodite have been performed in a Kawai-type multianvil apparatus (5000t Zwick press). Ringwoodite was synthesised from Fo1 in a 18/8 assembly at 21 GPa and 1200°C for 3 hours. Thin (200µm) samples slices were cut at 45° from this cylinder. Due to the difficulty to cut the slices in ringwoodite which is very brittle, no strain marker has been made for these experiments. The slices are placed in a shear deformation 18/8 assembly. The deformation conditions are summarised in Table III.10.

## RESULTS

Run #	Sample # Synthesis	Oil pressure (bar)	Nominal pressure (GPa)	Temp- erature (°C)	Duration (min)
Z367	Z366	295	22	1300	1
Z341	Z328	295	22	1300	180

Table III.10 – Experimental conditions for ringwoodite deformation in the multianvil apparatus. (Z: zwick press)

Deformation experiments have been performed at 22 GPa and 1300°C during one minute and three hours.

### III.1 – Phase identification

The phase identification has been made after synthesis and deformation on recovered samples using the micro-Raman spectroscopy. Figure III.31 presents Raman spectra of Z341 (black) and Z367 (grey). They display mainly two peaks around  $790\text{ cm}^{-1}$  and  $825\text{ cm}^{-1}$  which are characteristic of the ringwoodite phase (Liu *et al.*, 1994).

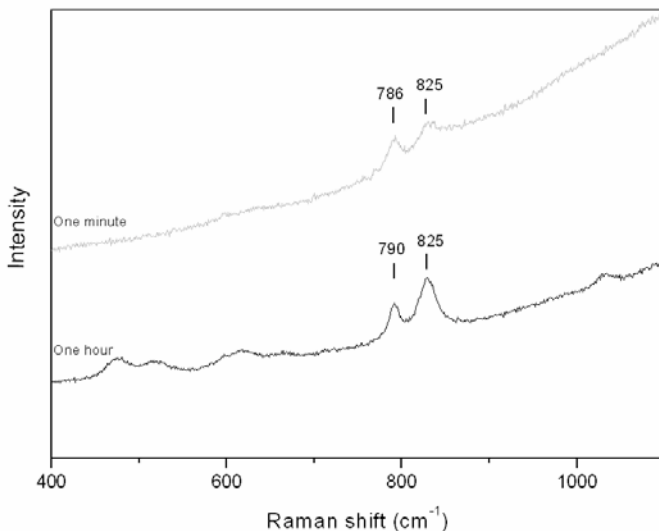


Figure III.31 – Raman spectra of ringwoodite samples Z367 (in grey) and Z341 (in black).

### III.2 – SEM and EBSD characterisation

Figure III.32 shows the microstructures observed on these two samples. The microstructures exhibit non-equilibrated grains with very heterogeneous grains sizes. The convex grain boundaries suggest grain growth even after one minute of heating. The grain size changes from 31  $\mu\text{m}$  (19  $\mu\text{m}$  of standard deviation) for Z367 to 55  $\mu\text{m}$  (25  $\mu\text{m}$  of standard deviation) for Z341 (grain sizes measured using ImageTool software).

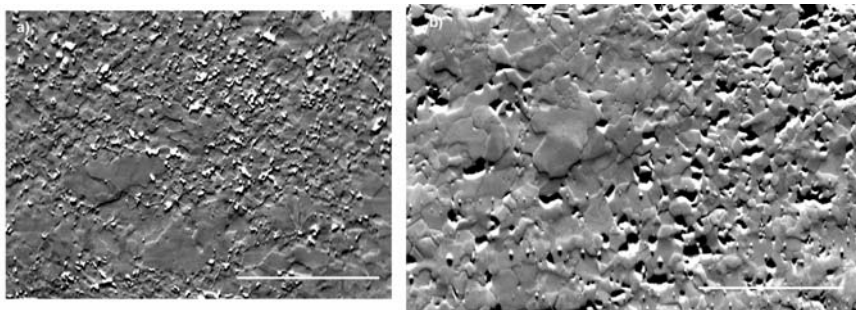


Figure III.32 - SEM pictures of ringwoodite samples (orientation contrast). Cross section, shear direction horizontal and shear sense dextral. The scale bar is equal to 20  $\mu\text{m}$

a) After one minute at 22 GPa and 12300°C (Z367) - b) After three hours at 22GPa and 1300°C (Z341)

The results of EBSD characterisation are presented in Figure III.33. X is aligned with the shear direction and Y is parallel to the normal of the shear plane. The shear sense is dextral.

As ringwoodite is very brittle, no as-synthesised sample could be kept for EBSD characterisation. After one minute of heating, the sample presents already a CPO. The  $\langle 100 \rangle$  axes exhibit a complex pattern with mainly two maxima: one at high angle of the shear direction and one close to the shear plane normal to the shear direction. Some secondary maxima can be observed roughly aligned with the shear direction and with the normal to the shear plane.  $\langle 111 \rangle$  is organized in two girdles at high angle to the shear direction. It also shows a weaker concentration in the shear plane.  $\langle 110 \rangle$  displays a rough six-fold symmetry pattern; one maximum is normal to the shear plane and the two others are at ca.  $45^\circ$  from the shear direction in the XZ plane. The CPO observed after three hours of heating is roughly similar with better clustering of the axes. The  $\langle 100 \rangle$  axes display a maximum in the

## RESULTS

---

shear direction and two maxima normal to the shear direction at ca.  $45^\circ$  from the shear plane. The  $\langle 111 \rangle$  axes present a girdle along the shear plane and two maxima at low angles at ca.  $30^\circ$  (clockwise and anticlockwise) from the normal to the shear plane. The  $\langle 110 \rangle$  axes display roughly a six-fold symmetry pattern; one maximum is the normal to the shear direction and the two other are at ca.  $45^\circ$  from the shear direction.

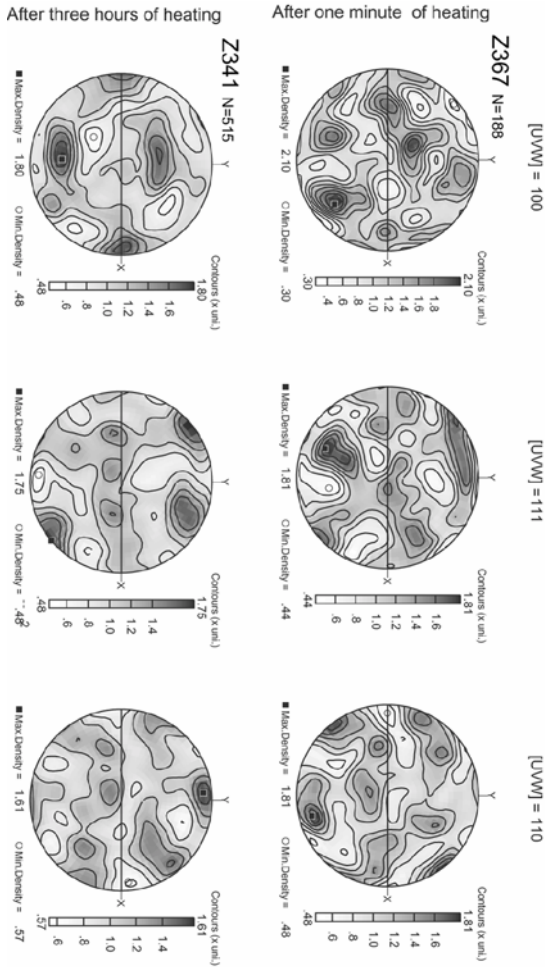


Figure III.33 – EBSD pole figures of crystal axis for ringwoodite samples after one minute of heating at 22GPa and 1250°C (Z367) and after three hours of heating at 22GPa and 1300°C (Z341). The shear direction of the samples is aligned with X and Y is perpendicular to the shear plane; the shear sense is dextral. Lower hemisphere equal-area projections, contours at intervals of 0.5 multiple of a uniform distribution.

### III.3 – TEM characterisation

Figure III.34a shows typical microstructures observed on ringwoodite samples after three hours of heating at 1300°C. The grains display such large density of dislocations that characterization of the slip systems is uneasy. Figure IV.34b and c present an example of grains where the dislocation density is lower. The occurrence of numerous junctions as well as observation under different diffraction conditions suggest that several slip systems have been activated. The curved form of dislocations does not point to very large the lattice friction. No dissociated dislocation has been observed.

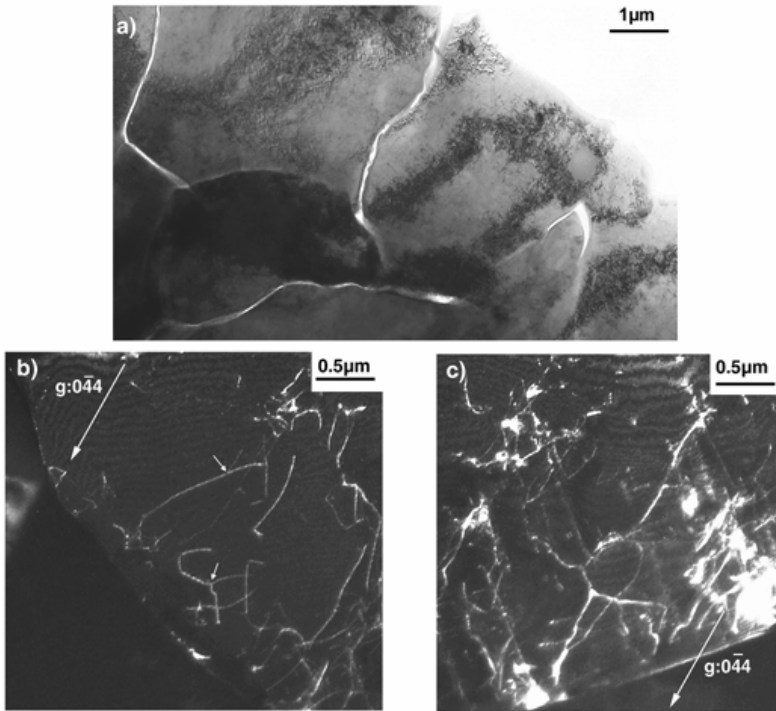


Figure III.34 - TEM micrographs of ringwoodite samples. Sample Z341 deformed 3 hours at 22GPa and 1300°C.

a) Typical microstructure. Bright field

b) and c) Examples of dislocation microstructures. Weak-beam dark-field. Small arrows on b) indicate the junctions

## IV – Influence of a phase transformation on plastic deformation: the case of the forsterite – wadsleyite transformation.

The mantle transition zone is associated with phase transitions, especially among the high-pressure polymorphs of olivine. The present study is mostly concerned with plastic deformation mechanisms and CPO within these polymorphs. It can not be excluded however that plastic deformation can be induced, or enhanced by the phase transitions. Surprisingly, this potentially important issue has received little attention until now. In this chapter, we investigate the behaviour of forsterite samples transformed to wadsleyite at high-pressure, high-temperature under shear stresses.

Experiments have been performed in the Kawai-type multianvil apparatus. Forsterite powders have been first hot-pressed from Fo1 in a standard 14/8 assembly at 11 GPa and 1400°C for 4 hours. Thin (200µm) samples slices were cut at 45° from this hot-pressed cylinder. A second vertical cut were made to divide the specimens into two parts and the two exposed surfaces were vacuum coated with platinum to provide the strain marker. The slices were then placed into the 18/11 shear deformation assembly.

In order to transform forsterite into wadsleyite under shear, the forsterite samples have been loaded into the wadsleyite pressure stability field and then heated. The experiments have been quenched after thirty minutes, forty five minutes and one hour of heating. The conditions of these experiments are presented in Table III.11.

**RESULTS**

Run #	Sample # Hot-pressed	Oil $P_{\max}$ bar	Nominal P (GPa)	T (°C)	Dura- tion (min)	Reco- vered phase	Piston display- cement ( $\mu\text{m}$ )	Sample thick- ness ( $\mu\text{m}$ )
S3253	S3244	500	16.5	1400	30	$\alpha$	323(6)	194(2)
S3412	S3411	500	16.5	1400	45	$\beta$	344(8)	167(13)
S3254	S3244	500	16.5	1400	60	$\beta$	416(7)	122(6)

*Table III.11 -Experimental conditions for forsterite-wadsleyite transformation under shear conditions in the multianvil apparatus (S: Sumitomo press).*

The phases present in the recovered samples have been identified using micro-Raman spectrometry. After thirty minutes of heating, the sample is still made of forsterite. After forty five minutes and one hour of heating, the sample is transformed in wadsleyite (Figure III.35)

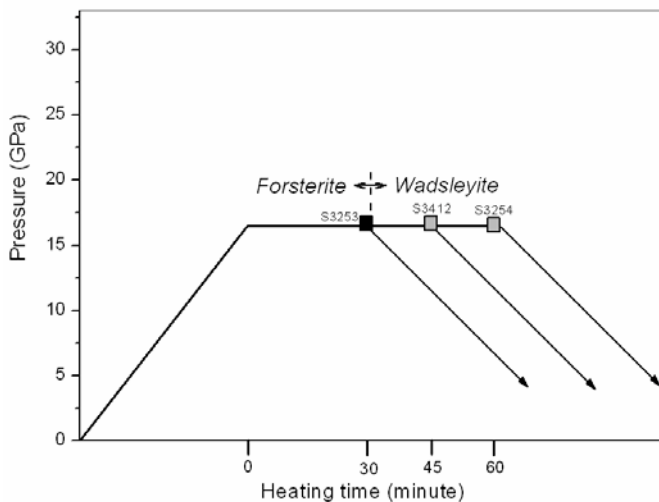
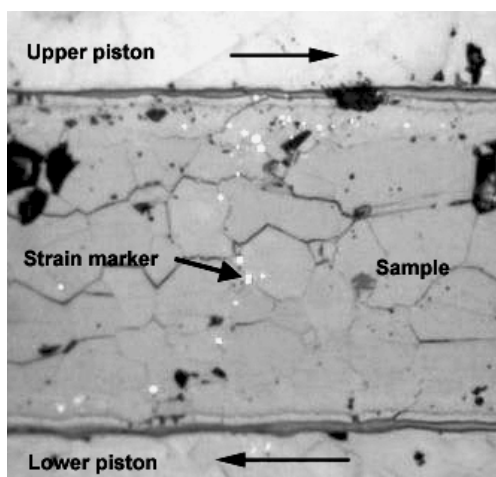


Figure III.35 – Pressure-temperature-time path followed for experiments S3253 (16GPa, 1400°C, 30 min), S3412 (16GPa, 1400°C, 45 min) and S3254 (16GPa, 1400°C, one hour).

#### IV.1 – SEM and EBSD characterisation

Recovered samples have been observed at the SEM. The shape of the strain marker is strongly affected by the phase transformation. In some samples, it exhibits a curved shape as shown in Figure III.36. No information of the total strain can thus be obtained from the rotation of the strain marker. As an alternative, we have measured the displacement of the upper piston relative to the lower piston as an indication of strain. The measurements are reported in Table III.13. An evolution of the displacement can be noticed: from a displacement of 323  $\mu\text{m}$  after thirty minutes of heating (S3253) to a displacement of 416  $\mu\text{m}$  after one hour of heating

(S3254). Moreover, the sample thicknesses have been measured on recovered sample. The thickness is initially about 200  $\mu\text{m}$  for every sample. The thickness of the samples decreases with the heating time from 194  $\mu\text{m}$  after thirty minutes of heating (S3253) to 122  $\mu\text{m}$  after one hour of heating. The phase transformation has induced a significant displacement of the pistons and a reduction of the sample thickness.



*Figure III.36 – Optical micrograph of the strain marker in S3254. The strain marker is made of the white dots. The shear sense is dextral*

The grain sizes of the samples have been measured from the SEM pictures (Figure III.37) using ImageTool software. The variation of the grain size with the heating duration is plotted Figure III.38. Forsterite annealed thirty minutes in the pressure stability field of wadsleyite displays large equilibrated grains with heterogeneous grains size (Figure III.37a). The grains have grown from ca. 50  $\mu\text{m}$  in the starting material to 115  $\mu\text{m}$  after thirty minutes of heating (Figure III.38). After forty five minutes of heating,

## RESULTS

---

the sample, transformed into wadsleyite, displays much smaller grains (ca. 50  $\mu\text{m}$ ). The phase transformation carries a decreasing of the grain size (Figure III.38). After one hour of heating, the wadsleyite grains have grown (up to ca. 70  $\mu\text{m}$ ). The grain size is heterogeneous (Figure III.37c) and the convex grain boundaries suggest occurrence of grain growth.

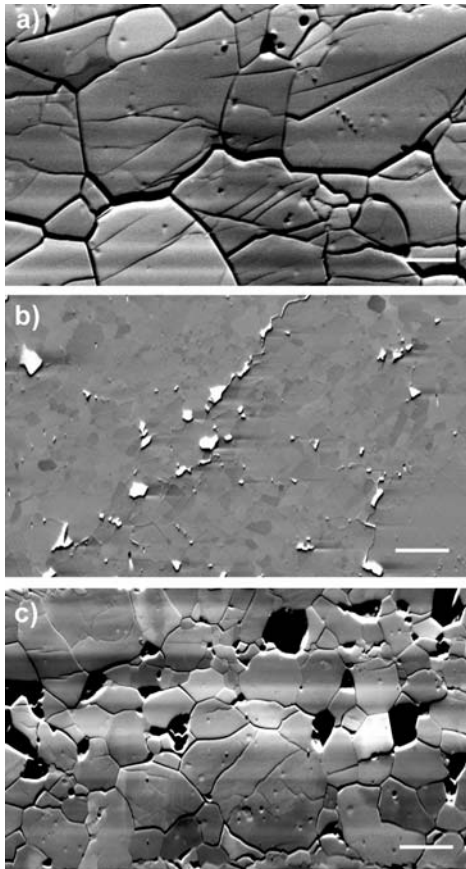


Figure III.37 – Forsterite-wadsleyite transformation under strain: SEM pictures (orientation contrast). Cross section, shear direction horizontal and shear sense dextral.

The bar scale is equal to 20  $\mu\text{m}$

a) After thirty minutes at 16GPa and 1400°C (S3253, forsterite)

b) After forty five minute of heating at 16 GPa and 1400°C (S3412, wadsleyite)

c) After one hour of heating at 16 GPa and 1400°C (S3254, wadsleyite)

The results of EBSD characterisation are presented in Figure III.39. The shear direction is aligned with X and the normal to the shear plane is parallel to Y. The shear sense is dextral.

After thirty minutes of heating, the forsterite sample displays an orthorhombic CPO. The [001] axes of the forsterite sample present a girdle aligned with the shear direction with a maximum close to the shear direction. [100] is roughly aligned toward the normal to the shear plane and [010] is clustered normal to the shear direction within the shear plane.

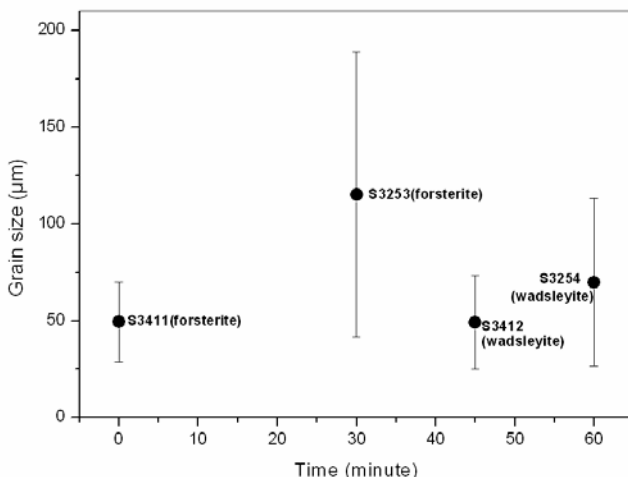


Figure III.38 – Forsterite-wadsleyite transformation under strain: evolution of the grain size with time. Bars represent data scattering ( $2\sigma$  standard deviation).

After forty five minutes of heating, the wadsleyite sample presents already a CPO. [100] is aligned at low angle to the shear direction (ca.  $30^\circ$ ). The [010] and [001] axes are in a girdle normal to [100]. They exhibit a

maximum at low angle (ca.  $30^\circ$ ) from the normal to the shear plane with a stronger clustering for the [001] axes.

After one hour of heating, the latter CPO presents some evolutions. The [100] axes are concentrated at low angle from the shear direction. [010] displays two maxima in the YZ plane, both at low angle from the normal to the shear direction. The [001] axes are concentrated at low angle (ca.  $30^\circ$ ) from the normal to the shear plane. This CPO is very similar to those obtained in the deformation experiments on wadsleyite previously presented (see paragraph II of this chapter)

The obliquity of the crystallographic axes relative to the shear direction and the normal to shear plane are in agreement with the dextral shear.

RESULTS

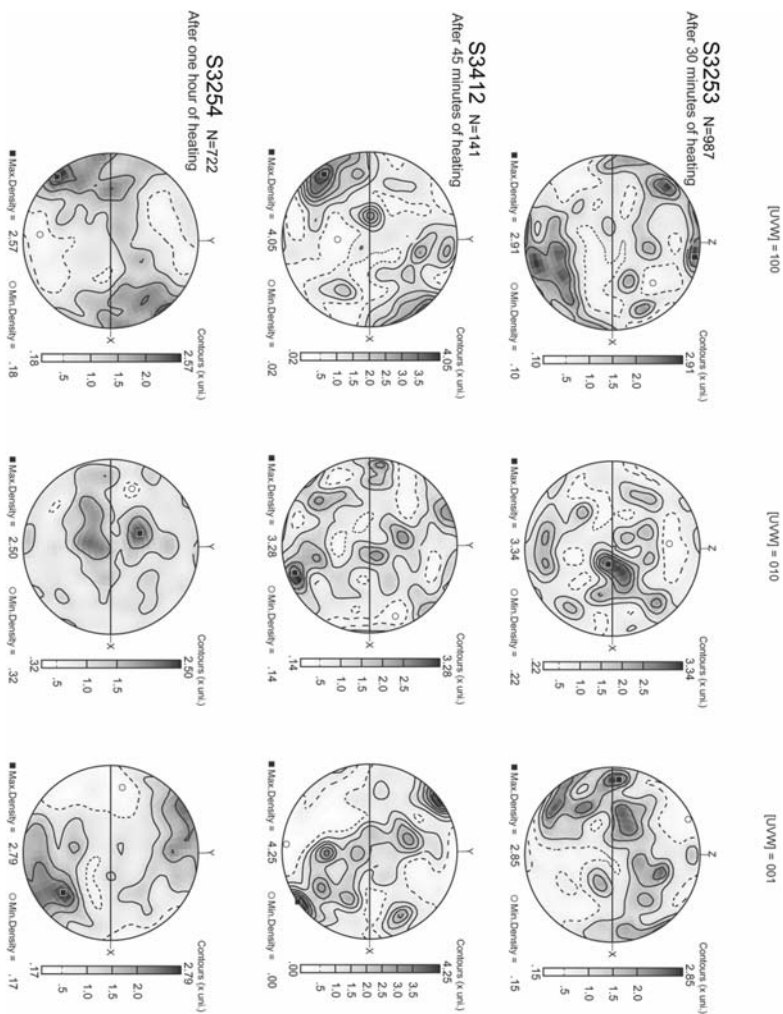


Figure III.39 – Forsterite-wadsleyite transformation under strain: EBSD pole figure of crystal axis of forsterite sample (S3253) and wadsleyite samples (S3412 and S3254). The shear direction of the samples is aligned with X and Y is perpendicular to the shear plane; the shear sense is dextral. Lower hemisphere equal-area projections, contours at intervals of 0.5 multiple of a uniform distribution.

## IV.2 – TEM characterisation

Figure III.40 presents typical grains of forsterite observed in S3253. Although Raman spectrometry and EBSD point to forsterite only, many inclusions of wadsleyite are found on grain boundaries as well as inside the grains (Figure III.40a and b). Forsterite grains present many [001] screw dislocations in glide configuration. No evidence of relationship between dislocations and wadsleyite inclusions has been found. We have looked for crystallographic relationships between the forsterite matrix and wadsleyite inclusions. Table III.12 presents these relationships for inclusions 1, 2 and 3 shown on Figure III.40a and b and two others. Although our study focuses on few grains only, no systematic and strong crystallographic relationship between the forsterite matrix and the wadsleyite has been found.

**RESULTS**

Inclusion #	forsterite matrix		wadsleyite inclusion	
	Zone axis	and plane	Zone axis	and plane
1		[-100]		[20-1]
		(021)		(010)
2		[-100]		[-310]
		(023)		(001)
3		[100]		[10-1]
		(011)		(111)
4		[0-10]		[11-1]
		(001)		(101)
5		[2-10]		[013]
		(121)		(100)

*Table III.12 – Planes and zone axis of forsterite matrix parallel to planes and zone axis of wadsleyite inclusions. Inclusions 1, 2 and 3 are presented Figure III.40.*

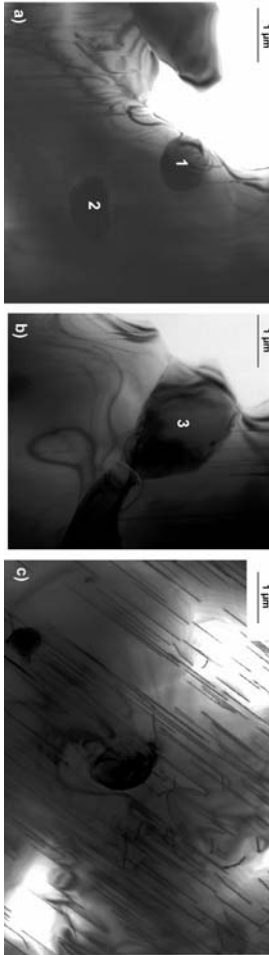


Figure III.40 – Forsterite-wadsleyite transformation under strain: bright field TEM micrographs of S3253 (after thirty minutes at 16 GPa and 1400°C). Three different grains of forsterite with wadsleyite inclusions. For c), [001] screw dislocations.  $g:004$  Weak beam

# Chapter IV

## Discussion

As the techniques used in the course of this study are not used in routine, some developments were needed. Our detailed microstructural characterisations have provided new insights on the behaviour of samples during deformation in those experiments. This aspect of our work is presented in this section. Then, we address the issue of the plastic deformation of the  $\text{Mg}_2\text{SiO}_4$  polymorphs under pressure and temperature conditions from the upper mantle to the transition zone. The first major result to be discussed is the pressure-induced change in deformation mechanism. The plastic behaviour of the three  $\text{Mg}_2\text{SiO}_4$  polymorphs is studied with a special emphasis on the formation of crystallographic preferred orientations. VPSC modelling is used to link the CPO with known elementary deformation mechanisms of these phases. Finally, implications on seismic anisotropy of the lowermost upper mantle and of the upper part of the transition zone are derived based on our results.



## I - Deformation experiments at high pressure and temperature: progresses and limitations

Since a decade, our possibilities in the field of experimental deformation have expanded considerably. Quasi-hydrostatic experiments (in the Kawai-type multianvil and in the diamond anvil cell) as well as the development of the D-DIA and of the Rotational Drickamer Apparatus (RDA; Yamazaki and Karato, 2001) make it possible today to investigate the mechanical properties of deep Earth materials under pressure conditions representative of the whole mantle. Despite this impressive evolution, we are still facing some severe limitations and high-pressure rheology remains a very challenging issue.

The present study is mostly concerned with the mechanical behaviour of olivine and its high-pressure polymorphs with a view to model seismic anisotropy of the upper mantle and the transition zone. This requires large strains to be achieved. The newly developed deformation-DIA provides a new opportunity to achieve such strains under well-controlled mechanical conditions. At higher pressures (those of the transition zone for instance), it is necessary to use the Kawai-type multianvil apparatus for which the shear design allows large strain experiments. The detailed microstructural investigations performed during this study bring further information about the experiments themselves, their possibilities, their limitations, that are presented below.

## I.1 – Deformation in the D-DIA

### I.1.1 – Sample preparation

Sample preparation is very important for D-DIA experiments. Our starting materials have been hot-pressed in order to start every experiment with a well-defined sample length. Indeed, hot-pressed samples are fully dense and sample shortening is only due to deformation and not by porosity reduction. Grain size distribution is another important parameter which controls the quality of X-rays diffraction for experiments involving *in situ* measurements. A small grain size allows a contribution of numerous grains to the formation of X-ray spectra and a better statistic representation of the bulk sample in the diffracting volume (cross-section about  $100 \times 100 \mu\text{m}^2$ ). A good compromise corresponds to grain sizes between 5 and 10  $\mu\text{m}$ .

### I.1.2 – Deformation history in D-DIA experiment

Experiments carried out online at NSLS (FOR21) shows that during pressurisation at room temperature large deviatoric stresses (of the order of 1.5-2 GPa) are applied to the sample. As the pressure cell is the same for all of our experiments, it is likely that all samples experienced this cold compression deformation. Despite an isotropic compression, differential stresses occur in response of the marked mechanical anisotropy of the pressure cell which contains alumina pistons. The crushable alumina plugs are obviously not sufficient to avoid this phenomenon. The length of the crushable alumina plugs might be increased to minimize differential stresses during compression. Indeed, multianvil experiments (S2964, S2970 and S3024) have shown that a large density of defects is introduced in forsterite

at this stage. Unfortunately, no TEM has been performed on samples just cold compressed in the D-DIA for comparison. The D-DIA experiments give us the possibility to anneal the sample prior to deformation to eliminate these defects. In experiments performed off-line in Bayreuth (DD12 and DD13) the specimens were annealed two hours at 1300°C before deformation began. Multianvil experiments have shown that the dislocation density decreases very rapidly during annealing at 1400°C (see Figure III.9b). In the present case a longer time at slightly lower temperature was chosen in order to minimize grain growth. Experiment DD14 showed that with starting material P0332, the grain size increased from 10 to ca. 60  $\mu\text{m}$  during this annealing stage. TEM characterisations of sample recovered after this heating stage (DD10) confirms that the microstructure is recovered. Most grains are free of defects. Some grains still exhibit some dislocations but no subgrain boundaries have been observed. The differential stresses decrease very rapidly once the specimen is heated (experiment FOR21, Figure III.20) to reach about 500 MPa. This drop is probably due to the relaxation of elastic strain stored during pressurisation.

The deformation stage starts when the oil pressure in differential rams overcome friction forces in the main ram. Strain and strain rate can be deduced either from transducer measurements in off-line experiments or from *in situ* radiograph images of the sample. Strain rate is easily adjusted by driving differential rams with stepping motors. A few minutes are generally needed to find the appropriate motor speed for a given strain rate. A few minutes are then necessary to reach a steady state regime. During deformation, the transducers placed between the guide blocks and the top or bottom anvils are crucial especially for off-line experiments. They indicate

precisely at which moment the anvils move and thus at which moment the deformation starts. Even following sample length with radiograph images, this starting point is very difficult to determine with accuracy because it corresponds to a very small shortening of the sample (about 2  $\mu\text{m}$  in 60s for a strain rate of  $10^{-5}\text{s}^{-1}$ ).

During deformation, the flow stress remains constant at a level of 500 MPa for a strain rate of  $10^{-5}\text{s}^{-1}$ . The loading pressure in the main ramp is maintained automatically constant by a slight retraction of side anvils. The nominal pressure (and volume) of the sample is thus kept constant during deformation as seen in Figure III.20. Deformation continues as long as the differential rams move. In the present study the maximal total strain reached is about 25 %. Once the desired strain is reached, the deformation is stopped and the sample is immediately quenched.

Decompression is another important step. Both differential rams and the main ram have to be unloaded in such a way that the sample is not deformed at this stage. This is checked either following the sample length *in situ* by radiography and/or by checking that the transducers do not indicate any displacement of the independent anvils.

The cell developed for this study can be operated at 1300–1400°C over long periods with a very stable graphite furnace (no evolution of the input power). Up to now, no temperature distribution map has been determined on D-DIA sample, although it is an important parameter especially for establishing flow law. The maximal pressure that can be reached depends of the anvils and on the cell materials. Tungsten carbide anvils are usually chosen for their high stress resistance and their easy

manufacturing. However, tungsten has a high atomic number and hence absorbs very much X-rays. These anvils are not very suitable for *in situ* measurements, especially for imaging the sample. Cubic boron nitride might be preferred for this application despite its lower strength. During this study, the maximal pressure reached with a pyrophyllite cubic cell was 7 GPa with WC anvils and 5 GPa with cBN anvils. The pressure efficiency of the cell can be enhanced using mullite or boron-epoxy instead of pyrophyllite as a pressure medium (Li Li, personal communication). The maximal nominal pressure might be slightly increased using sintered diamond anvils (Shimomura *et al.*, 1992) or using tapered anvils (Wang *et al.*, 1998). Price and manufacturing of anvils can be however considered as limiting parameters. Finally, we have observed in our experiments that the Pyrex sleeve behaves as a barrier against migration of water from the cell materials to the sample. Indeed, the annealing experiment DD14 performed from dehydrated sample (P0332: 369 H/10<sup>6</sup>Si) shows a slightly smaller hydroxyl content of 347 H/10<sup>6</sup>Si after two hours at 1300°C and 2 GPa.

D-DIA experiments can provide highly strained samples for which CPO can be measured by EBSD. Given the geometry of the experiment, these CPO are characteristic of compressed samples (DD12, DD31 and FOR21). These kinds of CPO are well adapted to identify the glide plane. The normal to the slip plane tends to concentrate toward the shortening axis (e.g. Turner, 1948). However, the slip direction is not as easily determined as in CPO obtained in shear configuration.

## I.2 – Deformation in the Kawai-type multianvil apparatus

Fundamentally, the Kawai-type multianvil apparatus is not a deformation apparatus. The only parameters that are actually monitored are pressure and temperature. We have seen however that modifications of the high-pressure cell (see details in Chapter II) allow deformation experiments to be carried out at high pressure and high temperature. The fact is that the Kawai-type multianvil press is the only tool which is able to deform millimetre-size samples in the pressure range 10–25 GPa. It is thus a critical facility to address the issue of the rheology of minerals from the transition zone.

In this study we have taken advantage of the shear deformation assembly designed by Karato and Rubie (1997) and described in Chapter II – §I.2.2. In order to deform the three polymorphs of  $\text{Mg}_2\text{SiO}_4$ , it has been necessary to adapt the original 14/8 shear deformation to 18/11 and 18/8 pressure cells. The advantage is that the sample size (a 200  $\mu\text{m}$  thick, elliptic slice, small diameter: 1.5 mm) has been kept constant for the three polymorphs. This has been made possible by using the 18/8 assembly in the 5000 tonnes press available at the Bayerisches Geoinstitut.

### I.2.1 – Starting material

The starting sample is the slice of solid material that has been hot-pressed in case of forsterite or pre-synthesised for high-pressure polymorphs. The reasons for starting from a fully dense material are many. Firstly, it is not technically possible from a powder to obtain reproducible slices, 200  $\mu\text{m}$  thick, between the pistons cut at 45°. Secondly, starting a

deformation experiment with a fully dense sample avoids compaction during pressurisation that would affect the strain marker rotation. Thirdly, the mean grain size of the sample can be chosen. The grain size has to satisfy EBSD requirements. A minimum of 100–150 grains measurements is necessary to be representative of a CPO (Ben Ismail and Mainprice, 1998). In our case we try to work with a mean grain size about 10–20  $\mu\text{m}$ .

In case of high-pressure polymorphs, the choice of pre-synthesised samples was made to avoid the influence of the phase transformation on the deformation experiment. In particular, the phase transformation is likely to relax stresses in the cell resulting in a loss of efficiency of the deformation experiments. We have seen (H1953, 1954, H1979 and H1981 of the wadsleyite deformation experiment series) that it was not always possible to avoid these effects, especially with wadsleyite which back-transformed during heating.

### I.2.2 - Deformation history in a shear deformation experiment

The detailed microstructural characterisations performed on our samples at various stages provide useful insights on the stress history during a shear experiment in the Kawai-type multianvil apparatus.

As in D-DIA experiments, the sample is first brought to pressure at room temperature. Thurel *et al.* (2003a) have shown that compressive deformation experiments performed in the multianvil apparatus introduce a large density of defects in wadsleyite during pressurisation. We have seen that the situation is likely be the same in the D-DIA given the stress levels measured at this stage. In contrast, the damages introduced during cold

compression in a shear deformation assembly have not been characterised so far. Our observations performed on forsterite and on wadsleyite suggest that, as in compression, large stresses are applied to the sample during pressure building. Dislocation density of forsterite samples measured by X-ray is of the order of  $1.6 \times 10^{15} \text{ m}^{-2}$  and dislocation density in cold compressed wadsleyite samples is evaluated at  $10^{16} - 10^{17} \text{ m}^{-2}$  (from TEM observations). Without *in situ*, direct, measurements, one might derive an estimate of the effective stress from dislocation densities using the Taylor equation:

$$\sigma_1 - \sigma_3 = \alpha b \mu \rho^{\frac{1}{2}}$$

where  $\alpha$  is a constant of order unity,  $b$  is the active Burger vector,  $\mu$  is the shear modulus and  $\rho$  is the dislocation density. This equation describing strain hardening (Friedel, 1967) has been verified experimentally for olivine (Kohlstedt and Goetze, 1974; Kohlstedt *et al.*, 1976; Wang *et al.*, 1988) from “free” dislocation density introduced during steady state creep. From Kohlstedt *et al.* (1976),  $\alpha$  has been determined equal to 3. Applied to our forsterite samples, Taylor equation suggest a stress level of the order of 1.5 GPa, very similar to the one measured *in situ* in the D-DIA (Figure III.20). The pistons displacement observed after cold-compression probably occurred very early, when friction forces were not high enough. Despite these high densities of defects, EBSD characterisations do not show any significant CPO suggesting that the samples were not macroscopically deformed.

Pressure calibration of the shear 14/8 assembly achieved at room temperature shows that a pressure of 20 GPa is obtained for an oil pressure of 264 bars whereas it would correspond to a pressure of 16 GPa only in a conventional 14/8 assembly. The fact that the sample is a thin slice sandwiched between two hard pistons seems to result in a higher pressure efficiency of the cell.

Once nominal oil pressure is reached, the sample is heated up. The temperature is raised to 1400°C within 12 to 15 minutes. In order to follow the evolution of deformation with time duration, different heating times were explored. In a first group of experiments, the temperature was held at 1400°C for one minute only before quench to room temperature within 2 to 3 seconds. The aim was to assess the influence of the heating ramp which can hardly be made shorter without breaking the WC cubes. In case of forsterite, we observe that after heating and one minute at 1400°C, the density of dislocations introduced during cold compression is significantly reduced (from  $1.6 \times 10^{15} \text{m}^{-2}$  to  $2 \times 10^{14} \text{m}^{-2}$ ). From this dislocation density, the stress is estimated to be  $500 \pm 200$  MPa. No CPO is observed at this stage however, demonstrating that the defects introduced during cold compression are not sufficient to produce enough strain (Figure III.5). This is important to make sure that subsequent CPO result from deformation mechanisms activated at high pressure and temperature. Wadsleyite samples exhibited a more complex behaviour. Phase determination using micro Raman spectroscopy showed that wadsleyite, which was still present after cold-compression, back-transformed systematically (experiments H1953, H1954, H1979 and

H1981) into forsterite. TEM characterisations done on H1954 show the nucleation of wadsleyite inclusions within forsterite grains or at grain boundaries (Figure III.30b).

The presence of forsterite suggests that, during heating, the pressure fell for some time into the forsterite stability field. From pressure calibration performed on the standard 14/8 assembly (Figure II.5), it appears that, for a given oil pressure, the nominal pressure at room temperature is lower than its counterpart at high temperature. Indeed, taking the Hymag press as an example, an oil pressure of 264 bars which corresponds to 16 GPa at 1200°C corresponds to 13 GPa only at room temperature. This explanation might be consistent with the absence of back-transformation in ringwoodite. Indeed, this mineral has been deformed in the 5000 tonnes press for which the nominal pressure at room temperature and at 1400°C are equal for an oil pressure of 295 bars. However, this explanation is difficult to reconcile with the pressure calibration which showed that the shear assembly corresponds, for a given oil pressure, to a higher pressure than the conventional pressure cell (Chapter II §1.3.2). Finally, one can not rule out the possibility that the large density of crystal defects introduced during cold compression shifts the phase boundary between olivine and wadsleyite. In any case, our study demonstrates that the greatest care must be taken with studies on high-pressure polymorphs about possible back-transformations.

Deformation experiments in Kawai-type multianvil are comparable to relaxation tests (Karato and Rubie, 1997). As soon as the temperature is raised, the elastic energy accumulated during cold compression is relaxed plastically and the sample deforms. This means that effects of cold pressurisation can not be erased by a long annealing stage at high

temperature before deformation as in the D-DIA. Annealing and deformation are not decoupled as in this press. For longer times at 1400°C, the forsterite observed after one minute of heating in wadsleyite deformation experiments is completely re-transformed into wadsleyite. Samples annealed one hour show no forsterite at the TEM. Stress relaxation goes on as illustrated by the evolution of the dislocation density measured on forsterite samples. The estimated stress level reached after eight hours of heating is about  $100\pm 50$ MPa in forsterite. One finds here lower stresses than with D-DIA for which the strain-rate is kept constant. EBSD characterisations on forsterite show that CPO develop after one hour of heating (S2917, S2994, S2995, S2993 and S2994) and become weaker after eight hours of heating (S2998 and S3079) whereas CPO of wadsleyite samples seem slightly more marked after eight hours of heating (H1864 and S3213) than after one hour of heating (H1882 and H1945). Moreover, microstructures observed after eight hours of heating in forsterite samples display subgrain boundaries and recovery effects that become predominant whereas in wadsleyite dislocations are still in glide configurations. The comparison between these two materials demonstrates that the evolution depends not only on the experimental conditions, but that the sample itself plays a major role in determining its evolution.

The total strain achieved for longer heating time is limited because the strain rate decreases resulting in a loss of efficiency. The strain marker suggest, for forsterite, a maximum strain of 0.3 which is significantly below the value of 1 previously found by Karato and Rubie (1997) and Karato *et al.* (1998). The difference might come from the position of the strain marker which was inclined at 45° from the axis of the furnace whereas it is parallel

to the furnace axis in our study. Inclined at  $45^\circ$ , the strain marker can record the compression of samples especially if it is not fully dense, or if some phase transformation occurs. Our study shows however that the strain marker, although it is the only way to evaluate the strain, is a very imprecise measurement and should just be used as a first order indicator.

Concerning temperature, our calibrations (see Chapter II, §1.3.2 and Figure II.14) indicate that the maximum difference between the actual temperature at the sample and the indication given by the thermocouple is of the order of  $100^\circ\text{C}$  with a maximal thermal gradient within the sample of  $50^\circ\text{C}$ . One of the possible limitations of the shear assembly is its use at high temperature. Possible reactions between the pistons and the sample must be considered. In this study, we observed a systematic reaction between  $\text{Al}_2\text{O}_3$  and  $\text{Mg}_2\text{SiO}_4$  resulting in a thin (about 100 nm see Figure IV.1) layer of garnet composition (characterisation made with microanalysis of SEM). This reaction layer does not seem to be highly sheared and we believe that it has no implication on the deformation experiments. Indeed, one would be concerned if the reaction product would result in a weak layer which could induce a mechanical decoupling between the sample and the pistons.

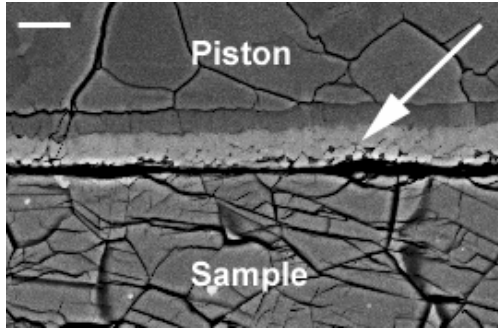


*Figure IV.1 – Interface piston-sample in a shear deformation assembly. SEM picture in Z-contrast. The arrow shows the garnet composition layer created by the reaction between alumina piston and forsterite (S2917, 1400°C, 11 GPa and 1 hour). Scale bar: 100 nm*

Finally, experiments performed twice or more with same pressure-temperature conditions indicate clearly that deformation experiments performed in Kawai-type multianvil press using the shear assembly are reproducible.

### I.3 – Conclusion on deformation techniques under high pressure and temperature

With the D-DIA we have now the capability to perform deformation experiments on Earth materials under pressure-temperature conditions representative of depths down to 300 km. It is important to point out that these deformation experiments offer capabilities which are very comparable to standard deformation experiments at low pressure:

- deviatoric stress is controlled independently from pressure
- several kind of tests are possible : constant strain-rate, stress relaxation

- relatively large strains (at least 30%) can be reached in compression
- pressure, deviatoric stress and strain can be measured *in situ* if the deformation experiments is coupled with a synchrotron beam line.

This instrument opens a new field in the domain of plastic deformation of materials from the upper mantle (it can be anticipated that technical developments will rapidly expand the pressure limit to ca. 15 GPa). To reach conditions of the transition zone, the Kawai-type multi-anvil press still represent the only way to achieve experiments with controlled pressure and temperature conditions on millimetre size samples. In the compression design, deformation experiments can be performed to 26 GPa (Cordier and Rubie, 2001; Cordier *et al.*, 2004). However, this compression assembly cannot produce large strains as the shear assembly developed by Karato and Rubie (1997) does. This assembly originally designed for the 14/8 assembly and thus limited to 17 GPa has been adapted to the 18/11 and 18/8 assemblies in this study. The pressure domain is therefore extended to 22 GPa at high temperature. This progress has been made possible by the use of the 5000 t press available in Bayreuth. We show however that damage induced during cold compression as well as possible back-transformation must be carefully characterised with these experiments.

## II – Deformation of $\text{Mg}_2\text{SiO}_4$ polymorphs under upper mantle and transition zone conditions

Most experiments of this study have been performed in Bayreuth using Kawai-type multianvil or D-DIA presses (not installed on a beam line) that do not give access to *in situ* measurements of mechanical properties. In the case of forsterite, a few complementary experiments have been performed at APS and BNL. Our main goal was to determine the CPO produced by deformation at high pressure and high temperature in the three polymorphs of  $\text{Mg}_2\text{SiO}_4$ . This knowledge is critical to model seismic anisotropy in the upper mantle and in the transition zone. Therefore, we have performed detailed microstructural characterizations on samples recovered at different stages of deformation experiments to have the best control and understanding in the mechanisms responsible for the resulting CPO.

### II.1 – Deformation mechanism of forsterite at 11 GPa and 1400°C

#### II.1.1 – Changing the deformation mechanisms with pressure

The most striking observation coming out of shear deformation experiments of forsterite performed in the Kawai-type multianvil press is the unusual character of the CPO produced (Figure III.7) and of the dislocation microstructures observed at the TEM (Figure III.10). Every

experiment heated one hour (but S2993) exhibit CPO with marked alignment of [001] toward the shear direction, which is indicative of [001] slip. Indeed, TEM observations on these samples showed pervasive evidence for [001] dislocations. Let us first discuss the observed dislocation microstructures, starting from those samples deformed in the Kawai-type apparatus at 11 GPa.

TEM characterisations of samples that were only cold compressed (S2964, S2970 and S3024) show that a large density of [001] dislocations is introduced in the sample at this stage. It is worth noticing that both edge and screw segments are present with comparable densities. This demonstrates that, at room temperature, edge [001] dislocation segments bear a high lattice friction as do screw segments.

In samples deformed in simple shear during one hour at 1400°C (S2917, S2954, S2955, S2993 and S2994), TEM observations show dislocation microstructures dominated by straight screw [001] dislocations.

For much longer times at high temperature (8 hours), the microstructures are quite different with the advent of numerous subgrain boundaries. This observation suggests that the strain rate has decreased after 8 hours (see Figure III.10d) such that recovery effects (promoted by climb) become predominant. It is important to note that this decrease of the strain rate is not accompanied by any visible change of the deformation mechanism (activation of [100] glide for instance). The deformed grains still exhibit [001] screw dislocations only, as in the samples annealed for only 1 hour.

TEM observations on experiments performed in the D-DIA (DD13 and D0501, Figure III.14 and 18) at lower pressures (2 to 6 GPa) also show numerous [001] dislocations although [100] dislocations are also present in those samples with a comparable frequency (in fact limited TEM observations do not allow a quantitative estimate of the activity of the two slip systems).

[001] glide is a known deformation mechanism in olivine. It has been mostly documented from room-pressure deformation studies of olivine single crystals (e.g. Kohlstedt and Goetze, 1974; Darot and Gueguen, 1981). The relative ease of [100] and [001] glide depend critically on temperature and strain-rate. Deformation experiments on oriented single crystals have been used to derive the Critical Resolved Shear Stresses (CRSS) for dislocation glide on a few particular slip systems. As an illustration, Figure IV.2 shows how the CRSS of [100] and [001] dislocations on (010) evolve with temperature at a strain-rate of  $10^{-5}\text{s}^{-1}$ . It is shown that slip along [001] is a dominant mechanism at low temperature, while [100] glide becomes easier at higher temperature. The influence of strain-rate is usually inferred by dislocation microstructures found in shocked olivine (either in meteorites or from experiments see for instance the recent review from Leroux (2001) and references herein) which are dominated by [001] dislocations.

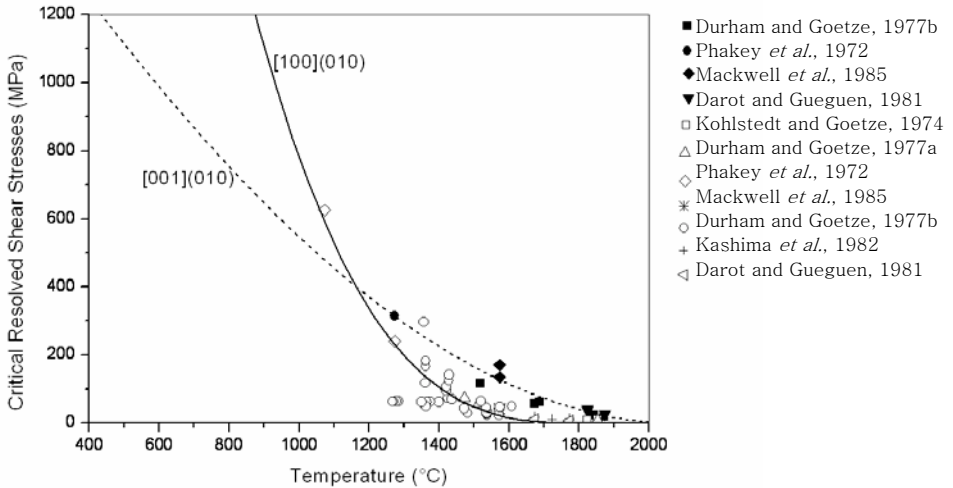


Figure IV.2 – Olivine: critical resolved shear stresses of slip systems  $[100](010)$  and  $[001](010)$  as a function of temperature. Data (corresponding to a strain rate of  $10^{-5} s^{-1}$ ) from experiments performed on single crystals oriented along  $[011]c$  (black-filled symbols) to promote  $[001](010)$  glide and along  $[110]c$  (open symbols) to promote  $[100](010)$  glide.

Previous studies have already reported evidence for  $[001]$  glide under high-pressure conditions. For instance,  $[001]$  glide has recently been reported by Raterron *et al.* (2004) and Li *et al.* (2003) at 8–9 GPa and 500–890°C. But, in this temperature range,  $[001]$  glide would be expected, as illustrated by Figure IV.2. Samples deformed at 15 GPa and 900°C for 30 min by Dupas–Bruzek *et al.* (1998b) also contained remnant olivine grains with high densities of  $[001]$  dislocations but the same conclusion holds.

The occurrence of [001] glide in high-pressure experiments is usually attributed to the application of high stresses. It is to be noted, however, that the present situation (high stresses at high temperature) cannot be compared easily with low-temperature or shock experiments.

Our microstructural investigation confirms that high stresses (1.5 GPa) result from pressurisation at room temperature in the shear-deformation assembly and that many [001] dislocations are introduced at this stage. Analysis of samples heated to 1400°C during one minute shows that most of these defects are eliminated shortly after heating the sample without producing significant macroscopic strain (CPO). The CPO observed in the one hour experiments must be then the result of the nucleation and glide of dislocations at 1400°C under stress levels below ca. 500 MPa. The usual creep experiments (Figure IV.2) suggest that, at room pressure, [100] glide should have been also activated under these conditions. Our results cannot be understood from the known CRSS of [100] and [001] glide presented in Figure IV.2. To understand the high pressure results, we must suppose either that [100] glide becomes so hard that it is inhibited or that [001] glide is enhanced with pressure. The striking observation is in fact more the absence of [100] dislocations rather than the occurrence of [001] slip. Indeed, [001] glide on {hk0} planes do not provide enough slip systems to satisfy the Von Mises criterion. Grain boundary mobility might be high enough at 1400°C to overcome this limitation. It is also possible that secondary [100] could be activated at larger strains. This question links with the observation of [100] dislocations in D-DIA experiments which can be either interpreted as the result of a lower pressure, or from the larger strains involved (between 6 to 25%).

Beyond the glide direction, we are interesting in identifying the dominant slip planes. In our study, CPO of shear deformation experiments suggest dominant [001] glide on (100) (S2954, S2955 and S2993) as well as on (010) (S2955 and S2994). This might be interpreted as a comparable ease of slip on those two planes. The final CPO would thus depend on the starting orientation distribution function of the grains. It must be noted that no confirmation on the slip plane can be drawn from the TEM observations as the dislocation microstructures are dominated by screw segments only. More information can be obtained from D-DIA experiments for which deformation is achieved in compression. The glide direction is less readily obtained from CPO resulting from compression experiments. However, the glide plane which normal tends to align with the compression direction, is easier to define. Experiments DD31 (6 GPa) show CPO with [010] axes parallel to the compression axis and [100] and [001] concentrated in the plane normal to the compression axis, more or less in a girdle (Figure III.13). As stated above, the slip direction is not well constrained by this observation ([100] and/or [001] can be involved). However, (010) seems to be the easiest slip plane.

Another line of evidence suggesting a pressure effect on the dominant slip systems in forsterite has been provided from a recent set of experiments performed by Paul Raterron (personal communication) at NSLS in a D-DIA press coupled with synchrotron beam line on forsterite single crystals. Since this work is linked to ours, its main lines and conclusions are briefly presented here. The D-DIA high-pressure cell contains two single crystals. One is aligned along [011]c (to promote [001](010) glide) and the other is oriented along [110]c to promote [100](010) glide. A direct

comparison of strain rates of both crystals can be obtained *in situ* from radiograph images. Samples have been deformed first at 2.7 GPa then at 7.2 GPa at high temperature (1100–1400°C) and under imposed strain rate. At 2.7 GPa and 1400°C, the single crystal oriented along [110]c deforms with a strain rate about  $4 \times 10^{-6} \text{s}^{-1}$  whereas the single crystal oriented along [011]c deforms with a strain rate about  $1.4 \times 10^{-6} \text{s}^{-1}$ . At 7.2 GPa and 1400°C, the situation changes as the single crystal oriented along [110]c deforms lower than the one aligned along [011]c with strain rate of about  $13 \times 10^{-6} \text{s}^{-1}$  and  $17 \times 10^{-6} \text{s}^{-1}$  respectively. A pressure-induced inversion of slip systems (between [100](010) and [001](010)) is thus evidenced by *in situ* measurements. Varying stress and strain-rate allows determination of rheological laws relative to these two slip systems as a function of pressure. An example corresponding to a stress level comparable to the one of our Kawai experiments is shown Figure IV.3.

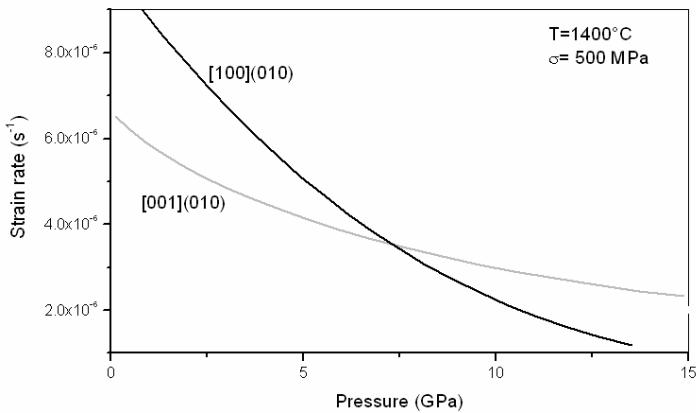


Figure IV.3 -Evolution of the strains rates of two single crystals of forsterite oriented along  $[110]c$  and  $[011]c$  as a function of pressure. The two crystals were deformed together in a D-DIA at  $1400^{\circ}\text{C}$  under a stress of 500 MPa (Courtesy of P. Raterron).

### II.1.2 – Physical origin for a pressure sensitivity of the olivine slip systems

The change of dominant slip systems with increasing pressure is likely to reflect an influence of pressure on dislocations mobility. This can arise from a pressure-induced modification of the dislocation core fine structure, i.e. at the atomic scale. Such an effect of pressure on dislocation core structure has already been reported in Ta (Yang *et al.*, 2001a; Yang *et al.*, 2001b), but there were no evidence yet for such an effect in minerals. To address this question, numerical simulations have been carried out at the atomic scale at the University of Lille by Julien Durinck (personal communication). As the experiments on single crystals presented above, this work to which we did not contribute, but which is connected to ours, will be

presented briefly. At present, the issue of dislocation mobility is far too complicated to be addressed directly. J. Durinck's approach consists in calculating generalised stacking faults, i.e. the stacking fault energy resulting from continuous rigid body plastic shear along a glide direction parallel to a glide plane. This gives an assessment of the intrinsic resistance of the crystal to plastic shear arising from corrugation of the glide plane at the atomic scale. It is possible from this approach to emphasize the influence of crystal chemistry on plastic shear anisotropy in minerals (see Durinck *et al.* (in press) for the application of this concept to olivine). Christian and Vitek (1970) have shown that the Peierls stress could be calculated from the generalised stacking faults within the frame of the Peierls-Nabarro model (e.g. Joòs and Duesbery, 1997). The energy barriers corresponding to the slip systems [001](010) and [100](010) have been calculated from first-principles using VASP code (Kresse and Hafner, 1993; Kresse and Furthmüller, 1996). For each plastic shear increment, some degree of freedom is given to the ions to relax their positions before the energy is calculated. The results are presented in Figure IV.4. At zero pressure, the energy barriers of [100](010) and [001](010) are very comparable with a maximum value at about 2000 mJ/m<sup>2</sup> (the barrier of [100] is slightly lower than the barrier of [001]). The same calculation gives a very different result at 10 GPa. Although the energy barrier for [001] glide is almost not affected, the one for [100] glide is significantly increased (about 50%). The reason can be understood from the atomic relaxations which show that [100] glide is accompanied with a dilation component perpendicular to the fault plane. This preliminary result provides the first theoretical frame for explaining the influence of pressure on plastic deformation of olivine. It

suggests that pressure inhibits  $[100]$  glide which involves more dilation than  $[001]$  glide.

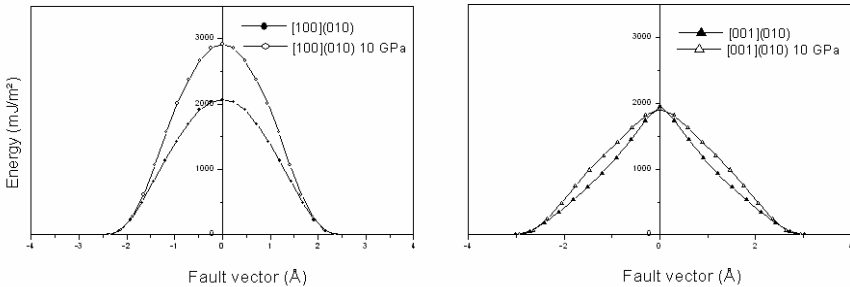


Figure IV.4 – Energy barriers associated with plastic shear in forsterite on  $[100](010)$  (left) and  $[001](010)$  (right). Calculations were performed *ab initio* at 0 GPa (black symbols) and 10 GPa (open symbols) (Courtesy of J. Durinck).

### II.1.3 – Linking microscopic to macroscopic: crystallographic preferred orientation

Plastic deformation of crystals occurs by shearing a few glide systems. In a polycrystal, this results in an extreme anisotropy of stress- and strain-components and in lattice rotations that cause orientations changes and CPO. CPO are thus related to the active deformation mechanisms and more specifically, to the geometry of slip. In present study, we have gained information independently on both the deformation mechanisms (from TEM characterizations) and on the resulting CPO (from EBSD). The goal of this section is to link the two aspects and to check for consistency between them. For that, the CPO will be calculated from the deformation mechanisms inferred from microscopic investigations. The

calculations have been performed by Andrea Tommasi and David Mainprice (Laboratoire de Tectonophysique, University of Montpellier, France) using a ViscoPlastic Self Consistent model (Molinari *et al.*, 1987; Lebensohn and Tomé, 1993) (see Appendix III for more details on these calculations). These simulations will be also very useful to derive the three-dimensional distribution of seismic velocities (presented below in § III.1).

VPSC modelling has been extensively tested for olivine (e.g Wenk *et al.*, 1991; Tommasi *et al.*, 1999; Wenk and Tomé, 1999; Tommasi *et al.*, 2000) and for various polycrystalline aggregates (e.g. Bascou *et al.*, 2002; Cordier *et al.*, 2004; Mainprice *et al.*, 2004). The initial condition is defined by the initial CPO and from initial crystal shapes. In the present simulations, the initial CPO is composed of 500 randomly oriented crystals with spherical shape. Our TEM investigations of specimens deformed at high pressure together with atomic scale calculations provide some constraints on the relative strength of the slip systems (CRSS) used for the simulations. VPSC simulations have been performed with the relative CRSS for [100](010), [100](001), [001](010), [001](100), [100]{011}, [100]{021}, [001]{110} slip systems with a ratio of 3:1:6 (Table IV.1) for shear strain of 0.5 (close to the shear strain of our shear experiments) and of 1.

**DISCUSSION**

Slip systems	[100](010) [100](001)	[001](010) [001](100) [001]{110}	[100](011) [100]{021}
Relative CRSS	3	1	6

*Table IV.1 - Relative critical resolved shear stresses of forsterite slip systems used in the simple shear VPSC simulations.*

Similarly to previous simulations in olivine, a stress exponent of  $n=3$  is used in the simulations. Indeed, VPSC simulations are not very sensitive to  $n$  values between 3 and 5 and almost all minerals have stress exponents in this range; the main effect of increasing  $n$  is an enhancement of the CPO for a given finite strain. Figure IV.5 presents the results of VPSC simulations after shear strain of 0.5 and 1. SD and NSP represent the shear direction and the normal to the shear plane respectively. After a shear strain of 0.5, [100] and [010] tend to form a girdle in a plane at high angle from the shear plane with a clear maximum at low angle from the normal to the shear plane while [001] tend to form a girdle in the foliation plane with strong concentration at low angle from the shear direction. Maximal obliquity (ca.  $30^\circ$ ) is in conformity with the imposed dextral shear sense. The maximal densities in this simulated CPO are slightly higher than in experimentally deformed CPO (see Figure III.7). CPO evolve with increasing strain toward a clustering of [100], [010] and [001] with faster concentration of [001]. Similar CPOs are predicted from tests with different CRSS values for all combinations in which glide in [001] systems is significantly easier than in [100] systems.

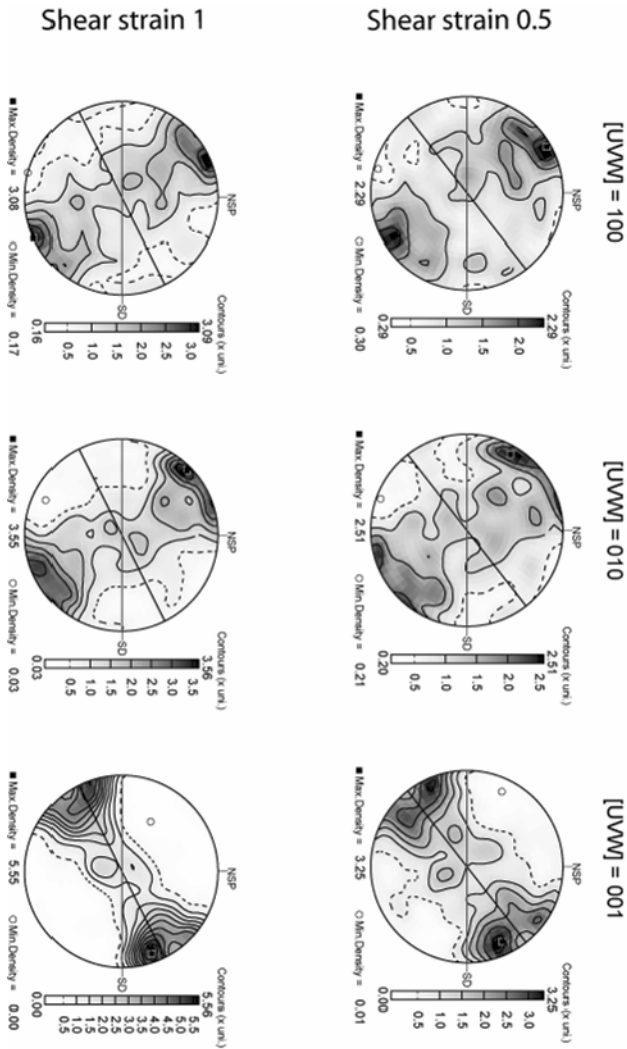


Figure IV.5 – Forsterite crystal preferred orientations predicted using VPSC modelling on 500 grains for shear strain of 0.5 and 1. Lower hemisphere equal-area projection, contours at 0.5 multiple of uniform distribution intervals. Dextral shear sense. SD= shear direction NSP= normal to shear plane. Inclined black line marks the foliation.

The evolution of the activities of the various slip systems are presented as a function of strain in Figure IV.6. A high activity of the [001] systems that accommodate 90% and 80% of the total strain at 0.5 and 1 shear strains, respectively, leads to stronger concentrations of the [001] axes relative to [100] and [010] ones. Activity of [100](010) increases rapidly from 0.05 % to 20% between 0 and 1 of shear strain while the activity of the [001] systems decreases slightly. These evolutions support the assumption made previously that larger strains enhance activation of secondary slip systems. Among the [001] systems, the activity of [001] slip on {110} is significantly higher than on the other planes. This highlights the importance of [001] slip on {110} in the formation of CPO in forsterite.

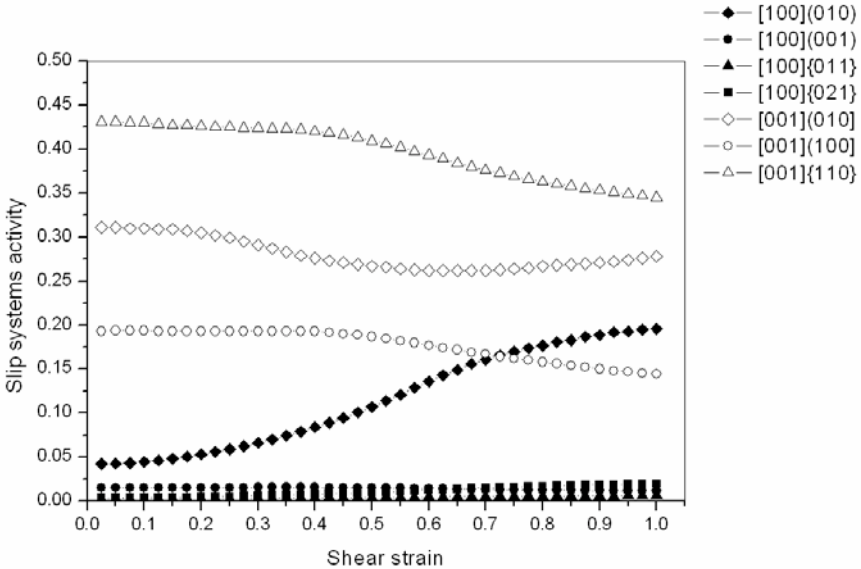


Figure IV.6 – Evolution of slip systems activities in forsterite as a function of shear strain in VPSC simulation (see Tables IV.1 for models). Black symbols: activity of [100] systems Open symbol: activity of [001] systems.

To conclude, VPSC modelling taking into account the pressure-induced change in deformation mechanisms accounts satisfactorily for experimental CPO of forsterite formed at 11 GPa and 1400°C in simple shear configuration (Figure III.7).

However, this type of CPO is unusual. Common CPO for olivine deformed under conditions prevailing in the first 200 km (up to 6 GPa) of the upper mantle are characterized by [100] parallel to the shear direction. Analysis of olivine naturally deformed (e.g. Nicolas *et al.*, 1973; Nicolas and

Christensen, 1987; Wedel *et al.*, 1992; Ben Ismail and Mainprice, 1998; Ben Ismail *et al.*, 2001), olivine experimentally deformed (Zhang and Karato, 1995; Bystricky *et al.*, 2000; Zhang *et al.*, 2000) as well as numerical modelling of CPO development in olivine polycrystals (Tommasi, 1998; Tommasi *et al.*, 1999; Wenk and Tomé, 1999) usually point to CPO characterized by [100] and [010] aligned parallel to the shear direction and normal to the shear plane respectively.

The first experimental observations of CPO characterized by [001] aligned toward shear direction at high pressure and high temperature have been done by Jung and Karato (2001). Water-bearing olivine polycrystals have been deformed at about 2 GPa and 1400–1570°C under moderate stresses (160 to 460 MPa). This type of CPO has been attributed to the enhancement of [001] slip (compared to [100] slip) as a result of the high water content. Following Jung and Karato results, CPO with [001] axes parallel to the lineation, recently discovered in two different occurrences of naturally deformed peridotites (Frese *et al.*, 2003; Mizukami *et al.*, 2004) have been interpreted from resulting from the presence of water. Comparable CPO characterized by [001] perpendicular to compression axis have been reported recently from *in situ* observations of olivine deformed between 9 and 43 GPa at room temperature (Wenk *et al.*, 2004). This observation which points toward activation of [001]{hk0} slip system is less surprising as it has been reported for many years that [001] glide dominates deformation of olivine single crystals at low temperature (e.g Raleigh, 1968; Young III, 1969; Phakey *et al.*, 1972). Pressure–temperature conditions (either below to 3 GPa or at low temperature) of these experimentally and naturally deformed CPO characterized by [001] glide are far from our

experimental conditions (11 GPa and 1400°C) and cannot be easily related to our observations. Unusual olivine CPO were reported recently in mantle xenoliths brought to the surface by the Labait volcano (Vauchez *et al.*, 2003). Those CPO are characterized by a bimodal concentration of both [100] and [001] axes close to the lineation. The temperature and pressure conditions of the xenoliths are 4.4 GPa–1269°C to 4.6 GPa–1336°C. They might indicate an increasing contribution of the [001] glide direction to the deformation at about 4.5 GPa and 1300°C.

#### **II.1.4 – Conclusion and open questions**

From the present work and further studies triggered by it, we have now a large body of compelling evidences that show a major change in the deformation mechanisms of forsterite induced by pressure. This has major potential implications as the CPO should evolve significantly with increasing depths in the upper mantle. Implications of the changes of deformation mechanisms on seismic anisotropy are discussed further (§ III.1). In this perspective, the pressure for the transition between the two regimes is a very important parameter which is not very well constrained yet. More experimental work is necessary to determine this transition pressure more precisely as well as the stress effect on this pressure.

The discovery of this pressure effect on olivine deformation shed new light on shock experiments. The pervasive occurrence of [001] dislocations observed in shock wave experiments (e.g. Leroux, 2001) is usually interpreted as a result of the high strain rates. It might be a consequence of the imposed pressure as well.

Dislocation mobility changes might also result from the presence of dissolved hydroxyls as suggested by the results of Jung & Karato (Jung and Karato, 2001) obtained at 2 GPa on water-bearing olivine. However, Jung & Karato's experiments lead to dislocation microstructures that are significantly different from ours, i.e. with [100] dislocations and [001] dislocations which no longer exhibit straight characters (Shun-ichiro Karato, personal communication). Certainly, water does play a role in our experiments, probably promoting grain boundary migration; but concerning dislocation mobility, the situation is less clear. More work is certainly needed to clarify this point.

## II.2 – Deformation of wadsleyite and ringwoodite under pressure-temperature conditions of the transition zone

### II.2.1 – Deformation of wadsleyite at 16 GPa-1400°C and effect of the phase transformation forsterite- wadsleyite on deformation

The first attempts to deform wadsleyite experimentally are only ca. ten years old. As this phase is not stable at ambient conditions, experimental deformation was possible only after the quasi-hydrostatic apparatus were adapted to deformation experiments. Numerous studies (Dupas *et al.*, 1994; Sharp *et al.*, 1994; Chen *et al.*, 1998; Dupas-Bruzek *et al.*, 1998a; Thurel and Cordier, 2003a; Thurel *et al.*, 2003b; Thurel *et al.*, 2003c) have enriched our understanding on the plastic behaviour of this high-pressure phase.

However, the development of crystal preferential orientations, essential for modelling seismic anisotropy in the transition zone, is still poorly constrained.

### II.2.1.1 – Deformation of wadsleyite at 16 GPa and 1400°C

Deformation experiments on wadsleyite have been performed at 16 GPa and 1400°C in the shear deformation assembly in order to produce CPO. As with forsterite we observe that cold compression induces significant damage in the samples (H1949 and H1967). The microstructures observed at the TEM show large dislocation densities estimated at about  $10^{16}$ – $10^{17}$  m<sup>-2</sup>. This density is one to two orders of magnitude higher than in cold-compressed forsterite ( $1.6 \times 10^{15}$  m<sup>-2</sup>). The large lattice strains after cold-compression do not allow sample characterisations with EBSD. It is thus impossible to assess the possibility that CPO can be formed at this stage.

We have seen (see § I.2.2) that after the temperature ramp (about 12–15 minutes) and one minute of heating at 1400°C in the wadsleyite stability field, wadsleyite is systematically back-transformed into forsterite (H1953, H1954, H1979 and H1981). At this stage, the newly formed forsterite grains are already twice as large as the original wadsleyite grains (Figure III.23 and Figure III.25). Moreover, these samples already developed an olivine CPO (Figure III.29). CPO of H1953 and H1954 present roughly the same characteristics. [001] is aligned toward the shear direction and [100] and [010] are normal to [001], with either [010] or [100] normal to the shear plane. These CPO are quite similar to the ones developed after deformation of forsterite during one hour at 1400°C and 11 GPa (see § II.1).

Indeed, TEM shows the same deformation microstructure dominated by [001] dislocations. However, no CPO was produced after one minute of heating in the forsterite deformation experiments. Both grain growth and deformation seem to be strongly enhanced when forsterite is deformed outside its stability field. Although EBSD suggests that only forsterite is present at this stage, TEM observations show many inclusions of wadsleyite (about 0.25 to 1  $\mu\text{m}$  of diameter) which are located inside the forsterite grains or at the grain boundaries (Figure III.30b). Due to the very small size of these inclusions, the crystallographic relationship between forsterite and inclusions could not be established.

After one hour at 1400°C, forsterite is completely transformed into wadsleyite (H1882 and H1945). TEM observations show no remnant forsterite. The wadsleyite grains exhibit deformation microstructures with dislocation densities of about  $10^{13} \text{ m}^{-2}$ . Some [100] dislocations have been identified (Figure III.30c). These dislocations usually appear as straight screw segments in glide configuration.

In samples heated eight hours (S3213 and H1864), we observed many pristine grains. The grains that contain dislocations exhibit the same kind of microstructures as the samples heated one hour. No subgrain boundaries have been observed. It is remarkable that only few stacking faults have been observed in samples deformed one and eight hours. The same observation has been made by Thurel *et al.* (2003a). In contrast, previous TEM observations on deformed wadsleyite (natural occurrence or experimentally deformed) report high densities of stacking faults on (010) (e.g. Price, 1883; Madon and Poirier, 1983; Sharp *et al.*, 1994; Thurel *et al.*, 2003b). The density of stacking faults cannot be related to stress (Dupas-

Bruzek *et al.*, 1998a) but the chemical composition of wadsleyite used in this study as well as the one used by Thurel *et al.* (2003a) (pure magnesium end-member) might be the cause of the low density the stacking faults. As suggested by Thurel *et al.* (2003b), iron could stabilise stacking faults in  $(\text{Mg,Fe})_2\text{SiO}_4$  wadsleyite.

Limited sampling and characterisation precludes any quantitative evaluation of the activity of the various slip systems in those samples. However, TEM clearly shows that the wadsleyite grains experienced plastic deformation during our experiments (despite the phase transformation at the beginning of the experiments). The deformation mechanisms observed are in agreement with previous studies of Thurel *et al.* (2003a; 2003b) with dislocation glide being the dominant deformation mechanism. Our experiments do not support the suggestion of Dupas-Bruzek *et al.* (1998a) that dislocation climb is active in wadsleyite at about 900°C.

EBSD characterisations show formation of CPO in our deformed wadsleyite samples. These CPO are similar in samples deformed one or eight hours (Figure III.27 and Figure III.28). In experiments heated for one hour (H1882 and H1945), the observed CPO is weak. [100] is concentrated close to the shear direction but with dispersion in the shear plane, [010] axes are perpendicular to the shear direction in the shear plane and [001] tend roughly to align toward the normal to the shear plane. In the experiments heated eight hours (H1864 and S3213), the CPO are slightly more pronounced. They display the same general trend than after one hour of heating except H1864 which displays also some alignment of [001] toward the shear direction.

Both the TEM observations and the EBSD characterisations show that we have succeeded in producing CPO of wadsleyite at high pressure and high temperature. However, our samples have experienced a complex history including phase transformations. It is difficult to know how far these phase transformations have overprinted the CPO. In order to clarify this question, CPO simulations based on the microscopic deformation mechanisms have been done and compared them with our experimental data. We have used the same procedure as for forsterite (§II.1.3), VPSC modelling being carried out by Andrea Tommasi and David Mainprice (Laboratoire de Tectonophysique, University of Montpellier, France).

As for olivine, the initial condition is defined by the initial CPO and initial crystal shapes. In the present simulations, the initial CPO is composed of 500 randomly oriented crystals with spherical shape. Lacking information, we assume here implicitly that the phase transformations create no starting CPO. The slip systems of wadsleyite were determined by TEM on polycrystalline specimens deformed in the multianvil apparatus (Thurel and Cordier, 2003a; Thurel *et al.*, 2003b). Several slip systems have been identified, namely:  $[100](010)$ ,  $[100](001)$ ,  $[100]\{011\}$ ,  $[100]\{021\}$ ,  $^{1/2}\langle 111 \rangle\{101\}$ ,  $[010](001)$ ,  $[010]\{101\}$ , and  $\langle 101 \rangle(010)$ . However, dislocations with large Burgers vectors ( $[010]$  and  $\langle 101 \rangle$ ) are likely to be nucleated in multianvil deformation experiments during cold compression, due to high deviatoric stress levels reached during this stage of the experiments (as previously discussed in § I.2.2). Indeed, Thurel *et al.* (2003b) have suggested that in shear deformation experiments, only the  $[100]$  and  $^{1/2}\langle 111 \rangle$  slip systems dominate deformation at high-temperature.

Although stress and strain-rate are significantly decreasing with time in those experiments, Thurel *et al.* (2003b) have shown that there is no detectable change in the slip system activity for times over eight hours. There is no mechanical data on wadsleyite single-crystals that would provide constraints on the relative strength of these slip systems (CRSS). TEM observations showing similar densities of [100] and  $\frac{1}{2}\langle 111 \rangle$  dislocations suggest as a first approach similar activities for those slip systems. Without more precise information, a series of VPSC simulations have been performed varying the relative CRSS for  $\frac{1}{2}\langle 111 \rangle$  and [100] slip systems with a maximum ratio of 1:5 (or 5:1) (Table IV.2) and for shear strains up to 1. Similarly, we lack specific information on strain hardening in wadsleyite. This parameter has been neglected in a first approach. Stress exponents are also unknown. Similarly to previous simulations in olivine, a value of  $n=3$  is used in all models. Indeed, VPSC simulations are not very sensitive to  $n$  values between 3 and 5 and almost all minerals have stress exponents in this range; the main effect of increasing  $n$  is an enhancement of the CPO for a given finite strain.

**DISCUSSION**

	[100]				<111>{101}
	(001)	[100](010)	[100]{011}	[100]{021}	
model 1	1	1	1	1	1
model 2	1	5	5	5	1
model 3	1	5	5	5	5
model 4	2	5	5	5	1

*Table IV.2 – Slip systems and relative critical resolved shear stresses used in the simple shear simulations.*

For all models (Figure IV.7), the [100] axes tend to form a girdle in the shear plane, with a clear maximum close to the shear direction and the [001] axes are distributed in a girdle at high angle to the shear direction, with a clear maximum roughly normal to the shear plane. Both maxima are slightly oblique ( $<20^\circ$  for a shear strain of 0.5) to the macroscopic shear, in conformity with the imposed dextral shear.

With increasing shear strain, the [100] axes tend to parallel the shear direction, while the [001] axes remain slightly oblique to the normal to the shear plane.

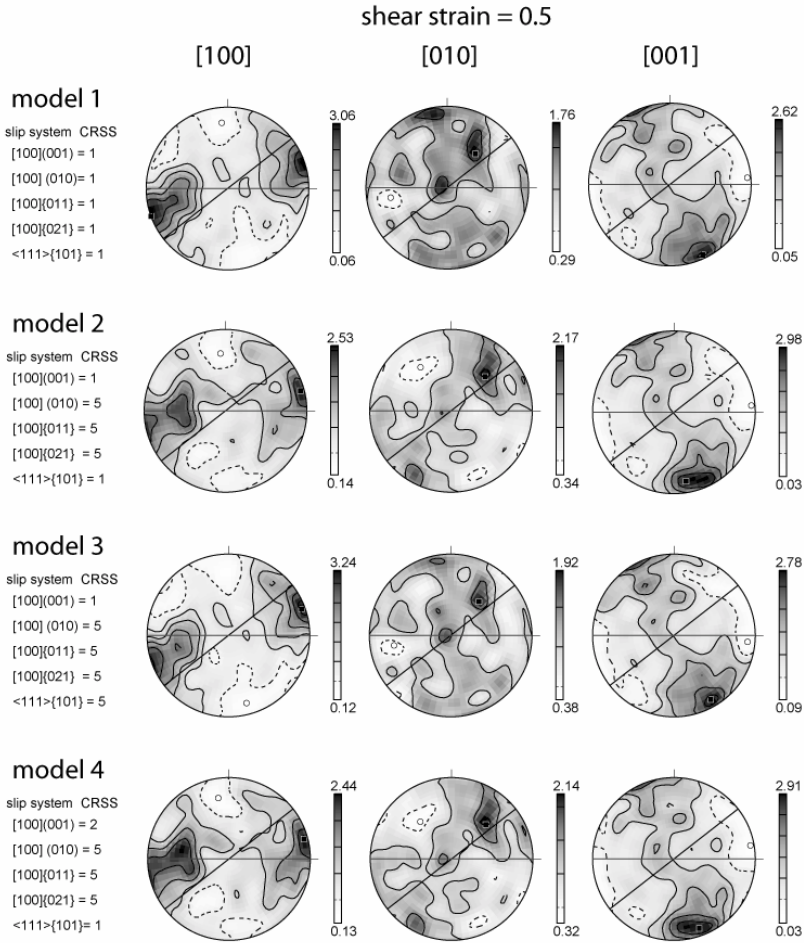


Figure IV.7 – Crystal preferred orientations of wadsleyite predicted by VPSC modelling. Critical resolved shear stresses for [100] and  $\frac{1}{2}\langle 111 \rangle$  slip systems used in model 1 to 4 are reminded on the left side of each pole figure. Lower hemisphere equal-area projections, contours at intervals of 0.5 multiple of a uniform distribution. Dextral shear sense. Shear direction is horizontal (gray line), foliation (flattering plane) in black line. Shear strain : 0.5

Varying the CRSS and, hence, the activity of the different slip systems (Figure IV.8) mainly modifies the strength of the [100] and [001] maxima. High activity of [100] systems, as observed in models 1 and 3 in which, altogether, these systems accommodate ca. 55% and 60% of the total strain respectively, lead to stronger concentrations of the [100] axes relative to [001] and [010]. On the other hand, dominant slip on  $\frac{1}{2}\langle 111 \rangle\{101\}$ , as observed in models 2 and 4 (ca. 65 %), results in similar concentrations for all three axes. The main difference between these models is found for the [010] axes distribution. High activity of [100] slip systems (models 1 and 3) results in a girdle distribution of [010] normal to the shear direction with weak maxima both normal and within the shear plane. Dominant activity of  $\frac{1}{2}\langle 111 \rangle\{101\}$  results, in contrast, in a girdle distribution of [010] roughly parallel to the foliation with weak maxima at ca. 10-30° to the shear direction.

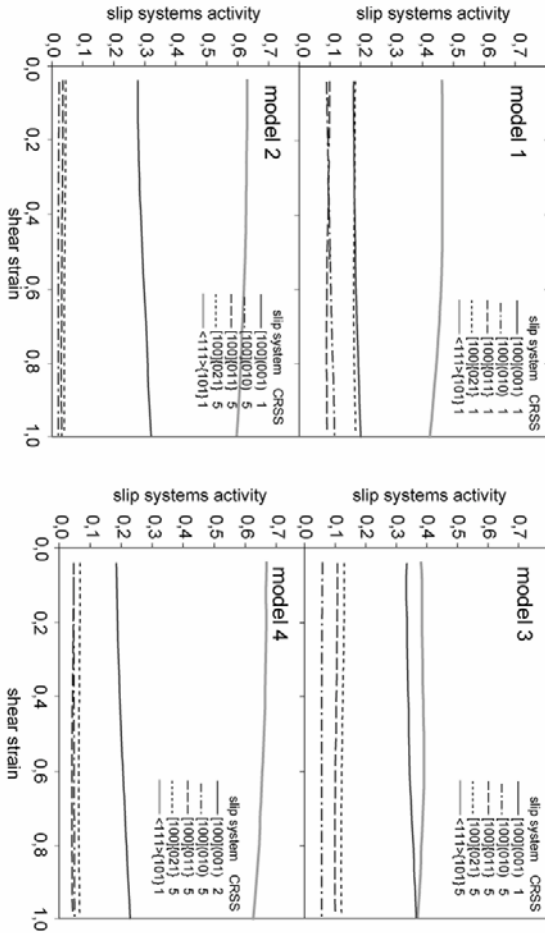


Figure IV.8 – VPSC modelling of plastic deformation of wadsleyite: slip systems activities as a function of strain for the various models.

None of these simple shear models can satisfactorily reproduce our experimental wadsleyite CPO (Figure III.27 and Figure III.28). In particular, the concentration of  $[010]$  normal to the shear direction within the shear

plane observed in the experimentally deformed wadsleyite differs from VPSC models. Several possibilities can be put forward to account for this discrepancy. The first one is the influence of the back transformation of wadsleyite in forsterite at the beginning of the experiments. Preferred orientations can result from wadsleyite nucleation under stress. The assumption of a random starting grain distribution would thus be erroneous. Alternatively, this discrepancy might point to an insufficient understanding of the elementary deformation mechanisms of wadsleyite. However, it is important to note that beyond these differences, some features are always present in the simulated CPO (whatever the model) that are common to the experimental ones: the alignment of [100] toward the shear direction and of [001] toward the normal to the shear plane. Our study suggests that these features are robust characteristics of wadsleyite CPO. They will be used to calculate seismic properties presented below (§III.2).

### II.2.1.2 - Influence of the forsterite → wadsleyite phase transformation

It is legitimate in mineral physics to design simple experiments which focus on a single mechanism. For that reason, the back-transformation of wadsleyite in olivine was not desired as it is likely to overprint the measured CPO in an uncontrolled manner. However, it must be remembered that the transition zone is a complex region of the interior of the Earth where both convection and phase transformations are likely to take place. The interplay between plastic deformation and phase transformations is complex. There is no general framework and specific features of each system are likely to be important. It is thus difficult to

withdraw information on studies carried out on metals, ceramics, or ice (e.g. Kot and Weiss, 1970; Johnson *et al.*, 1975; Zamora and Poirier, 1983; Dunand *et al.*, 2001; Taleb *et al.*, 2001). Surprisingly, and despite a strong potential interest, little attention has been given up to now to this topic. To study the influence of the phase transformation on plastic deformation at the forsterite–wadsleyite transition, we have performed a series of specific experiments in which forsterite samples have been brought and sheared in the wadsleyite stability field (see Chapter III, §IV).

For these experiments (S3252, S3412 and S3254) hot-pressed forsterite samples have been used as starting material. The samples have been loaded at pressures corresponding to the wadsleyite stability field and heated at 1400°C during thirty minutes (S3253), forty five minutes (S3412) and one hour (see Figure III.35). Raman spectroscopy allowed us to determine the phases of the recovered samples. After thirty minutes at 1400°C, the sample is still made of forsterite (S3253) although TEM showed that nucleation of wadsleyite has already occurred. Complete transformation of forsterite occurs between thirty and forty five minutes of heating at 1400°C and 16.5 GPa. The SEM pictures of those three experiments (Figure III.37) show roughly equilibrated grains with heterogeneous grains size. The grains size decreases after the phase transformation forsterite–wadsleyite to increase for longer heating times of the wadsleyite sample.

The orthorhombic CPO of the forsterite sample (Figure III.39) is similar to those obtained on forsterite deformed at 11 GPa, 1400°C during one hour (Figure III.7) and which have been defined as characteristic of

[001] glide (see § II.1.1). The observation of this CPO in sample S3253 demonstrates that phase transformation to wadsleyite starts from deforming forsterite. After phase transformation, the CPO developed in wadsleyite are similar to those previously reported in wadsleyite deformed at 16 GPa at 1400°C during one and eight hours (Figure III.27 and figure III.28). Once again, the relative contributions to the CPO of phase transformation under stress and subsequent plastic deformation cannot be separated.

TEM observations of the forsterite sample (S3253) show wadsleyite inclusions (Figure III.40). The phase transformation already starts after thirty minute of heating at 1400°C. The inclusions either nucleate inside the grains or at the grains boundaries. No systematic crystallographic relationships could be evidenced between forsterite and wadsleyite inclusions (Table III.12). For instance, inclusions 1 and 2 from Figure III.40 and Table III.12, are inside the same forsterite grain; however, they do not display the same orientations. Moreover, no connection has been made between the dislocations gliding in forsterite (mainly straight [001] screw dislocations, Figure III.40c) and the inclusions. The transformation from forsterite to wadsleyite occurs by nucleation and growth of incoherent precipitates. This mechanism has been observed in previous works studying the transformation mechanism under quasi hydrostatic pressure (e.g. Guyot *et al.*, 1991; Brearley *et al.*, 1992; Brearley and Rubie, 1994). There seems to be no significant influence of strain on wadsleyite nucleation.

We have seen that precise determination of strain is difficult in shear deformation experiments. This is even more the case here because

the shape of the strain marker is so much altered by the phase transformation that it cannot be used, even for a rough estimate. The change in thickness of the samples after transformation is compatible with the volume reduction at the forsterite-wadsleyite transformation and is not large enough to suggest large shears (Table III.11). This is compatible with the wadsleyite grain shapes which do not exhibit marked flattening or elongation (Figure III.37). Moreover, the relative displacement of the pistons does not indicate strains significantly larger than for our other experiments. Finally, even in the absence of reliable quantitative measurements, our results do not suggest that the forsterite-wadsleyite phase transformation strongly enhance the plasticity of the aggregate. Along the same line, we have seen (Figure III.25) that some grain size reduction is associated with the phase transformation at the forsterite-wadsleyite transition. However, it must be noted i) that this grain-size reduction is modest, ii) that very rapidly (on the hour scale), the original grain size is recovered. Phase transformation is sometimes invoked as one of the mechanisms for grain size reduction in the mantle with the possibility, at phase boundaries, to have very small grain sizes with possible implications on the rheology (superplasticity) (e.g. Karato, 1995; Riedel and Karato, 1997). Our observations do not support this hypothesis at the forsterite-wadsleyite transition.

### II.2.2 – Deformation of ringwoodite at 22 GPa and 1300°C

As for wadsleyite, it is only recently that plastic deformation have been made possible in the pressure-temperature stability field (18-24 GPa at 1300°C) of ringwoodite (e.g. Chen *et al.*, 1998; Karato *et al.*, 1998; Kavner

and Duffy, 2001; Thurel, 2001; Cordier *et al.*, 2002; Kavner, 2003; Xu *et al.*, 2003; Wenk *et al.*, 2004). None of these studies provide a crystallographic preferred orientation of ringwoodite at high pressure and temperature.

Our goal in this study has been to provide CPO of ringwoodite at 22 GPa and 1300°C in shear configuration in order to contribute to constrain of the forward seismic modelling of the transition zone.

Pre-synthesised ringwoodite has been deformed in a shear deformation assembly at 22 GPa and 1300°C. This temperature has been chosen slightly lower than with forsterite and wadsleyite experiments due to the shape in the pressure-temperature space of the ringwoodite stability field (see Figure 8). A first experiment (Z367) has been held one minute at 1300°C after the temperature ramp of about 12-15 minutes. Phase characterisation performed on recovered sample indicates that the sample is still made of ringwoodite (Figure III.31). The back-transformation observed with wadsleyite did not occur here. The second experiment (Z341) has been heated for 3 three hours at 1300°C.

The EBSD characterisations show that both samples display CPO (Figure III.33). After one minute of heating, the CPO is not very well developed although some alignment of  $\langle 110 \rangle$  toward the normal to the shear plane can be noticed. After three hours, the CPO is more developed with the  $\langle 100 \rangle$  axes concentrated in the shear direction and the  $\langle 110 \rangle$  axes aligned toward the normal to the shear plane and. This type of CPO would suggest  $\langle 100 \rangle \{110\}$  slip systems as dominant. The few TEM investigations (Figure III.34) performed so far cannot support this assumption.

The CPO observed in this study, after three hours of heating, is not also comparable to the one observed in fcc materials (Siemes and Hennig-

Michaeli, 1985; Merkel *et al.*, 2002; Yamazaki and Karato, 2002; Heidelbach *et al.*, 2003). Those CPO are characterised by the  $\langle 110 \rangle$  axes aligned parallel to the shear direction (normal to the compression axis) and the  $\langle 111 \rangle$  axes are normal to the shear plane. Moreover, a very recent *in situ* observation of ringwoodite CPO developed in DAC between 20 and 50 GPa at room temperature shows that the  $\langle 110 \rangle$  align with the normal to the compression axis (Wenk *et al.*, 2004), pointing toward  $\langle 110 \rangle$  glide as dominant. Previous TEM investigation on ringwoodite (Madon and Poirier, 1983; Karato *et al.*, 1998; Thurel, 2001), on spinel structures (e.g. Mitchell *et al.*, 1976; Veyssi re *et al.*, 1978; Dupas-Bruzek *et al.*, 1998b; Mitchell, 1999) show that  $\frac{1}{2} \langle 110 \rangle$  is the shortest perfect Burger vector and the most commonly observed and generally gliding on  $\{111\}$ ,  $\{110\}$  or  $\{100\}$  (less observed).

As for forsterite and wadsleyite, the experimental CPO are compared with those simulated by VPSC (David Mainprice and Andrea Tommasi, Laboratoire de Tectonophysique, University of Montpellier, France). The initial conditions are defined by the initial CPO and initial crystal shapes. In the present simulations, the initial CPO is composed of 1000 randomly oriented crystals with spherical shape. There is no mechanical data on ringwoodite single-crystals that would provide constraints on the relative strength of the slip systems (CRSS). Without more precise information, VPSC simulations have been performed with the equal relative CRSS for:  $\frac{1}{2} \langle 110 \rangle \{111\}$ ,  $\frac{1}{2} \langle 110 \rangle \{110\}$  and  $\frac{1}{2} \langle 110 \rangle \{100\}$  slip systems observed in previous studies (Table IV.3) and VPSC simulations have been performed with the relative CRSS for:  $\frac{1}{2} \langle 110 \rangle \{111\}$ ,

**DISCUSSION**

---

$\frac{1}{2}\langle 110 \rangle \{110\}$ ,  $\frac{1}{2}\langle 110 \rangle \{100\}$  and  $\langle 100 \rangle \{110\}$  slip systems with a ratio of 2:1 (Table IV.3). Note that the slip system  $\langle 100 \rangle \{110\}$  has never been observed in ringwoodite. The maximum shear strain is 2 (Figure IV.9).

	$\frac{1}{2}\langle 110 \rangle \{111\}$	$\frac{1}{2}\langle 110 \rangle \{110\}$	$\frac{1}{2}\langle 110 \rangle \{100\}$	$\langle 100 \rangle \{110\}$
model 1	1	1	1	Not used
model 2	2	2	2	1

*Table IV.3 – Slip systems and the relative resolved shear stresses used in the simple shear simulations.*

Similarly to wadsleyite, lacking specific information on strain hardening in ringwoodite, this parameter has been neglected in a first approach. A stress exponents  $n=3$  is used in all models.

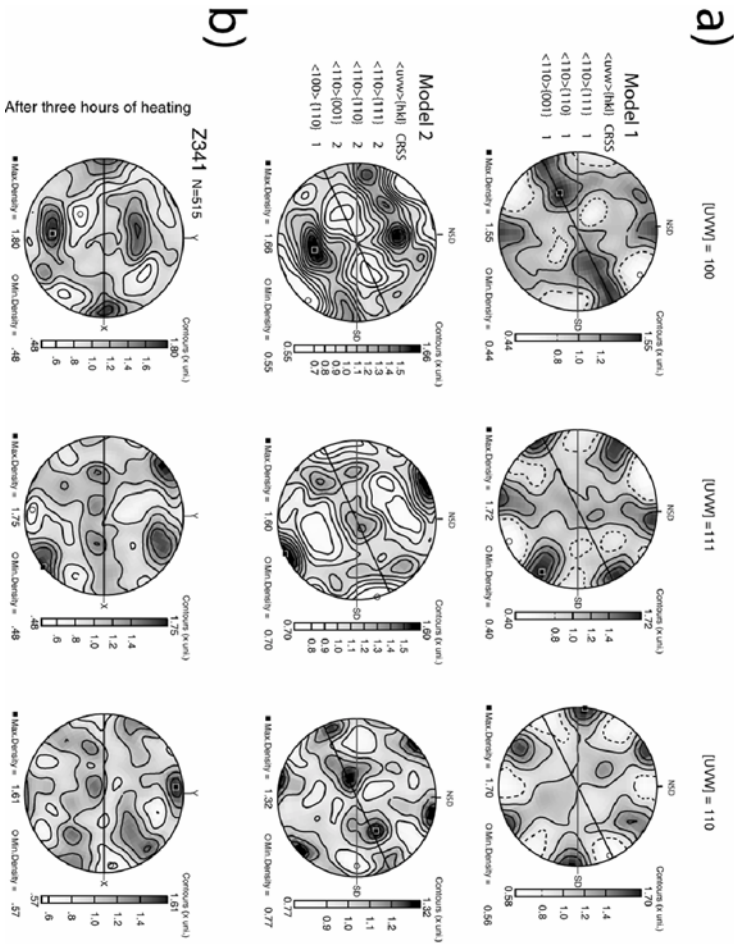


Figure IV.9 – a) Crystal preferred orientations of ringwoodite predicted by VPSC modelling. Critical resolved shear stresses and slip systems used in model 1 to 2 are reminded on the left side of each pole figure. Lower hemisphere equal-area projections, contours at intervals of 0.5 multiple of a uniform distribution. Dextral shear sense. Shear direction is horizontal (gray line), foliation (flattening plane) in black line. Shear strain :2

b) For comparison, EBSD pole figure of crystal axis for ringwoodite sample (Z341) after three hours of heating (from Figure III.34).

The CPO simulated with the model 1 shows that  $\langle 111 \rangle$  displays a six-fold symmetry pattern; one maximum is normal to the shear plane and the two others are at ca.  $45^\circ$  from the shear.  $\langle 110 \rangle$  displays also a six-fold symmetry pattern with one maximum aligned with the shear direction and the two others at ca.  $45^\circ$  from the normal to the shear plane.

The CPO simulated with the model 2 is different. The  $\langle 100 \rangle$  axes present two maxima; one in the shear direction and one normal to the shear direction at low angle (ca.  $30^\circ$ ) from the shear plane.  $\langle 110 \rangle$  displays a maximum at low angle of the normal to the shear plane and a girdle aligned in a plane at low angle from the shear plane.  $\langle 111 \rangle$  displays a six-fold symmetry pattern; one maximum is normal to the shear plane and the two others are at ca.  $45^\circ$  from the shear.

The model 1 does not display common features with the experimental CPO of ringwoodite (Figure IV.10b, Z341), even at higher shear strain or with various relative CRSS. The introduction of  $\langle 100 \rangle \{110\}$  slip system in the modelling is necessary to reproduce this kind of CPO. However, no TEM observation has report the existence of this slip system in ringwoodite. No accurate CPO of ringwoodite developed at high pressure and temperature can be proposed.

### II.3 – Main conclusions on the deformation in the Mg<sub>2</sub>SiO<sub>4</sub> system

During this experimental study, we have shown that forsterite deforms at 11 GPa and 1400C by dislocation glide and that pressure induces a major change in the dominant slip systems. At high pressure, [001] glide becomes dominant compared to [100] glide usually observed at lower pressure. The transition pressure still needs to be constrained. Dislocation glide is also an important deformation mechanism for wadsleyite and ringwoodite at high pressure and high temperature. Deformation experiments performed on ringwoodite show that the back-transformation observed with wadsleyite is not systematic. Despite no completely reliable CPO has been obtained in wadsleyite, some robust characteristics came out of our deformation experiments and of the CPO simulations. The difficulty to relate macroscopic strain features like CPO with microscopic strain (active slip systems) is well illustrated with ringwoodite. Our understanding on the elementary deformation mechanisms and/or our modelling of the plasticity of aggregates is not sufficient to account for experimental CPO. The important question of the crystallographic preferred orientation of ringwoodite is still open. Therefore the three-dimensional distribution of seismic velocity cannot be calculated for the lower part of the transition zone based on mineral physics data. Finally, it must be noted that, although we lack quantitative measurements of rheological parameters in this study, our macro- and microstructural investigations do not suggest a large rheological contrast between forsterite and its high pressure polymorphs.

### III - Implications for seismic anisotropy of the Earth's upper mantle and the transition zone

One of the major causes of seismic anisotropy is the crystal preferred orientation caused by plastic deformation. This information is very important as crystallographic preferred orientations are likely to record some aspects of the deformation history of the mantle. In the present section, the information gained on the CPO of forsterite and wadsleyite are used for modelling seismic anisotropy in the mantle.

#### III.1 Pressure sensitivity of olivine slip systems: implications of the seismic anisotropy of the lowermost upper mantle

The relationship between seismic anisotropy and CPO of olivine is well established in an upper mantle deforming by dominant [100](010) slip, system traditionally used in relating flow and anisotropy of physical properties in the mantle down to 250 km depth (e.g. Silver, 1996; Tommasi, 1998). [100](010) slip produces CPO characterized by [100] aligned toward the flow direction, [010] normal to the flow plane. This type of CPO has been often observed in nature and experiments e.g. Nicolas *et al.*, 1973; Zhang and Karato, 1995; Ben Ismail and Mainprice, 1998; Ben Ismaïl *et al.*, 2001) as well as in numerical simulations (e.g. Tommasi *et al.*, 1999; Wenk and Tomé, 1999; Tommasi *et al.*, 2000). It may produce a strong seismic anisotropy with fastest propagation of compressional waves parallel to the

concentration of olivine [100] axes, i.e. parallel to the shear direction, and slowest velocities parallel to the [010] maximum, i.e. normal to the shear plane. It also results in shear wave splitting. The polarisation of the fast split shear wave is primarily controlled by orientation of the olivine [100] axes and the maximal delay times are observed for shear waves propagating at high angle to both the [100] and [010] axes.

The shear experiments on forsterite aggregates at 11 GPa and 1400°C, conditions equivalent to those at depths of 330 km, have exhibited a change in deformation mechanism induced by pressure from [100] glide to [001] glide (§II.1). CPO resulting of dominant activation of [001] glide is characterized by the concentration of [001] parallel to the shear direction and of [100] and [010] normal to the shear plane (Figure III.7). Dominant [001] slip in the lowermost upper mantle requires re-evaluation of the interpretation of anisotropic physical properties.

The pressure, or pressure interval, at which the transition from [100] to [001] slip occurs is an important parameter. Our D-DIA experiments show activation of both [100] and [001] slip and suggest a progressive transition. *In situ* deformation experiments performed by Paul Raterron and co-workers give an indication on the crossover between [100](010) and [001](010) slip. Under laboratory conditions, this crossover takes place at about 7 GPa (Figure IV.3). The rheological laws derived by Raterron and co-workers suggest that, under mantle conditions, this change in deformation mechanisms might occur at greater depths: 300–350 km. It must be remembered however that several [001] slip systems contribute to the deformation of a polycrystalline aggregate. Among them, [001]{110} seems to be more important than [001](010) or [001](100). Further studies

should focus on these slip systems to clarify this issue. Constraints on the minimum depth for this transition may be derived from the analysis of olivine CPO patterns in naturally deformed mantle rocks (Ben Ismail and Mainprice, 1998). Spinel-peridotites that are equilibrated above 70 km depth, display solely CPO characteristic of [100] slip. This CPO is also dominant in high-pressure garnet-peridotites from South Africa equilibrated between 70 and 150 km (Ben Ismail *et al.*, 2001). CPO suggesting activation of both slip directions at high-temperature conditions is restricted to rare high-pressure peridotite mylonites from the Tanzanian and Kaapvaal cratons equilibrated at ca. 140 km depth (Vauchez *et al.*, 2003). This suggests that [100] slip dominates in the mantle above 150 km depth

Several lines of evidence point to seismic anisotropy decreasing with depth in the upper mantle. Most global one-dimensional models (PREM, IASP, AK135 and AK303) show horizontally propagating P waves ( $V_{PH}$ ) faster than vertical ones ( $V_{PV}$ ) (Figure IV.10), but the difference in velocity reduces with depth, resulting in isotropic behaviour at 350 km (Montagner and Kennett, 1996). Some models (AK135 and 303) even show  $V_{PV}$  slightly faster than  $V_{PH}$  below 350 km. The S wave polarisation anisotropy also decreases monotonically from the surface to become isotropic at 250 km. For horizontally-propagating S waves, horizontally polarised ( $V_{SH}$ ) waves show a higher velocity than vertically polarised ( $V_{SV}$ ) waves down to about 250 km. Between 300 km and 400 km  $V_{SV}$  is higher than  $V_{SH}$ , but anisotropy is five times lower than in the uppermost mantle. High-resolution global tomographic models based on S wave data (Ekstrom and Diewonski, 1998) or on the inversion of three-component surface and body waveform data (Gung

*et al.*, 2003) support these general findings with strong anisotropy characterized by  $V_{SH} > V_{SV}$  above 250 km depth. At greater depth, these models require a strong decrease in anisotropy with a minimum around 300 km depth. S wave data also call for weak anisotropy with  $V_{SV} > V_{SH}$  at the base of the upper mantle beneath the central Pacific and Pre-Cambrian cratons (Ekstrom and Diewonski, 1998).

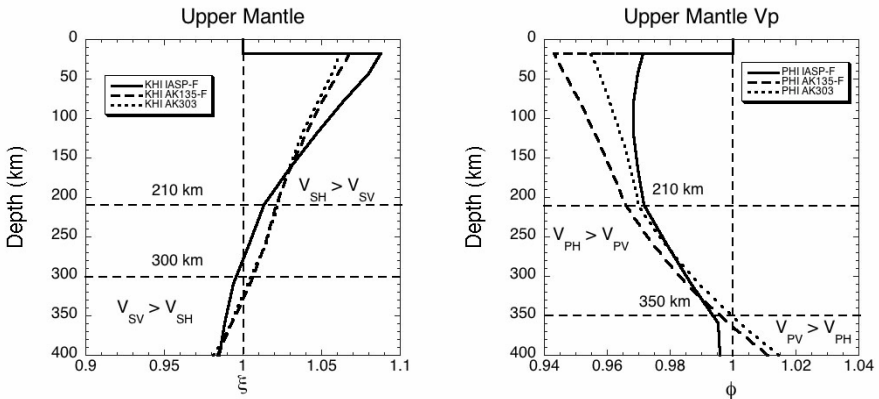


Figure IV.10 – Evolution with depth of the shear wave polarisation anisotropy (left) and of the compressional wave propagation anisotropy (right) in global one-dimension velocity models (courtesy of J.P. Montagner)

Regional surface waves studies in the Pacific and Indian ocean basins also suggest that anisotropy is present from the surface to ca 250–300 km with  $V_{SH}$  being greater than  $V_{SV}$  (Montagner, 1985; Cara and L ev eque, 1988; Nishimura and Forsyth, 1989; L ev eque *et al.*, 1998). Analysis of two-station surface wave profiles in the Pacific and Philippine plates imply a still shallower anisotropy limited to upper 160 km of the mantle (Gaherty *et al.*, 1996. SKS studies cannot constrain the depth of the

anisotropic layer, but the strong correlation of the direction of polarization of the fast shear wave with the surface geology and delay times  $\leq 2$ s (Silver, 1996) suggest that SKS splitting occurs in the upper 200–250 km of the mantle.

Finally, a regional seismic discontinuity, the Lehmann discontinuity (Lehmann, 1955), has been detected at about 220 km by various seismic methods (reflection, surface waves, ScS reverberations and P to S conversions) mainly beneath continents. This discontinuity has been interpreted as due to either a strong anisotropy caused by intense deformation of olivine in a zone of mechanical coupling between the lithosphere and the asthenosphere (Revenaugh and Jordan, 1991) or to the transition between an anisotropic uppermost mantle deforming by dislocation creep, which produces a CPO of olivine, and an isotropic deep mantle deforming by diffusion creep, which does not produce CPO (Karato, 1992). However, the results of the deformation experiments made in this study on forsterite at 11GPa and 1400°C as well as recent high-pressure, high-temperature experiments (Li *et al.*, 2003; Li *et al.*, 2004) show that even in fine-grained aggregates ( $\sim 20$ – $30 \mu\text{m}$ ), dislocation creep is the dominant deformation mechanism under conditions equivalent to those prevailing at 300 km depth.

The three-dimensional distribution of seismic velocities in a polycrystalline aggregate may be estimated by averaging the individual grain elastic constants tensors as a function of the crystallographic orientations and mineralogical composition of the aggregate. This calculation has been made by David Mainprice and Andrea Tommasi (Laboratoire de

Tectonophysique, University of Montpellier, France). Seismic properties (Figure IV.11) of an upper mantle sample with pyrolitic composition (63% olivine, 17% garnet, 20% clinopyroxene) at a pressure of 11.8 GPa and temperature of 1380 °C, corresponding to 355 km depth, were calculated using recent elastic constants tensors of olivine (Abramson *et al.*, 1997), pyrope-rich garnet (Chai *et al.*, 1997), diopside (Collins and Brown, 1998). For olivine CPO, the simulated CPO performed in § II.1.3 has been used as it takes in account the dominant activity of [001] glide at high pressure and temperature (Figure IV.5). Garnet has a random CPO, in agreement with predictions of VPSC simulations and observations in naturally-deformed garnet-rich rocks that show that garnet CPO are always very weak (Mainprice *et al.*, 2004). We have assumed that diopside also has a random orientation as high-pressure data is lacking for this mineral. However, if diopside has a CPO similar to the one developed under high temperature and low pressure conditions (Bascou *et al.*, 2002), it will tend to reduce anisotropy by destructive interference with olivine (Mainprice *et al.*, 2000).

In Figure IV.12, both compressional and shear waves display weak anisotropies: 0.9% and 1.9% respectively. The fastest compressional waves propagate at a high angle to the shear plane. The variation of compressional waves velocities within the shear plane (SD) is very small. Thus in a mantle deforming by horizontal shearing almost no azimuthal variation of  $V_P$  would be observed and vertically propagating P waves would be only slightly faster than horizontal ones. Shear waves polarization anisotropy is characterized by faster propagation of waves polarized at high angle to the shear plane and the largest delay times are observed for propagation oblique to the shear direction and shear plane. For propagation in the shear plane the fastest S

waves are polarised normal to the shear plane. Hence, for horizontal flow,  $V_{SV}$  is greater than  $V_{SH}$ .

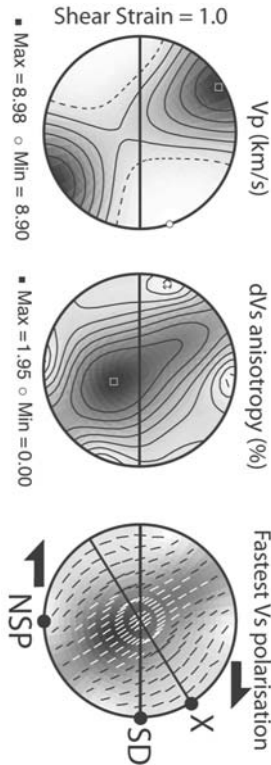


Figure IV.11 – Modelled three-dimensional compressional waves velocity and shear wave anisotropy distribution, and fastest wave polarisation for an aggregate composed of 63% of anisotropic olivine, 17% of isotropic garnet and 20% of isotropic diopside at 11.8 GPa, 1380°C and with shear strain of 1. Shear sense is dextral. Lower hemisphere equal-area projections, contours at 0.1 km/s intervals for compressional waves, 0.02 km/s intervals for shear waves and 0.5% anisotropy intervals for shear wave polarisation anisotropy. Maximum P wave and S wave anisotropy is 0.9% and 1.9% respectively. The black line represents the shear plane.

All the predictions deriving from our experiments are consistent with global and regional seismic observations (Montagner, 1985; Cara and L ev eque, 1988; Nishimura and Forsyth, 1989; Montagner and Kennett, 1996; Ekstrom and Diewonski, 1998; L ev eque *et al.*, 1998; Gung *et al.*, 2003) that show a weak anisotropy (<2%) below 250 km for P and S waves. The predicted S-wave anisotropy, although weak, at 1.9%, is twice as strong as the anisotropy for P waves as observed in global models (Montagner and Kennett, 1996). Anisotropy patterns observed in global models (transverse isotropy with a vertical symmetry axis) are best reproduced for horizontal shearing. For such a flow pattern, our simulations predict that vertical P waves propagate faster than horizontal ones and that for horizontally propagating S waves  $V_{SV}$  is greater than  $V_{SH}$ , in agreement with global models anisotropy patterns for depths greater than 300 km. In addition, vertically propagating shear waves will detect no anisotropy.

To conclude, the dominant activity of [001] glide in forsterite at high pressure is entirely compatible with the available seismic data indicating a weak anisotropy of the upper mantle below 300 km. It is difficult to imagine another scenario that would reproduce the P and S waves anisotropy patterns in such detail. The interpretation presented here allows one to consider that the weakly anisotropic upper mantle below 250 km is actively deforming by dislocation creep and hence may be strongly coupled up to 400 km depth. The hypotheses that regions in the deep Earth of weak seismic anisotropy should be interpreted as zones of poor coherence of the deformation at the seismic length scale, or that the dominant deformation mechanism (for example diffusion creep (e.g. Karato, 1992; Karato *et al.*, 1993)) does not produce CPO are challenged by our predictions for olivine-

rich aggregates deforming by [001] glide in the deep upper mantle. Indeed, transition from dominant [100] to [001] glide at high pressure may explain the variation with depth in P and S waves anisotropy patterns even if the entire upper mantle deforms coherently with a dominant horizontal shearing component as expected in a convective system with large-scale plates at the surface, like the Earth's mantle.

### III.2 - Predicting strain-induced seismic anisotropy in the upper part of the transition zone

As shown in § II.2.1.1, the issue of CPO in wadsleyite is still to be solved. Neither the experimental CPO nor those simulated by VPSC can be considered as fully reliable. However, we have seen that some features are common to both CPO: the alignment of [100] toward the shear direction and of [001] toward the normal to the shear plane. These features can be regarded, as a first approach, as robust characteristics of wadsleyite CPO. A first attempt to constraint the seismic anisotropy properties of the upper part of the transition zone has been done based on this assumption.

As for olivine, the three-dimensional distribution of seismic velocities (Figure IV.12) of an aggregate composed of 100% wadsleyite (Figure IV.7, model 2) and of an upper transition zone aggregate of pyrolytic composition (60% wadsleyite (Figure IV.7 model 2) and 40% garnet) have been calculated using recent elastic constants tensors of wadsleyite (Zha *et al.*, 1997; Sinogeikin *et al.*, 1998) and of pyrope-rich garnet (Chai *et al.*, 1997). As for the upper mantle, we assume that garnet CPO are always very

weak (Mainprice *et al.*, 2004). Moreover, garnet is nearly elastically isotropic and its main contribution is to dilute the rock anisotropy. This can be observed in Figure IV.12, where we can easily observe that the difference between the seismic velocity distribution of an aggregate 100% wadsleyite and of an aggregate 60% wadsleyite - 40% garnet is the intensity of anisotropy. Since temperature-dependences of wadsleyite elastic constants were not known, seismic properties were evaluated for transition zone pressures, but ambient temperature.

In Figure IV.12, both compressional and shear waves display weak anisotropies, 2.4% and 1%, respectively for the aggregate with pyrolytic composition. Compressional waves that propagate within the shear plane are faster than those travelling normal to it, the fastest velocities being observed for waves propagating at low angles to the shear direction. Shear waves polarization anisotropy is characterized by faster propagation of waves polarized at low angles to the shear direction (SD) and the largest delay times are observed for propagation within the shear plane at high angle to the shear direction. A roughly isotropic behaviour should be recorded by shear waves propagating either at low angle to the shear direction or normal to the shear plane (NSP). Shear waves azimuthal anisotropy is characterized by faster propagation at low angles to the shear direction independent of polarization. However, shear waves polarized at low angles to the shear direction (S1) display a roughly transverse isotropic pattern with a slow symmetry axis at high angle to the shear plane, whereas those polarized normal to the shear direction show a fast symmetry axis at low angle to the shear direction. Thus, shear waves propagating within the shear plane display high velocities for propagation directions parallel to the shear

direction for both polarizations, but the fastest waves (S1), which are polarized at low angles to the shear direction, display almost no azimuthal anisotropy, whereas the slowest waves (S2) show maximum anisotropy (1%). In contrast, for propagation normal to the shear direction, shear waves polarized parallel to the shear direction (S1) show maximum azimuthal anisotropy; whereas those polarized normal to it (S2) show no azimuthal anisotropy. In agreement with the small differences observed between the modelled wadsleyite CPO using different CRSS values (§II.2.1.1 and Figure IV.7), the same type of three-dimensional distribution of seismic velocity can be observed whatever the model taken into account.

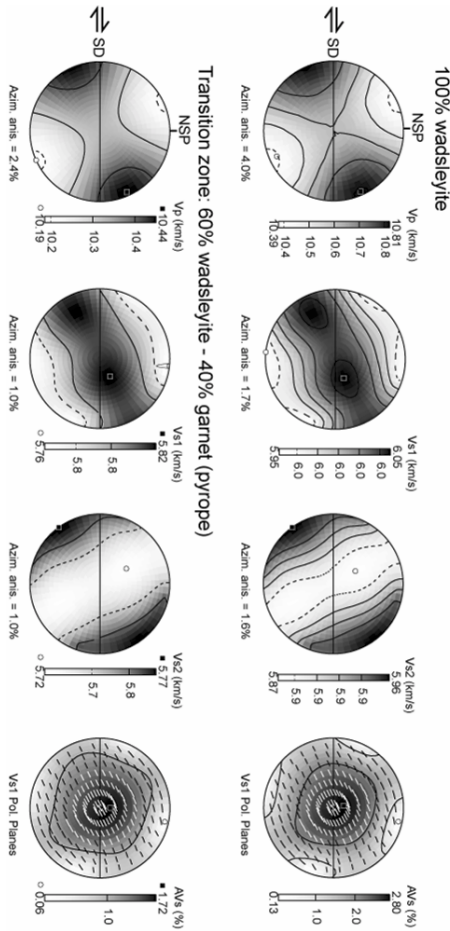


Figure IV.12 – Modelled three-dimensional compressional and shear wave velocity distribution and fastest wave polarisation for an aggregate composed of 110% of wadsleyite and an aggregate composed of 60% of anisotropic wadsleyite and 40% of isotropic garnet. Shear strain of 1. Shear sense is dextral. Lower hemisphere equal-area projections, contours at 0.1 km/s intervals for compressional waves, 0.02 km/s intervals for shear waves and 0.5% anisotropy intervals for shear wave polarisation anisotropy. The black line represents the shear plane.

The three-dimensional distribution of seismic velocities has been also estimated from the experimentally deformed wadsleyite, in which the orientation of the [010] axes differs of the modelled CPO (Figure IV.13). The calculation has been done on S3254 (sample coming from the series about the influence of forsterite-wadsleyite transition). Equivalent distribution would be found for all experimental wadsleyite CPO of this study.

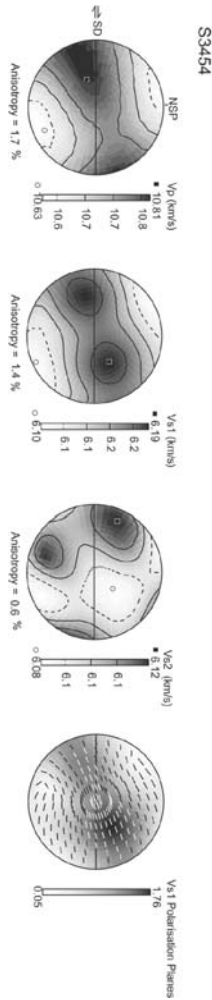


Figure IV.13\_– Three-dimensional compressional and shear waves velocity distribution and fastest wave polarisation from CPO of S3454 deformed at 16.5 GPa and 1400°C. Shear sense is dextral. Lower hemisphere equal-area projections, contours at 0.1 km/s intervals for compressional waves, 0.02 km/s intervals for shear waves and 0.5% anisotropy intervals for shear wave polarisation anisotropy. The black line represents the shear plane.

Comparing this distribution with the modelled distribution presented in Figure IV.12, we can notice that they share strong similarities. The main difference is in the P wave propagation which is now fastest at ca.  $40^\circ$  to the shear direction within the shear plane. In both case, horizontal propagation is still faster than in vertical direction. Shear wave splitting patterns are also similar, with faster propagation of horizontally-polarized shear waves. Very weak anisotropy is sampled by vertically-propagating shear wave. Therefore, the difference between CPO developed after the phase transformation forsterite-wadsleyite and modelled CPO influences only weakly the P wave distribution.

Comparison between the modelled seismic properties and seismological observations of anisotropy in the transition zone provides constraints on the geometry of flow in the upper transition zone. Indeed, solely "horizontal", i.e., tangential shearing may produce faster velocities both for horizontally-propagating compressional waves ( $P_H$ ) and for horizontally-polarized shear waves ( $S_H$ ) (Montagner and Kennett, 1996), as well as an azimuthal anisotropy for vertically-polarized shear waves ( $S_V$ ) twice as strong than the one for horizontally-polarized shear waves ( $S_H$ ) (Trampert and van Heijst, 2002). Azimuthal anisotropy of  $S_V$ -waves predicted in the models (1%) is weaker than the one inferred from Love overtones data (up to 2%). Higher shear strains may result in slightly higher anisotropies, but CPO predictions at high strains cannot be constrained by the present experimental data. In addition, intensity of shear waves azimuthal anisotropy is a still poorly constrained parameter in Love

overtone inversions (J. Trampert, personal communication). More refined inversions and high shear strain experimental data are thus required to infer strain intensity in the upper transition zone. Finally, a horizontally-sheared upper transition zone would be seen as an isotropic medium by vertically-propagating core shear waves, such as SKS. Changes in the mantle flow pattern at the vicinity of subduction zones may however explain observations that point a contribution of the transition zone to SKS splitting along northern Pacific subduction zones (Fouch and Fisher, 1996). Indeed, in the present models, the highest delay times are predicted for SKS waves propagating along the flow plane, but at high angle to the flow direction. Vertical flow, on the other hand, should result in very weak polarization anisotropies for core shear waves. Dominant horizontal flow in the upper transition zone suggests that variations in physical properties related to phase changes in the transition zone do slow and maybe partially block material flow between the upper and lower mantle. Similar conclusions may be obtained from circulation models, which compute the present-day mantle convective flow driven both by plate motions and internal density anomalies distribution such as revealed by global tomographic models (Thoraval *et al.*, 1995). These models show that taking into account phase changes leads to local layering of mantle flow and enhances the tangential flow in the transition zone, compared to models that only include a viscosity jump at 670 km depth. Local blocking of radial flow and material accumulation in the transition zone is also suggested by mantle convection models that take into account phase changes in the transition zone (Brunet and Machetel, 1998) and by seismic tomography images that show flattening of high velocity

anomalies associated with some subduction zones, like Japan, Ryukyu, and Izu-Bonin, within the transition zone (Gorbatov and Kennet, 2003).

### III.3 – Conclusion

To summarize, strain-induced CPO of olivine deforming under high-pressure by dominant [001] glide and of wadsleyite deforming by an association of [100] and  $1/2 \langle 111 \rangle$  glide might be responsible of the seismic anisotropy observed in the lowermost upper mantle and the transition zone. Change in dominant slip system in forsterite can explaining the weak seismic anisotropy below 300 km. Distribution of seismic velocity calculated from the common features of both experimental and modelled wadsleyite CPO point toward a dominant tangential flow in the upper part of the transition zone. Accurate ringwoodite CPO are now needed to establish a more complete forward modelling of the transition zone seismic anisotropy.

## Conclusions and open questions



In this study, the mechanical properties of forsterite, wadsleyite and ringwoodite have been studied with a view to understand development of their crystallographic preferred orientations. These data are important to decipher our observations of seismic anisotropy which are one of the few relics of past convection in the Earth's mantle.

Various points have been highlighted from this study:

- 1) The D-DIA offers a new possibility to perform deformation experiments up to 10 GPa with capabilities comparable to standard deformation experiments at low pressure (control on strain rate, strain, *in-situ* measurement of stress and strain). The deviatoric stress is controlled independently from pressure and different kinds of test can be performed. Moreover, the damage introduced during the cold compression can be annealed before deformation. However, for higher pressures, the Kawai-type multianvil is still the only tool to deform millimeter-size samples up to 26 GPa at high temperature. We have seen in this study that, taking advantage of the 5000t press available at the Bayerisches Geoinstitut, shear deformation experiments have been performed at 22 GPa. We show that this possibility of exploring the mechanical behavior of Earth's minerals at conditions corresponding to depths down to ca. 700 km is not yet a routine. In particular, we show that detailed microstructural characterizations are necessary to check for the active mechanisms.

- 2) One of the salient information brought from this study is the occurrence of a pressure-induced change in the deformation mechanisms of forsterite. With pressure increase, [001] glide takes over [100] glide as dominant deformation mechanism. More work is needed to have a more precise understanding on the sensitivity of the various slip systems (including the actual planes) to this pressure effect. We also need to have more information on the transition pressure and on whether this transition is gradual (as suggested by our D-DIA experiments) or not.
  
- 3) The change of dominant slip system of olivine is determinant to explain the weak seismic anisotropy observed in the lowermost upper mantle. VPSC simulations and calculation of seismic anisotropy have shown that the variation of the P and S waves anisotropy patterns are fully compatible with the transition from [100] to [001] glide.
  
- 4) Deformation experiments on wadsleyite have shown that back-transformation occurs at the beginning of the deformation experiment. The influence of this phase transformation on the CPO development is uncertain. However, the comparison of experimental CPO with those from VPSC simulations allows to extract robust features characterized by the alignment of [100] axes parallel to the shear direction and by the alignment of [001] axes normal to the shear plane. More experimental work on wadsleyite is necessary to constrain the alignment of [010] axes.

- 5) The comparison between seismic anisotropy observed in the transition zone and the seismic properties calculated from wadsleyite CPO is compatible with a dominant tangential flow in the upper part of the transition zone.
  
- 6) The influence of the phase transformation from forsterite to wadsleyite on the rheology has been studied more precisely from dedicated experiments. Wadsleyite grains nucleate as incoherent precipitates either inside the grains or at the grain boundaries of forsterite with no influence of the defect microstructure of deforming forsterite on wadsleyite nucleation. The phase transition does not seem to strongly enhance the plasticity of the aggregate (no marked flattening or elongation of wadsleyite grains for instance). Moreover, the phase transition does not induce significant grain size reduction that could affect rheology.
  
- 7) The deformation experiments on ringwoodite have shown that the back-transformation observed in wadsleyite is not systematic. The CPO observed in ringwoodite cannot be simulated with VPSC taking into account known  $\frac{1}{2}\langle 110 \rangle$  slip systems only. The CPO can only be reproduced numerically if  $\langle 100 \rangle \{110\}$  slip systems (that have never been reported) are introduced in the simulation. Our preliminary TEM observations on deformed ringwoodite cannot support this assumption (nor can we rule it out...). More work is needed on ringwoodite to link microscopic deformation mechanisms and CPO before those are used to model seismic anisotropy

To conclude, we show that although they are still very challenging, deformation experiments under high pressure and high temperature represent one of the most exciting issues in minerals physics. Impressive progresses have been made in the last years. No doubt that many more must be awaited in the next ones.

# Appendix

In this appendix are presented the strain calculation from the rotation of the strain marker as well as the complementary techniques used through collaborations with other groups:

- X-ray diffraction peak broadening techniques (T.Ungár and K. Nyilas from the Department of General Physics, University Budapest, Hungary).
- ViscoPlastic Self Consistent modelling (Andrea Tommasi and David Mainprice from the Laboratoire de Tectonophysique, University of Montpellier, France).



## Appendix I

### Strain calculation from the strain marker rotation

The strain marker is a thin film of platinum vacuum deposited on a cut made into the sample disc. The cut is made at an angle  $\alpha \approx 45^\circ$  in order to be vertical in the assembly.

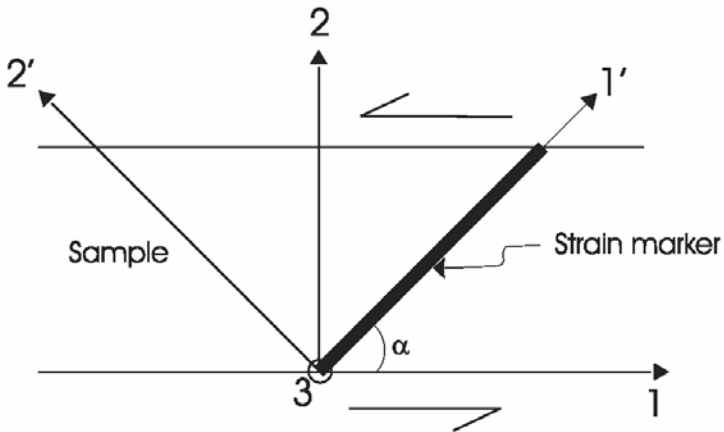


*Figure A.1 – Geometry of the sample and of the strain marker.*

The geometry of the sample is described within a reference frame based on three Cartesian axes (1, 2, 3) (Figure A.1). In this frame, the sample undergoes a simple shear (Figure A.2).

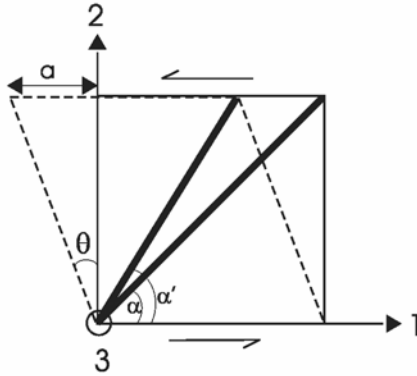


Figure A.2 – Rotation of the strain marker when the sample undergoes a simple shear

It is possible from Figure A.2 to evaluate the distortion tensor. Only one term is not zero:

$$\theta > 0$$

$$\beta_{21} < 0$$

$$\beta_{21} = \frac{\partial u_1}{\partial x_2} = \text{tg}\theta = -a \text{ with } a > 0$$

The distortion tensor is then:

$$\underline{\underline{\beta}} = \begin{pmatrix} 0 & -a & 0 \\ 0 & 0 & 0 \\ 0 & 0 & 0 \end{pmatrix}$$

The strain tensor is given from the symmetrical part of the distortion tensor (the asymmetrical part represents the rigid-body rotation):

$$\underline{\underline{\varepsilon}} = \begin{pmatrix} 0 & -a/2 & 0 \\ -a/2 & 0 & 0 \\ 0 & 0 & 0 \end{pmatrix}$$

After the sample has been sheared, the strain marker has rotated to make an angle  $\alpha'$  with axis (1). To calculate the strain marker rotation (i.e.  $\alpha - \alpha'$ ) one can build a second reference frame ( $1', 2', 3'$ ) in such a way that ( $1'$ ) is aligned with the strain marker (Figure A.1). The strain marker rotation  $\alpha - \alpha'$  will correspond to the distortion  $\beta_{1'2'}$ , (Figure A.3).

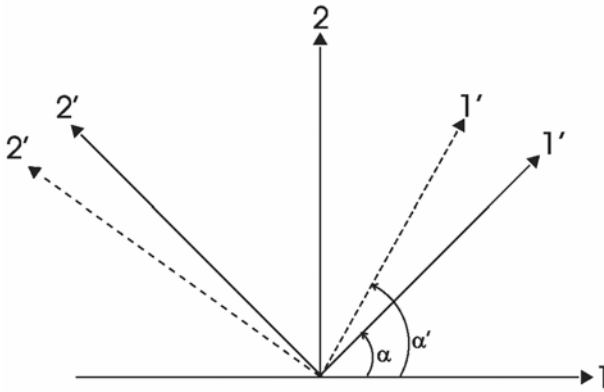


Figure A.3 – Shear-induced rotation of the Cartesian axes ( $1', 2, 3'$ ).

This term can be calculated and related to the shear term  $\varepsilon_{12}$  from the transformation of coordinate axis:

$$\begin{aligned}
 \beta_{1'2'} &= \operatorname{tg}(\alpha' - \alpha) \\
 &= \langle 1'/2 \rangle \langle 2'/1 \rangle \beta_{21} \\
 &= \sin \alpha (-\sin \alpha) \beta_{21} \\
 &= -\sin^2 \alpha (-a) \\
 &= \sin^2 \alpha (2\varepsilon_{12})
 \end{aligned}$$

The shear strain is then related to the strain-marker rotation by:

$$\gamma = 2 \times |\varepsilon_{12}| = \frac{\operatorname{tg}(\alpha' - \alpha)}{2 \sin^2 \alpha}$$

## Appendix II

### X-ray diffraction peak broadening analysis technique and evaluation of strain anisotropy

#### II.1 – X-ray diffraction peak broadening analysis

Dislocations are characterised by a long-range strain field causing a peak broadening of the fundamental Bragg reflections. Conventional peak profile analysis methods of Williamson & Hall (1953) and Warren & Averbach (1950) have been upgraded by taking into account the contrast effect of dislocations on peak broadening (Ungár and Borbély, 1996). The contrast factor,  $C$ , is a function of the  $hkl$  indices of the reflection, the Burgers and line vectors of the dislocations,  $b$  and  $l$ , and the elastic constants of the crystal in a similar way as in TEM.  $C$  is thus characteristic for a given slip system. The anisotropic contrast effect of dislocations has been used to model the strain anisotropy observed on X-ray diffraction profiles of cubic and hexagonal crystals (Ungár *et al.*, 1999; Ungár and Tichy, 1999; Ungár *et al.*, 2001). Here the technique has been extended to orthorhombic crystals. This technique has the advantage over TEM in that it provides information on a large number of dislocations that are more statistically relevant and it can be applied to high dislocation densities, e.g.  $10^{18} \text{ m}^{-2}$ . Besides the *modified* Williamson-Hall and Warren-Averbach methods (Ungár *et al.*, 2001) whole profile fitting procedures (Ribárik *et al.*, 2001; Ribárik *et al.*, 2004) have been developed and used here for the determination of the experimental values of dislocation contrast factors.

The specimens were cut as in Figure III.1 (cross-section). Consequently, the forsterite is surrounded by alumina and contains some platinum. Three windows have been found in the entire diffraction angle range where only the reflections of forsterite are present. In these three windows the profiles of five reflections have been investigated: {021}, {101}, {002}, {130}, {220}. Monochromatic  $\text{CuK}\alpha$  radiation from a fine focus rotating anode (Nonius FR 521), operated at 40kV, 70 mA was used. The footprint of the beam on the specimen was 0.1x0.8mm. The diffraction profiles were registered by a linear position sensitive gas filled detector (OED 50 Braun, Munich) at a distance of 140mm from the specimen. The linear resolution of the detector is about 80  $\mu\text{m}$ . The specimen was mounted on a two axis standard crystallographic goniometer-head with additional x-y translations in the horizontal plane in order to move the specimen within the X-ray beam with high precision.

### III.2 - Evaluation of strain anisotropy

Strain anisotropy in X-ray line-profile analysis means that neither the full-width at half maximum (FWHM) nor the integral breadths nor the Fourier coefficients in the Warren-Averbach plot are monotonous functions of the diffraction vector or its square,  $g$  or  $g^2$ . It can be rationalised by the dislocation contrast factors,  $C$ , which, on the other hand provide useful further information on the dislocation structure of the specimen (Wilkens, 1970; Ungár and Borbély, 1996; Ungár *et al.*, 2001). If all possible slip systems are randomly populated or if the specimen is more or less texture free the contrast factors corresponding to the same  $hkl$  indices can be

averaged over the permutations of the indices (Ungár and Tichy, 1999). Since the specimen is a fine grained polycrystal, these average contrast factors can be used. For cubic and hexagonal crystals the numerical parameters in the average contrast factor formula are well understood (Ungár and Tichy, 1999; Dragomir and Ungar, 2002). For orthorhombic crystals, the average contrast factors are:

$$\bar{C} = \alpha + \beta \times \left( (h^4 + a_1 k^4 + a_2 l^4 + a_3 h^2 k^2 + a_4 h^2 l^2 + a_5 l^2 k^2) / \left( \left( \frac{h^2}{a^2} + \frac{k^2}{b^2} + \frac{l^2}{c^2} \right)^2 \right) \right)$$

where  $a, b$  and  $c$  are the lattice constants,  $h, k$  and  $l$  are the Miller indices and  $a_i, i=1-5$ , are numerical constants depending on the dislocation type and the elastic constants of the crystal.  $\alpha$  and  $\beta$  are auxiliary constants which influence only the absolute value of  $\bar{C}$ , but do not influence the  $hkl$  dependence of it (Ungár *et al.*, 2001). The average contrast factors for orthorhombic crystals are calculated numerically by using the general formula for contrast factors (Klimanek and Kuzel, 1988; Ungár and Tichy, 1999). The physical interpretation of the  $a_i$  constants in terms of different dislocation types and/or elastic constants is, however, not yet available. In the present case, the  $a_i$  numerical constants are determined by fitting the FWHM of the five measured profiles according to the *modified* Williamson-Hall equation, (c.f., Eq (9) in Ungár *et al.*,(2001)). From the  $a_i$  values,

obtained here, relative values of the contrast factors,  $\bar{C}^*$  were calculated. A large number of experiments (Wilkins, 1970; Ungár *et al.*, 2001) have shown that the approximate mean of the average contrast factors is :  $\langle \bar{C} \rangle \cong 0.4$ . The mean of the  $\bar{C}^*$  values were adjusted accordingly. With these calculated and adjusted  $\bar{C}$  values the dislocation densities are calculated by using the *multiple whole profile* (MWP) fitting procedure that applies physically well established profile functions for the size and strain profiles, respectively (Ribárik *et al.*, 2001).

## Appendix III

### Crystal preferred orientation modelling: ViscoPlastic Self Consistent (VPSC) method

Crystal preferred orientations developed under simple shear are predicted using a viscoplastic self-consistent model (VPSC) (Molinari *et al.*, 1987), which was extended to anisotropic plasticity by Lebensohn and Tomé (1993). The pioneering work in Earth Sciences of Wenk and co-workers (e.g., Wenk *et al.*, 1991) has established that this model provides a robust solution, which reproduces the essential features of crystal preferred orientations of experimentally deformed plastically anisotropic minerals. It has also been successfully applied to polycrystalline ice (Castelnau *et al.*, 1996), olivine (Tommasi *et al.*, 2000), clinopyroxene (Bascou *et al.*, 2002) and garnet (Mainprice *et al.*, 2004). In contrast to classical lower or upper bound approaches, which impose respectively homogeneous stress (Sachs, 1928) or strain (Taylor, 1938) within the aggregate, the VPSC approach allows both the microscopic stress and strain rate to differ from the corresponding macroscopic quantities. Strain compatibility and stress equilibrium are ensured only at the aggregate scale.

At the grain scale, deformation is accommodated by dislocation glide only; other deformation processes such as grain boundary sliding or dynamic recrystallization are not taken into account. The shear rate in a slip system  $S$  is related to the local deviatoric stress tensor  $\underline{\underline{S}}$  by a visco-plastic law:

$$\dot{\gamma}_s = \dot{\gamma}_0 \left( \frac{\tau_r^s}{\tau_0^s} \right)^{n^s} = \dot{\gamma}_0 \left( \frac{r_{ij}^s S_{ij}}{\tau_0^s} \right)^{n^s}$$

where  $\dot{\gamma}_0$  is a reference strain rate, taken as  $1s^{-1}$ , and  $n^s$ ,  $\tau_r^s$ , and  $\tau_0^s$  are respectively the stress exponent, the resolved shear stress, and the CRSS for the system  $s$ , whose orientation relative to the macroscopic axis is expressed by its Schmid tensor  $\underline{r}^s$ .

The problem lies in the calculation of a microscopic state  $(\mathbf{s}, \dot{\boldsymbol{\varepsilon}})$  for each grain, whose volume average determines the response of the polycrystal  $(\bar{\boldsymbol{\Sigma}}, \bar{\mathbf{D}})$ . The “1-site” approximation (Molinari *et al.*, 1987; Lebensohn and Tomé, 1993) is used in the anisotropic VPSC formulation; interactions between neighbouring grains are hence not taken into account. Interactions between each grain and its surroundings are successively replaced by the interaction between an inclusion with similar lattice orientation and an infinite homogeneous equivalent medium (HEM), whose behaviour is the weighted average of the grains behaviour. This leads to:

$$\dot{\boldsymbol{\varepsilon}}_{ij} - D_{ij} = -\alpha \tilde{\mathbf{M}}_{ijkl} (S_{ijkl} - \bar{\Sigma}_{kl})$$

where  $\tilde{\mathbf{M}}$  is the interaction tensor and  $\alpha$  is a constant used to parameterize the interaction between grains and the HEM.  $\alpha = 0$  corresponds to the upper bound model (homogeneous strain),  $\alpha = 1$  is the classical self-consistent model (a linear relationship between volume averaged stress and strain rate)  $\alpha = \text{infinity}$  to the lower bound model (stress equilibrium).

The strain history is imposed by prescribing a constant macroscopic velocity gradient tensor  $\mathbf{L}$ ; which for simple shear (with a vorticity number  $Wk=0.9$ ) is :

$$\mathbf{L} = \begin{bmatrix} 0 & 1 & 0 \\ 0 & 0 & 0 \\ 0 & 0 & 0 \end{bmatrix} \text{ and } \mathbf{L} = \begin{bmatrix} 0 & 1 & 0 \\ 0 & -.237 & 0 \\ 0 & 0 & 0.237 \end{bmatrix}$$

respectively, and a time increment,  $d\tau$ , set to achieve an equivalent strain of 0.025 in each deformation step. The equivalent strain is defined as:

$$\varepsilon_{eq} = \int D_{eq}(\tau) d\tau$$

where the Von Mises equivalent strain rate is:

$$D_{eq} = \sqrt{2/3 D_{ij} D_{ij}}$$

The only tuning parameters are therefore the active slip systems for the phase, their CRSS and stress exponents, a strain hardening parameter, and the strength of the interaction between grains and the HEM, defined by the parameter  $\alpha$ . The initial condition is defined by the initial CPO and initial crystal shapes.



# References



## REFERENCES

---

- Abramson, E. H., M. Brown, L. J. Slutsky and J. Zaug (1997). The elastic constants of San Carlos olivine up to 17 GPa. *J. Geophys. Res.* **102**: 12,252–12,263.
- Adams, B. L., S. I. Wright and K. Kunze (1992). Orientation imaging: The emergence of a new microscopy. *Metallurgical Transactions A* **24A**(819–831).
- Agee (1998). Phase transformations and seismic structure in the upper mantle and transition zone. *in* *Ultrahigh-pressure mineralogy: Physics and chemistry of the Earth's deep interior*. R. J. Hemley. Washington, D.C. **37**: 165–203.
- Bai, Q. and D. L. Kohlstedt (1992a). High-temperature creep of olivine single crystals III. Mechanical results for unbuffered samples and creep mechanisms. *Philosophical Magazine A* **66**(6): 1149–1181.
- Bai, Q. and D. L. Kohlstedt (1992b). High-temperature creep of olivine single crystals, 2. Dislocation structures. *Tectonophysics* **206**: 1–29.
- Bai, Q. and D. L. Kohlstedt (1993). Effects of chemical environment on the solubility and incorporation mechanism for hydrogen in olivine. *Phys. Chem. Miner.* **19**: 460–471.
- Bai, Q., S. J. Mackwell and D. L. Kohlstedt (1991). High-temperature creep of olivine single crystals 1. Mechanical results for buffered samples. *Journal of Geophysical Research* **96**(B2): 2441–2463.
- Bascou, J., A. Tommasi and D. Mainprice (2002). Plastic deformation and development of clinopyroxene lattice preferred orientations in eclogites. *J. Struct. Geol.* **24**(8): 1357–1368.
- Ben Ismaïl, W., G. Barruol and D. Mainprice (2001). The Kaapvaal craton seismic anisotropy: petrophysical analyses of upper mantle

## REFERENCES

---

- kimberlite nodules. *Geophysical Research Letters* **28**(13): 2497–2500.
- Ben Ismail, W. and D. Mainprice (1998). An olivine fabric database: an overview of upper mantle fabrics and seismic anisotropy. *Tectonophysics* **296**: 145–157.
- Binns, R. A., R. J. David and S. J. B. Reed (1969). Ringwoodite, natural  $(\text{Mg,Fe})_2\text{SiO}_4$  spinel in the Tenham meteorite. *Nature* **221**: 943.
- Blacic, J. D. and J. M. Christie (1973). Dislocation substructure in experimentally deformed olivine. *Contrib. Mineral. Petrol.* **42**: 141–146.
- Brearely, A. J. and D. C. Rubie (1994). Transformation mechanisms of San Carlos olivine to  $(\text{Mg,Fe})_2\text{SiO}_4$   $\beta$ -phase under subduction zone conditions. *Physics of the Earth and Planetary Interiors* **86**: 45–67.
- Brearely, A. J., D. C. Rubie and E. Ito (1992). Mechanisms of the transformations between the  $\alpha$ ,  $\beta$  and  $\gamma$  polymorphs of  $\text{Mg}_2\text{SiO}_4$  at 15 GPa. *Physics and Chemistry of Minerals* **18**: 343–358.
- Brunet, D. and P. Machetel (1998). Large-scale tectonic features induced by mantle avalanches with phase, temperature, and pressure lateral variations of viscosity. *J Geophys Res Solid Earth* **103**: 4929–4945.
- Bussod, G. Y., T. Katsura and D. C. Rubie (1993). The large volume multi-anvil press as a high P–T deformation apparatus. *Pageoph* **141**(1): 142–161.
- Bystricky, M., K. Kunze, L. Burlini and J.-P. Burg (2000). High shear strain of olivine aggregates: rheological and seismic consequences. *Science* **290**: 1564–1567.

## REFERENCES

---

- Cara, M. and J. L. L ev eque (1988). Anisotropy of the asthenosphere: The higher mode data of the Pacific revisited. *Geophys. Res. Lett.* **15**: 205-508.
- Carter, N. L. and H. G. Ave'lallemant (1970). High temperature flow of dunitite and peridotite. *Geological Society of America Bulletin* **81**: 2181-2202.
- Castelnau, O., M. Drakopoulos, C. Schroer, I. Snigireva, A. Snigirev and T. Ung ar (2001). Dislocation density analysis in single grains of steel by x-ray scanning microdiffraction. *Nuclear Instruments and Methods in Physics Research* **A467-468**: 1245-1248.
- Castelnau, O., P. Duval, R. A. Lebensohn and G. R. Canova (1996). Viscoplastic modelling of texture development in polycrystalline ice with a self-consistent approach: comparison with bound estimates. *J. Geophys. Res.* **101**(B6): 13851-13868.
- Chai, M., J. M. Brown and L. J. Slutsky (1997). The elastic constants of a pyrope-grossular-almandine garnet to 20 GPa. *Geophys. Res. Lett.* **24**(5): 523-526.
- Chen, J., L. Li, D. J. Weidner and M. Vaughan (2004). Deformation experiments using synchrotron X-rays: in situ stress and strain measurements at high pressure and temperature. *Physics of the Earth and Planetary Interiors* **143-144**: 347-356.
- Chen, J. H., T. Inoue, D. J. Weidner, Y. J. Wu and M. T. Vaughan (1998). Strength and water weakening of mantle minerals, olivine, wadsleyite and ringwoodite. *Geophysical Research Letters* **25**: 50.
- Chiang, Y. and W. D. Kingery (1989). Grain boundary migration in nonstoichiometric solid solution of magnesium aluminate spinel: I, Grain growth studies. *J. Am. Ceram. Soc* **72**: 271.

## REFERENCES

---

- Chopra, P. N. and M. S. Paterson (1981). The Experimental Deformation of Dunite. *Tectonophysics* **78**: 453-473.
- Chopra, P. N. and M. S. Paterson (1984). The role of water in the deformation of dunite. *J Geophys Res Solid Earth* **89**: 7861-7876.
- Christian, J. W. and V. Vitek (1970). Dislocations and stacking faults. *Rep. Prog. Phys.* **33**: 307-411.
- Coleman, L. C. (1977). Ringwoodite and majorite in the Catherwood meteorite. *Canadian Mineralogist* **15**: 97-101.
- Collins, M. D. and J. M. Brown (1998). Elasticity of an upper mantle clinopyroxene. *Phys. Chem. Minerals* **26**: 7-13.
- Cordier, P., D. Mainprice and J. L. Mosenfelder (2004). Mechanical instability near the stishovite-CaCl<sub>2</sub> phase transition: implication for crystal preferred orientations and seismic properties. *European Journal of Mineralogy* **16**: 387-399.
- Cordier, P. and D. C. Rubie (2001). Plastic deformation of minerals under extreme pressure using a multi-anvil apparatus. *Materials Sciences and Engineering* **A309-310**: 38-43.
- Cordier, P., E. Thurel and J. Rabier (2002). Stress determination in multianvil deformation experiments based on dislocation curvatures measurements: Application to wadsleyite and ringwoodite. *Geophysical Research Letters* **29**(9): 101029-101033.
- Darot, M. (1980). Déformation expérimentale de l'olivine et de la forsterite. PhD Dissertation, Université de Nantes.
- Darot, M. and Y. Gueguen (1981). High-temperature creep of forsterite single crystals. *Journal of Geophysical Research* **86**(B7): 6219-6234.

## REFERENCES

---

- Dingley, D. (1984). Diffraction from sub-micron areas using electron backscattering in a scanning electron microscope. Scanning Electron Microscopy **II**: 569-575.
- Dragomir, I. C. and T. Ungar (2002). Contrast factors of dislocations in the hexagonal crystal system. J. Appl. Cryst. **35**: 556-564.
- Dunand, D. C., C. Schuh and D. L. Goldsby (2001). Pressure-induced transformation plasticity of H<sub>2</sub>O ice. Physical Review Letters **86**(4): 668-671.
- Dupas, C., N. Doukhan, J. C. Doukhan, H. W. Green II and Y. T.E. (1994). Analytical electron microscopy of a synthetic peridotite experimentally deformed in the  $\beta$  olivine stability field. Phys. Chem. Minerals **25**: 501-514.
- Dupas-Bruzek, C., T. G. Sharp, D. C. Rubie and W. B. Durham (1998a). Mechanisms of transformation and deformation in Mg<sub>1.8</sub>Fe<sub>0.2</sub>SiO<sub>4</sub> olivine and wadsleyite under non-hydrostatic stress. Physics of the Earth and Planetary Interiors **108**: 33-48.
- Dupas-Bruzek, C., T. N. Tingle and H. W. Green II (1998b). The rheology of olivine and spinel magnesium germanate (Mg<sub>2</sub>GeO<sub>4</sub>): TEM study of the defect microstructures. Phys. Chem. Minerals **25**: 501-514.
- Durham, W. B. (1975). Plastic flow of single crystals of olivine. PhD dissertation, M.I.T, Cambridge, Massachusetts.
- Durham, W. B. and C. Goetze (1977a). A comparison of the creep properties of pure forsterite and iron-bearing olivine. Tectonophysics **40**: T15-T18.
- Durham, W. B. and C. Goetze (1977b). Plastic flow of oriented single crystals of olivine 1. Mechanical data. Journal of Geophysical Research **82**(36): 5737-5753.

## REFERENCES

---

- Durham, W. B., D. J. Weidner, S.-i. Karato and Y. Wang (2002). New developments in deformation experiments at high pressure. *in* Plastic deformation of minerals and rocks. S.-i. Karato and H.-R. Wenk. Washington, D.C., MSA. **51**: 21-49.
- Durinck, J., A. Legris and P. Cordier (in press). Influence of the crystal chemistry on ideal shear strength in forsterite: First-principle calculation. *American Mineralogist*.
- Dziewonski, A. M. and D. L. Anderson (1981). Preliminary reference Earth model. *Physics of the Earth and Planetary Interiors* **25**: 297-356.
- Ekstrom, G. and A. M. Diewonski (1998). The unique anisotropy of the Pacific upper mantle. *Nature* **394**: 168-172.
- Fouch, M. J. and K. M. Fisher (1996). Mantle anisotropy beneath northwest Pacific subduction zones. *J. Geophys. Res.* **101**: 15987-16002.
- Frese, K., V. Trommsdorff and K. Kunze (2003). Olivine [001] normal to foliation: lattice preferred orientation in prograde garnet peridotite formed at high H<sub>2</sub>O activity, Cima di Gagnone (Central Alps). *Contrib. Mineral Petrol.* **145**: 75-86.
- Friedel, F. (1967). *Dislocations*. Oxford, Pergamon.
- Frost, D. J., B. T. Poe, R. G. Tronnes, C. Liebske, A. Duba and D. C. Rubie (2004). A new large-volume multianvil system. *Physics of the Earth and Planetary Interiors*.
- Fujimura, A., S. Endo, M. Kato and M. Kumazawa (1981). Preferred orientation of  $\beta$ -Mn<sub>2</sub>GeO<sub>4</sub>.
- Gaherty, J. B., T. H. Jordan and L. S. Gee (1996). Seismic structure of the upper mantle in the central Pacific corridor. *J. Geophys. Res.* **101**: 22,291-22,309.

## REFERENCES

---

- Getting, I. C. (1998). New determination of the bismuth I-II equilibrium pressure: A proposed modification to the practical pressure scale. *Metrologia* **35**: 119-132.
- Gillet, P., I. Daniel and F. Guyot (1997). Anharmonicity of  $\text{Mg}_2\text{SiO}_4$ -forsterite measured from the volume dependence of the Raman spectrum. *European Journal of Mineralogy*(9): 255-262.
- Gleason, G. C. and J. Tullis (1993). Improving flow laws and piezometers for quartz and feldspar aggregates. *Geophysical Research Letters* **20**: 20,2111-20,2114.
- Gorbatov, A. and B. L. N. Kennet (2003). Joint bulk-sound and shear tomography for Western Pacific subduction zones. *Earth Planet. Sci. Lett.* **210**: 527-543.
- Green, D. H. and A. E. Ringwood (1963). Mineral assemblages in a model mantle composition. *J Geophys Res Solid Earth* **68**: 937-945.
- Green II, H. W. and R. S. Borch (1989). A new molten salt cell for precision stress measurement at high pressure. *European Journal of Mineralogy* **1**: 213-219.
- Griggs, D. T., F. J. Turner and H. C. Heard (1960). Deformation of rock at 500°C and 800°C. *Men. Geol. Soc. Am.* **79**: 39-104.
- Gueguen, Y. (1979a). Dislocations in naturally deformed terrestrial olivine: classification, interpretation, applications. *Bulletin de minéralogie* **102**: 178-183.
- Gueguen, Y. (1979b). Les dislocations dans l'olivine des péridotites. PhD Dissertation, Université de Nantes.
- Gung, Y., M. Panning and B. Romanowicz (2003). Global anisotropy and the thickness of continents. *Nature* **422**: 707-711.

## REFERENCES

---

- Guyot, F., G. D. Gwamnesia and R. C. Liebermann (1991). An olivine to beta phase transformation mechanism in  $\text{Mg}_2\text{SiO}_4$ .
- Heidelbach, F., I. Stretton, F. Langenhorst and S. J. Mackwell (2003). Fabric evolution during high shear strain deformation of magnesiowüstite ( $\text{Mg}_{0.8}\text{Fe}_{0.2}\text{O}$ ). *Journal of Geophysical Research* **108**(B3): 2154–2168.
- Hinds, W. C. (1982). *Aerosol Technology: Properties, behavior and measurement of airborne particles*. New York, Wiley.
- Hirth, G. and D. L. Kohlstedt (1995a). Experimental constraints on the dynamics of the partially molten upper mantle. Diffusion in the diffusion creep regime. *J. Geophys. Res.* **100**: 1981–2001.
- Hirth, G. and D. L. Kohlstedt (1995b). Experimental constraints on the dynamics of the partially molten upper mantle. Diffusion in the dislocation creep regime. *J. Geophys. Res.* **100**: 15441–15449.
- Horiuchi, H. and H. Sawamoto (1981).  $\beta$ - $\text{Mg}_2\text{SiO}_4$ : single-crystal X-ray diffraction study. *American Mineralogist* **66**(568–575).
- Ito, E., E. Takahashi and Y. Matsui (1984). The mineralogy and chemistry of the lower mantle: An implication of the ultrahigh pressure phase relations in the system  $\text{MgO-FeO-SiO}_2$ . *Earth and Planetary Science Letters* **67**: 238–248.
- Jaoul, O., M. Michaut, Y. Gueguen and B. Ricoult (1979). Decorated dislocations in forsterite. *Phys. Chem. Miner.* **5**: 15–19.
- Johnson, C. A., R. C. Bradt and J. H. Hoke (1975). Transformational plasticity in  $\text{Bi}_2\text{O}_3$ . *Journal of American Ceramic Society* **58**(1–2): 37–40.
- Joòs, B. and M. S. Duesbery (1997). The Peierls stress of dislocations: an analytic formula. *Physical Review Letters* **78**: 266–269.

## REFERENCES

---

- Jung, H. and S.-i. Karato (2001). Water-induced fabric transitions in olivine. *Science* **293**: 1460–1463.
- Karato, S., M. S. Paterson and J. D. FitzGerald (1986). Rheology of synthetic olivine aggregates: influence of grain size and water. *J. Geophys. Res.* **91**: 8151–8176.
- Karato, S.-i. (1992). On the Lehmann discontinuity. *Geophysical Research Letters* **19**(22): 2255–2258.
- Karato, S.-i. (1995). Phase transformations and rheological properties of the mantle minerals. *in* Earth's deep interior. D. Crossley and A. M. Soward. New York, Gordon and Breach: 223–272.
- Karato, S.-i., C. Dupas-Bruzek and D. C. Rubie (1998). Plastic deformation of silicate spinel under the transition-zone conditions of the Earth's mantle. *Nature* **395**: 266–269.
- Karato, S.-i. and H. Jung (2003). Effect of the pressure on high-temperature dislocation creep in olivine. *Philosophical Magazine* **83**(3): 401–414.
- Karato, S.-i. and D. C. Rubie (1997). Toward an experimental study of deep mantle rheology: A new multianvil sample assembly for deformation studies under high pressures and temperature. *Journal of Geophysical Research* **102**(B9): 20111–20122.
- Karato, S.-i., D. C. Rubie and H. Yan (1993). Dislocation recovery in olivine under deep upper mantle conditions: implications for creep and diffusion. *Journal of Geophysical Research* **98**(B6): 9761–9768.
- Kashima, K., I. Sunagawa and K. Sumino (1982). Plastic deformation of olivine single crystals. *Science Report of Tohoku University series III* **15**: 218–407.

## REFERENCES

---

- Kavner, A. (2003). Elasticity and strength of hydrous ringwoodite at high pressure. *Earth and Planetary Science Letters* **6783**: 1-10.
- Kavner, A. and T. S. Duffy (2001). Strength and elasticity of ringwoodite at upper mantle pressures. *Geophysical Research Letters* **28**(14): 2691-2694.
- Kawai, N. and S. Endo (1970). The generation of ultrahigh hydrostatic pressures by a split sphere apparatus. *Rev. Sci. Instruments* **41**: 1178-1181.
- Klimanek, P. and J. R. Kuzel (1988). X-ray diffraction line broadening due to dislocations in non-cubic materials. 1. General considerations and the case of elastic isotropy applied to hexagonal crystals. *J. Appl. Cryst.* **21**: 59-66.
- Kohlstedt, D. L. and C. Goetze (1974). Low-stress high -temperature creep in olivine single crystals. *Journal of Geophysical Research* **79**(14): 2045-2051.
- Kohlstedt, D. L., C. Goetze and W. B. Durham (1976). Experimental deformation of single crystal olivine with application to flow in the mantle. *in* *The Physics and Chemistry of Minerals and Rocks*. R. G. J. Strens, John Wiley and Sons: 35-49.
- Kot, R. A. and V. Weiss (1970). Transformation plasticity in iron-nickel alloys. *Metallurgical Transactions* **1**: 2685-2693.
- Kresse, G. and J. Furthmüller (1996). Efficiency of ab-initio total energy calculation for metals and semiconductors using a plane-wave basis set. *Comput. Mat. Sci.* **6**: 15-50.
- Kresse, G. and J. Hafner (1993). Ab initio molecular dynamics for liquid metals. *Physical Review* **B47**: 558.

## REFERENCES

---

- Lebensohn, R. A. and C. N. Tomé (1993). A self-consistent anisotropic approach for the simulation of plastic deformation and texture development of polycrystal: application to zirconium alloys. *Acta Metall. Mater.* **41**: 2611–2624.
- Lehmann, I. (1955). The times of P and S in northeastern America. *Ann. Geofis.* **8**: 351–370.
- Leroux, H. (2001). Microstructural shock signatures of major minerals in meteorites. *European Journal of Mineralogy* **13**: 253–272.
- Lévêque, J. J., E. Debayle and V. Maupin (1998). Anisotropy in the Indian Ocean upper mantle from Rayleigh and Love waveform inversion. *Geophys. J. Int.* **133**: 529–540.
- Li, L., P. Raterron, D. J. Weidner and J. Chen (2003). Olivine flow mechanisms at 8 GPa. *Physics of the Earth and Planetary Interiors* **138**: 113–129.
- Li, L., D. J. Weidner, J. Chen and M. Vaughan (2004). Stress measurements of deforming olivine at high pressure. *Physics of the Earth and Planetary Interiors* **143–144**: 357–367.
- Liebermann, R. C. and Y. Wang (1992). Characterization of sample environment in a uniaxial split-sphere apparatus. *in* High-Pressure Research; Application of the Earth and Planetary Sciences. Y. Syono and M. H. Manghnani. Washington D.C., American Geophysical Union. **67**: 19–31.
- Liu, L., T. P. Mernagh and T. Irifune (1994). High-pressure Raman spectra of  $\beta$ -Mg<sub>2</sub>SiO<sub>4</sub>,  $\gamma$ -Mg<sub>2</sub>SiO<sub>4</sub>, MgSiO<sub>3</sub>-ilmenite and MgSiO<sub>3</sub>-pervoskite. *Phys. Chem. Minerals* **55**(2): 185–193.
- Lloyd, E. C. (1971). Accurate characterization of the high pressure environment. *in* NBS Special Publication. Washington DC. **326**: 1–3.

## REFERENCES

---

- Mackwell, S. J., D. L. Kohlstedt and M. S. Paterson (1985). The role of water in the deformation of olivine single crystals. *Journal of Geophysical Research* **90**(B13): 11319–11333.
- Madon, M. and J. P. Poirier (1980). Dislocation in spinel and garnet high pressure polymorphs of olivine and pyroxene: implications for mantle rheology. *Science* **207**: 66–68.
- Madon, M. and J. P. Poirier (1983). Transmission electron microscope observation of  $\alpha$ ,  $\beta$  and  $\gamma$   $(\text{Mg,Fe})_2\text{SiO}_4$  in shocked meteorites: planar defects and polymorphic transitions. *Physics of the Earth and Planetary Interiors* **33**: 31–44.
- Mainprice, D., G. Barruol and W. Ben Ismaïl (2000). The seismic anisotropy of the Earth's Mantle: From single crystal to polycrystal. *in* *Earth's deep interior: Mineral physics and tomography from the atomic to the global scale*. S.-i. Karato, A. M. Forte, R. C. Liebermann, G. Master and L. Stixrude. Washington, D.C., American Geophysical Union. **117**: 237–264.
- Mainprice, D., J. Bascou, P. Cordier and A. Tommasi (2004). Crystal preferred orientations of garnet: Comparison between numerical simulations and electron back-scattered diffraction (EBSD) measurements in naturally deformed eclogites. *J. Struct. Geol.* **26**: 2089–2102.
- Mei, S. and D. L. Kohlstedt (2000a). Influence of water on plastic deformation of olivine aggregates 1. Diffusion creep regime. *J. Geophys. Res. Solid Earth* **105**: 21457–21469.
- Mei, S. and D. L. Kohlstedt (2000b). Influence of water on plastic deformation of olivine aggregates 2. Dislocation creep regime. *J. Geophys. Res. Solid Earth* **105**: 21471–21481.
- Merkel, S., H. R. Wenk, J. Shu, G. Shen, P. Gillet, H.-k. Mao and R. J. Hemley (2002). Deformation of polycrystalline MgO at pressures of the

## REFERENCES

---

- lower mantle. *Journal of Geophysical Research* **107**(B11): 2271-2288.
- Mitchell, T. E. (1999). Dislocations and mechanical properties of MgO-Al<sub>2</sub>O<sub>3</sub> spinel single crystal. *J. Am. Ceram. Soc* **82**: 3305-3316.
- Mitchell, T. E., L. Hwang and A. H. Heuler (1976). Deformation in spinel. *Journal of Materials Science* **11**: 264-272.
- Mizukami, T., S. R. Wallis and J. Yamamoto (2004). Natural examples of olivine lattice preferred orientation patterns with a flow-normal *a*-axis maximum. *Nature* **427**: 432-436.
- Molinari, A., G. R. Canova and S. Azhy (1987). A self-consistent approach of the large deformation crystal polycrystal viscoplasticity. *Acta Metall.* **35**: 2983-2994.
- Montagner, J. P. (1985). Seismic anisotropy of the Pacific Ocean inferred from long-period surface waves dispersion. *Physics of the Earth and Planetary Interiors* **38**: 28-50.
- Montagner, J. P. and B. L. N. Kennett (1996). How to reconcile body-wave and normal-mode reference Earth models? *Geophys. J. Int.* **125**: 229-248.
- Morimoto, N., S. Akimoto, K. Koto and M. Tokonami (1969). Modified spinel, beta-manganous orthogermanate: Stability and crystal structure. *Science* **165**: 586-588.
- Morishima, H., T. Kato, M. Suto, E. Ohtani, S. Urakawa, W. Utsumi, O. Shimomura and T. Kikegawa (1994). The phase boundary between  $\alpha$  and  $\beta$ -Mg<sub>2</sub>SiO<sub>4</sub> determined by in situ X-ray observation. *Science* **265**: 1202-1203.

## REFERENCES

---

- Nickel, K. G., G. P. Brey and L. Kogarko (1985). Orthopyroxene-clinopyroxene equilibria in the system CaO-MgO-Al<sub>2</sub>O<sub>3</sub>-SiO<sub>2</sub> (CMAS): new experimental results and implications for two-pyroxene thermometry. *Contrib. Mineral Petrol.* **91**: 44-53.
- Nicolas, A., F. Boudier and A. M. Boullier (1973). Mechanism of flow in naturally and experimentally deformed peridotites. *American Journal of Science* **273**: 853-876.
- Nicolas, A. and N. I. Christensen (1987). Formation of anisotropy in upper mantle peridotites - A review. *in* Composition, structure and dynamics of the lithosphere-asthenosphere system. K. Fuchs and C. Froidevaux. Washington, D.C., AGU. **16**.
- Nishimura, C. E. and D. W. Forsyth (1989). The anisotropic structure of the upper mantle in the Pacific. *Geophysical Journal* **96**: 203-230.
- Osugi, J., K. Shimizu, K. Inoue and K. Yasunami (1964). A compact cubic anvil high pressure apparatus. *Review of Physical Chemistry of Japan* **34**(1): 1-6.
- Paterson, M. S. (1970). A high-pressure, high-temperature apparatus for rock deformation. *Int. J. Rock Mech. Min. Sci.* **7**: 517-526.
- Paterson, M. S. (1982). The determination of hydroxyl by infrared absorption in quartz, silicates glasses and similar materials. *Bulletin de minéralogie* **105**: 20-29.
- Phakey, P., G. Dollinger and J. Christie (1972). Transmission Electron Microscopy of Experimentally Deformed Olivine Crystals. *in* Flow and fracture of rocks. H. C. Heard, I. Y. Borg, N. L. Carter and C. B. Raleigh. Washington, D.C., American Geophysical Union. **16**: 117-138.

## REFERENCES

- Price, G. D. (1883). The nature and significance of stacking faults in wadsleyite, natural  $\beta$ -(Mg,Fe)<sub>2</sub>SiO<sub>4</sub> from the Peace River meteorite. *Physics of the Earth and Planetary Interiors* **33**: 137-147.
- Price, G. D. (1983). The nature and significance of stacking faults in wadsleyite, natural  $\beta$ -(Mg,Fe)<sub>2</sub>SiO<sub>4</sub> from the Peace River meteorite. *Physics of the Earth and Planetary Interiors* **33**: 137-147.
- Raleigh, C. B. (1968). Mechanisms of plastic deformation of olivine. *Journal of Geophysical Research* **73**(14): 5391-5406.
- Raterron, P., Y. Wu, D. J. Weidner and J. Chen (2004). Low-temperature olivine rheology at high-pressure. *Physics of the Earth and Planetary Interiors* **145**: 149-159.
- Revenaugh, J. and T. Jordan (1991). Mantle layering from ScS reverberations 3. The upper mantle. *J. Geophys. Res.* **96**: 19,781-19,81009.
- Ribárik, G., J. Gubicza and T. Ungár (2004). Correlation between strength and microstructure of ball milled Al-Mg alloys determined by X-ray diffraction. *Mater. Sci. Eng. A* **In press**.
- Ribárik, G., T. Ungár and J. Gubicza (2001). MWP-fit: a program for multiple whole-profile fitting of diffraction peak profile by ab initio theoretical functions. *Journal of Applied Crystallography* **34**: 669-676.
- Riedel, M. R. and S.-i. Karato (1997). Grain-size evolution in subducted oceanic lithosphere associated with the olivine-spinel transformation and its effects on rheology. *Earth and Planetary Science Letters* **148**: 27-43.
- Ringwood, A. E. and A. Major (1966). Synthesis of Mg<sub>2</sub>SiO<sub>4</sub>-Fe<sub>2</sub>SiO<sub>4</sub> spinel solid solutions. *Earth and Planetary Science Letters* **1**: 241-245.

## REFERENCES

---

- Ringwood, A. E. and A. Major (1970). The system  $\text{Mg}_2\text{SiO}_4\text{-Fe}_2\text{SiO}_4$  at high pressure and temperatures. *Physics of the Earth and Planetary Interiors* **3**(89-108).
- Rubie, D. C. (1999). Characterizing the sample environment in multianvil high pressure experiments. *Phase Transitions* **68**: 431-451.
- Rybacki, E., J. Renner, K. Konrad, W. Harbott, F. Rummel and B. Stöckhert (1998). A servohydraulically-controlled deformation apparatus for rock deformation under conditions of ultra-high pressure metamorphism. *Pure and Applied Geophysics* **152**: 579-606.
- Sachs, G. (1928). Zur Ableitung einer Fließbedingung. *Z. Ver. Dtsch. Ing.* **72**: 734-736.
- Schafner, E., M. Zehetbauer and T. Ungár (2001). Measurement of screw and edge dislocation density by means of x-ray Bragg profile analysis. *Materials Sciences and Engineering* **A319-321**: 220-223.
- Sharp, T. G., G. Y. A. Bussod and T. Katsura (1994). Microstructures in  $\beta\text{-Mg}_{1.8}\text{Fe}_{0.2}\text{SiO}_4$  experimentally deformed at transition-zone conditions. *Physics of the Earth and Planetary Interiors* **86**: 69-83.
- Shimomura, O., W. Utsumi, T. Taniguchi, T. Kikegawa and T. Nagashima (1992). A new high pressure and high temperature apparatus with sintered diamond anvils for synchrotron radiation use. *in* High pressure research: Application to Earth and planetary sciences. Y. Syono and M. H. Manghnani. Tokyo, Terra Scientific Publishing Company. **3**: 3-11.
- Siemes, H. and C. Hennig-Michaeli (1985). Ore minerals. *in* Preferred orientation in deformed metals and rocks: an introduction to modern texture analysis. H. R. Wenk, Academic Press.

## REFERENCES

- Siesler, H. M., Y. Ozaki, S. Kawata and H. M. Heise (2002). Near-infrared spectroscopy, principles, instruments, applications. Weinheim, Wiley-VCH.
- Silver, P. G. (1996). Seismic anisotropy beneath the continents: Probing the depths of geology. *Ann. Rev. Earth Planet. Sci* **24**: 385-432.
- Singh, A. K., C. Balasingh, H.-k. Mao, R. J. Hemley and J. Shu (1998). Analysis of lattice strain measured under nonhydrostatic pressure. *Journal of Applied Physic* **83**(12): 7567-7575.
- Sinogeikin, S. V., T. Katsura and J. D. Bass (1998). Sound velocities and elastic properties of Fe-bearing wadsleyite and ringwoodite. *J. Geophys. Res. B.* **103**: 819-825.
- Smith, J. V. and B. Mason (1970). Pyroxene-garnet transformation in Coorara meteorite. *Science* **168**: 832-833.
- Suzuki, A., E. Ohtani, H. Morishima, T. Kubo, Y. Kanbe and T. Kondo (2000). In situ determination of the phase boundary between wadsleyite and ringwoodite in  $Mg_2SiO_4$ . *Geophysical Research Letters* **27**: 803-806.
- Taleb, L., N. Cavallo and F. Waeckel (2001). Experimental analysis of transformation plasticity. *International Journal of plasticity* **17**: 1-20.
- Taylor, G. I. (1938). Plastic strain in metals. *J. Inst. Met.* **62**: 307-324.
- Thoraval, C., P. Machetel and A. Cazenave (1995). Locally layered convection inferred from dynamic models of the Earth's mantle. *Nature* **375**: 777-780.
- Thurel, E. (2001). Etude par microscopie electronique en transmission des mécanismes de déformation de la wadsleyite et de la ringwoodite. PhD Dissertation, Université des Sciences et Technologies de Lille.

## REFERENCES

---

- Thurel, E. and P. Cordier (2003a). Plastic deformation of wadsleyite: I. High-pressure deformation in compression. *Phys. Chem. Minerals* **30**: 256–266.
- Thurel, E., P. Cordier, D. J. Frost and S.-i. Karato (2003b). Plastic deformation of wadsleyite: II. High-pressure deformation in shear. *Phys. Chem. Minerals* **30**: 267–270.
- Thurel, E., J. Douin and P. Cordier (2003c). Plastic deformation of wadsleyite: III. Interpretation of dislocations and slip systems. *Phys. Chem. Minerals* **30**: 271–279.
- Tommasi, A. (1998). Forward modeling of the development of seismic anisotropy in the upper mantle. *Earth and Planetary Science Letters* **160**: 1–13.
- Tommasi, A., D. Mainprice, G. Canova and Y. Chastel (2000). Viscoplastic self-consistent and equilibrium-based modeling of olivine lattice preferred orientations: Implications for upper mantle seismic anisotropy. *Journal of Geophysical Research* **105**: 7893–7908.
- Tommasi, A., B. Tikoff and A. Vauchez (1999). Upper mantle tectonics: Three-dimensional deformation, olivine crystallographic fabric and seismic properties. *Earth and Planetary Science Letters* **168**: 173–186.
- Trampert, J. and H. J. van Heijst (2002). Global anisotropy, azimuthal anisotropy in the transition zone. *Science* **296**: 1297–1299.
- Turner, F. J. (1948). Mineralogical and structural evolution of the metamorphic rocks. *Mem. geol. Soc. Am.* **30**.
- Ungár, T. and A. Borbély (1996). The effect of dislocation contrast on X-ray line broadening: a new approach to line profile analysis. *Appl. Phys. Lett.* **69**: 3173–3175.

## REFERENCES

- Ungár, T., I. Dragomir, A. Révész and A. Borbely (1999). The contrast factor of dislocations in cubic crystals: The dislocation model of strain anisotropy in practice. *Journal of Applied Crystallography* **32**: 992–1002.
- Ungár, T., J. Gubicza, P. Hanak and I. Alexandrov (2001a). Densities and character of dislocations and size-distribution of subgrains in deformed metals by x-ray diffraction profile analysis. *Materials Sciences and Engineering* **A319–321**: 274–278.
- Ungár, T., J. Gubicza, G. Ribarik and A. Borbely (2001b). Crystallite size distribution and dislocation structure determined by diffraction profile analysis: principles and practical application to cubic and hexagonal crystals. *Journal of Applied Crystallography* **34**: 298–310.
- Ungár, T. and G. Tichy (1999). The effect of dislocation contrast on X-ray line profiles in untextured polycrystals. *Phys. Stat. Sol. A* **147**: 425–434.
- Vauchez, A., F. Dineur and R. Rudnick (2003). Microstructure, texture and seismic anisotropy of the lithospheric mantle above a mantle plume. Insights from the Labait volcano xenoliths (Tanzania). **submitted**.
- Veyssiére, P., J. Rabier, H. Garem and J. Grilhé (1978). Influence of temperature on dissociation of dislocation and plastic deformation in spinel oxides. *Philosophical Magazine A* **38**(1): 61–79.
- Wang, Y., W. B. Durham, I. C. Getting and D. J. Weidner (2003). The deformation-DIA: A new apparatus for high temperature triaxial deformation to pressures up to 15 GPa. *Review of Scientific Instruments* **74**(6): 3002–3011.
- Wang, Y., I. C. Getting, D. J. Weidner and M. Vaughan (1998). Performance of tapered anvils in a DIA-type, cubic-anvil, high -pressure apparatus for X ray diffraction studies. *in* Properties of Earth and planetary

## REFERENCES

---

- materials at high pressure and temperature. M. H. Manghnani and T. Yagi. Washington, American Geophysical Union. **101**: 35–39.
- Wang, Y., R. C. Liebermann and J. N. Boland (1988). Olivine as in situ piezometer in high pressure apparatus. *Physics and chemistry of minerals* **15**: 493–497.
- Warren, B. E. and B. L. Avenbach (1950). The effect of cold work distortion on X-ray pattern. *J. Appl. Phys.* **21**: 595–610.
- Wedel, A., W. Skrotzki and K. Weber (1992). Microstructure and texture in peridotite xenoliths from the Hessian Depression. *Geotektonische Forschungsheft* **78**: 89–125.
- Weidner, D. J. (1998). Rheological studies at high pressure. *in* *Ultrahigh-Pressure Mineralogy*. R. J. Hemley. Washington, DC, Mineralogical Society of America. **37**: 493–524.
- Weidner, D. J., Y. Wang, G. Chen, J. Ando and M. T. Vaughan (1998). Rheology measurements at high pressure and temperature. *in* *Properties of Earth and Planetary Materials at High Pressure and Temperature*. M. H. Manghnani and Y. Syono. Washington D.C., American Geophysical Union: 473–482.
- Wenk, H. R., K. Bennett, G. R. Canova and A. Molinari (1991). Modelling plastic deformation of peridotite with the self-consistent theory. *J. Geophys. Res.* **96**: 8337–8349.
- Wenk, H.-R., I. Lonardeli, J. Pehl, J. Devine, V. Prakapenka, G. Shen and H.-K. Mao (2004). *In situ* observation of texture development in olivine, ringwoodite, magnesiowustite and silicate perovskite at high pressure. *Earth and Planetary Science Letters* **226**(3–4): 507–519.
- Wenk, H. R. and C. N. Tomé (1999). Modeling dynamic recrystallisation of olivine aggregates deformed in simple shear. *J Geophys Res Solid Earth* **104**: 25513– 25527.

## REFERENCES

---

- Wilkins, M. (1970). The determination of density and distribution of dislocations in deformed single crystals from broadened X-ray diffraction profiles. *Phys. Stat. Sol. A* **2**: 359–370.
- Williamson, G. K. and W. H. Hall (1953). X-ray line broadening from filed aluminium and wolfram. *Acta Metall.* **1**: 22–31.
- Xu, Y., D. J. Weidner, J. Chen, M. T. Vaughan, Y. Wang and T. Uchida (2003). Flow-law for ringwoodite at subduction zone conditions. *Physics of the Earth and Planetary Interiors* **136**: 3–9.
- Yamazaki, D. and S.-i. Karato (2001). High-pressure rotational deformation apparatus to 15 GPa. *Rev. Sci. Instruments* **72**(11): 4207–4211.
- Yamazaki, D. and S.-i. Karato (2002). Fabric development in (Mg,Fe)O during large strain, shear deformation: implications for seismic anisotropy in Earth's lower mantle. *Physics of the Earth and Planetary Interiors* **131**: 251–267.
- Yang, L. H., P. Söderlind and J. A. Moriarty (2001a). Accurate atomistic simulation of  $(a/2)\langle 111 \rangle$  screw dislocations and other defects in bcc tantalum. *Philosophical Magazine A* **81**: 1355.
- Yang, L. H., P. Söderlind and J. A. Moriarty (2001b). Atomistic simulation of pressure-dependent screw dislocation properties in bcc tantalum. *Materials Science and Engineering A* **309–310**: 102–107.
- Young III, C. (1969). Dislocations in the deformation of olivine. *American Journal of Science* **267**: 841–852.
- Zamora, M. and J. P. Poirier (1983). Experiments in anisothermal transformation plasticity: the case of cobalt. *Geophysical implication. Mechanics of Materials* **2**: 193–202.

## REFERENCES

---

- Zha, C.-s., T. S. Duffy, H. Mao, R. T. Downs, R. J. Hemley and D. J. Weidner (1997). Single-crystal elasticity of beta -Mg (sub 2) SiO (sub 4) to the pressure of the 410 km seismic discontinuity in the Earth's mantle,. *Earth Planet. Sci. Lett.*, **147**: E9-E15.
- Zhang, J., B. Li, W. Utsumi and R. C. Liebermann (1996). In situ X-Ray observations of the coesite-stishovite transition: Reversed phase boundary and kinetics. *Physics and Chemistry of Minerals* **23**: 1-10.
- Zhang, S. and S.-i. Karato (1995). Lattice preferred orientation of olivine aggregates deformed in simple shear. *Nature* **375**: 774-777.
- Zhang, S., S.-i. Karato, J. Fitzgerald, U. H. Faul and Y. Zhou (2000). Simple shear deformation of olivine aggregates. *Tectonophysics* **316**: 133-152.

# Erklärung

Hiermit erkläre ich, dass ich die vorliegende Arbeit selbständig verfasst und keine anderen als die von mir angegebenen Quellen und Hilfsmittel verwendet habe.

Ferner erkläre ich, dass ich anderweitig mit oder ohne Erfolg nicht versucht habe, diese Dissertation einzureichen. Ich habe außerdem keine gleichartige Doktorprüfung an einer Hochschule endgültig nicht bestanden.

Bayreuth, 01.12.2004

Hélène Couvy



## Shear deformation experiments of forsterite at 11 GPa - 1400°C in the multianvil apparatus

HÉLÈNE COUVY<sup>1,2</sup>, DANIEL J. FROST<sup>1</sup>, FLORIAN HEIDELBACH<sup>1</sup>, KRISZTIÁN NYILAS<sup>3</sup>, TAMÁS UNGÁR<sup>3</sup>,  
STEPHEN MACKWELL<sup>1,\*</sup> and PATRICK CORDIER<sup>2,\*\*</sup>

<sup>1</sup>Bayerisches Geoinstitut, Universität Bayreuth, Germany

<sup>2</sup>Laboratoire de Structure et Propriétés de l'Etat Solide, UMR CNRS 8008, Université des Sciences  
et Technologies de Lille, Villeneuve d'Ascq, France

<sup>3</sup>Department of General Physics, Eötvös University Budapest, H-1445 Múzeum krt. 6-8,  
Budapest VIII, P.O.B. 323, Hungary

**Abstract:** Synthetic forsterite samples were shear-deformed at 11 GPa, 1400°C in the multianvil apparatus. The deformation microstructures have been characterised by SEM, EBSD, X-ray diffraction peak broadening and strain anisotropy analysis, and TEM. Different time durations have been characterised with a view to follow the evolution of strain and stress in high-pressure deformation experiments. A high density of [001] dislocations is introduced during pressurization at room temperature although no significant macroscopic shear or crystal preferred orientations are induced at this stage. The deviatoric stress is probably on the order of 1.5 GPa. Heating at 1400°C leads to a rapid decrease of the density of these dislocations. The shear deformation at high-temperature leads to measurable strain and development of crystal preferred orientations after one hour. Stress and strain-rate continue to decrease with time, such that eight hour experiments exhibit microstructures where recovery is apparent. At this stage, the stress level is estimated at *ca.* 100 MPa from dislocation density measurements. Crystal preferred orientations and TEM characterisation show that glide of [001] dislocations on (100) or (010) is the dominant deformation mechanism. Further investigation is needed to determine whether inhibition of [100] glide in these experiments is due to the role of water or whether a physical effect of pressure is also contributing.

**Key-words:** shear deformation, high-pressure, forsterite, dislocations, core structure.

### 1- Introduction

Olivine is by far the most abundant mineral of the upper mantle. It is also considered to be the weakest phase and hence to control the rheology of the upper mantle. For this reason, it has been clear for a long time that modelling the nature of convection in the outer 400 km of the Earth's mantle requires a good knowledge of the plastic properties of olivine. Many studies have been conducted to investigate the deformation mechanisms and flow laws of olivine single crystals (Blacic & Christie, 1973; Kohlstedt & Goetze, 1974; Durham & Goetze, 1977a and b; Darot, 1980; Darot & Gueguen, 1981; Mackwell *et al.*, 1985; Bai *et al.*, 1991; Bai & Kohlstedt 1992a and b, 1993) and polycrystals (*e.g.*, Chopra & Paterson, 1981, 1984; Karato *et al.*, 1986; Hirth & Kohlstedt, 1995a and b; Mei & Kohlstedt, 2000a and b). Bai *et al.* (1991) and Bai & Kohlstedt (1992a and b) have shown that flow laws in olivine can be described by an equation of the form:

$$\dot{\epsilon} = A \sigma^n f_Q^m a_{\text{Opx}}^q \exp(-\Delta H / RT) \quad (1)$$

where A is a constant for each particular slip system. This equation shows that the creep rate  $\dot{\epsilon}$  exhibits a dependence on stress (exponent n), oxygen fugacity (exponent m) and orthopyroxene activity (exponent q). Olivine is found to deform mostly along [001] (on (100) and (010)) at low temperature and high stress whereas [100] glide (on (010), (021), (031) and (001)) dominates at high temperature (and low stress). Although a wide range of thermochemical environments have been considered in the past, the physical conditions investigated remained quite narrow (mostly 1 atm pressure and high-temperature). Only recently has the influence of large strains (Bystricky *et al.*, 2000; Zhang *et al.*, 2000) and high-pressure (Karato & Rubie, 1997; Jung & Karato, 2001; Li *et al.*, 2003, 2004; Raterron *et al.*, 2003) been considered. Pressure has been shown to have a strong influence on the point defect chemistry (and hence on rheology) under "wet" conditions (Mackwell *et al.*, 1985; Mei & Kohlstedt, 2000a and b; Jung & Karato, 2001). Experiments performed on olivine powders at 8 GPa and temperatures to 1475 K in a multianvil apparatus have

\*E-mail: presently at : Lunar and Planetary Institute, 3600 Bay Area Blvd, Houston, TX 77058-1113, USA

\*\*Patrick.Cordier@univ-lille1.fr

## Strain-induced seismic anisotropy of wadsleyite polycrystals and flow patterns in the mantle transition zone

Andréa Tommasi,<sup>1</sup> David Mainprice,<sup>1</sup> Patrick Cordier,<sup>2</sup> Catherine Thoraval,<sup>1</sup> and Héléne Couvy<sup>2,3</sup>

Received 29 April 2004; revised 4 October 2004; accepted 8 October 2004; published 17 December 2004.

[1] We use forward models based on recent high-pressure experimental data on mantle minerals to predict the seismic anisotropy produced by plastic strain of orthorhombic wadsleyite, the dominant mineral in the upper transition zone. These models predict a weak seismic anisotropy for a polycrystal of pyrolytic composition (60% wadsleyite, 40% garnet) at transition zone conditions:  $\sim 2\%$  for  $P$  and  $\sim 1\%$  for  $S$  waves for a shear strain of 1. Both  $P$  and  $S$  wave anisotropy patterns show an orthorhombic symmetry.  $P$  waves propagate faster at low angle to the shear direction and slower at high angle to the shear plane.  $S$  wave anisotropy is characterized by faster propagation of waves polarized at low angle to the shear direction. Horizontal shearing results therefore in higher velocities for horizontally propagating  $P$  waves ( $PH$ ) and horizontally polarized  $S$  waves ( $SH$ ), as well as in weak azimuthal variation of  $SV$  and  $SH$  velocities. On the other hand, vertical flow leads to higher velocities for vertically propagating  $P$  waves ( $PV$ ) and vertically polarized  $S$  waves ( $SV$ ) and to a weak azimuthal variation of  $SV$  velocity but to a roughly constant  $SH$  velocity. Analysis of global observations of seismic anisotropy in the transition zone in the light of these models supports dominant horizontal flow in the uppermost transition zone, in agreement with predictions of geodynamical models that explicitly introduce phase transitions. **INDEX TERMS:** 3902 Mineral Physics: Creep and deformation; 8120 Tectonophysics: Dynamics of lithosphere and mantle—general; 8121 Tectonophysics: Dynamics, convection currents and mantle plumes; 7207 Seismology: Core and mantle; **KEYWORDS:** mantle convection, seismic anisotropy, crystal preferred orientation

**Citation:** Tommasi, A., D. Mainprice, P. Cordier, C. Thoraval, and H. Couvy (2004), Strain-induced seismic anisotropy of wadsleyite polycrystals and flow patterns in the mantle transition zone, *J. Geophys. Res.*, 109, B12405, doi:10.1029/2004JB003158.

### 1. Introduction

[2] Convection patterns in the Earth's mantle depend strongly on how physical properties are modified by the pressure-induced phase changes that take place in the transition zone, i.e., between 410 and 670 km depth. After a long debate on whether mantle convection was double- or single-layered, current models tend to favor a single-layer convection in which the transition zone behaves as a more or less permeable barrier. Indeed, geodynamical models show that, because of its negative Clapeyron slope [Akoogi *et al.*, 1989], the ringwoodite to perovskite + magnesiowüstite phase change at the base of the transition zone slows material transfer across the transition zone, leading to intermittently layered convection [Christensen and Yuen, 1985; Machel and Weber, 1991]. This convection style, in between whole mantle and layered convection, may

explain, for instance, that some slabs, like the Marianas and Java, plunge steeply across the transition zone, penetrating promptly into the lower mantle, whereas others, like the Japan, southern Kurile, and Izu-Bonin, are deflected within the transition zone [van der Hilst *et al.*, 1991]. Partially (or locally) layered convection also reconciles dynamic topography predicted in mantle circulation models with observations [Thoraval *et al.*, 1995; Cadek and Fleitout, 1999].

[3] Knowledge of flow patterns within the transition zone layer is thus essential to constrain the structure of mantle circulation. Seismic anisotropy observations are undoubtedly the best tool to image flow patterns in the deep Earth, since anisotropy, as in the upper mantle, may result from strain-induced crystal-preferred orientation (CPO) of elastically anisotropic minerals. Seismic anisotropy in the transition zone at a global scale was first suggested by a joint analysis of body wave travel times and free oscillation frequencies [Montagner and Kennett, 1996], which showed that these data may be reconciled by a weak radial anisotropy in the transition zone. This anisotropy is characterized by higher velocities of horizontally propagating compressional waves ( $PH$ ) and horizontally polarized shear waves ( $SH$ ) relatively to vertically propagating compressional waves ( $PV$ ) and vertically polarized shear waves ( $SV$ ), respectively. Faster

<sup>1</sup>Laboratoire de Tectonophysique, CNRS/Université de Montpellier II, Montpellier, France.

<sup>2</sup>Laboratoire Structure et Propriétés de l'Etat Solide, CNRS/Université de Lille, Villeneuve d'Ascq, France.

<sup>3</sup>Bayerisches Geoinstitut, Universität Bayreuth, Bayreuth, Germany.

**Acknowledgements** We thank A. Moore and P. T. Atkins for field and laboratory assistance. This research was supported by grants from the A. W. Mellon Foundation to L.A.D. and O.A.C., and from the N.S.F. to L.A.D., O.A.C. and A.C.K.

**Competing interests statement** The authors declare that they have no competing financial interests.

**Correspondence** and requests for materials should be addressed to L.A.D. (lad9@cornell.edu).

## Pressure sensitivity of olivine slip systems and seismic anisotropy of Earth's upper mantle

David Mainprice<sup>1</sup>, Andréa Tommasi<sup>1</sup>, H  le  ne Couvy<sup>2,3</sup>, Patrick Cordier<sup>2</sup> & Daniel J. Frost<sup>3</sup>

<sup>1</sup>Laboratoire de Tectonophysique, CNRS/Universit   de Montpellier II, F-34095 Montpellier cedex 5, France

<sup>2</sup>Laboratoire Structure et Propri  t  s de l'Etat Solide, CNRS/Universit   de Lille I, F-59650 Villeneuve d'Ascq, France

<sup>3</sup>Bayerisches Geoinstitut, Universit  t Bayreuth, D-95440 Bayreuth, Germany

The mineral olivine dominates the composition of the Earth's upper mantle and hence controls its mechanical behaviour and seismic anisotropy. Experiments at high temperature and moderate pressure, and extensive data on naturally deformed mantle rocks, have led to the conclusion that olivine at upper-mantle conditions deforms essentially by dislocation creep with dominant [100] slip. The resulting crystal preferred orientation has been used extensively to explain the strong seismic anisotropy observed down to 250 km depth<sup>1-4</sup>. The rapid decrease of anisotropy below this depth has been interpreted as marking the transition from dislocation to diffusion creep in the upper mantle<sup>5</sup>. But new high-pressure experiments suggest that dislocation creep also dominates in the lower part of the upper mantle, but with a different slip direction. Here we show that this high-pressure dislocation creep produces crystal preferred orientations resulting in extremely low seismic anisotropy, consistent with seismological observations below 250 km depth. These results raise new questions about the mechanical state of the lower part of the upper mantle and its coupling with layers both above and below.

Despite the considerable effort to characterize olivine's deformation mechanisms over the past 30 yr, it is only recently that deformation experiments could be conducted at pressure-temperature conditions of the entire upper mantle<sup>6-8</sup>. New simple-shear experiments on olivine aggregates at 11 GPa and 1,400   C, conditions equivalent to those at depths of 330 km, have shown that deformation takes place by dislocation creep, with dominant activation of [001]{hk0} slip systems<sup>9</sup>, suggested by the concentration of [001] parallel to the shear direction and of [100] and [010] normal to the shear plane (Fig. 1). Transmission electron microscopy shows the exclusive presence of dislocations with [001] Burgers vectors in a screw orientation, compatible with [001]{hk0} slip. Dominant [001] slip in the deep upper mantle requires re-evaluation of the interpretation of anisotropic physical properties. For instance, the fastest P-wave velocity will no longer parallel the shear direction as in an upper mantle deforming by dominant [100]{010} slip, which is the assumption traditionally used in relating flow and seismic anisotropy in the mantle<sup>10,11</sup>.

Several lines of evidence point to seismic anisotropy decreasing with depth in the upper mantle. Most global one-dimensional models (PREM, IASP, AK135 and AK303) show horizontally propagating P waves travelling (at velocity  $v_{PH}$ ) faster than vertical ones (at  $v_{PV}$ ), but the difference in velocity reduces with depth, resulting in isotropic behaviour at 350 km depth<sup>1</sup>. Some models (AK135 and 303) even show  $v_{PV}$  slightly faster than  $v_{PH}$  below 350 km. The S-wave polarization anisotropy also decreases monotonically from the surface to become isotropic at 250 km. For horizontally propagating S waves, horizontally polarized waves show a higher velocity ( $v_{SH}$ ) than vertically polarized waves ( $v_{SV}$ ) down to about 250 km depth. Between 300 km and 400 km depth,  $v_{SV}$  is higher than  $v_{SH}$ , but anisotropy is five times lower than in the uppermost mantle. High-resolution global tomographic models based on S-wave data<sup>12</sup> or on the inversion of three-component surface and body waveform data<sup>13</sup> support these general findings, with strong anisotropy characterized by  $v_{SH} > v_{SV}$  above 250 km depth. At greater depth, these models require a strong decrease in anisotropy, with a minimum around 300 km depth. S-wave data also call for weak anisotropy, with  $v_{SV} > v_{SH}$  at the base of the upper mantle beneath the central Pacific and Pre-Cambrian cratons<sup>12</sup>. Regional surface wave studies in the Pacific and Indian ocean basins also suggest that anisotropy is present from the surface to ~250-300 km depth<sup>1-3,14</sup>, with  $v_{SH}$  being greater than  $v_{SV}$ . Analysis of two-station surface wave profiles in the Pacific and Philippine plates imply a still shallower anisotropy limited to the upper 160 km of the mantle<sup>15</sup>. SKS studies cannot constrain the depth of the anisotropic layer, but the strong correlation of the direction of polarization of the fast shear wave with the surface geology and the observed delay times  $\approx 2$  s (ref. 14) suggests that SKS splitting occurs in the upper 200-250 km of the mantle.

Finally, a regional seismic discontinuity, called the Lehmann discontinuity, has been detected at about 220 km depth by various seismic methods (reflection, surface waves, ScS reverberations and P to S conversions), mainly beneath continents. This discontinuity has been interpreted as being due to either (1) a strong anisotropy caused by intense deformation of olivine in a zone of mechanical coupling between the lithosphere and the asthenosphere<sup>16</sup>, or (2) the transition between an isotropic uppermost mantle deforming by dislocation creep (which produces a crystal preferred orientation, CPO, of olivine) and an isotropic deep mantle deforming by diffusion creep (which does not produce CPO)<sup>3</sup>. However, recent high-pressure, high-temperature experiments show that even in fine-grained aggregates (~20-30   m), dislocation creep is the dominant deformation mechanism under conditions equivalent to those prevailing at 300 km depth<sup>9,17,18</sup>.

The pressure, or pressure interval, at which the transition from

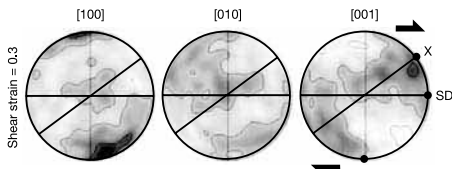


**Figure 1** Preferred orientation of [100], [010] and [001] crystallographic axes in synthetic olivine polycrystal S2954 deformed at 1,400   C and 11 GPa confining pressure in simple shear<sup>9</sup>. Lower hemisphere equal-area projection, contours at intervals of 0.5 multiples of a uniform distribution. 3,269 measured orientations. Dextral shear (top to the right) is indicated by half-arrows; SD, shear direction; NSP, normal to shear plane; X, finite strain extension direction. Shear strain ~0.3. Inclined black line marks the foliation (flattening plane).

## letters to nature

[100](010) to [001](*hk*0) slip occurs has still not been characterized, but it must be less than 11 GPa, which corresponds to 330 km depth<sup>9</sup>. Constraints on the minimum depth for this transition may be derived from the analysis of olivine CPO patterns in naturally deformed mantle rocks<sup>19</sup>. Spinel-peridotites that are equilibrated above 70 km depth display solely CPO characteristic of [100] slip. This CPO is also dominant in high-pressure garnet-peridotites from South Africa equilibrated between 70 km and 150 km depth<sup>20</sup>. CPO suggesting activation of both slip directions at high-temperature conditions is restricted to rare high-pressure peridotite mylonites from the Tanzanian and Kaapvaal cratons equilibrated at ~140 km depth<sup>21</sup>. This suggests that [100] slip dominates in the mantle above 150 km depth.

We simulated development of CPOs in olivine polycrystals deformed in simple shear under high-pressure conditions, using a viscoplastic self-consistent (VPSC) model<sup>22</sup> that has been extensively tested for olivine<sup>23,24</sup>. In this model, as in all polycrystal plasticity approaches, CPO evolution is essentially controlled by the imposed deformation, the initial texture, and the active slip systems. The last depend on the mineral structure, but also on the temperature and pressure conditions, which control their relative strength or critical resolved shear stress (CRSS). In Fig. 2, we show the CPO developed in an aggregate of 500 initially spherical and randomly oriented olivine grains after a shear strain of 0.3 and 1.0; [001] axes tend to align in-between the stretching and the shear direction, and [100] and [010] axes concentrate at high angles to the shear plane. In this simulation, CRSS for the [001](*hk*0), [100](001) and [100](010), and [100](011) and [100](021) systems are 1:3:6; that is, slip on [001](*hk*0) is three times easier than slip on [100](010) and six times easier than on [100](021). Yet tests with different CRSS values predicted similar CPO for all combinations in which slip in [001] systems is significantly easier than in [100] systems. Comparison with olivine CPO formed in recent high-temperature high-pressure experiments in simple shear (Fig. 1) provides evidence that these models give good estimates of olivine CPO in the lower part of the upper mantle.

The three-dimensional distribution of seismic velocities in a polycrystalline aggregate may be estimated by averaging the individual grain elastic constant tensors as a function of the crystallographic orientations and mineralogical composition of the aggregate. Seismic properties (Fig. 3) of an upper-mantle sample with pyrolytic composition (63% olivine, 17% garnet, 20% dino-

pyroxene) at a pressure of 11.8 GPa and temperature of 1,380 °C, corresponding to 355 km depth, were calculated using recently determined elastic constant tensors of olivine<sup>25</sup>, pyrope-rich garnet<sup>26</sup> and diopside<sup>27</sup>. Olivine displays the modelled CPO (Fig. 2). Garnet has a random CPO; this agrees with predictions of VPSC simulations and observations in naturally deformed garnet-rich rocks that show that garnet CPOs are always very weak<sup>28</sup>. We have assumed that diopside also has a random orientation as high-pressure data are lacking for this mineral. However, if diopside has a CPO similar to that developed under high-temperature/low-pressure conditions<sup>29</sup>, it will tend to reduce anisotropy by destructive interference with olivine<sup>30</sup>. Both compressional and shear waves display weak anisotropies (0.9% and 1.9%, respectively). The fastest compressional waves propagate at a high angle to the shear plane. The variation of compressional waves' velocities within the shear plane is very small. Thus in a mantle deforming by horizontal shearing, almost no azimuthal variation of P-wave velocity ( $v_P$ ) would be observed and vertically propagating P waves would be only slightly faster than those propagating horizontally. The polarization anisotropy of shear waves is characterized by faster propagation of waves polarized at a high angle to the shear plane, and the largest delay times are observed for propagation at a high angle to the shear direction in the shear plane. For propagation in the shear plane, the fastest S waves are polarized at a high angle to the shear plane. Hence, for horizontal flow,  $v_{SV}$  is greater than  $v_{SH}$ .

All the above predictions are consistent with global and regional seismic observations<sup>1-4,12-14</sup>, which show a weak anisotropy (<2%) below 250 km depth for P and S waves. The predicted S-wave anisotropy, although weak (1.9%), is twice as strong as the P-wave anisotropy observed in global models<sup>4</sup>. Anisotropy patterns observed in global models (transverse isotropy with a vertical symmetry axis) are best reproduced for horizontal shearing. For such a flow pattern, our simulations predict that vertical P waves propagate faster than horizontal ones, and that for horizontally propagating S waves  $v_{SV}$  is greater than  $v_{SH}$ , in agreement with global models of anisotropy patterns for depths greater than 300 km. In addition, vertically propagating shear waves will detect no anisotropy.

We conclude that dominant activity of [001](*hk*0) in olivine at high pressure is entirely compatible with the available seismic data, which indicate a weak anisotropy in the upper mantle below 300 km. It is difficult to imagine another scenario that would reproduce the anisotropy patterns of P and S waves in such detail. The interpretation presented here allows us to consider that the

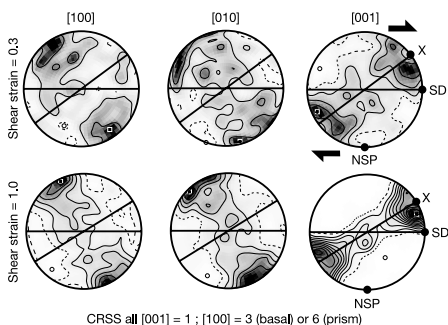


**Figure 2** Olivine crystal preferred orientations predicted using a viscoplastic self-consistent model. Data are shown for a shear strain of 0.3 (top) and 1.0 (bottom). Lower hemisphere equal-area projection, contours at intervals of 0.5 multiples of a uniform distribution, 500 grains. Symbols and abbreviations as Fig. 1.

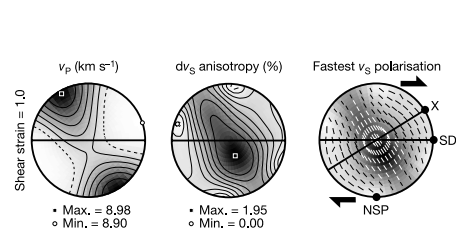


**Figure 3** Modelled three-dimensional compressional velocity and shear wave anisotropy distributions, and fastest shear wave polarization. Data shown for an aggregate composed of 63% anisotropic olivine and isotropic garnet and diopside (17% and 20%, respectively) at 11.8 GPa and 1,380 °C. Lower hemisphere equal-area projections; contours at 0.1 km s<sup>-1</sup> intervals for compressional waves, 0.02 km s<sup>-1</sup> intervals for shear waves, and 0.5% anisotropy intervals for shear wave polarization anisotropy. Dashed line marks minimum contours. Maximum P-wave and S-wave anisotropy is 0.9% and 1.9%, respectively. Black and white lines (for low and high anisotropy, respectively) in right panel indicate the direction of polarization of the fast shear wave.

weakly anisotropic upper mantle layer below 250 km depth is actively deforming by dislocation creep, and hence the top and bottom layers may be strongly coupled down to 400 km depth. Our predictions (that weak seismic anisotropy will develop in olivine-rich aggregates deforming by [001] (*hk*0) slip in the deep upper mantle) challenge the two traditional interpretations for regions in the deep Earth of weak seismic anisotropy; (1) that they represent zones of poor deformation coherence at the seismic length scale, or (2) that the dominant deformation mechanism (for example, diffusion creep) in these regions does not produce CPO. Indeed, transition from dominant [100] to [001] slip at high pressure may explain the variation with depth of the anisotropy patterns of P and S waves, even if the entire upper mantle deforms coherently with a dominant horizontal shearing component (as expected in a convective system with large-scale plates at the surface, like the Earth's mantle). □

Received 11 August; accepted 30 November 2004; doi:10.1038/nature03266.

1. Montagner, J.-P. Seismic anisotropy of the Pacific Ocean inferred from long-period surface waves dispersion. *Phys. Earth Planet. Inter.* **38**, 28–50 (1985).
2. Cara, M. & Lèvéque, J. L. Anisotropy of the asthenosphere: The higher mode data of the Pacific revisited. *Geophys. Res. Lett.* **15**, 205–208 (1988).
3. Nishimura, C. E. & Forsyth, D. W. The anisotropic structure of the upper mantle in the Pacific. *Geophys. J.* **96**, 203–230 (1989).
4. Montagner, J.-P. & Kennett, B. L. N. How to reconcile body-wave and normal-mode reference earth models. *Geophys. J. Int.* **125**, 229–248 (1996).
5. Karato, S.-I. On the Lehman discontinuity. *Geophys. Res. Lett.* **19**, 2255–2258 (1992).
6. Karato, S.-I. & Rubie, D. C. Toward an experimental study of deep mantle rheology: a new multi-anvil sample assembly for deformation studies under high pressures and temperatures. *J. Geophys. Res.* **102**, 20111–20122 (1997).
7. Cordier, P. & Rubie, D. C. Plastic deformation of minerals under extreme pressure using a multi-anvil apparatus. *Mater. Sci. Eng. A* **309–310**, 38–43 (2001).
8. Durham, W. B., Weidner, D. J., Karato, S.-I. & Wang, Y. in *Plastic Deformation of Minerals and Rocks* (eds Karato, S.-I. & Wenk, H.-R.) (American Mineralogical Society, Washington, 2002).
9. Couvy, H. *et al.* Shear deformation experiments of forsterite at 11 GPa – 1400 °C in the multi-anvil apparatus. *Eur. J. Mineral.* (in the press).
10. Tommasi, A. Forward modeling of the development of seismic anisotropy in the upper mantle. *Earth Planet. Sci. Lett.* **160**, 1–13 (1998).
11. Silver, P. G. Seismic anisotropy beneath the continents: Probing the depths of geology. *Annu. Rev. Earth Planet. Sci.* **24**, 385–432 (1996).
12. Ekström, G. & Diewonski, A. M. The unique anisotropy of the Pacific upper mantle. *Nature* **394**, 168–172 (1998).
13. Gung, Y., Panning, M. & Romanowicz, B. Global anisotropy and the thickness of continents. *Nature* **422**, 707–711 (2003).
14. Lèvéque, J. J., Dehayle, E. & Maupin, V. Anisotropy in the Indian Ocean upper mantle from Rayleigh and Love waveform inversion. *Geophys. J. Int.* **133**, 529–540 (1998).
15. Gaherty, J. B., Jordan, T. H. & Gee, L. S. Seismic structure of the upper mantle in the central Pacific corridor. *J. Geophys. Res.* **101**, 22291–22309 (1996).
16. Revenaugh, J. & Jordan, T. Mantle layering from ScS reverberations 3. The upper mantle. *J. Geophys. Res.* **96**, 19781–19810 (1991).
17. Li, L., Raterron, P., Weidner, D., Chen, J. & Vaughan, M. T. Stress measurements of deforming olivine at high pressure. *Phys. Earth Planet. Inter.* **143–144**, 357–367 (2004).
18. Li, L., Raterron, P., Weidner, D. & Chen, J. Olivine flow mechanisms at 8 GPa. *Phys. Earth Planet. Inter.* **138**, 113–129 (2003).
19. Ben Ismail, W. & Mainprice, D. An olivine fabric database: an overview of upper mantle fabrics and seismic anisotropy. *Tectonophysics* **296**, 145–158 (1998).
20. Ben Ismail, W., Barruol, G. & Mainprice, D. The Kaapvaal craton seismic anisotropy: petrophysical analysis of upper mantle kimberlite nodules. *Geophys. Res. Lett.* **28**, 2497–2500 (2001).
21. Vauchez, A., Dincor, F. & Rudnick, R. Microstructure, texture, and seismic anisotropy of the lithospheric mantle above a plume. Insights from the Labait volcano xenoliths. *Earth Planet. Sci. Lett.* (in the press).
22. Lebensohn, R. A. & Tomé, C. N. A self-consistent anisotropic approach for the simulation of plastic deformation and texture development of polycrystals: Application to zirconium alloys. *Acta Metall. Mater.* **41**, 2611–2624 (1993).
23. Wenk, H.-R., Bennet, K., Canova, G. R. & Molinari, A. Modelling plastic deformation of peridotite with the self-consistent theory. *J. Geophys. Res.* **96**, 8337–8349 (1991).
24. Tommasi, A., Mainprice, D., Canova, G. & Chastel, Y. Viscoplastic self-consistent and equilibrium-based modeling of olivine lattice preferred orientations. Implications for upper mantle seismic anisotropy. *J. Geophys. Res.* **105**, 7893–7908 (2000).
25. Abramson, E. H., Brown, M., Slutsky, L. J. & Zaugg, J. The elastic constants of San Carlos olivine up to 17 GPa. *J. Geophys. Res.* **102**, 12252–12263 (1997).
26. Chai, M., Brown, J. M. & Slutsky, L. J. The elastic constants of a pyrope-grossular-almandine garnet up to 20 GPa. *Geophys. Res. Lett.* **24**, 523–526 (1997).
27. Collins, M. D. & Brown, J. M. Elasticity of an upper mantle clinopyroxene. *Phys. Chem. Miner.* **26**, 7–13 (1998).
28. Mainprice, D., Bascou, J., Cordier, P. & Tommasi, A. Crystal preferred orientations of garnet: Comparison between numerical simulations and electron back-scattered diffraction (EBSD) measurements in naturally deformed eclogites. *J. Struct. Geol.* **26**, 2089–2102 (2004).
29. Bascou, J., Tommasi, A. & Mainprice, D. Plastic deformation and development of clinopyroxene lattice preferred orientations in eclogites. *J. Struct. Geol.* **24**, 1357–1368 (2002).

30. Mainprice, D., Barruol, G. & Ben Ismail, W. in *Earth's Deep Interior: Mineral Physics and Tomography from the Atomic to the Global Scale* (eds Karato, S.-I., Forte, A. M., Liebermann, R. C., Masters, G. & Stixrude, L.) 237–264 (AGU, Washington DC, 2000).

**Acknowledgements** This Letter is dedicated to the memory of G. Canova, who introduced A.T. and D.M. to VPSC modelling. H.C. was supported by the Deutsche Forschungsgemeinschaft.

**Competing interests statement** The authors declare that they have no competing financial interests.

**Correspondence** and requests for materials should be addressed to D.M. (David.Mainprice@dstu.univ-montp2.fr).

## Stratigraphic placement and age of modern humans from Kibish, Ethiopia

Ian McDougall<sup>1</sup>, Francis H. Brown<sup>2</sup> & John G. Fleagle<sup>3</sup>

<sup>1</sup>Research School of Earth Sciences, Australian National University, Canberra, ACT 0200, Australia

<sup>2</sup>Department of Geology and Geophysics, University of Utah, Salt Lake City, Utah 84112, USA

<sup>3</sup>Department of Anatomical Science, Stony Brook University, Stony Brook, New York 11794, USA

In 1967 the Kibish Formation in southern Ethiopia yielded hominid cranial remains identified as early anatomically modern humans, assigned to *Homo sapiens*<sup>1–4</sup>. However, the provenance and age of the fossils have been much debated<sup>5,6</sup>. Here we confirm that the Omo I and Omo II hominid fossils are from similar stratigraphic levels in Member I of the Kibish Formation, despite the view that Omo I is more modern in appearance than Omo II<sup>1–3</sup>. <sup>40</sup>Ar/<sup>39</sup>Ar ages on feldspar crystals from pumice clasts within a tuff in Member I below the hominid levels place an older limit of 198 ± 14 kyr (weighted mean age 196 ± 2 kyr) on the hominids. A younger age limit of 104 ± 7 kyr is provided by feldspars from pumice clasts in a Member III tuff. Geological evidence indicates rapid deposition of each member of the Kibish Formation. Isotopic ages on the Kibish Formation correspond to ages of Mediterranean sapropels, which reflect increased flow of the Nile River, and necessarily increased flow of the Omo River. Thus the <sup>40</sup>Ar/<sup>39</sup>Ar age measurements, together with the sapropel correlations, indicate that the hominid fossils have an age close to the older limit. Our preferred estimate of the age of the Kibish hominids is 195 ± 5 kyr, making them the earliest well-dated anatomically modern humans yet described.

The principal outcrops of the Kibish Formation are along the Omo River where it skirts the Nkalabong Range (Fig. 1), with the highest outcrops close in elevation to that of the watershed between the Omo and the Nile rivers<sup>7,8</sup>. Former hydrographic links are apparent from Nilotic fauna in the Turkana Basin sequence<sup>8–10</sup>.

The Kibish Formation (about 100 m thick) consists of flat-lying, tectonically undisturbed, unconsolidated sediments deposited mainly in deltaic environments over brief periods. It comprises the youngest exposed sedimentary sequence in the Omo Basin, and lies disconformably upon the Nkalabong Formation<sup>11,12</sup> or on the underlying Mursi Formation<sup>12</sup>. Strata are composed principally of claystone and siltstone, with subordinate fine sandstone, conglomerate and tuffs (Fig. 2).

Butzer *et al.*<sup>13</sup> and Butzer<sup>14</sup> divided the Kibish Formation into Members I to IV on the basis of disconformities with up to 30 m relief (Fig. 2). The members record discrete times of deposition